3-D Biogeochemical and hydrodynamic models in the Azores – A tool to understand marine ecosystems

Tese de Doutoramento

Cláudia Neto Viegas

Doutoramento em

CIÊNCIAS DO MAR

Horta

2022

3-D Bio-geochemical and hydrodynamic models in the Azores – A tool to understand marine ecosystems

Tese de Doutoramento

Cláudia Neto Viegas

Orientadores

Doutora Professora Maria Manuela Fraga Juliano

Doutora Maria Ana Colaço

Tese especialmente elaborada para obtenção do grau de Doutor em Ciências do Mar

Esta bolsa de doutoramento com a referência refª SFRH/BD/129683/2017
foi financiada pela Fundação para a Ciência e Tecnologia .

Host Institution:

Marine and Environmental Sciences Centre (MARE)

Resumo

A aplicação de ferramentas de modelação numérica permite simular e estudar os processos do ambiente físico marinho e a sua influência nos processos biológicos que regem os ecossistemas marinhos, desde a interface com a atmosfera até ao mar profundo. O trabalho desenvolvido nesta tese de doutoramento contemplou a implementação de um modelo hidrodinâmico e de qualidade da água para simular os processos físicos e biogeoquímicos na região dos Açores. E a aplicação de um modelo biofísico para estudar a dispersão larvas e a conectividade física entre populações de organismos bentónicos no mar profundo.

O trabalho desenvolvido iniciou pela validação do modelo hidrodinâmico (MOHID Water) para a região dos Açores. O modelo foi validado à superfície utilizando dados de maré. Resultados de temperatura à superfície foram validados com dados de detecção remota, e ao longo da coluna de água temperatura e salinidade foram validados com dados Bóias Argo. Aplicado na região dos Açores o modelo consegue simular as principais correntes e massas de água que influenciam o ambiente marinho da região.

Com a componente hidrodinâmica validada, foi implementado um modelo de qualidade da água (MOHID WaterQuality), para reproduzir os principais processos bióticos e abióticos na coluna de água. Este modelo biogeoquímico foi parametrizado e calibrado, tendo-se verificado uma reprodução fiável das variáveis-estado (nutrientes, fitoplâncton e oxigénio) à superfície e ao longo da coluna de água. A validação com dados de detecção remota mostrou que o modelo consegue representar os seus padrões sazonais e espaciais de fitoplâncton na região: o típico bloom de fitoplâncton que acontece no início da primavera, e um menor no Outono; e o característico máximo de clorofila em profundidade (deep chlorophyll maximum – DCM), que ocorre em zonas oligotróficas como é o caso dos Açores, entre os 25 e os 100 metros de profundidade, caracterizado pela sua grande variação espacial e temporal. A validação com a climatologia (World Ocean Atlas-WOA), e com o modelo CMEMS mostrou que o modelo tem capacidade de simular as dinâmicas de nutrientes (nitrato, fosfato e silicato) e oxigénio ao longo da coluna de água. Os resultados dos capítulos 2 e 3 deste trabalho são da maior importância para caracterizar a dinâmica do ecossistema marinho dos Açores.

Para estudar a conectividade entre populações bentónicas no mar profundo dos Açores foi implementado um modelo lagrangiano Connectivity Modeling System (CMS), acoplado no modelo hidrodinâmico MOHID Water. Duas espécies alvo foram selecionadas: uma espécie séssil, *Pheronema carpenteri*, esponja do mar profundo que nos Açores se pode encontrar de forma dispersa ou em densas agregações; e uma espécie não séssil, *Chaceon Affinis*, um caranguejo de profundidade. Diferentes parâmetros biológicos foram estudados: duração do período larvar (pelagic larval duration- PLD), comportamentos larvares (larvas passivas, e larvas com capacidade de nadar (velocidade vertical ascendente e descendente). Foi feita uma análise temporal e espacial da dispersão larvar e da conectividade entre diferentes populações.

Resultados do modelo mostram que existe conectividade entre as agregações de esponjas nos Açores, sobretudo no Grupo Central (CG). As agregações dos montes submarinos do Condor, Princesa Alice e Banco Açores representam importantes locais de retenção e fonte de larvas. Estes resultados reforçam a importância de manter os esforços de proteção das Áreas Marinhas Protegidas (AMP) do Condor e Princesa Alice. Em contraponto, agregações de esponjas no Grupo Oriental, e Grupo Ocidental são mais vulneráveis, apresentando menor conectividade com as restantes agregações em estudo, e menores níveis de auto-recrutamento.

No caso de estudo do caranguejo de profundidade, *Chaceon Affinis*, foi simulada a dispersão larvar atribuindo comportamento às partículas (larvas), para que estas simulassem o comportamento que estas larvas têm de nadar e chegar à superfície. Ao contrário das larvas passivas, que arrastadas pelas correntes do mar profundo, com velocidades mais baixas (0-0.1m/s), deslocam-se poucos quilómetros (na ordem das unidades ou dezenas), as larvas que chegam à superfície, podem-se deslocar até centenas de quilómetros, transportadas pelas correntes superficiais (0 - a >0.25 m/s). Este comportamento, juntamente com o maior PLD (PLD 23, 81 e 125 dias) resulta numa conectividade mais dispersa entre as diferentes populações nos Açores. Populações no Mar da Prata, no Grupo Oriental apresentam conectividade física com populações do Grupo Ocidental. No entanto com menores probabilidades de auto-recrutamento e conectividade. Resultados do modelo mostram que populações da Crista Média Atlântica (CMA), como o Monte submarino Voador podem constituir uma importante local de retenção e fonte de larvas.

No último capítulo os resultados dos modelos implementados foram utilizados para estudar a ecologia das agregações de esponjas em estudo. Recentemente classificados como Ecossistemas Marinhos Vulneráveis (VMEs), o estudo destes ecossistemas é tópico cada vez mais relevante na comunidade científica. Os resultados do modelo mostram que estas comunidades bentónicas encontram-se em locais com baixas velocidades (entre 0.02 e 0.06m/s), e com poucos gradientes nutrientes e de temperatura (mínimo 8,7 máximo 11,9 ºC).

Os resultados gerais da tese demonstram as vantagens da aplicação de modelos para estudar os ecossistemas marinhos, e em particular a conectividade e dispersão larval. A metodologia implementada pode ser aplicada noutros estudos e aplicações, podendo servir de apoio para estudo do ecossistema marinho dos Açores, e, entre outros, no suporte à gestão dos recursos de pesca e seus ecossistemas, ou no ordenamento do espaço marinho.

Palavras chave: modelação; hidrodinâmica; biogeoquímica; mar profundo; dispersão larvar; conectividade

Abstract

The principal objective of this thesis was to implement biological and biophysical 3-D models to simulate the most significant physical and biological processes which affect the Azores archipelago and assess larval dispersal and connectivity among deep-sea populations.

Marine systems are driven primarily by physical processes. Validation of the hydrodynamic model is of paramount importance. As such, the biogeochemical and biophysical models used in this work, are coupled with the results of this 3-D hydrodynamic model (MOHID Water), and for this reason, the implementation and validation of the hydrodynamic model was undertaken in the first stage of this thesis.

The hydrodynamic model validation against tidal gauge station data showed that the model can simulate observed water levels with accuracy, effectively reproducing the amplitude and phase of tidal motions. Ultimately, model estimations were validated against remote sensing data for sea surface temperature, and along the water column against Argo buoys data for temperature and salinity. The results indicated that the model satisfactorily reproduced the data obtained *in situ* over the entire domain at the surface and along the water column. The hydrodynamic model revealed a capacity to simulate the dominant currents and the major water masses that influence the Azores region.

The third chapter focuses on the implementation of a bio-geochemical model for the Azores region. For this purpose, the MOHID water quality model was implemented, calibrated and validated. This task revealed the versatility of the MOHID water quality module in simulating different biotic and abiotic bio-geochemical processes. The results showed that the model parameterization achieved enabled a representation of seasonal and spatial phytoplankton dynamics. Validated against remote sensing data, model seasonal phytoplankton patterns were well reproduced, with the typically strong spring bloom, and the lesser autumn bloom. The model was able to simulate the deep chlorophyll maximum (DCM), at a depth of between 25 and 100 metres depth, with its characteristic spatial and seasonal variations. These upper ocean phytoplankton dynamics play an important role in ocean processes, also affecting the deep-sea environment. Model assessment against World Ocean Atlas (WOA), and a global model (CMEMS) revealed that MOHID is able to simulate vertical profiles of nutrients (nitrate, phosphate and silicate) as well as oxygen concentration. The methodology used in this dissertation revealed the possibility of future improvements to the model, and its capability to study marine systems, even as new scientific objectives emerge. The results of the Chapters 2 and 3 are of greatest importance to the characterizing of marine dynamics, from the surface up to the deep-sea.

Taking advantage of the hydrodynamic model validated in chapter 2, a biophysical particle tracking model was implemented to study larval dispersal and population connectivity in the deep-sea. Two target species were selected: a sessile organism, *Pheronema carpenteri,* a deep-sea sponge; and a non-sessile organism, *Chaceon affinis*, a deep-sea red crab (DSRC).

Different scenarios and biological characteristics were studied: the seasonality of spawning, larval pelagic duration (PLD), and larval swimming behaviour (surface-oriented and bottom-oriented swimming).
Model results show how the regional patterns of the currents drive larval dispersion, shaping population connectivity. Spawning time and PLD are determinant factors for larval dispersion and population connectivity. The lagrangian model output suggests the existence of connectivity between *Pheronema carpenteri* sponge aggregations in the Azores, mainly among populations in the Central Group (CG) of Azorean islands. The populations of the Condor Seamount, Princess Alice, and Azores Bank reveal high retention rates, receiving larvae from several sponge aggregations. These are also important source populations. The results reinforced the importance of maintaining the protection efforts in the Marine Protected Areas (MPA) of Condor and Princess Alice. The swimming behaviour simulated for DSRC larvae contributes to the higher larvae travel distances and dispersal patterns. Larval dispersal shows potential connectivity between populations across the Azores archipelago, with variable seasonal connectivity. Uneven connectivity can occur between the furthermost populations (e.g. between Mar da Prata on the eastern and Flores island on the western extremities of the archipelago). However, the low percentage of larvae exchange also indicates that the populations might be isolated and that despite the connected populations, caution should be made in the management of the populations before their exploitation. Model estimates that the populations in the Mid-Atlantic Ridge (MAR), namely Voador seamount, may constitute an important sink and source of larvae for the Azores region.
The ultimate goal of this thesis was to showcase the utilization of the constructed models to better understand the ecology of the target sponge species. In Chapter 5, physical and bio-geochemical model results are analysed, revealing that *P. Carpenteri* aggregations in the study are located in regions with low nutrient and temperature gradients (from 8.7 to 11.9 ºC), and low current velocities (from 0 to 0.06 m/s).
The thesis provides an initial description of the processes which drive larval dispersion in the deep-sea. It further demonstrates the capacity of the model to facilitate the study of various biological traits, serving as a baseline for assessing deep-sea connectivity and supporting management actions and marine spatial planning studies.
The main results highlight the advantages of coupled model systems for studying complex marine systems and various associated scenarios. The primary objective was to provide modelling methodologies and useful data to increase the current understanding of the marine ecosystem of the Azores, from the surface to the deep-sea. These hydrodynamic and bio-geochemical results can be used in further studies, like food-web and ecosystem studies, or fisheries management studies, among others.

Keywords: modelling; hydrodynamics; biogeochemical; deep-sea; larval dispersal; connectivity.

Acknowledgments

I would like to express my thanks to all the people who, in one way or another, contributed to the development of this thesis.

My deepest and sincere gratitude goes to Ana Colaço, who challenged me to pursue this PhD project, for her enthusiasm, trust, friendship, scientific advisory and unconditional support. For always believing in me, and for giving me so many opportunities to develop my scientific skills throughout these 4 years. Also for her contagious deep-sea enthusiasm.

I would like to extend my gratitude to Manuela Juliano, for her unstoppable dedication, for all the hours and days around MOHID, for helping me with these model applications, and for her pragmatism and continuous support and friendship.

I would also like to thank IMAR-Instituto do Mar for all the support, and for financing my attendance to ATT: Marine Biogeochemistry Training School on biogeochemical and ecological dimensions of a changing ocean. To the European Marine Board for the internship opportunity. I am really thankful to be given this opportunity to work in this leading European think-tank in marine science policy. Thanks to Sheila Heymans, Paula Kellet, Ángel Piniella, and Kate Larkin. To all the participants in the EXPLOSEA2 cruise, in the northern Mid-Atlantic Ridge and Azores Archipelago. To the enthusiastic PI Luiz Somosa, all the crew, the scientific team, and especially the EMEPC team (Inês Tojeira, Luísa Pinto Ribeiro, and the incredible ROV team). And to Ana Colaço for giving me this opportunity.

I would like to thank to my colleagues in DOP, especially to my open-space colleagues and friends making every day a better working day. To Neus for her help in the statistical analysis.

Because life is made of moments, friends and family, I would like to thank all of you:

"Powers" gang: Cristina, Sara, Hilda e Carina, for your friendship, and all our (un)useful conversations, since the very beginning of my journey In the Azores. "Bics" gang: a special thanks. To Maria Rakka for all the support and for being an inspiration. Ana Alves, thanks for your friendship and positive mood (and for taking care of my cats). A special thanks to David for all the hugs and the special energy. Meri, thanks for your joy and motivation. Miriam, you are an example of a strong woman. For my Shrekhouse friends: Anita, Margarida, João, Noélia e Marie (Salmi and Hortaliça are also thankful). To Cineclube do Faial-CCF friends, thanks for all the moments and all the movies. To my friends Rita e Carolina for our long-lasting friendship. Eva, my first friend in primary school, thanks for everything. Carina, is very good to have a good old friend, here in the Azores, thanks for everything. And, last but not least to all the Azorean family!

Finally, I would like to express my deepest gratitude to my mother, my father, and my sister, who always gave me unconditional support. Especially to my mother, for all her words, the unconditional love and care in all moments of my life.

Contents

Chapter 1

General introduction

1.1. Overview

Marine ecosystems are complex systems governed by hydrodynamic, meteorological and biological drivers (Vallino 2000). Primary production in the upper layer of the ocean (in the euphotic zone) and its transportation to deeper layers are key mechanisms responsible for the interaction between the surface and the deep-sea (De La Rocha and Passow, 2007). Marine plankton dynamics drive this biological pump, acting on the ocean's biogeochemical cycling, and on the entire pelagic food web, from the surface to the deep-sea (Chenillat et al. 2021). The need to understand, monitor simulate and forecast these dynamics has motivated the development of coupled biogeochemical-circulation models (Berline et al. 2007)

Over the past 30 years, the use of modelling tools and remote sensing has prompted our understanding on marine ecosystems and biogeochemical processes (Bracher et al. 2017). However, hampered by the difficulty of studying and monitoring, knowledge about the deep-sea is still very scarce. In the Azores, extensive scientific research efforts are increasing this knowledge on the functioning of oceanic, deep-sea and seamount ecosystems, as well as the impacts of human activities (Morato et al. 2020a).

A holistic approach to the biological and physical processes that influence oceanic and deep-sea ecosystem dynamics requires the use of modelling tools (Lindemann & St. John 2014). Numerical models are used to study several ocean processes (i.e. ocean circulation, coastal upwelling), while in recent years biogeochemical models have been developed to understand and quantify the main biogeochemical processes and complex dynamics between nutrients and plankton (Arhonditsis et al. 2006). Biogeochemical models have been proven to be useful tools for ecological research, to represent the feedback between the pelagic ecosystem and the physical processes (Vichi et al. 2007a, Kane et al. 2011, Aumont et al. 2015) and (3) to predict the response

of marine ecosystems to climate changes (Kishi et al. 2007, Fennel et al. 2019, Losa et al. 2019), (4) to feed other models namely: fisheries modelling and stock assessment (Fennel 2009, Mitra et al. 2014, Gutknecht et al. 2016); larval dispersal models ((Vic et al. 2018), and more recently for deep-sea habitat studies (Liu et al., 2021). Transport processes can be studied with particle tracking models, a popular approach among physical and biological oceanography studies unravelling the influence of transport processes on marine ecosystems (Paris et al. 2013). These biophysical models have emerged as an important tool for assessing structural connectivity in the deep-sea by studying pelagic larvae dispersal.

The current thesis focuses on the application of several modelling tools to better understand the oceanographic and ecosystem dynamics in the Azores, from the surface to the bottom layers. It includes the implementation and validation of a hydrodynamic model, a biogeochemical model, as well as the development of a particle tracking model to study physical connectivity (larvae dispersion) at the deep-sea, and closes with the implementation of the constructed models to study a deep-sea sponge ground, and a potential commercial fisheries species.

1.2. The Azores Archipelago

The Azores archipelago, Figure 1.1, is composed of nine volcanic islands, spanning along 600 km in the Northeast Atlantic, between 23ºW and 33ºW and 37ºN and 40ºN, and . It is located above the Mid-Atlantic Ridge (MAR), which divides the archipelago in two, leaving two islands on the American plate and the others on the Eurasian plate. The Exclusive Economic Zone (ZEE) of the Azores covers an area of more than 950 000 km^2, with more than 460 seamount-like features and several designated protected areas (Morato et al., 2008; Peran et al., 2016).

With an average depth of nearly 3000 m, the Azores region is mainly consisted of deep-sea and is dominated by a diverse mosaic of deep-sea habitats (Tempera et al. 2013, Peran et al. 2016). The deep-sea in the Azores is characterized by the presence of numerous seamounts and hydrothermal vents hosting high biodiversity and rich communities which constitute feeding grounds for fishes, marine mammals and seabirds (Morato et al. 2008, 2016b, 2020a, Giacomello & Menezes 2012, Gomes-Pereira et al. 2017). These hotspots of biodiversity, are considered extremely important to the Azores both on an ecological and socio-economic level (Giacomello & Menezes 2012).

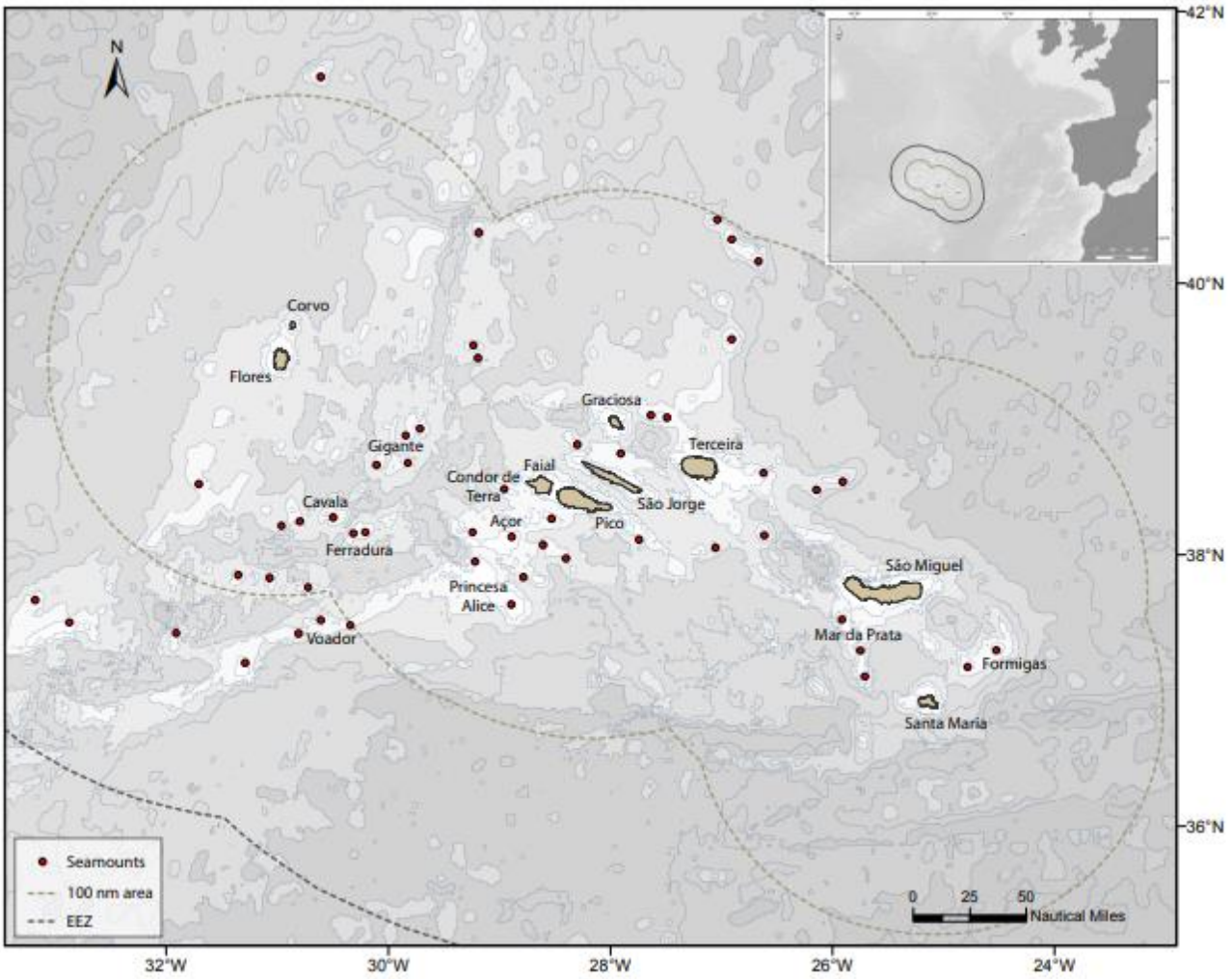

Figure 1.1- Map of the Azores archipelago, and the limits of the ZEE, the representation of the Azores islands (Flores, Corvo, Faial, Pico, São Jorge, Graciosa, Terceira, São Miguel and Santa Maria), and several seamounts, represented with a red circle. Adapted from: Braga-Henriques et al., 2013

The Azores deep-sea benthos includes a high diversity of sponges and cold-water corals which build rich communities (Pham et al. 2015, Gomes-Pereira et al. 2017, Creemers et al. 2019, Colaço et al. 2020, Morato et al. 2021). These communities have been identified as vulnerable marine ecosystems (VMEs) since they meet several of the vulnerability criteria, like fragility and low recovery potential (FAO 2008). These deep-sea organisms rely upon a planktonic larval stage for dispersal, therefore, the study of the environmental patterns responsible for their distribution is critical to inform and support the development of appropriate conservation measures (Maldonado & Young 1999, Cowen & Sponaugle 2009, Wang et al. 2021, Xavier et al. 2021).

The Azores region is affected by several water masses (Figure 1.2), the Mediterranean Water (MW), arriving at the region at 1100m depth approximately (Juliano & Alves 2006). The East North Atlantic Central Water (ENACW) fills the depths between 100 and 600m depths and the North Atlantic Deep Water (NADW) below 1500m depth. (Palma et al. 2012, Lázaro et al. 2013, Amorim et al. 2017).

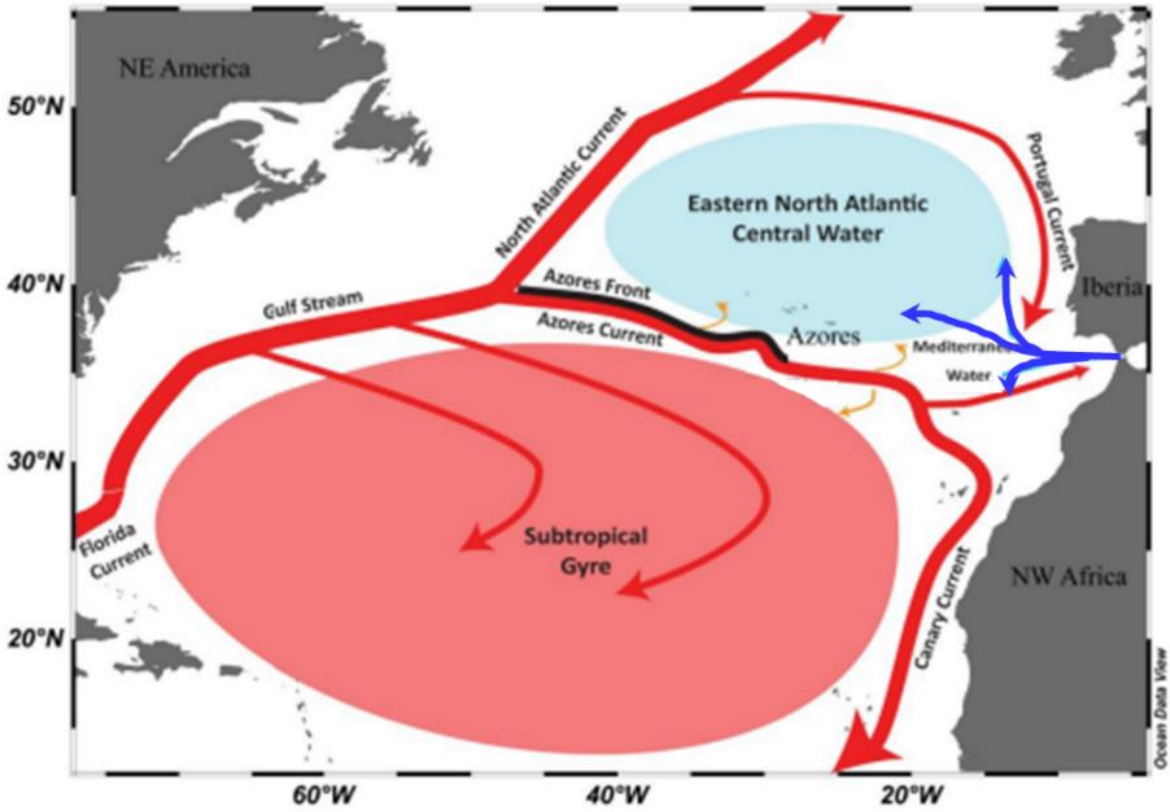

Figure 1.2- Schematic representation of the main circulation in the North Atlantic Ocean, and major water masses. Adapted from Bonfardeci et al., 2018.

The ocean climatology in the Azores is characterized by spatial, seasonal and interannual variability typical of mid-latitudes (Amorim et al. 2017). The northernmost islands are under the influence of the southward branches of the North Atlantic Current (NAC), which transport colder, less saline and possibly more productive waters into the archipelago (Narciso et al. 2016). In the South, the Azores Current, is a quasi-permanent feature, forming a thermohaline front, separating fresher and colder waters to the north and warmer and saltier water masses to the south (Juliano & Alves 2007). These different physical factors that influence ocean circulations

around the Azores archipelago, also influence the oceanographic biological processes controlling the distribution of nutrients and oxygen (Palma et al. 2012).

The Azores is an oligotrophic region, characterized by the lower nutrient concentration, where light is not a limiting factor and marine phytoplankton growth is limited by nutrients (Barcelos Ramos et al. 2017). Phytoplankton is on the base of the marine food web and drives the biogeochemical cycles in the ocean (Lan Smith et al. 2011). While nutrients are consumed by phytoplankton and diatoms, they are replaced in the water column by mineralization from those organisms, but also by vertical transport (Figure 1.3). Nutrient enrichment into the ocean surface in the Azores depends mainly on annual changes in the mixed layer depth and subsurface nutrient fields related to ocean circulation, causing nutrient upwelling from deeper layers (winter convection) (Valente, 2013). This primary winter convection that drives nutrients from the bottom until the surface layers, is induced by seasonal climatological drivers (McKinley et al. 2018).

Phytoplankton dynamics in the Azores are characterized by seasonal variation at the surface, with typical spring blooms beginning in late February/March, and weaker autumn blooms in October-November (Macedo et al. 2000, Carmo et al. 2013). Stronger spring blooms may be related to the deeper winter convection and the upper ocean layer stratification, but may also be linked to the better conditions for photosynthesis: optimal solar radiation and temperature, as well as an increase of nutrients in the surface layers caused by deep winter mixing, that induce growth of primary producers. Therefore, during summer, nutrient uptake by primary producers together with the summer stratification contributes to the decrease of nutrient concentration at the surface. During fall, the mixing of surface waters with deeper nutrient-rich waters is induced by meteorological conditions, providing the necessary nutrients for phytoplankton growth (Martinez et al. 2011).

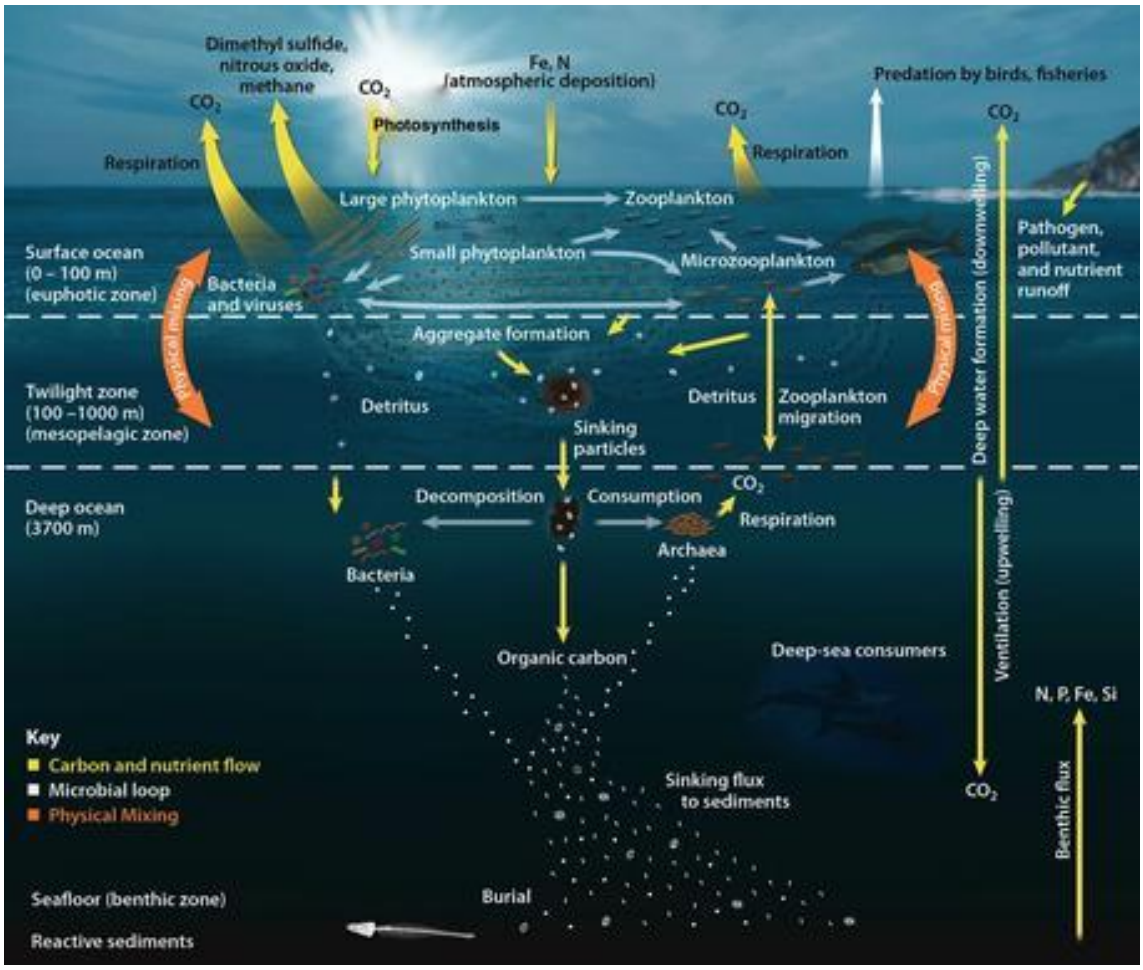

Figure 1.3- Schematic representation of the Ocean Carbon Cycle, with the processes at the surface, in the mesopelagic zone, in the deep ocean and at the seafloor. Image credit: Oak Ridge National Laboratory(obtained from https://serc.carleton.edu/eslabs/carbon/6a.html

In the Azores, like in the sub-tropical oligotrophic regions, the vertical phytoplankton distribution is characterized by a deep chlorophyll maximum (DCM) below the surface at 75-150m depth, approximately (Macedo et al. 2000). Its formation is a consequence of different physical, chemical and biological processes, including an accumulation of sinking phytoplankton with higher nutrient concentrations. It also depends of biological processes like a physiological acclimation of phytoplankton to low light levels in the presence of high nutrient concentrations, with a higher in-situ growth at the nutricline than in the upper mixed layer (Fasham et al. 1985, Marañón et al. 2007). Macedo et al., 2009 described a progressive descent of the DCM during spring and summer following the deepening of the nutricline, and a North-South gradient, with lower DCM in the Azores, than south of the Azores. South of the Azores, at 34^{o}N, under the

influence of the Azores Front-Current system, a high productivity region, the DCM was identified between 90 and 100ms depth.

1.3. Introduction to larval dispersal

Many marine organisms disperse via a larval phase. Larval dispersal is an important ecological process. Rather than dispersing as adults, many marine organisms rely upon this phase as the only means to colonize new areas, being crucial for individual survival, population dynamics and persistence (Ross et al. 2020). Dispersing larvae connect populations of species that live in patches of benthic habitat separated by vast expanses of ocean. These larvae hatch in the water column and are advected by the ocean currents (Phelps 2015). During the pelagic larval duration (PLD) larvae can be lecithotrophic (feed upon yolk stored in egg), or planktotrophic (feed upon planktonic food) (Yearsley & Sigwart 2011).

Figure 1.4- Conceptual framework for considering larval dispersal models. The model includes transition probabilities for general migration and larval dispersal among sites. Exchange of larvae can occur between different sites (connectivity), or by self-recruitment with larvae settling in the same population

Larvae can have swimming behaviour, and ontogenic vertical migration (Mariani et al. 2006, Cowen & Sponaugle 2009, Treml et al. 2012, Maldonado et al. 2016). Though the behaviours governing how larvae disperse are under-described (Gary et al. 2020). After the pelagic larval duration (PLD), which can vary from few minutes to weeks or even months (Wang et al. 2021), the larvae return to the seabed and settle in a suitable substrate to develop into a juvenile. This exchange of individuals between subpopulations is known as connectivity (Phelps 2015). Connectivity is crucial for population regulation, persistence and resilience to natural and anthropogenic disturbance (Cunha et al. 2020). Many subpopulations would likely go and stay extinct if they were not connected demographically to other subpopulations (Gaines et al. 2005)

Larval dispersal is an important ecological process of great interest to marine ecology and conservation. In the design of effective networks of marine protected areas (MPAs) (Ross & Howell 2013, Ross et al. 2017, Combes et al. 2021); protection of Vulnerable Marine Ecossystems (VME) (Kenchington et al. 2019); deep-sea sponges (Howell et al. 2016, Ross et al. 2019, Wang et al. 2021, Samuelsen et al. 2022); corals (Botsford et al. 2009, Connolly & Baird 2010, Foster et al. 2012, Wood et al. 2014); on the spatial management of marine capture fisheries (Roman & Boicourt 1999, Fogarty & Botsford 2007, Kough et al. 2013).

1.4. Modelling tools

The use of models is an essential tool, when dealing with oceanographic studies and management questions, enabling the study of specific scenarios and hypotheses. Ocean circulation is driven mainly by physical drivers like geostrophic factors (gravitational and deflective force by earth's rotation - the Coriolis force); oceanic factors (i.e. pressure gradient, water temperature and salinity variations); atmospheric factors; but also bathymetry (Hirose and Kamiya, 2003). Local ocean conditions are often controlled by large-scale processes, leading to the need for downscaling from global and larger-scale models into local models, representing, as accurately as possible, the ocean conditions, to estimate local and regional features in a higher resolution scale (Katavouta & Thompson 2016).

Several global and regional models were developed and applied in the Atlantic Ocean, continental shelf and coastal areas, simulating physical ocean properties, namely: CMEMS (Lellouche et al., 2018); NEMO- Nucleus for European Modelling of the Ocean (Gutknecht et al., 2016;); FOAM- Forecasting Ocean Assimilation Model (Bell et al., 2004); MOHID (Juliano et al., 2012), ROMS- Regional Ocean Modelling System (Costa et al., 2012).

During the development of this thesis different models are used, namely a hydrodynamic model, a biogeochemical model and finally a biophysical particle tracking model to study larval dispersal (Figure 1.5).

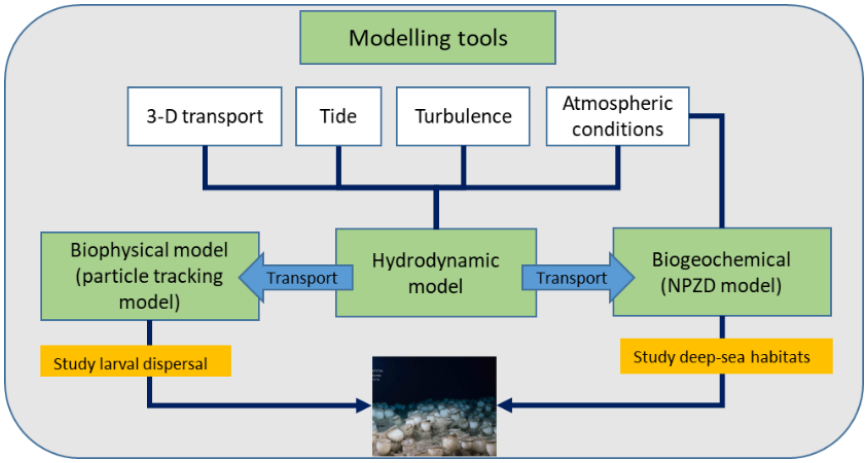

Figure 1.5- Diagram of modelling tools used in this thesis to study deep-sea habitats: a physical hydrodynamic model; a coupled biogeochemical (nutrient, phytoplankton, zooplankton and detritus model); a biophysical particle tracking model (bio: larval behaviour, mortality pelagic larval duration etc.; physical: transport and particles tracking);

Biogeochemical models

While hydrodynamic models are widely used and implemented, and their physical equations of state are relatively well known (Berline et al. 2007), when biogeochemical dynamics are incorporated into the models the complexity increases, increasing concomitantly the diversity of options for model building (Robson 2014). The number of phytoplankton functional groups (PFG) to consider in biogeochemical models is an issue under discussion in model development and depending on their level of simplicity, complexity and objectives, different models can consider different groups (Kwiatkowski et al. 2014).

Many biogeochemical models simulate the marine biological productivity following a nutrient–phytoplankton–zooplankton–detritus (NPZD) relation, (Figure 1.6) where biogeochemical cycles are connected to the trophic levels through the uptake of nutrients by phytoplankton and remineralisation of organic matter (Peña et al. 2016). Different NPZD models are applied at a regional and global scale such as FASHAM (Haney & Jackson 1996), PISCES (Aumont 2005), HAMMOC (Ilyina et al. 2013). Although marine biogeochemical models have increased their complexity in the last decade, global-scale models continue to use simple phytoplankton growth models with simplification of phytoplankton physiology, namely using constant Carbon:Nitrogen ratios (C:N) assuming constant stoichiometry between carbon, nitrogen and phosphorus (Redfield ratio) (Ayata et al. 2013). Similarly, simple Chlorophyll a:Carbon (Chl:C) ratios are used,

based on the classical Michaelis–Menten representation of nutrient uptake (Anugerahanti et al. 2021).

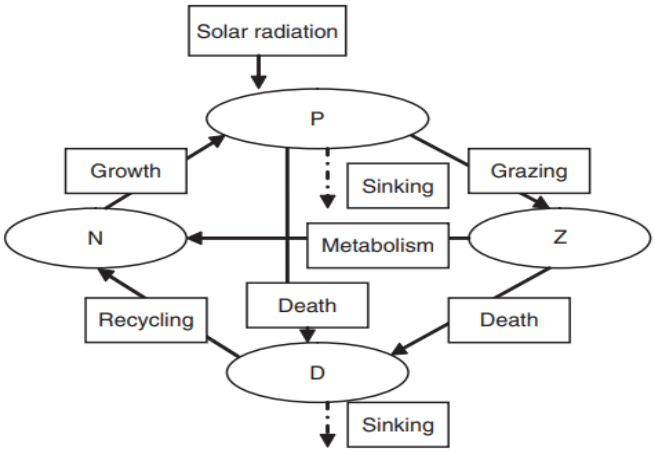

Figure 1.6- Schematic diagram of the NPZD (nutrient-phytoplankton zooplankton-detritus) model. Image from: (Xu et al. 2008)

Applications coupling both physical and biogeochemical models are used to: support the European Marine Strategy Framework Directive (MSFD) requirements (Piroddi et al. 2015); to simulate the lower trophic levels of marine ecosystems (Aumont et al. 2015), study pelagic biogeochemistry (Vichi et al. 2007b), or to study the response of ocean biogeochesmitry to climate changes (Buchanan et al. 2018), revealing the importance of using biological models to study space and time variations.

Biophysical models

In recent years, many studies integrated multidisciplinary approaches using biophysical modelling (Cowen & Sponaugle 2009, Ross et al. 2016, 2020, Criales et al. 2019, Pata et al. 2021) and genetic markers (Vic et al. 2018, Bracco et al. 2019).

Biophysical models provide researchers a tool to study larval dispersal, using 3-dimensional circulation models and particle tracking models. These particles represent larvae, with passive or swimming behaviour, likewise other biological traits (e.g. PLD, spawning seasonality, mortality, buoyancy, diel vertical migration) (North et al. 2009, Helgers et al. 2013, Leis 2020). Ultimately such models simulate the likely paths of larval dispersal and can be used for population connectivity studies (Metaxas & Saunders 2009, Paris et al. 2013).

Coupled with hydrodynamic models these models allow for to study of dispersal scenarios, considering different organisms and larval behaviours, under different environmental conditions. These offline particle tracking models have been used to study larval distribution, estimating larval transport to study populations connectivity in VMEs (Ross et al. 2017, Kenchington et al. 2019, Wang et al. 2020), and specifically on deep-sea sponges (Ross et al. 2019, Busch et al. 2021); fisheries management (Hinrichsen et al. 2011, Mitra et al. 2014); and on the design of marine protected area (MPA) networks (Kough 2014, Kenchington et al. 2019, Combes et al. 2021).

1.5. MOHID modelling system

In this thesis, the MOHID modelling system (Neves et al. 2003), has been used as the main modelling tool. The MOHID Water model is a 3D finite volume model developed at MARETEC (IST - University of Lisbon) which solves the 3D incompressible primitive equations (Martins 1998, Leitão et al. 2008) built and developed using an object-oriented philosophy (Braunschweig et al., 2004)

MOHID Water is open-source and the most relevant key strengths are its ability to: deal with 2D and 3D simulations, with sigma, cartesian or lagrangian vertical coordinates; with eulerian or lagrangian transport references; and solve biogeochemical formulations. MOHID has been applied in ocean and coastal models (de Pablo et al., 2019; Franz et al., 2017; Riflet et al., 2008; Trancoso et al., 2009), taking advantage from downscaling approach from global circulation models to regional and local models (Campuzano et al. 2013).

MOHID has been applied also the Azores region, coupled with Biophysical Connectivity Model System (CMS), to study deep-sea mining plumes, and larval dispersion in hydrothermal vents (Morato et al. 2016a). Biogeochemical MOHID modules have been used in several applications (Mateus 2006, Bernardes 2007, Leonardo 2022). A deeper description of the processes and the governing equations of the transfer fluxes among the several biogeochemical water properties involved in the biogeochemical model are included in Chapter 3. Also on the MOHID water quality model website (www.mohid.com, quality). Figure 1.7 represents schematically the different modules included in MOHID Water distributed along the different environmental compartments.

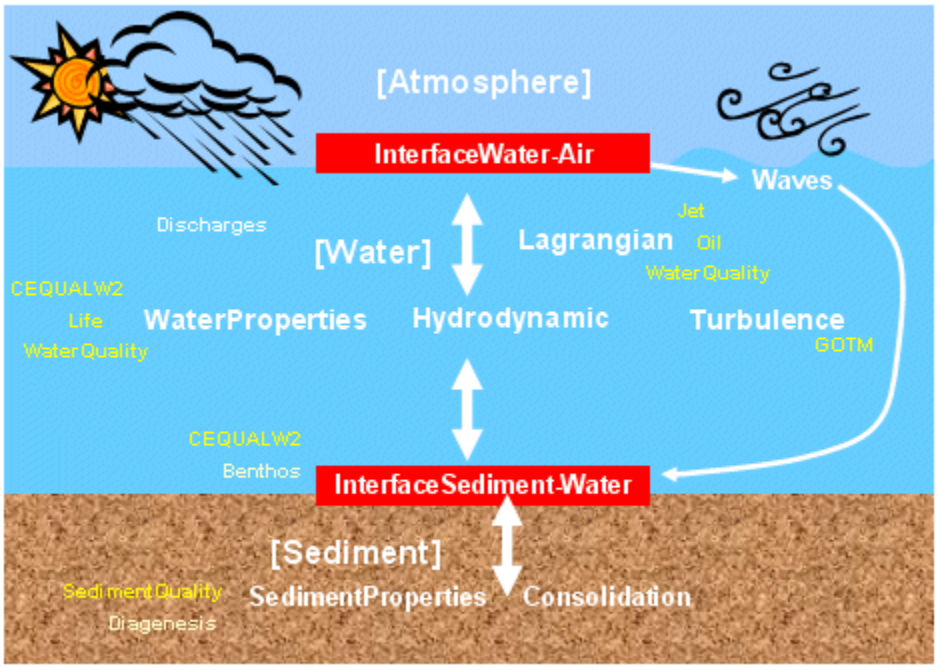

Figure 1.7. Schematic representation of MOHID Water. Adapted from (IST 2003)

1.6. Thesis outline and objectives

The main aim of this dissertation is to provide modelling tools to better understand marine ecosystem processes and population connectivity in the deep-sea. The work performed in this thesis was based on the implementation of a 3-D hydrodynamic (Chapter 2) and a biogeochemical model (Chapter 3) to simulate the physical and biological processes in the Azores, as well as a biophysical model to study deep-sea larval dispersal and population connectivity (Chapter 4). The major objective of this modelling work is to provide data to better understand marine dynamics. In the last chapter, the constructed models are applied to a specific case, focusing on deep-sea sponge grounds in the Azores (Chapter 5).

The current Chapter 1 presents a general introduction to the Azores study region, with a characterization of the major hydrodynamic and biological patterns of the region. It also includes a brief review on the modelling approaches in use.

Chapter 2 focuses on the implementation and validation of a hydrodynamic model. Model results were used to describe the major currents and water masses influencing the Azores region. All

other model tools built in this thesis are based on this hydrodynamic model, thus specific importance has been given to model validation.

Chapter 3 consists of the development and implementation of a biogeochemical model. The building process included a calibration performed by testing different parameterizations for the Azores region to find the optimal. Model results were validated against remote sensing data, climatology and global models, and were used to describe the major seasonal and spatial biotic and abiotic processes that control phytoplankton abundance in the Azores.

In Chapter 4 a biophysical model is implemented to study the larval dispersal and population connectivity for two case studies: Case study 1 focuses on the deep-sea sponge *Pheronema carpenteri*; case study 2 focuses on *Chaceon affinis*, a deep-sea red crab. Different scenarios were studied considering different biological traits: spawning seasonality, larval pelagic duration (PLD), and larval behaviour, including surface-oriented swimming. Results revealed seasonal patterns of connectivity and the importance of hydrodynamics on larval dispersal.

Chapter 5 focused at studying the spatial and temporal biogeochemical properties at specific sponge grounds of the species *Pheronema carpenteri*, taking advantage of the 3-D biogeochemical model built in Chapter 3. The ultimate goal of the chapter was to showcase the utilization of the constructed models to better understand the ecology of the target sponge species.

Chapter 6 presents the final remarks of this thesis and suggestions for further research.

Chapter 2

Azores hydrodynamic model

2.1. Abstract

This chapter focus in the implementation and validation of the hydrodynamic model for the Azores region. A detailed description of its implementation is presented, together with model validation using Argo buoys profiles of temperature and salinity and remote sensing data. Model results are used to identify the major physical and oceanographic phenomena in the Azores region, including the leading currents and the main water masses.

2.2. Introduction

The use of models is an essential tool, when dealing with oceanographic studies and management questions, enabling to study of scenarios and hypotheses. Local ocean conditions are often controlled by large scale processes, leading to the need for downscaling from global and larger-scale models into local models (Katavouta & Thompson 2016), representing, as accurate as possible, the ocean conditions, to estimate local and regional features in a higher resolution scale. The need of improving the representation of regional and coastal models from global models is one of the big challenges in ocean modelling and Earth System Science. The present generation of ocean models is capable to provide relatively high-resolution results using data assimilation, downscaling technics, and nested grids (Neves et al. 2003, Gutknecht et al. 2016, Lellouche et al. 2018, Salon et al. 2019).

Ocean ecosystems have nonlinear dynamics, and their modelling requires an adequate representation of both physical and biological processes (Siddorn et al. 2007). Ocean circulation is driven mainly by physical factors like geostrophic factors (gravitational and deflective force by earth's rotation - the Coriolis force); oceanic factors (i.e. pressure gradient, water temperature and salinity variations); atmospheric factors; but also by the bathymetry (Hirose & Kamiya 2003).

Several global and regional models were developed and applied in the Atlantic Ocean, continental shelf and coastal areas, simulating physical ocean properties, namely: CMEMS (Lellouche et al. 2018); NEMO- Nucleus for European Modelling of the Ocean (Gutknecht et al. 2016); FOAM- Forecasting Ocean Assimilation Model (Bell et al. 2004); MOHID (Juliano et al. 2012), ROMS- Regional Ocean Modelling System (Costa et al. 2012).

Hydrodynamic and circulation models, coupled with biogeochemical models, provide an advantageous tool to better understand and monitor the general marine biogeochemical cycles, being able to simulate complex interactions between ocean physics, chemistry and biology (Berline et al. 2007). It is fundamental to have well calibrated and validated hydrodynamic models on the base of any circulation, biogeochemical, or particle tracking model (North et al. 2009).

This chapter develops the validation for the most relevant physical parameters considering: water column temperature and salinity, sea surface temperature, and water level, using in-situ and remote data sources (Argo buoys, gauge stations, ocean observatories, and satellite images), and different validation methodologies, including Taylor diagrams. Therefore, this model application can be used as an essential tool for biological studies, and to describe and identify the main oceanographic characteristics.

2.3. Methodology

2.3.1. MOHID hydrodynamic model

This work is based on MOHID modelling tools. MOHID modelling system is a three-dimensional numerical program used to simulate hydrodynamics, water quality, circulation and dispersion processes in water. Several MOHID applications have been developed to study ocean processes (e.g. Atlantic NorthEast (Riflet et al. 2008, Campuzano et al. 2013) (Riflet et al. 2008)); Atlantic SouthWest (Juliano et al. 2012), Oil spills (J. C. Leitão 2003, Juliano et al. 2012), estuaries and coastal areas (Viegas et al. 2009, Pinto et al. 2014, de Pablo et al. 2019).

MOHID is an open-source model, available online at (https://github.com/Mohid-Water-Modelling-System/Mohid) programed in ANSI FORTRAN 95, following an object-oriented

approach allowing the integration of different modules in a 3-dimensions and implicit way (IST 2003). Spatial discretization using the finite volume approach technique (the spatial coordinates are independent, and any geometry can be chosen for every dimension), allows flexibility in the subdivision of vertical and horizontal domains, and the implementation of different vertical coordinates (cartesian and sigma), adaptable to each particular case. Sigma coordinate system is commonly used in oceanographic and meteorological models and other fluid dynamic models (Janjic 2003). In sigma layers, the scale is divided evenly, each layer occupies a constant percentage of the water column thickness and the number of layers becomes independent of the local depth, although in terms of meters it depends on the tide level. These non-hydrostatic layers simplify the surface boundary conditions, considering the topographic variations of the earth's surface, in this specific case the tide level variations. The sigma coordinate transformation in the upper layers allows having a better accuracy considering the tide level evolution in these layers. Also, the Cartesian coordinate in the remaining water column layers allows the reduction of the computational cost (Lin & Li 2002), using a hydrostatic approach for the entire water column.

In this application, MOHID model has a 3-dimensional configuration, with 50 vertical layers, being the bottom 43 layers in Cartesian coordinates, with a constant size, and the top 7 layers defined with sigma coordinates, changing their size considering the tide level evolution.

MOHID hydrodynamic module (Figure 2.1) is responsible for all hydrodynamic properties. In this MOHID application, several modules are used: Hydrodynamic; Water Properties; Atmosphere; Interface Water-Air; Interface Sediment-water; Turbulence; Geometry and Assimilation.

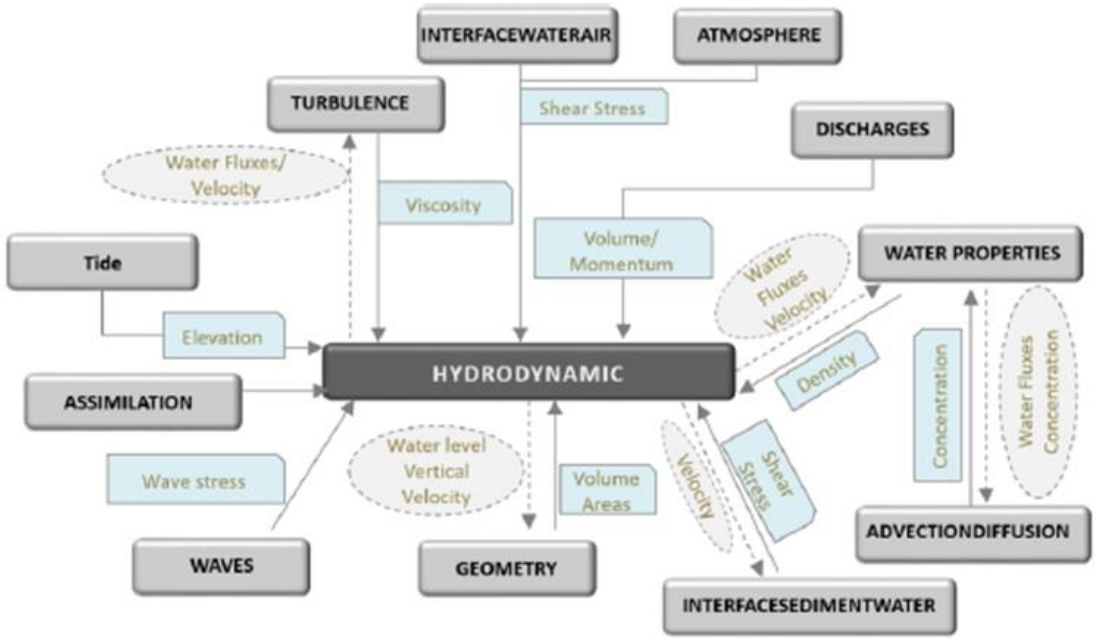

Figure 2.1- Schematic configuration of MOHID Hydrodynamic model. Modules are represented in grey rectangles. (Adapted from (Leonardo 2022)

MOHID hydrodynamic module is responsible for all hydrodynamic properties. Considering water level, velocities and water fluxes, it determines the turbulent transport of momentum, mass and heat. MOHID uses the finite volumes approach to solve the Navier-Stokes equations, considering the Boussinesq and hydrostatic approximations. These equations are solved numerically considering the generic vertical discretization enabling the use simultaneously of both sigma or cartesian vertical coordinates. Momentum, mass and heat transport are computed using a generic 3D advection-diffusion library including various advection schemes namely: first, second and third-order upwind; centred differences; and TVD (Total Variation Diminishing). Advection is solved in the three directions as a one-dimensional case, and various time discretization can be combined: explicit, semi-implicit or fully implicit. The horizontal diffusion of momentum is computed with a bi-harmonic formulation (IST 2003). To solve the turbulence of the entire domain, MOHID has coupled the GOTM module. This General Ocean Turbulence Model (GOTM) consists of a one-dimensional water column to solve the most important hydrodynamic and thermodynamic processes related to vertical mixing in natural waters (Burchard, H., Bolding, K., Villarreal 1999). The inverse barometer effect is used to compute water level (Dorandeu & Le

Traon 1999). MOHID turbulence module allows to parameterize turbulence, decreasing the horizontal diffusion towards the boundary in nested models. This horizontal flow relaxation scheme can be applied for velocity U and V vectors, temperature and salinity, being advantageous when downscaling from a global circulation model solution to a local solution (IST 2003).

MOHID Water Properties module computes the 3D eulerian transport of different water properties in the different phases (dissolved, particulate and adsorbed) in the water column that is subjected to one more transport variable: the settling velocity. It also uses the *Advection Diffusion* module that computes the properties transport. The settling velocity is computed by the *Freevertical movement* module.

Because the physical and ecological processes in the ocean are often non-linear and depend on several environmental forces, a data assimilation procedure is essential, allowing to combine information from global models, boundary conditions models, and monitoring data. In this model, the assimilation is performed considering the global ocean model for velocity U, velocity V, water temperature and salinity, and the meteorological model for the atmospheric forcing.

2.3.2. Model implementation

The model implementation uses 3 nested levels (Figure 2.2), providing hydrodynamic results from 2015 to 2017. Model configuration, description, and boundary conditions are listed in Table 2.1. These results were validated and can be used as boundary conditions for a biogeochemical model being developed for this study area.

The implementation of the study domain uses a one-way downscaling strategy of nested domains. Tide is imposed at the open boundary of Level 1 using the FES2014 global tide model (Lyard et al. 2021), with a regular grid of 1/16º. It is an enhanced version of FES2012 and FES2004, used with success in different applications (Leitão et al. 2008, Juliano et al. 2012, Toublanc et al. 2018). Model is forced by Mercator Global Ocean (PSY4V3R1) model. PSY4V3R1 is a global ocean system at 1/12° horizontal resolution, and 50 vertical levels developed at Mercator Océan by the Copernicus Marine Environment Monitoring Service (CMEMS) (Lellouche et al. 2018). Available

online at http://marine.copernicus.eu/. This product is referred to as Mercator hereafter. This model provides 3D daily mean fields for different parameters: temperature, salinity and currents; and 2D sea surface level, between other parameters.

For the atmospheric forcing, the boundary conditions are provided by the Global Forecast System (GFSmodel), provided by NOAA- America National Ocean and Atmospheric Administration, available at https://www.ncdc.noaa.gov/. With hourly fields of surface wind, temperature, relative humidity, pressure, and solar radiation.

The open boundary conditions are resolved by imposing a Flow Relaxation Scheme, providing a simple and stable extrapolation of the interior solution. This relaxation is applied to temperature, salinity, and velocity parameters, combined with a radiation scheme from Flather (Flather, 1976). The initialization of the 3-Dimensional fields of temperature and salinity are made by a direct interpolation of Mercator fields for these two parameters, using bilinear interpolation in the horizontal and linear interpolation in the vertical fields.

Table 2.1- Hydrodynamical model configuration

Parameter	Level 1	Level 2	Level 3- Window from Level 2
Model caracterization	2D - Barotropic	3D – Baroclinic	3D- Baroclinic
Domain	31.8121°N to 43.63212 °N, -20.74776°W to -37.1278°W	32.4721°N to 42.91211°N, -21.40775°W to -36.2878°W	36.25°N to 40.74°N, and-23.9854°W to -32.2628°W
Bathymetry	EMODNET 1/16 arc-minuts [a)]	EMODNET 1/16 arc-minuts [a)]	Same as level 2
Horizontal Resolution	6km	6km	
Vertical resolution	1 layer(0-6000meters depth)	50 vertical layers: 7 sigma layers + 43 cartesian layers	
Tide	Tide: FES2014[b)]	From level 1	
Δt	180 seconds	120 seconds	
Boundary conditions:	--		
Meteorological forcing	--	Global Forecast System model (GFS) 0.25° resolution 1*) [c)]	
Hydrodynamical forcing	--	Mercator Global Ocean (PSY4V3R1) model (1/12°)[d)]	
Model output	3600	3600	3600
Simulation lenght	Jan/2015 – Dec/2018	Jan/2015 – Dec/2018	Jan/2017– Dec/2018

a) EMODnet Bathymetry Consortium, 2018; b) Lyard et al., 2021; c) National Centers for Environmental Prediction, National Weather Service, NOAA, 2015; d) Lellouche et al., 2018;Table 2.2- Hydrodynamical model configuration

Nested models

The numerical model was implemented with a 0.06° (1/16) resolution using a three-level nesting model (Figure 2.2).

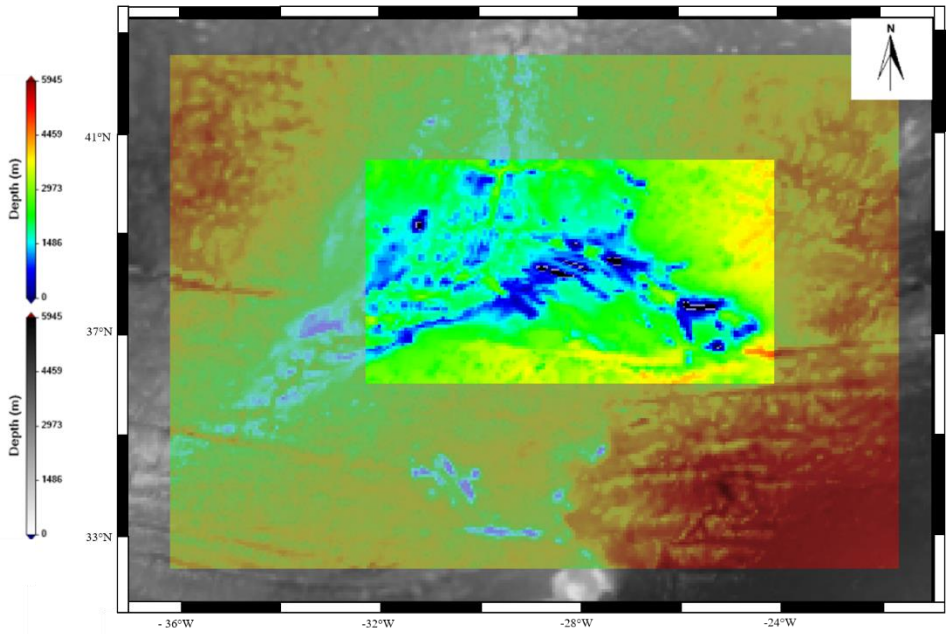

Figure 2.2 –Model domain and depth in meters: Level 1 in greyscale, level 2 and level 3 in red-blue scale.

Level 1, represented with greyscale in Figure 2.2 is a 2D model that provides the tide solution for the 3D model, using the FES2014 model. This first level covers the geographic area from 31.8121º N to 43.63212º N, -20.74776º W to -37.1278º W, covering the entire Azores Economic Exclusive Zone (AEEZ).

Level 2 is three-dimensional (3-D), also covering the entire AEEZ, from 32.4721ºN to 42.91211ºN, -21.40775ºW to -36.2878ºW. This second level is slightly smaller than the first one, to avoid instability problems in the boundaries. This 3-D baroclinic model with the same horizontal resolution as the first level, has 50 vertical layers. The bottom 43 layers are in cartesian coordinates, with a constant size, and the top 7 layers are sigma coordinate layers, totalizing the upper 10 meters of the water column. Below these sigma layers, the 43 cartesian layers increase in size along the water column, from top to bottom, with the top ones less than 2 meters in length. In the upper layers, the sigma coordinate layers change their size considering the tide level evolution. Model bathymetry was obtained from the EMODNET database, available online at www.emodnet, grid resolution of 1/16 * 1/16 arc-minutes (EMODnet Bathymetry Consortium, 2018).

Level 3 is a model window of Level 2, limited from 36.25ºN to 40.74ºN, and-23.9854ºW to -32.2628ºW, covering the Azores archipelago. With the same grid resolution, Level 3 was created

to provide results in an area closed-by the archipelago. Results of level 3 are used for further model applications like the biogeochemical and biophysical models implemented in the scope of this dissertation. This nested methodology allows for saving disc space. Otherwise, when using the entire Level 2, the biogeochemical model would be computationally heavy not only in terms of computer performance but also in data storage volume.

2.3.3. Data for model Validation

The validation of the results of MOHID model is crucial because hydrodynamics is the basis for the transport of any biogeochemical variable through advection and/or diffusion processes, from the eulerian and lagrangian points of view. Sea surface temperature (SST), vertical profiles of sea temperature and salinity, and water level (directly dependent on tide level) are the parameters being validated in this work.

Water level

Several gauge stations are available in the Azores region, Table 2.3. However, only the Ponta Delgada station, managed by Instituto Hidrográfico da Marinha (Portugal), has data for the required period. Tide gauge data was retrieved freely from the Permanent Service for Mean Sea Level website (Holgate et al. 2013, PSMSL 2018). Ponta Delgada Station was the only station with historical data available for this validation period (2014-2016), making it infeasible to perform any comparative study between different stations. Water level model results from 2014 to 2016 were compared with the *in situ* gauge stations data. Model time-series for the same location and time step as tide gauge station data were used.

Sea Surface Temperature validation

For SST validation, model results are compared with remote sensing data, using a satellite global product- UKMO-L4HRfnd-GLOB-OSTIA (from now on refered as OSTIA), available online1i (UK Met Office 2005). OSTIA is a L4 sea surface temperature analysis produced daily on an operational basis at the UK Met Office using optimal interpolation on a global 0.054 (1/20)

[1] https://podaac.jpl.nasa.gov/dataset/UKMO-L4HRfnd-GLOB-OSTIA

degree grid. Has a highly smoothed SST field and was specifically produced to support SST data assimilation into numerical weather prediction models (Stark, J.D., C. J. Donlon 2007). Comparisons were performed systematically using daily remote sense data and Mohid results at the same time.

Table 2.3- Gauge stations available in the Azores region, name, ID, location, data of available data (*https://www.psmsl.org/), and data used.

Gauge Station	ID*	Location Lat	Long	Data available	Data used
Ponta Delgada	258	37.74N	-25.67W	1978 – 2018	2014-2017
Ponta Delgada	245	37.73 N	-25.67W	1978 – 2012	-
Horta	156	38.53N	-28.63W	1905 – 1996	-
Lajes das Flores	2171	39.34N	-31.17W	2006 – 2013	-
Santa Cruz das Flores	843	39.45 N	-31.12W	1957 – 2009	-
Angra do Heroísmo	380	38.65N	-27.23W	1933 – 1996	-

Water Temperature and salinity along the water column

Model validation for salinity and temperature along the water column was performed by comparing model results with Argo floats data available online (Argo, 2020), considering all the Argo buoys profiles available for the study area, a total of 462 boys during 2015, represented on Figure 2.3.

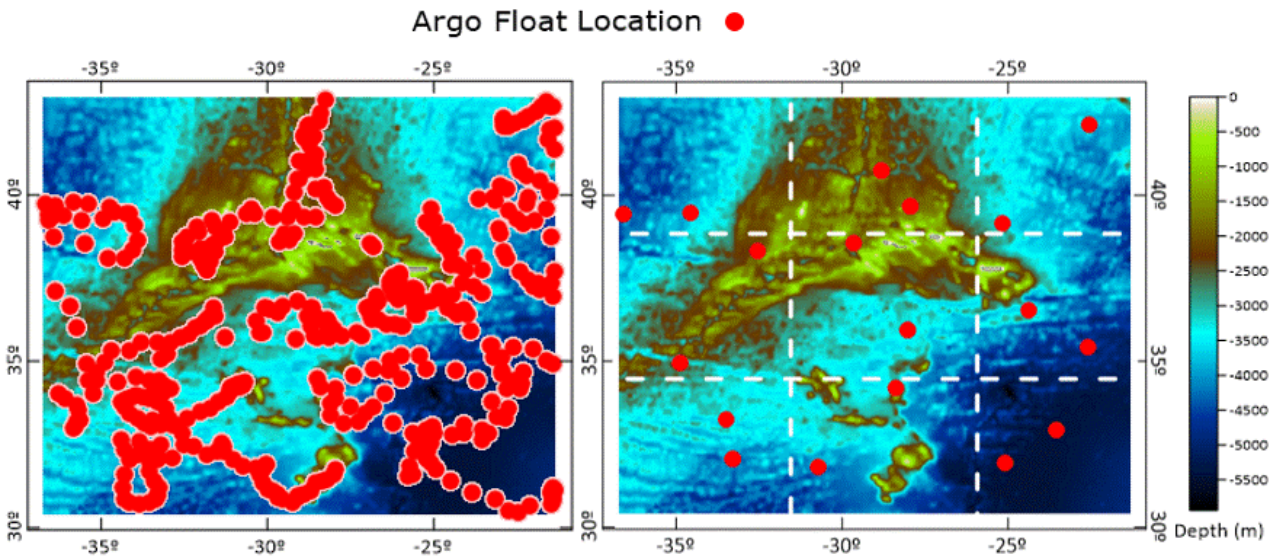

Figure 2.3- Argo buoys available in the study area in 2015, (462 buoys) on left, and on right, the 18 Argo buoys used to evaluate model performance in the different 9 subareas of the study domain.

To have deeper analyses of model performance along the water column, the study domain was divided into 9 subareas: NorthWest (NW), NorthCenter (NC), NorthEast (NE), CenterWest (CW), CenterCenter (CC), CenterEast (CE), SouthWest (SW), SouthCenter (SC), and SouthEast (SE), represented in Figure 2.3 (right). From each subdomain 2 Argo buoys were selected, considering their location (selecting buoys spread out in the different subdomains), and at different bathymetric conditions, comprising different geographic and topographical situations. These Argo profiles of salinity and temperature were compared with the paired model results profiles (for the same location, depth and time).

To characterize the different water masses in the domain and along the water column, all the Argo profiles, together with respective model results, were considered, through their T-S diagrams. These T-S diagrams also include the MERCATOR model results, providing the means to do a comparative analysis of MOHID and the boundary conditions model performances.

2.3.4. Statistical methods

The most common statistical indexes used for model validation, as recommended by Allen et al. (2007), are: the root mean square error (RMSE) (eq. 2.1), which is one of the most widely used for calibration and validation, together with bias (eq. 2.2), and Pearson correlation coefficient (r) (eq. 2.3) (Gómez-Zambrano et al. 2017), and finally Taylor diagrams, (Allen & Somerfield 2009).

The RMSE error is interpreted as a deviation of the simulated results from the measurements and it has the benefit of penalizing large errors, (de Pablo et al. 2019). Small absolute values of RMSE indicate a good agreement between model and observations.

$$RMSE = [\frac{1}{N}\sum_{i=1}^{N}(O_i - M_i)^2]^{0.5} \quad \text{eq. 2.1}$$

Model Bias is a simple statistic parameter that measures the mean deviation between modelled (M) and observed data (O), which yields a positive bias as an indicator for the model's overestimation and, conversely, a negative bias for the model's underestimation (eq. 2.2).

$$Bias = \sum_{i=1}^{n}\frac{1}{n}(M_i - O_i) \quad \text{eq. 2.2}$$

The correlation Pearson coefficient (referred to as correlation), (eq. 2.3), measures the statistical relationship, or association, between two variables, in this case, the observed data (*O*), and the modelled data (*M*).

$$R = \frac{\sum_{i=1}^{n}(M_i - \bar{M}_i) - (O_i - \bar{O}_i)}{\sqrt{\sum_{i=1}^{n}(M_i - \bar{M}_i)^2}\sqrt{\sum_{i=1}^{n}(O_i - \bar{O}_i)^2}} \quad \text{eq. 2.3}$$

Taylor diagrams are an advantageous tool to evaluate model performance, aggregating in the same diagram correlation, standard deviation, the centred RMSE (eq. 2.5) and bias, between model and reference data. Standard deviation (σ_m), defined by eq. 2.4, is used to measure the spread of data around the mean.

$$\sigma_m^2 = \frac{1}{n}\sum_{i=1}^{n}(M_i - \bar{M}_i)^2 \quad \text{eq. 2.4}$$

The centred RMSE error (CRMSE) is the mean-removed RMSE, thus calculated as follows:

$$CRMSE = [\frac{1}{N}\sum_{i=1}^{N}(M_i - \bar{M})_i - (O_i - \bar{O}_i)^2]^{0.5} \quad \text{eq. 2.5}$$

Taylor diagrams use the Law of Cosines (Taylor, 2001), where the radial coordinate is r = σ_m and the angle is θ = arccos(R). Centred RMSE then appears as the radial distance from the position of a perfect model (r = σ_0, θ = 0), (eq. 2.5). These diagrams can be normalized, comparing different variables, or variables with different variances, by normalizing (i.e., making dimensionless) their standard deviations (Elvidge et al., 2014).

2.4. Model validation results

Water Level

Statistical results for water level validation, including correlation, RMSE and the average, are summarized in Table 2.4.

Table 2.4- Statistical results (correlation (R), Bias, RMSE and averages) for water level validation comparing Mohid water level results and measured data from Ponta Delgada Gauge Station for 2014, 2015, and 2016.

Year	R	Bias	RMSE	average gauge station (m)	average model (m)
2014	0.973	0	0.089	1.17	1.17
2015	0.9781	0.045	0.094	1.155	1.200
2016	0.973	-0.14	0.16	1.14	1.00

Tide validation results show a correlation between model results and measured data, higher than 97%, for 2014, 2015 and 2016 evidencing a good model performance for simulating water level. Despite good correlation results, a diference of 0.14 meters is verified, and an RMSE of 0.16 meters in 2016 (Table 2.4). Nevertheless, the good correlation results together with a constant difference in average values, indicate that mismatches between model results and gauge data are not related to tide amplitude or neither irregular along the year, nor related to spring or neap tides. When using modelling tools, errors can increase over time and create instabilities (Ménesguen et al. 2007, Guillou et al. 2018) which was not the case in this study, since no instabilities were identified.

Sea Surface Temperature

For sea surface temperature validation, model results were compared with OSTIA remote sense product. Comparisons were performed systematically, with the statistical results of this validation, using the year 2015 as a reference, summarized in Table 2.5. Correlation, Bias, and RMSE results are represented as maps in Figure 3, from left to right respectively. Temporal evolution of SST (domain average), Bias, and RMSE, along the reference year, are represented in Figure 2.4 and Figure 2.5, respectively.

Table 2.5- Statistical analysis (correlation (R), Bias, RMSE and averages)for sea surface temperature validation comparing model SST with remote sensing data.

R	Bias (°C)	RMSE (°C)	Model average (°C)	Satellite average (°C)
0.992	0.042	0.367	20.267	20.225

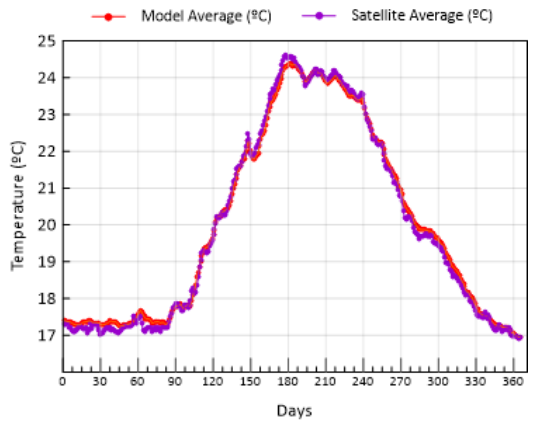

Figure 2.4- Temporal evolution of SST average from MOHID (red) and satellite (purple) along the reference year.

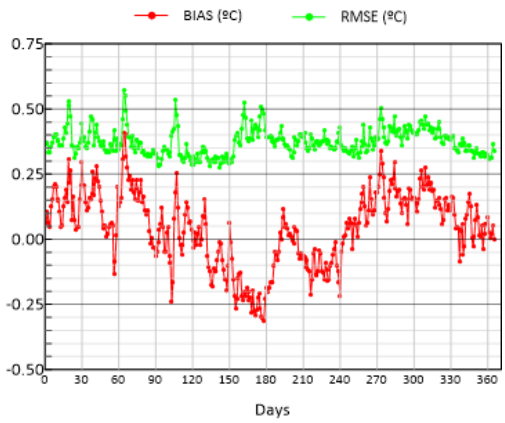

Figure 2.5- Temporal evolution of the statistical analysis for SST validation considering Bias (red) and RMSE (green), along the reference year.

The graph of the temporal evolution of SST simulated by MOHID, and measured by satellite, reveals that MOHID can simulate the seasonal variations of SST values in the domain (Figure 2.4). Results show a strong correlation, higher than 99%, indicating that Mohid can simulate with accuracy the yearly variation of SST, and along the domain.

MOHID have on average a positive bias of 0.042^{o}C. However, during spring and summer the bias is negative (Figure 2.5). This negative bias can be a consequence of different MOHID and satellite vertical results resolution. While the satellite measures are related to the first centimetres of the water column, model results refer to the first Cartesian layer (located at 3 meters depth). This limitation was also identified in CMEMS models (Legaloudec et al. 2015).

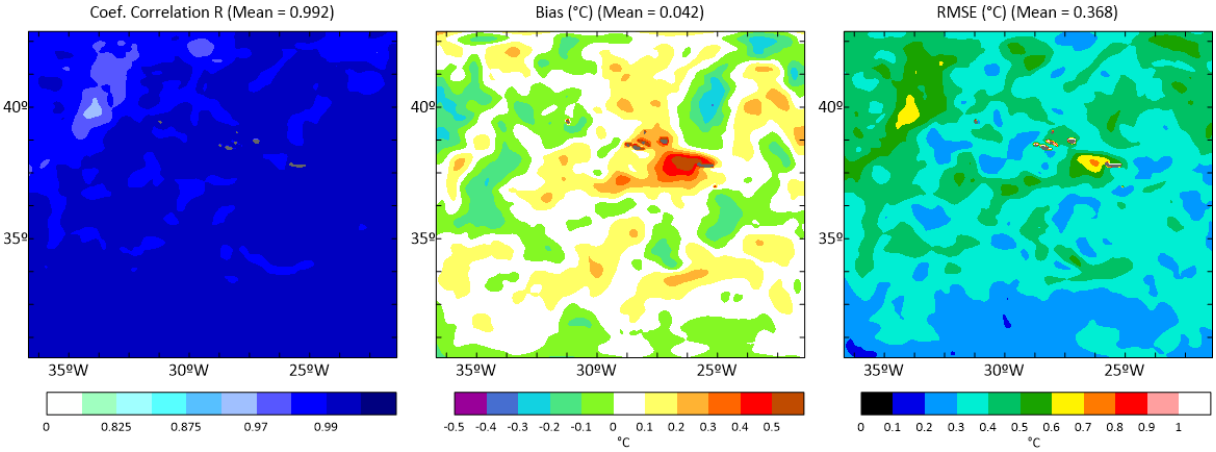

Figure 2.6- Maps of statistic analysis results along the domain for coefficient correlation R (left), Bias (center) and RMSE (right) for the comparison between sea surface temperature from MOHID and satellite data

Model bias ranged from 0.25°C to 0.5°C, with positive and higher bias near the islands (Figure 2.6). The higher RMSE also near the islands. This uncertainty around the archipelago can be a consequence of remote sensing quality data, once they are influenced by cloud covering. This is a known limitation, identified in the Azores region (Lafon et al. 2004). This bigger bias around the archipelago can also be a result of the local and punctual phenomena that occur near the islands (islands' effects), not solved by the model. These limitations can be easily surpassed using a higher resolution model in the coastal areas. However, considering the objectives of this study, the resolution used was the best commitment resolution/computational demand.

Water Temperature and salinity along the water column

Vertical profiles of temperature and salinity from Argo buoys are matched-up with model results for the same position, depth and instant, producing time series of paired model and observation profiles. Statistical analysis is performed, integrating each vertical profile, and comparing model results with Argo measured data. The general statistical analysis results are resumed in Table 2.6, and on Taylor diagrams, Figure 2.7, with the representation of all the pared buoys/model statistical results (correlation, normalized standard deviation, normalized centred RMSE, and normalized bias). These Taylor diagrams are normalized by the standard deviation of each pared Argo buoy/model comparison.

Table 2.6- Statistical results for model validation of sea temperature and salinity along the water column comparing Mohid results with Argo buoys data for 2015.

	n	R	R*R	Bias	RMSE	Sdev		average	
						Model	Argo	Model	Argo
Temperature (°C)	462	0.996	0.9993	0.440	0.646	4.72	4.77	11.63	11.19
Sanity (PSU)	429	0.983	0.968	0.042	0.098	0.406	0.414	35.70	35.66

To better analyse the model's performance along the water column, 2 Argo buoys from each subdomain were selected, as represented in Figure 2.3 (subdomains: NW; NC; NE; CW; CC; CE; SW; SC; SE). Each Argo profile was compared with the equivalent model depth profile (same location, depth, and time), for temperature (Figure 2.8), and salinity (Figure 2.9).

Validation results evidence MOHID capability to simulate vertical variability of temperature and salinity, with a correlation of 99% for temperature, and 98% for salinity; and RMSE of 0.65°C, and 0.042 PSU respectively.

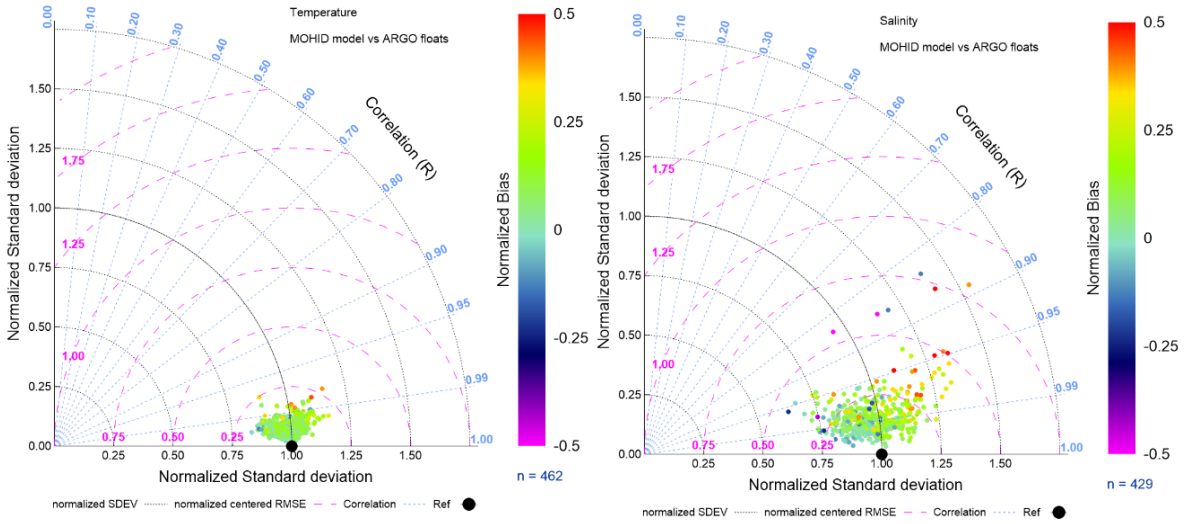

Figure 2.7 - Taylor diagram of statistical comparison between modelled and Argo buoys vertical profiles for temperature (left), and salinity (right). The black dot is the reference (Ref), representing the perfect adjustment between model results and Argo buoy data. Coloured dots represent each comparison Argo/model: the colour represents the normalized bias; the azimuthal angle represents the correlation (Pearson (R)); the normalized standard deviation is the radial distance to the reference point (Ref); the pink semicircles centred at the Ref are the normalized centred RMSE scale. Bias, SDEV and RMSE are normalized by the standard deviation of each buoy.

Taylor diagram analysis indicates that for temperature, paired model/Argo comparisons are highly correlated, with a normalized RMSE lower than 0.25, for all the comparisons except one. For salinity, results are more heterogeneous, nevertheless with a correlation higher than 95%. Some outliers can be identified, by their extreme bias and a normalized RMSE higher than 0.5. These outliers can be associated with salinity sensor limitations. The calibration drift of salinity sensors over time is a common problem in oceanography, known in the Argo buoys (Wong et al. 2020). Even with all the research, technology developments, and data quality procedures from the Argo program, this is still a limitation from Argo buoys. This limitation on salinity sensor calibration justifies the number of Argo buoys profiles with salinity (n=429) lower than the temperature profiles (n=462).Vertical profiles of temperature (Figure 2.8), and salinity (Figure 2.9)), point out that MOHID can reproduce the vertical variability, in the different parts of the domain, with a positive bias. This MOHID overestimation was identified in other model

applications in the Azores and North-East Atlantic, using ROMS (Sala et al. 2013), and HYCOM (Sala et al. 2016). A bigger variability for salinity than for temperature values is notorious along the water column.

Vertical profiles show that Argo buoys can detect small local phenomena, not represented by the model. This is a consequence of its bigger data frequency of Argo floats, which provides dozens of values along the water column, (up to 150), while MOHID, provides 23. One for each vertical layer from the surface up to the 2000 meters depth.

These results highlight the importance of gathering both methodologies, with monitoring data detecting local phenomena, and rising essential questions, and model tools helping to understand them, and to study hypotheses around different phenomena.

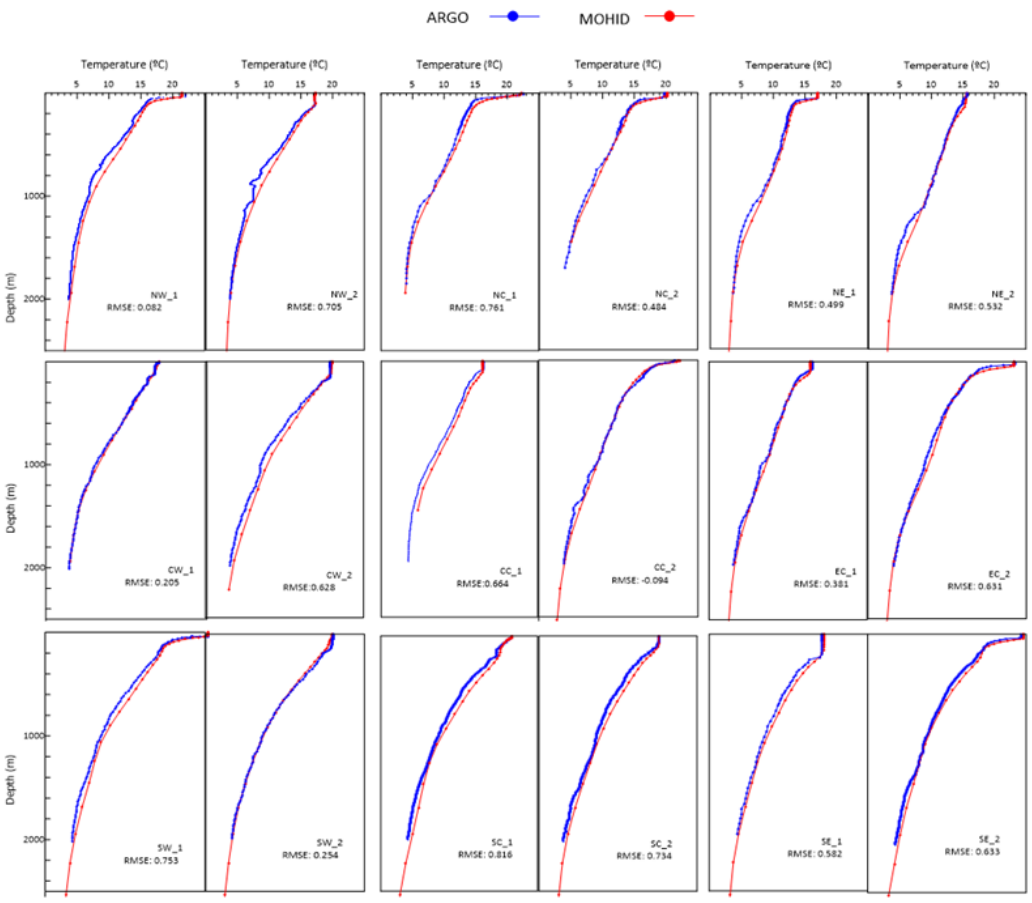

Figure 2.8- Depth profiles of temperature measured by Argo buoys (blue) and predicted by Mohid (red), and RMSE values.

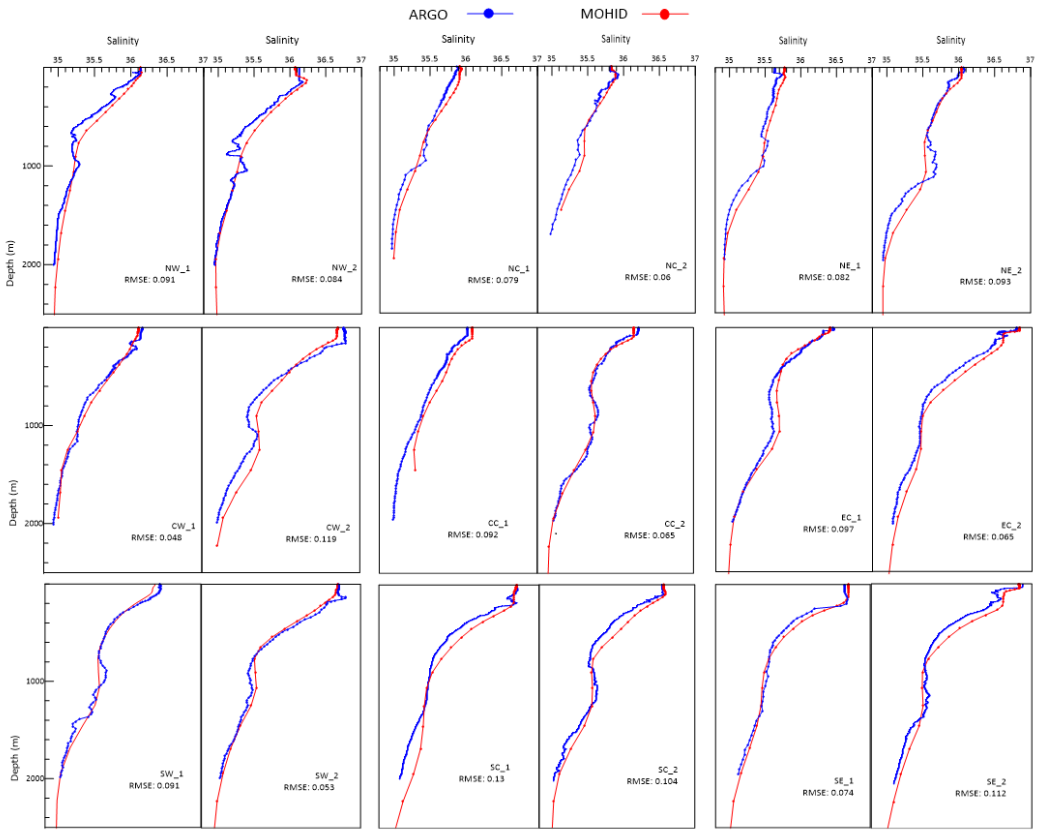

Figure 2.9- Depth profiles of salinity measured by Argo buoys (blue) and predicted by Mohid (red), and RMSE values.

2.5. Model results

Water masses in the Azores region

In the T-S diagrams, the temperature on the vertical axis is plotted against the salinity on the horizontal axis. All the T-S diagrams obtained from the Argo buoys and respective MOHID results are plotted and compared in Figure 2.10 T-S diagrams, together with the horizontal distribution of annual temperature (Figure 2.12) and salinity (Figure 2.13) averages, at different depths, allows for the identification of different water masses in the study area.

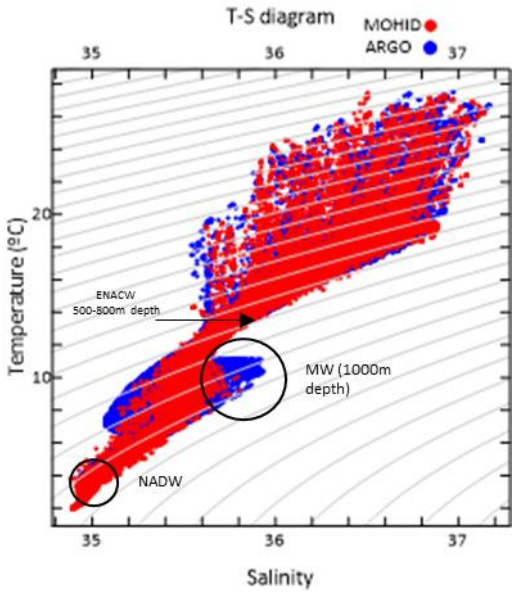

Figure 2.10 - Temperature-Salinity diagram for all the Argo buoys profiles (blue) and respective model results (red) in the study area during 2015.

To study of the distribution of the water masses along the study area, the T-S diagrams were analysed in the 9 domain subdivisions, as shown in Figure 2.3. These T-S diagrams also include the MERCATOR model results providing additional information about the models performance.

T-S diagrams for the entire domain, show that like Argo buoys profiles, model results can be used to identify different water masses. T-S diagrams (Figure 2.10) evidence the existence of a mixed layer, until the 200meters depth, characterized by its big variability temperature and salinity. This mixed-layer heterogeneity is a result of the seasonal variations in the ocean-atmosphere exchange (Marrero-Díaz et al. 2006), affecting the water properties until the 150-200meters depth. Average model results show the variability along the Azores region, in the surface layer, from SST and salinity, with a strong positive gradient of SST and salinity from North to South.

The Mediterranean Water mass (MW) is characterised by temperature and salinity ranges of 2–11 °C and 35.0–36.2 (Palma et al. 2012), in the intermediate depths, around 1000 to 1500 meters depth (Juliano & Alves 2007, Palma et al. 2012). MW signal is stronger in all the Eastern quadrants (NE, CE and SE), where the T-S diagrams show higher salinity values for water temperature values of around 10 degrees Figure 2.11.

The Eastern North Atlantic Central Water (ENACW), characterized by a nearly straight T-S curve, with temperature and salinity ranges of 7-20^{o}C and 35-37PSU respectively (Emery, 2001), is

recognizable in the T-S diagrams by the long segments along the density lines, up to the highest values of salinity. North Atlantic Deep Water (NADW) can be detected in the down left corner of the T-S diagram, due to its characteristics' lower temperature and salinity values. NADW is characterised by a temperature of 2.5°C and a salinity of 35.03 (Palma et al. 2012)

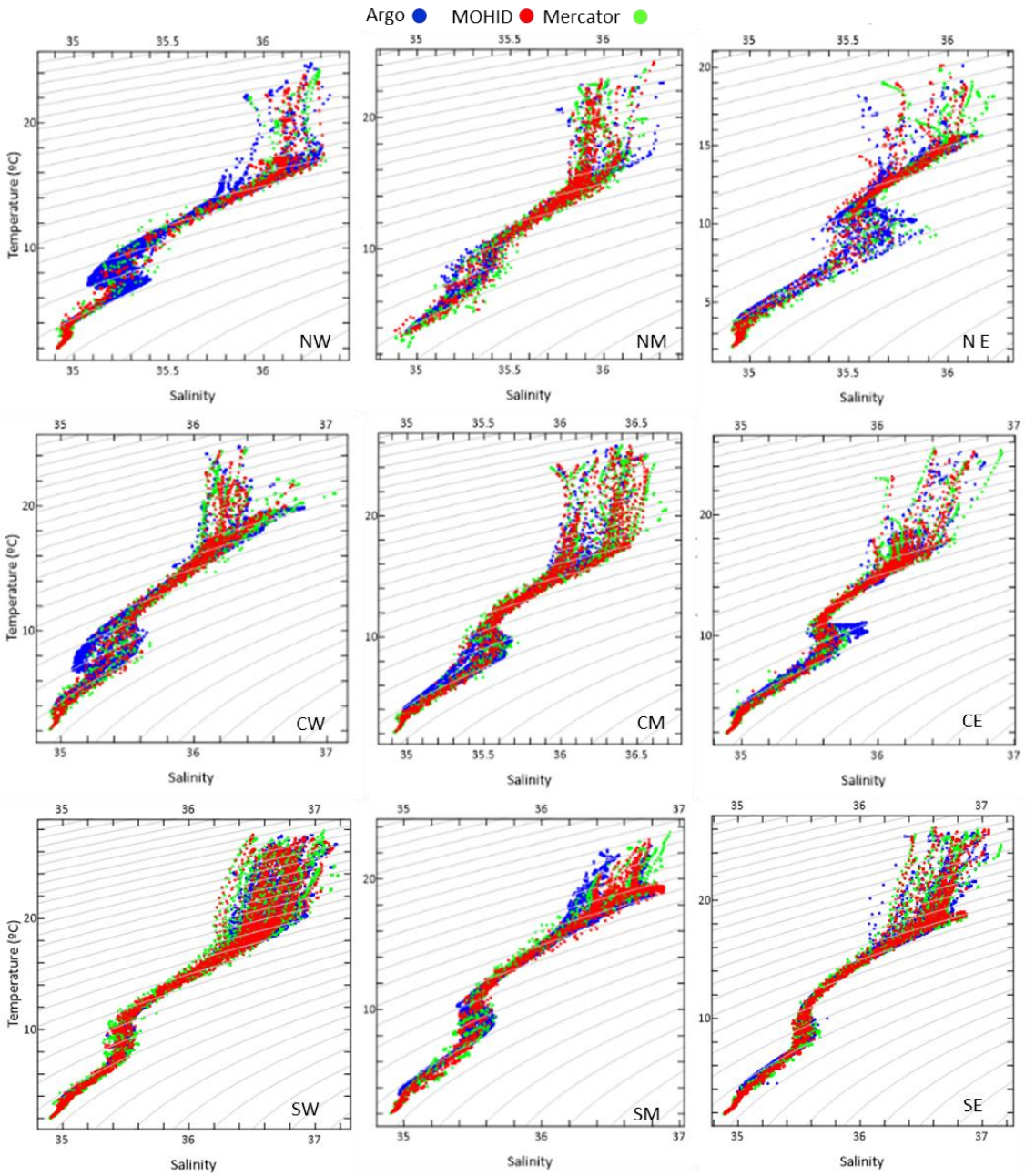

Figure 2.11- Temperature-Salinity diagram for all the Argo buoy profiles (blue), MOHID model results (red), and MERCATOR (green), in each study domain sub-area

The MW, ENACW, and NADW signals can be identified in these T-S diagrams. However, MOHID and MERCATOR don't detect it with the same accuracy as Argo buoys. This limitation is a consequence of model resolution, lower than ARGO buoys resolution (Lellouche et al., 2018)

Surface average results of velocity modulus and direction (Figure 2.14a) represent the general sea-surface ocean circulation for the study area. Two main currents are visible and have influence in this zone. The Azores Current (AC), located in the south of the archipelago, and moving eastward, and the North Atlantic Current (NAC) moving northward, West and North of the archipelago. The AC, as it was described by Comas-Rodríguez et al., 2011, has its originas a branch of the Gulf Stream, heading south-eastward and crossing the Mid-Atlantic Ridge south of the Azores (Comas-Rodríguez et al. 2011). The signal of the AC is visible in Figure 2.14 a e b) with higher velocities at 500 meters depth, Figure 2.14 b). Below the 500m depth, the velocities are lower, and the major currents are located near the island's platform, following mainly the Southwest direction Figure 2.14c) and d)). In the superficial layers, the NAC moves northward and is visible West and North of the archipelago..

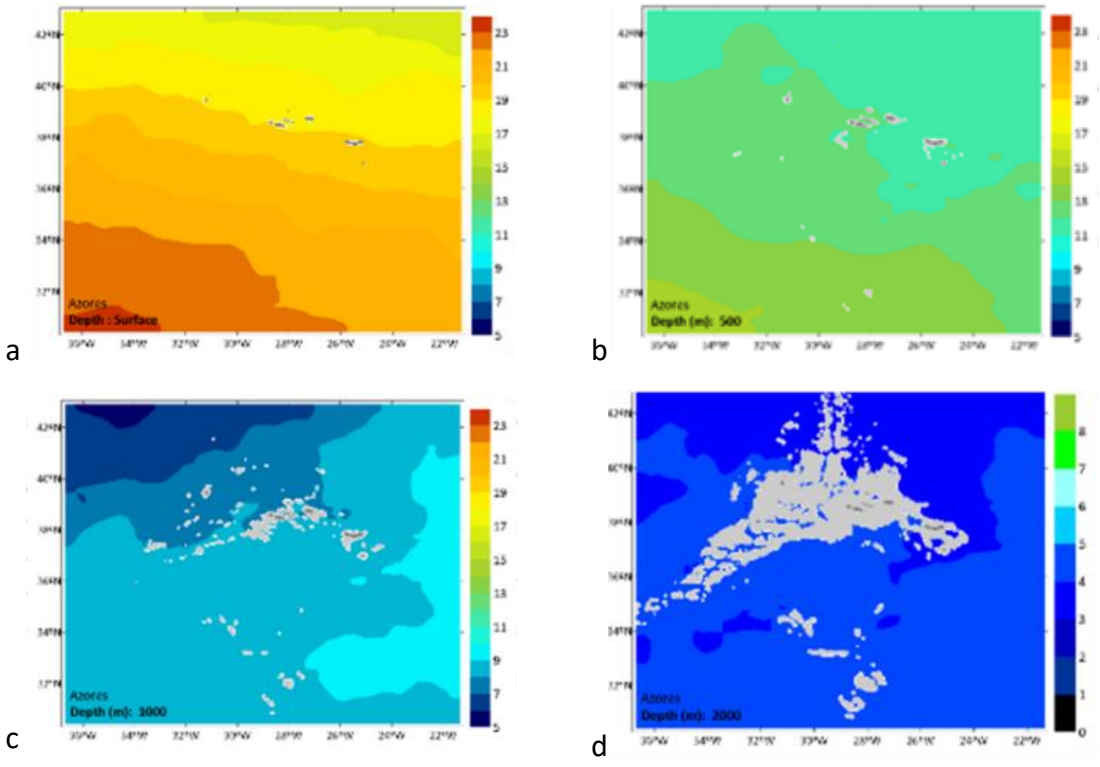

Figure 2.12 Horizontal distribution of annual average temperature from model results, at different depths: a)surface, b)500m, c) 1000m, and d) 2000m depth.

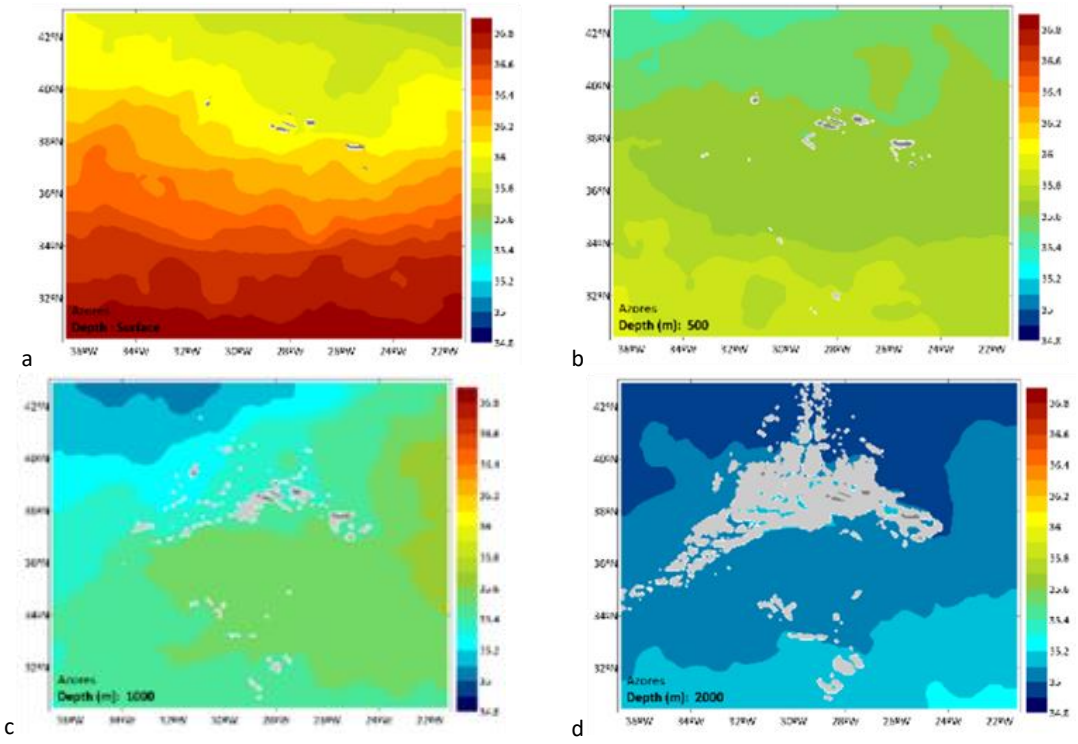

Figure 2.13 Annual average for Sea salinity model results at different depths: a)surface, b)500m, c) 1000m, and d) 2000m depth.

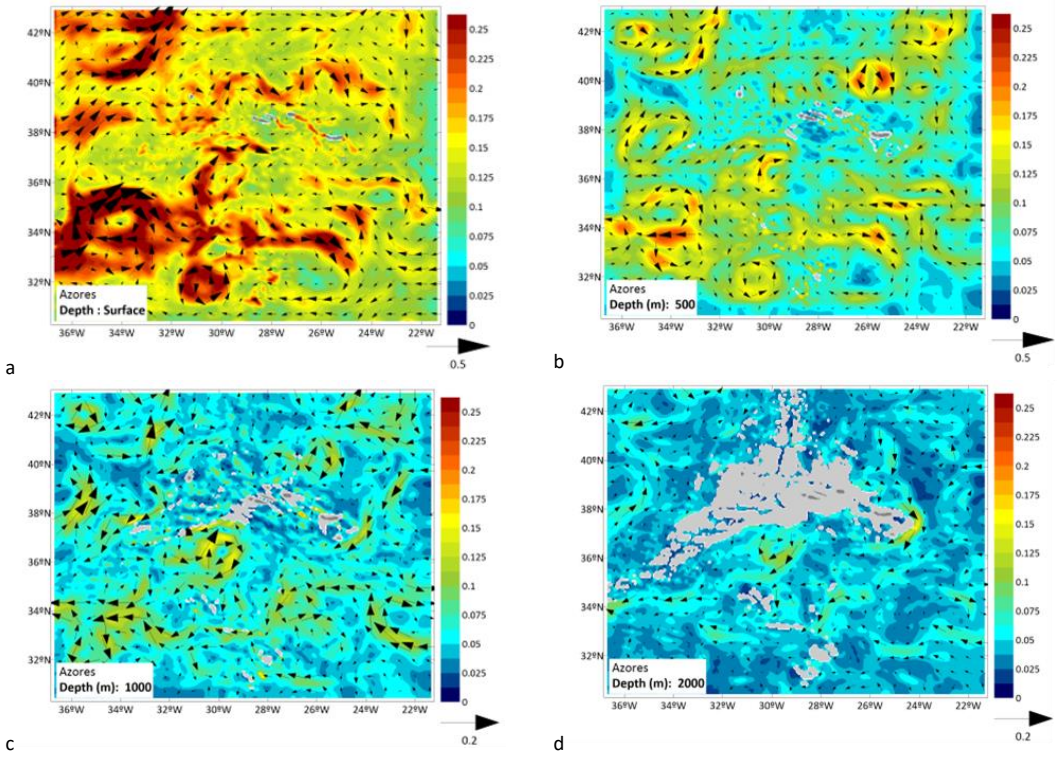

Figure 2.14- Horizontal distribuiton of annual average of velocity modulus (color scale) and direction (vector scale), from MOHID results, at different depths: a)surface, b)500m, c) 1000m, and d) 2000m depth.

2.6. Final discussion

In the present work, a 3D-MOHID Water model application was implemented for the Azores region. Results show that MOHID adequately represents physical oceanographic properties: water level, SST, and water temperature and salinity along the water column.

Validation against the tidal gauge located at Ponta Delgada showed that MOHID is able to simulate observed water levels with accuracy, reproducing the amplitude and tidal phases. Although the Azores has been an object of study and hydrodynamic model applications and validation, few model applications for this area consider tide. It would have been desirable to have more gauge stations to conduct this validation at a wider range of locations, either on other islands, or on the open ocean.

For SST, a good agreement between MOHID and the satellite-derived observations has been proved, with a correlation higher than 95% for the entire domain, emphasizing the strength of MOHID results. Some differences were detected around the archipelago. In further applications this limitation can be surpassed trought downscaling with higher resolution model to local regions.

For the entire water column, MOHID evidences the ability to simulate the general patterns of temperature and salinity, with a correlation higher than 95% with Argo buoys data. The deeper analysis of these results shows the importance of a 3D high-resolution model, to better understand and describe the heterogeneity of water properties in the different water depths. Results reveal that the accuracy of MOHID to reproduce the physical properties of the study area was adequate, and comparing with other studies, MOHID reveals a good, or even better performance than other models for this area.

The general currents and water masses are well simulated by MOHID.

Validation results analysis evidences the importance of the monitoring data programs. Even with the higher vertical model resolution (50 vertical layers), small scale variations identified in the Argo data are not represented with this modelresolution. Also, model tools can help to have a holistic approach to the entire study area, and to study different hypotheses, enhancing the importance of the monitoring work for model validation, to rise and to answer to several study hypotheses, or to give more detailed and in-situ data.

This implementation and validation work for the main physical parameters, shows that this regional model can represent the patterns observed by monitoring data. Thus, this regional model is capable of providing adequate boundary conditions for a higher resolution local and biogeochemical model, to study biological patterns.

Chapter 3

Biogeochemical model in the Azores

3.1. Abstract

The focus of this chapter is the biogeochemical model implementation. It describes the model implementation, parametrization, calibration and validation. Validation results are presented for the surface and along the water column. Finally, model results are discussed to characterize the major biotic and abiotic processes, their spatial and seasonal variability in the Azores region.

3.2. Introduction

Biogeochemical dynamics in an ocean region are complex, and their study will benefit from a modelling approach. A biogeochemical model helps to study the transfer functions linking biological and chemical standing stocks. Different models follow several parametrizations, with prioritization of the different processes (Kwiatkowski et al. 2014). While the hydrodynamic models are widely used and implemented, and their physical equations of state are relatively well known, when considering biogeochemical dynamics, the complexity increase, and consequently the diversity of options (Ménesguen et al. 2007). The hydrodynamic model, by solving the advection-diffusion equations, provides the physical variables to the biogeochemical model (water temperature, salinity, velocity and density).

Many biogeochemical models simulate marine biological productivity and describe the biogeochemical cycles following a nutrient–phytoplankton–zooplankton–detritus (NPZD) approach. NPZD models connect biogeochemical cycles and trophic levels through the uptake of nutrients by phytoplankton and remineralisation of organic matter. Other examples of NPZD models are PISCES (Pelagic Interactions Scheme for Carbon and Ecosystem Studies) (Aumont 2005) or HAMMOC(Hamburg ocean carbon cycle model) (Ilyina et al. 2013), among others

(Fasham et al. 1990, Berline et al. 2007, Xu et al. 2008, Fennel 2009) (Haney & Jackson 1996applied in regional and global domains.

The number of phytoplankton groups to consider in biogeochemical models, is under discussion in model developments, considering their simplicity, complexity and objectives. Different models can consider different phytoplankton functional groups (PFG), different dynamics and parametrizations. Namely: in the CCSM-BEC model, the light dependency of growth plays an important role in the North Atlantic, while in the NEMURO (North Pacific Ecosystem Model for Understanding Regional Oceanography) and PlankTOM5 ocean biogeochemistry mode, the difference in the maximum growth rates is the major factor for this calibration (Hashioka et al. 2013). Also, different top-down or bottom-up controls can have different effects on phytoplankton growth. While in PISCES, CCSM-BEC, and PlankTOM5 models the top-down control, by zooplankton grazing, helps to control phytoplankton and diatoms dynamics, in other models this control is more effective by bottom-up processes, calibrating the nutrient dependence of diatom growth compared to phytoplankton (bottom-up control), by the half-saturation constants a stronger nutrient dependence of diatom growth compared to phytoplankton (bottom-up control) (Gnanadesikan et al. 2011).

Although marine biogeochemical models have increased their complexity in the last decade, global-scale models continue to use simple phytoplankton growth models, with simplification of phytoplankton physiology, namely using constant C:N stoichiometry, and constant Chl:C ratio using the classical Michaelis–Menten representation of nutrient uptake (Anugerahanti et al. 2021) and assume constant stoichiometry between carbon, nitrogen and phosphorus (Redfield ratio) (Ayata et al. 2013).

3.3. Methodology

A 3-D biogeochemical model is implemented in the Azores region to simulate the major biogeochemical processes in the region. First a general description of the major processes simulated by the biogeochemical model was performed. Second, the model was applied to the Azores region, it was parameterized and calibrated, and finally, was validated against available data.

In this case, when applying the model for the Azores region, those major processes were calibrated by tunning the different parameterizations, to adjust the physical-biological model formulations, to better represent the highly dynamic marine environment observed in the Azores

Associated with the parametrization process a successive calibration analysis was performed by comparing model results and analyzing its temporal, seasonal and spatial dynamics, comparing it with the available in-situ data, climatology for the region or any other registered information. Model assessment and validation were performed using several statistical methods and comparisons with other model results.

3.3.1. MOHID Water Quality module

MOHID Water Quality module is integrated into MOHID solution (www.mohid.com) (Instituto Superior Técnico 2003). This biogeochemical module, like all the MOHID solution, is *opensource* and available online (https://github.com/Mohid-Water-Modelling-System/Mohid).

The model was initialy initially developed by EPA (Bowie et al. 1985) considering general state variables including phytoplankton, zooplankton, oxygen, silicate, nitrogen and phosphorous cycles. The Water Quality module is coupled in a physical model, using an off-line approach, where the numerical scheme of the biogeochemical processes is solved offline, over the physical solution. Biogeochemical processes are solved using the advection-diffusion equations with biogeochemical source and sink terms. The process is 0-D, grid-independent, the processes take place inside the control volume, which undertakes local production and destruction terms. To improve computational costs, time step is independent and lower than the hydrodynamic time step (Trancoso et al. 2009).

MOHID Water Quality simulates the marine biological productivity and the major biogeochemical cycles. It is a nutrient–phytoplankton–zooplankton–detritus (NPZD) model (Vallino 2000). Nutrients are incorporated into phytoplankton biomass through phytoplankton growth, and then by grazing are transferred into zooplankton biomass. Hereafter, by phytoplankton and zooplankton's mortality, the nutrients are incorporated into the detritus pool, and by nitrification and mineralization, nutrients will be available again in the water column, closing this cycle.

State variables include the main inorganic nutrients (nitrate, phosphate and dissolved silica), dissolved oxygen, two phytoplankton groups (small phytoplankton and diatoms), and zooplankton. The carbon cycle is estimated explicitly, (like in other biogeochemical models (e.g. MEDUSA (Yool et al. 2013)), from other elemental cycles (N, P, Si), using a fixed stoichiometry for carbon-nitrogen-Phosphorous, following the Redfield ratio (C:N:P ~106:16:1). This Relfied ratio, created by Redfield in 1958, is based on the proportions of the life's essential elements (C/N/P), which are essential to the metabolic requirements of phytoplankton (Hirose & Kamiya 2003, Weber & Deutsch 2010). Redfield ratio was extended to include silicon (C:Si:N:P = 106:15:16:1; (Brzezinski 1985)).

Three living compartments are represented: zooplankton, and two Phytoplankton Functional Types (PFTs): small phytoplankton, and diatoms. These PFTs differ in how the environment influences their growth (influenced by light and nutrient concentration), their respiration, excretion and metabolic rates, and, therefore, their effects on biogeochemistry (Litchman et al. 2015).

Similarly to other model applications for the Atlantic ocean (Ward et al. 2013), MOHID doesn't consider large dinoflagellates because they are assumed to be of limited importance in open ocean waters (Vichi et al. 2007a). Diatoms differ from the other groups because their growth is limited by dissolved silicate. Diatoms are the main source of biogenic silica in the model. Table 3.1 list all the state variables in use in this MOHID module.

MOHID follows the Monod approach for phytoplankton growth (Monod, 1942), where growth is limited by the availability of external nutrients.

Phytoplankton and zooplankton groups are quantified in mgC/l. Phytoplankton carbon biomass is often inferred from chlorophyll_a measurements (Chl) using a constant carbon to chlorophyll ratio (Arteaga et al. 2016). In situ observations of phytoplankton Chl:C are scarce, and this carbon-to-chlorophyll ratio is a major unknown variable in marine ecosystems understanding (Taylorl et al. 1997). Factors like nutrients and light influence physiological changes in phytoplankton, and consequently this Chl:C ratio (Arteaga et al. 2016). The use of a constant Chl:C ratio, is mostly used in biogeochemical models. Table 3.2 summarises the different Chl:C ratios used in different models (Fasham et al. 1985, Macedo et al. 2000, Fennel et al. 2006,

Aumont et al. 2015, Itoh et al. 2015, Arteaga et al. 2016). This carbon to chlorophyll conversion allows comparing model results with remote sensing data, and other data sources, for model calibration and validation. Non-biological state variables used in the model are inorganic nutrients (nitrogen, phosphorus and silicate acid), oxygen and organic matter.

Table 3.1- State variables considered inWater Quality module

Variable	Description		Units
ϕPhy	Phytoplankton concentration (mainly flagellates)	Organism	mgC/l
ϕDia	Diatoms concentration		mgC/l
ϕZoo	Mesozooplankton concentration		mgC/l
ϕNH4	Ammonia concentration	Nitrogen	mgN/l
ϕNO2	Nitrite		mgN/l
ϕNO3	Nitrate		mgN/l
ϕPON	Particulate Organic Nitrogen Concentration		mgN/l
ϕDONnr	Dissolved organic nitrogen non-refractory concentration		mgN/l
ϕDONre	Dissolved organic nitrogen refractory concentration		mgN/l
ϕIP	Inorganic phosphorous concentration	Phosphorous	mgP/l
ϕPOP	Particulate Organic Phosphorous concentration		mgP/l
ϕDOPnr	Dissolved organic Phosphorous non-refractory concentration		mgP/l
ϕDOPne	Dissolved organic Phosphorous refractory concentration		mgP/l
ϕDissSi	Dissolved silica concentration	Silica	mgSi/l
ϕBioSi	Biogenic Silica		mgSi/l
ϕOxy	Dissolved Oxygen concentration	Oxygen	mgO2/l

Table 3.2- Chlorophyll to carbon ration used in several models or obtained on several studies

Parameter	Model /In-situ location	Source	Value	units
minimum chl/C	PISCES (global model)	Aumont et al, 2015	0.0033	mgChl.mgC-1
maximum chl/C	PISCES (global model)	Aumont et al, 2015	0.05	mgChl.mgC-1
Chl/C	Azores front	Macedo et al, 2000; Irwin et al. 1983	0.03125	mgChl.mgC-1
Chlorophyll/C	Model / Local study	Itoh et al., 2015	0.036	mgChl.mgC-1
Chlorophyll/C	MEDUSA (coastal zones)	Yool et al., 2013	0.05	mgChl.mgC-1
Carbon/Chlorophyll	Global /study	Arteaga et al. 2016	< 0.01 to 0.05	mgChl.mgC-1
maximum Chlorophyll/C	ROMS-Bio Fennel (global model)	Fennel et al, 2006	0.053	mgChl.mgC-1
Chlorophyll/C	Azores Front EAW	Fasham et al., 1985	0.031	mgChl.mgC-1
Chlorophyll/C	Azores Front WAW	Fasham et al., 1985	0.0115	mgChl.mgC-1
Chlorophyll/C	Azores Front combined	Fasham et al., 1985	0.0185	mgChl.mgC-1
Chlorophyll/C	MOHID	*this application	0.0125	mgChl.mgC-1

3.3.1.1. State Variables

Organisms

Three living compartments are represented in this application: zooplankton, and two Phytoplankton Functional Types (PFTs): small Phytoplankton (Phy) and Diatoms (Diat). Diatoms are unicellular photosynthetic algae, part of phytoplankton. This group is estimated to contribute for 20 to 40% of the primary production in the ocean, and an even greater percentage of the export production for the euphotic zone (DeMaster 2001), making them major players in the cycling of all biological elements (Yool & Tyrrell 2003).

One of the distinctive features of diatoms is that they form a major portion of their cell walls out of silica, and they develop a strategy to take up silicon from the environment, mineralizing it and forming biogenic silica (DeMaster 2001). On the other side, typically its larger size can require higher maximum growth rates (Marañón 2005), and higher half-saturation constants for nutrient-limited growth or nutrient uptake, contrasting with smaller phytoplankton (Litchman et al. 2015). However, it is not correct to take this assumption on a broad base. When considering biogeochemical models different combinations of these mechanisms can result in different rates.

Phytoplankton

Phytoplankton simulation in MOHID follows several statements (Figure 3.1). The organisms consume inorganic nutrients (ammonia and nitrate from the nitrogen cycle, and inorganic phosphorus from the phosphorus cycle). During the photosynthetic process, dissolved oxygen is produced. Phytoplankton growth is limited by nutrient availability, temperature, and light availability as a source of energy for photosynthesis. Oxygen is consumed during the respiration process, accompanied by the production of ammonia. Phytoplankton concentration reduces by excretion, mortality, grazing and settling. By excretion produces dissolved organic material (Refractory Dissolved Organic Nitrogen, Non-Refractory Dissolved Organic Nitrogen, Refractory Dissolved Organic Phosphorus and Non-Refractory Dissolved Organic Phosphorus). By mortality,

phytoplankton increases the dissolved organic material and the particulate organic material (Particulate Organic Nitrogen and Particulate Organic). The settling process is modelled in the water properties module. The simulation of the diatoms cycle in MOHID follows similar internal fluxes to small phytoplankton, nonetheless including dissolved silica, which is an essential chemical requirement for diatoms Figure 3.2. By mineralization diatoms produce biogenic silica.

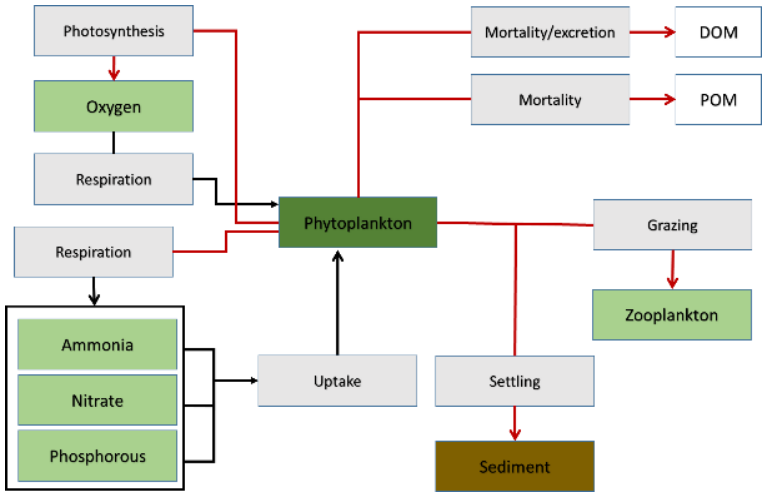

Figure 3.1- Internal flux of Phytoplankton (small phytoplankton) in WQ module

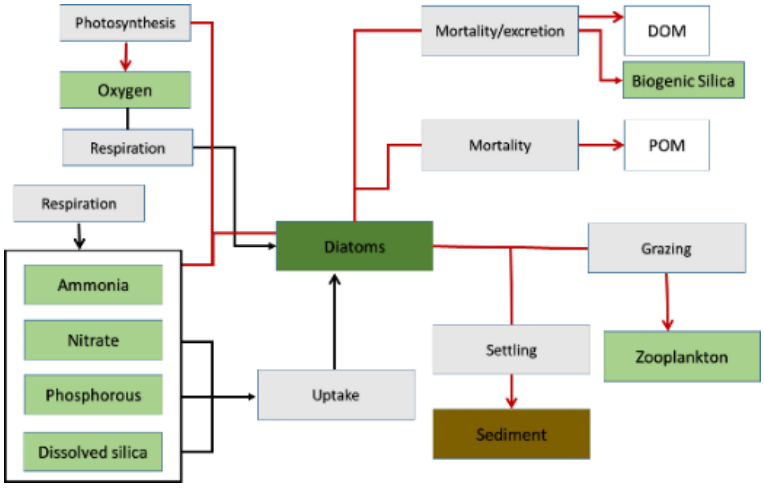

Figure 3.2- Internal flux of Diatoms in WQ module

Zooplankton

Zooplankton is essential in biogeochemical cycles because it controls the phytoplankton abundancy, by grazing. Zooplankton consumes oxygen by respiration, and phytoplankton by grazing (Figure 3.3.). Zooplankton by mortality and excretion contributes to the detrital pool, returning particulate and dissolved organic matter into the water column. Large and small detritus, as well as phytoplankton, have an associated vertical sinking rate.

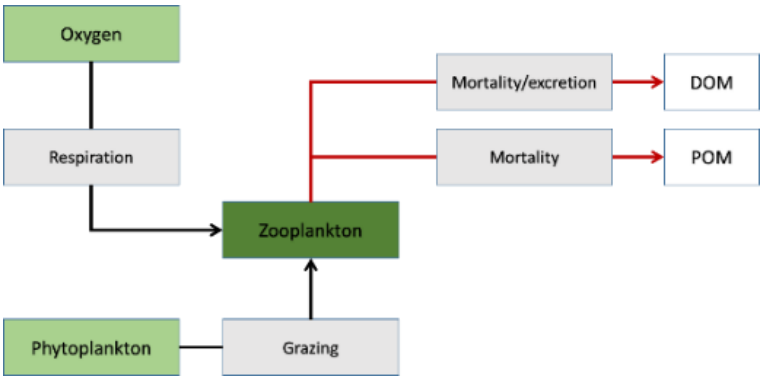

Figure 3.3- Internal flux of zooplankton in WQ module

Zooplankton's pool is induced by gross growth rate and by phytoplankton grazing (gz), losses are due to respiration (r_z), non-predatory mortality of the zooplankton (m_z), and predatory mortality (g_z) and dependent on the zooplankton concentration (eq. 3.1). Zooplankton's gross growth rate depends on a minimum concentration of phytoplankton for grazing and is limited also by temperature and light (however with different constants than phytoplankton).

Zooplankton gross growth rate is given by:

$$\frac{\partial \phi_z}{\partial t} = (g_z - r_z - m_z) * \phi_z * G_z \qquad \text{eq. 3.1}$$

Zooplankton concentration is given by eq. 3.2, where Z_1 is the zooplankton concentration in (mgC/l), μ_{z1} is the zooplankton gross growth rate, in 1/day, e_{z1} the excretion rate in 1/day, and m_{z1} the mortality, in 1/day.:

$$\frac{\partial Z_1}{\partial t} = (\mu_{z1} - e_{z1} - m_{z1}) * Z_1 \qquad \text{eq. 3.2}$$

Finally, *G*, the rate of mortality due grazing, is given by:

$$G = \frac{g_z}{E} \times Z \qquad \text{eq. 3.3}$$

where g_z is the net growth rate of zooplankton, E the assimilation efficiency, and Z zooplankton concentration.

By grazing, zooplankton consumes phytoplankton and diatoms, with different preferences and assimilation coefficients. This grazing is dependent on the ingestion rate and limited by the concentration of phytoplankton and diatoms, from the capture efficiency, from the half-saturation constant for ingestion, and from a minimum threshold standing stock of phytoplankton and diatoms below which predation ceases.

It is assumed that zooplankton mortality is related to starvation, being directly related to the concentration of prey, where below a threshold of prey, the mortality is maximum. By zooplankton mortality particulate organic matter is released.

Nutrients

Nitrogen

The WQ module includes nitrogen as organic and inorganic nitrogen. The inorganic nitrogen is divided into ammonia (NH4), nitrite (NO2) and nitrate (NO3). The organic nitrogen is divided into particulate organic nitrogen (PON), dissolved organic nitrogen non-refractory (DONnr) and dissolved organic nitrogen refractory (DONre). DONnr includes small molecular substrates, assumed to be degraded in the way of production and DONre with a longer turnover. The sources of ammonia are the inorganic matter from the excretion and respiration of phytoplankton and zooplankton , and the mineralization of the refractory and non-refractory dissolved nitrogen (Figure 3.4). The sinks of ammonia are the uptake by phytoplankton and the nitrification of ammonia (producing nitrite).

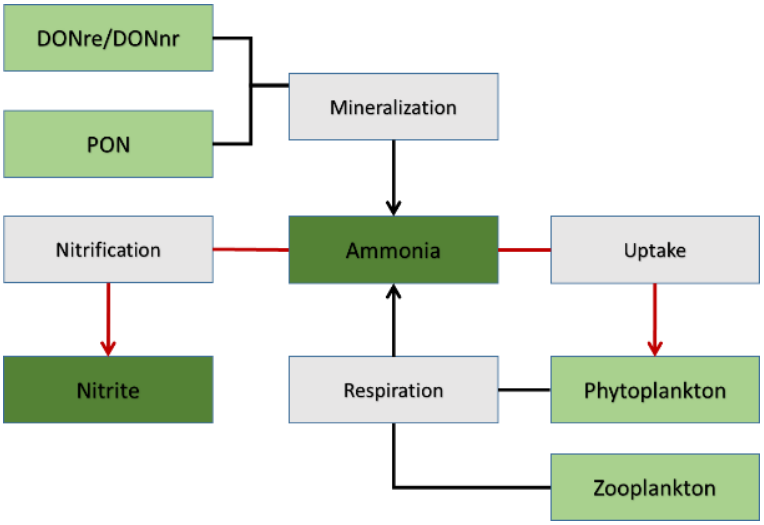

Figure 3.4- internal fluxes of ammonia in WQ module

The nitrification process considers two-stage processes, the oxidation of ammonia to nitrite (NO_2^-), and then to nitrate (NO3). Nitrification rate, PON decomposition rate, and DON mineralization rates, at a reference temperature, can be parametrized in MOHID. They are temperature dependents with a specific temperature coefficient for each case. Nitrification and denitrification rates, are calculated as a half-saturation function, with specific, and also parametrized half-saturated constants.

Phosphorous

Like nitrogen, phosphorous also is simulated in the organic and inorganic forms (Figure 3.5). The inorganic phosphorus is assumed to be available as orthophosphate (PO4) for uptake by phytoplankton. The organic phosphorus is divided into particulate organic phosphorus (POP), dissolved organic phosphorus non-refractory (DOPnr) and dissolved organic phosphorus refractory (DOPre). The rate equations of phosphorus are implemented in the same way as the nitrogen cycle, except that there is just one compartment of inorganic phosphorus.

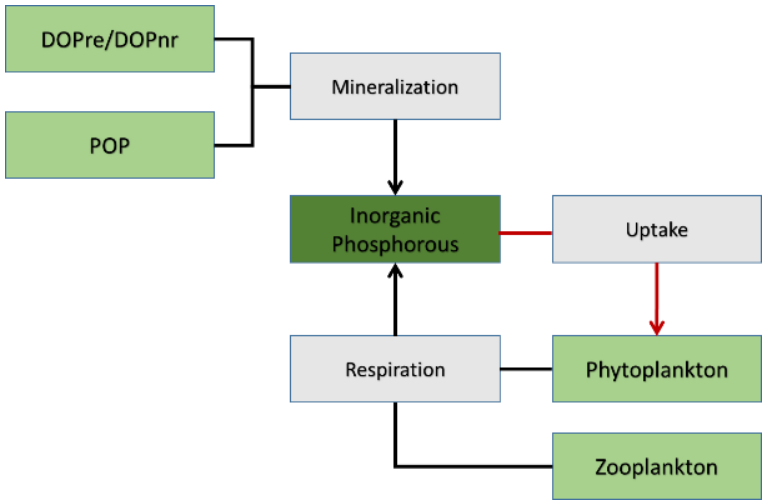

Figure 3.5- Internal fluxes for inorganic phosphorous cycle in WQ module

The inorganic phosphorous sources are the respiration and excretion from phytoplankton and zooplankton, and the mineralization of the DOP and the POP. The sink of Inorganic phosphorous is the phytoplankton uptake. The respective POP, DOPre, and DOPnre, mineralization rates at a reference temperature, and respective temperature coefficients are parameterizable in MOHID.

Silicate

Unlike the other major nutrients such as nitrate and phosphate, which are needed by almost all marine planktonic organisms, silicate is an essential chemical requirement only for some, such as diatoms or siliceous sponges (DeMaster 2001). The recirculation of Si in the ocean is essentially through its utilization by planktonic diatoms, which consume dissolved silica to elaborate a skeleton of biogenic silica (BSi) but also other siliceous consuming organisms like sponges can have a negligible contribution in the silica cycle (Maldonado et al. 2019).

In MOHID silica's cycle, Figure 3.6, Diatoms are the sinks of dissolved silica, and this process is controlled by the biogenic dissolution rate in the water column. A source of silica is silica that has been recycled by upwelling from the deep ocean and seafloor (Yool & Tyrrell 2003).

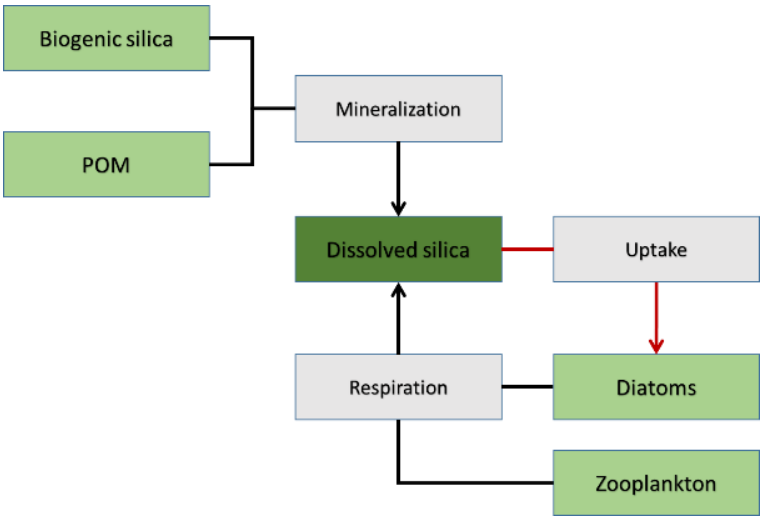

Figure 3.6- Internal fluxes for dissolved silica cycle in MOHID WQ module

Dissolved oxygen

Oxygen is an essential component of animal life, playing an important role throughout the nutrients cycle. The sources of oxygen, in the WQ module are: the photosynthesis of the phytoplankton; the denitrification of the nitrate, and the nitrate uptake by phytoplankton (Figure 3.7). The sinks of oxygen in this Water-Quality module are the nitrification; the mineralization of the inorganic nitrogen forms into DOM and POM; and the phytoplankton and zooplankon respiration.

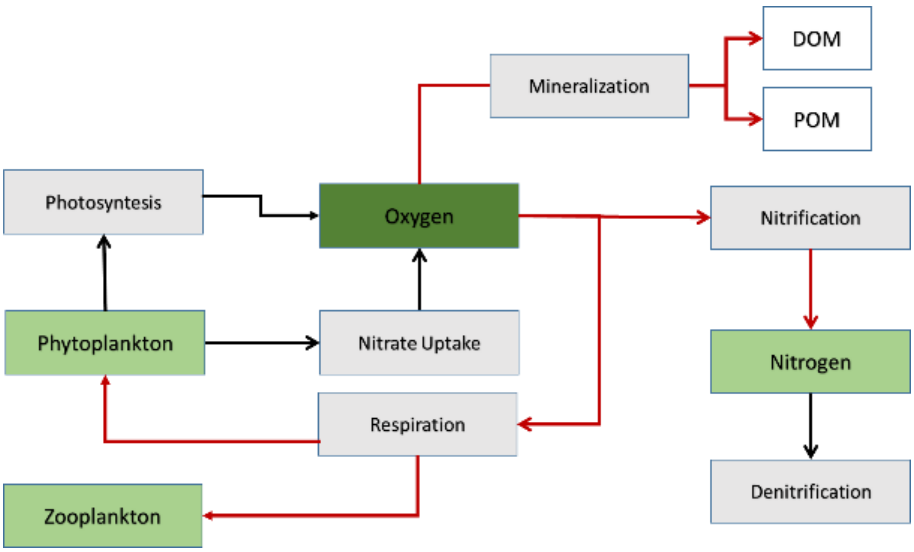

Figure 3.7- Internal fluxes for oxygen cycle in MOHID

3.3.1.2. MOHID parameterization

Limitation growth factors (Phytoplankton and zooplankton growth)

From now on, in this document, the Phytoplankton term, (Phy), will be used to refer to the total phytoplankton, considering both groups: small phytoplankton (Phy_s) and diatoms, (Diat).

Phytoplankton and diatoms growth is limited by several factors: nutrient limitation Ψ(Nut), considering Nitrogen and Phosphorous (N and P), and silicate (Si) only for diatoms; temperature limitation $\Psi(T)$, and light limitation $\Psi(L)$ (eq. 3.4).

Each growth limitation factor can range from a value of 0 to 1. A value of 1 means the factor does not limit the growth (i.e., is at optimum intensity, nutrients are available in excess, etc.) and a value of 0 means the factor is so severely limiting that growth is inhibiting entirely.

$$\mu Phy = \boldsymbol{\mu}_{Phy}^{max}.\ \Psi\ (T)_{Phy}.\Psi\ (L)_{Phy}.\Psi\ (N)_{Phy} \qquad \text{eq. 3.4}$$

Mohid uses a multiplicative formulation in which all factors are multiplied together. The major criticism of this approach is that the computed growth rates may be excessively low when several limitation factors are considered (Baird et al. 2001), mainly for the nutrients limitation.

Phytoplankton growth

Phytoplankton groups are described in terms of carbon concentration (mgC/l). The phytoplankton net growth is dependent on different processes, where μ_{Phy} is the growth rate (d^{-1}), r the respiration, ex the excretion, and m the non-predatory mortality of phytoplankton, and G the grazing by zooplankton.

$$\frac{\partial \Phi_{Phy}}{\partial t} = \left(\mu_{Phy} - r_{Phy} - ex_{Phy} - m_{Phy}\right)\Phi_{Phy} - G \qquad \text{eq. 3.5}$$

Phytoplankton growth rate is limited by temperature, light intensity and nutrients available. The respiration is divided in dark respiration and photorespiration, being re the dark respiration and rp the photorespiration.

$$r = re + rp \quad \text{eq. 3.6}$$

Following Park et al. (1980) considerations (Bowie et al. 1985), dark respiration is defined by eq. 3.7, where k_{er} is the Phytoplankton endogenous respiration constant (FENDREPC).

$$r_e = K_{er} e^{0.069T} \quad \text{eq. 3.7}$$

Photorespiration (r_p) is proportional to the gross photosynthetic rate being k_p the proportionality factor (designated as PHOTORES in the MOHID parameters) (eq. 3.9).

$$r_p = k_p \mu \quad \text{eq. 3.8}$$

By excretion (ep. 3.9) phytoplankton produces dissolved organic material. Excretion is formulated similarly to photorespiration, being highest at both low light levels and inhibitory at high light levels (Collins 1980). In MOHID the excretion rate is expressed as:

$$ex_{Phy} = \varepsilon_{Phy} * \mu_{Phy} * (1 - \Psi\,(L)_{Phy}) \quad \text{eq. 3.9}$$

Where ε_{Phy} is the phytoplankton excretion constant, and $\Psi\,(L)_{Phy}$ the phytoplankton Light limitation factor.

Phytoplankton mortality

The natural mortality, also called non-grazing mortality, m_{phy}(day^{-1}), follows the Michaelis-Menten formulation and is given by:

$$m_{Phy} = m_{max} * \frac{\frac{\Phi_{Phy}}{\mu_{Phy}}}{Km + \frac{\Phi_{Phy}}{\mu_{Phy}}} \quad \text{eq. 3.10}$$

Natural mortality considered maximum mortality, m_{max} , and the Michaelis-Menten formulation, being proportional to the biomass of phytoplankton and inversely proportional to the gross growing rate μ, where Km is the half-saturation constant for mortality. Finally, *G*, the rate of mortality due to grazing, is given by eq. 3.11.

$$G = \frac{g_z}{E} \times Z \quad \text{eq. 3.11}$$

where g_z is the net growth rate of zooplankton, and Z zooplankton concentration.

Nutrients limitation

For nutrients limitation, $\Psi(\mathrm{Nut})_{Phys}$ Mohid uses the minimum formulation, where the most severely limiting factor alone is assumed to limit growth, between N or P for phytoplankton (eq. 3.12) and between N, P and Si for diatoms (eq. 3.13).

$$\Psi(Nut)_{Phys} = min(L_N^{pn}, L_P^{pn}) \quad \text{eq. 3.12}$$

$$\Psi(Nut)_{Dia} = min(L_N^{pd}, L_P^{pd}, L_{Si}^{pd}) \quad \text{eq. 3.13}$$

Nutrients limitation in MOHID follows the Michaelis-Menten function, considering the half-saturation constant concept, K. In the case of Nitrogen limitation for Phytoplankton, the model considers (eq. 3.14):

$$\Psi\,(N)_{Phys} = \frac{N}{K_N + N} \quad \text{eq. 3.14}$$

Where K_N is the half-saturation constant for Nitrate, in mgN/l; N is the useful concentration of inorganic nitrogen (ammonia + nitrate), in mgN/l.

The same formalism is used for the other nutrients (Inorganic phosphorous, and silicate (for diatoms)). Using this formulation, the half-saturation constant takes more importance for lower concentrations of each nutrient.

For Phosphorous, the above equation takes the form (eq. 3.15):

$$\Psi\,(P)_{Phys} = \frac{PO4}{K_{PO4} + PO4} \quad \text{eq. 3.15}$$

And for silica (eq. 3.16):

$$\Psi\,(Si)_{Diat} = \frac{Si}{K_{Si} + Si} \quad \text{eq. 3.16}$$

where Ψ(P) represents the nutrient limitation due phosphorus presence, PO4 the phosphorus concentration (assumed to be completely available as orthophosphate) (mg $P.l^{-1}$) and Kp the half-saturation constant for phosphorus limitation (mg $P.l^{-1}$).

The Nitrate half-saturation constant for Phytoplankton is set to relatively low values, giving to phytoplankton a reasonably strong preference for Nitrate.

Temperature limitation

The concept of Thornton and Lessen, (1978), is adopted to compute the temperature limitation factor (Ψ(T)) on autotrophic and heterotrophic organisms, this function uses optimum temperature curves for which the growth rate increases up to an optimum and then decreases at higher temperatures.

$$\Psi(T) = K_A^{(T)} * K_B^{(T)} \quad \text{eq. 3.17}$$

$$K_A^{(T)} = \frac{K_1 . e^{\gamma_1 (T - T_{min})}}{1 + K_1 . (e^{\gamma_1 (T - T_{min})} - 1)} \quad \text{eq. 3.18}$$

$$K_B^{(T)} = \frac{K_4 . e^{\gamma_2 (T_{max} - T)}}{1 + K_4 . (e^{\gamma_2 (T_{max} - T)} - 1)} \quad \text{eq. 3.19}$$

With

$$\gamma_2 = \frac{ln \frac{k_3 (1 - k_4)}{k_4 (1 - k_3)}}{T_{max} - T_{max}^{opt}} \quad \text{eq. 3.20}$$

$$\gamma_1 = \frac{ln \frac{k_2 (1 - k_1)}{k_1 (1 - k_2)}}{T_{min}^{opt} - T_{min}} \quad \text{eq. 3.21}$$

Where Toptmin (°C) and Toptmax (°C) represent the temperature interval for an optimal process, and Tmax (°C) and Tmin (°C) the maximum and minimum tolerable temperatures where processes are completely inhibited. The remaining constants (K1, K2, K3 and K4) control the shape of the response curve of the temperature effect; these values are assumed equal for all organisms in this model.

Different organisms have different light affinity. Using this different coefficients model, we can limit the growth differentially for the different organisms. Figure 3.8 shows the result of different MOHID parametrizations for diatoms and for small phytoplankton temperature limitation factors, where the temperature interval for an optimal process is different. For small phytoplankton (Phys) TopTmin is 16,5^{o}C, TopTmax is 26,5^{o}C, and for diatoms are 15^{o}C ad 26.5^{o}C

respectively. With these different optimal temperature intervals, the growth of the diatom is more limited at lower temperatures than phytoplankton growth.

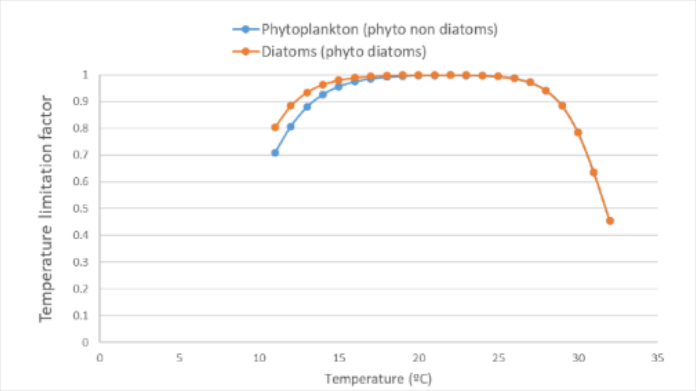

Figure 3.8- Temperature limitation factor for small phytoplankton and diatoms

Light limitation

Primary producers' photosynthetic rate is dependent on the light intensity. The light limitation factor (Ω_L) defines the relationship between the ambient light levels and, phytoplankton and diatoms growth(Haney & Jackson 1996). Phytoplankton is limited to the uppermost layers of the water column where light intensity is sufficient because photosynthesis is possible only when light reaching the algae cell is above certain intensity. The depth to which light will penetrate in water, and hence the depth at which production can occur, is dependent on several factors, including absorption of light by water, the wavelength of light, transparency of water, reflection from the surface of the water, reflection from suspended particles, latitude, and season of the year.

Like in other models (e.g. ERSEM (Vichi et al. 2007b), MOHID assumes that light extinction in-depth follows the decay given by Lambert- Beer's law, eq. 3.22 e eq. 3.23, which considers that shortwave radiation decays exponentially with depth according to the attenuation coefficient ((Zhang et al. 2018)), where I_0 is the solar radiation at the sea surface ($W.m^{-2}$); k_d, the light extinction coefficient (m^{-1}) and Z, the water column height which states that light intensity at depth z.

The photosynthetic rate increases with the light intensity until a maximum photosynthetic rate P_{max} (d^1) is reached (at optimal shortwave radiation S_{opt}). For values higher than S_{opt}, the

photosynthetic rate decreases. The photosynthetic response to the light is given by the Steele's formula:

$$\Psi\,(L)_P = \frac{I(z)}{I_s}.e^{[1-\frac{I(z)}{I_s}]} \quad \text{eq. 3.22}$$

With:

$$I(z) = I_0.e^{-k_d.z} \quad \text{eq. 3.23}$$

where:

I_s- optimum light intensity for photosynthesis (Wm^{-2})

I_o- effective solar radiation at the water surface (Wm^{-2})

z – vertical position (depth) (m)

Kd- light extinction factor (m^{-1})

Light extinction coefficient, can be calculated using Parsons ocean formulation (Leitão et al. 2008), however, satellite-based remote sensing is a more effective and rapid method for acquiring Kd over large areas than conventional measurement methods (Shen et al. 2017). The Kd value at the wavelength of 490 nm (Kd(490)) is one of the most commonly used standard water colour remote sensing products (Mouw et al. 2016, Sathyendranath et al. 2019).

Kd is obtained from an Ocean Color product, Aqua/MODIS Level-3 Binned Downwelling Diffuse Attenuation Coefficient Data Version 2018, available online at https://oceancolor.gsfc.nasa.gov/.[2] This product computes an algorithm using the empirical relationship derived from in situ measurements of Kd_490 and blue-to-green band ratios of remote sensing reflectances (Rrs), to calculate the light extinction coefficient (Kd) for downwelling irradiance at 490 nm (Kd_490) in m-1, using the product provided by NASA (Losa et al. 2017). It is a daily product with 4km resolution.

[2] https://oceancolor.gsfc.nasa.gov/data/10.5067/AQUA/MODIS/L3B/KD/2018/.

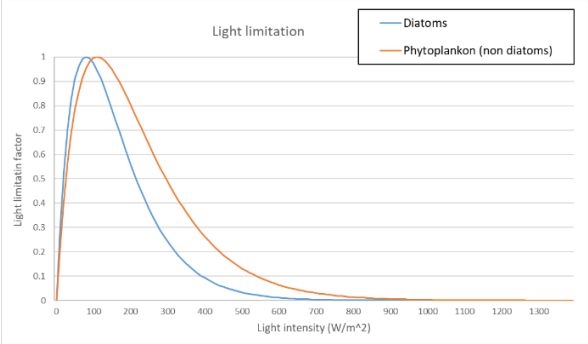

Figure 3.9- Light limitation factor considering for different optimum light intensity for photosynthesis considering diatoms and phytoplankton values used in MOHID (80 and 110 W.m-2 respectively)

Different PFT have different responses to light. MOHID computes the different light limitation factors for the different PFT optimum light intensity (Figure 3.9) shows the light limitation factor for small phytoplankton and diatoms' optimal light intensity used in MOHID (80W/m2 and 110W/m2 respectively).

Zooplankton top-down control

Zooplankton plays an important role in biological cycles and the food web, establishing a link between primary production and higher trophic levels (Lenz et al. 2000), and has an essential role in recycling and exporting nutrients through the water column (Mitra et al. 2014).

Zooplankton's grazing pressure over the phytoplankton is named top-down control. Where total phytoplankton biomass is controlled by the zooplankton grazing pressure (Hashioka et al. 2013).

In MOHID, zooplankton can feed differentially on several organisms (preys), having a preference for small phytoplankton or diatoms. The limitation factor for zooplankton *Grossgrowth rate* depends on its efficiency in the capture of small phytoplankton and diatoms, and the zooplankton's *Assimilation Coefficient* of Phyto and diatoms.

Zooplankton growth is limited by the total biomass of prey, the maximum ingestion rate ($Zoo_{IngestionMax}$), and by water temperature.

In this formulation, it is assumed that zooplankton will try to feed up to the maximum ingestion capacity, although it will give preference to each type of food (small phytoplankton, or

diatoms). The capacity to graze is quantified using a Monod equation with a half-saturation constant (ZooHalfSat). The zooplankton ingestion rate is given by:

$$Zoo_{Ingestion} = Zoo_{IngestionMax} * \frac{\sum_{i=1}^{NPreys} Food_i}{ZooHalfSat + \sum_{i=1}^{NPreys} Food_i} \quad \text{eq. 3.24}$$

$Food_i$ is computed based on the preference of Zoo for $Prey_i$ and on hunting efficiency of that Prey and also on the minimum value of that prey (*ZooPreyMin*). This value is imposed in the model to guaranty that the prey is not extinguished.

$$Food_i = ZooPreferencePrey_i * ZooHuntingEfficiency_i(Prey_i - ZooPreyMin_i) \quad \text{eq. 3.25}$$

Grazing is distributed among preys according to their contribution for $Zoo_{Ingestion}$. This contribution is accounted by the contribution of $Food_i$for total ingestion:

$$PreyConsumption_i = Zoo_{Ingestion} * \frac{Food_i}{\sum_{i=1}^{NPreys} Food_i} \quad \text{eq. 3.26}$$

Summing up all Prey Consumptions gets:

$$\sum_{i=1}^{NPreys} PreyConsumption_i = Zoo_{Ingestion} \quad \text{eq. 3.27}$$

Zooplankton can feed differently on several organisms (preys) (in this case by small phytoplankton and diatoms differently).

3.3.2. Model implementation

The Water Quality model is coupled to the 3-D hydrodynamic MOHID model over the domain from 25-32 ^{o}W to 36-41^{o}N, with 6 km resolution (1/18^{o}). The physical model is a MOHID hydrodynamic model previously implemented and validated for this domain. The configurations, as well the model validation are described in detail in the Chapter 2 of this dissertation. Model implementation is represented in Figure 3.10, and detailed in Table 3.3. Model bathymetry was

obtained from EMODNET database, available online at www.emodnet, with a grid resolution of 1/16*1/16 arc-minutes (EMODnet Bathymetry Consortium 2018).

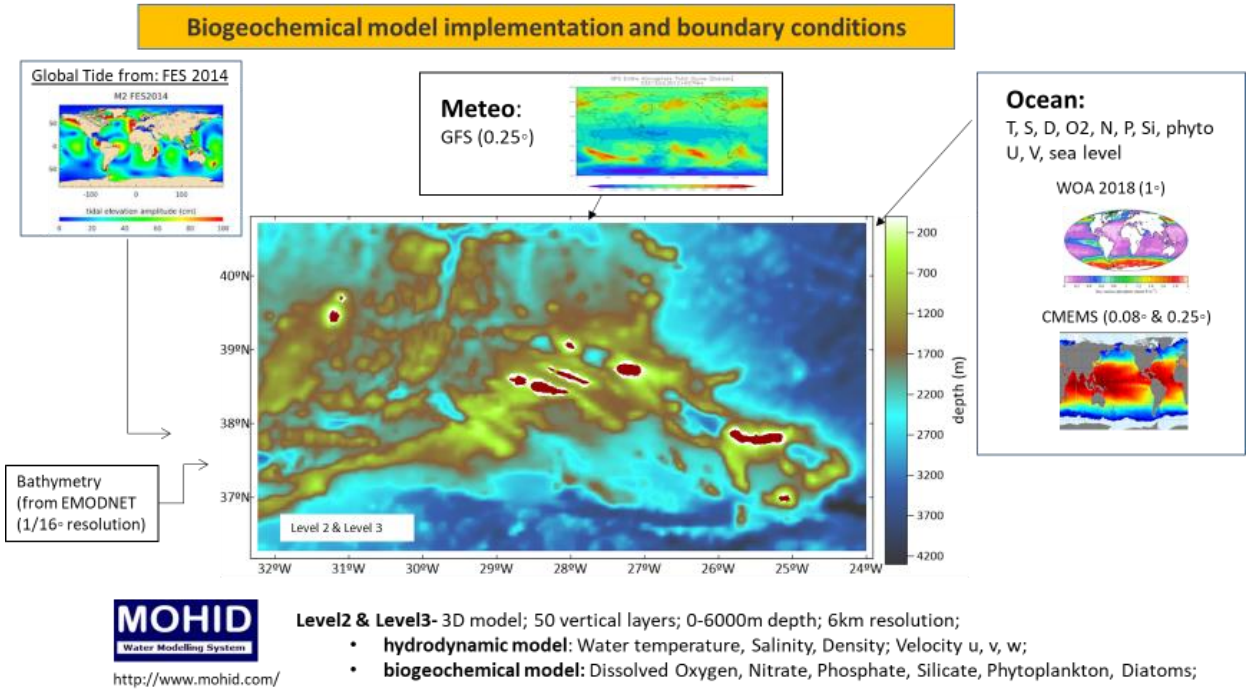

Figure 3.10- Schematic configuration and boundary conditions for MOHID Water Quality model

3.3.2.1. Initial conditions and open boundary conditions

Tide was imposed from the model using the FES2017 model (Lyard et al. 2021). The biogeochemical model runs over a 3D hydrodynamic model solution, detailed descripted on Chapter 2 using as open boundary conditions the Mercator Global Ocean (PSY4V3R1) model results, with a 1/12^{o} resolution. For the atmospheric forcing, the boundary conditions are provided by the Global Forecast System model (GFS), with a 0.25^{o} resolution, provided by NOAA-America National Ocean and Atmospheric Administration, available at https://www.ncdc.noaa.gov/.

Table 3.3- Biogeochemical model confirguration

Parameter	Biogeochemical model
Model caracterization	3D – Baroclinic
Domain	36.25°N to 40.74°N, and-23.9854°W to -32.2628°W
Bathymetry	EMODNET 1/16 arc-minuts [a)]
Horizontal Resolution	6km
Vertical resolution	50 vertical layers: 7 sigma layers + 43 cartesian layers
Tide	From level 1(FES2017[b])
Δt	120 seconds
Boundary conditions:	
Meteorological forcing	Global Forecast System model (GFS) 0.25° resolution) [c)]
Hydrodynamical forcing	MERCATOR12V1 (1/12°)[d)]
Initial conditions	N; P; Si; O2 from Operational Mercator Ocean biogeochemical global product with 0.25°resolution [d)] Phytoplankton and zooplankton constants along the domain;
Assimilation	No
Model output	3600
Simulation lenght	Jan/2017– Dec/2018
Biogeochemical variables	N; P; Si; O2; Phytoplankton (small phytoplankton + diatoms); Zooplankton (see Table 3.1)
Physical variables	Velocity u, v, z; Salinity; temperature; Water level * from the hydrodynamic model

a) EMODnet Bathymetry Consortium, 2018; b) Lyard et al., 2021; c) National Centers for Environmental Prediction, National Weather Service, NOAA, 2015; d) Julien, 2019

Biogeochemical parameters were initialized using Operational Mercator Ocean Biogeochemical global ocean analysis and forecast systems with 0.25° resolution model, a product provided by CMEMS, with 1/4 degree resolution (Julien 2019). From now on referd as CMEMS_Bio.

Initialization using World Ocean Atlas (WOA) climatology is frequently used in ocean model applications (e.g. PISCES (Kane et al. 2011); METB (Aumont et al. 2015); MEDUSA (Yool et al. 2013); FASHAM (Haney & Jackson 1996). WOA climatology with 1 degree of horizontal resolution (Garcia et al., 2018) available online at https://www.ncei.noaa.gov/access/world-ocean-atlas-2018/. WOA climatology is based on a collection of scientifically quality-controlled oceanographic *in-situ* data (Garcia et al. 2018), however, it is a monthly climatology. Whereas CMEMS_Bio model is a daily product regularly calibrated and validated (Perruche C et al. 2016). Both data sources have a variable vertical resolution: until 150 meters' depth resolution goes up to 25 meters; from 150m until 1000m, up to 100 meters per depth layer; above 1000 meters depth until the bottom layers, resolution decreases, with each layer with more than 300 meters in

length. Table 3.4 summarises the different initialization data sources used in this work, with examples of other models or applications using the same methodology.

Table 3.4- Initial conditions used in MOHID, and other models applications, for the biogeochemical parameters.

Parameter	Initial conditions in MOHID	Initial conditions in other model applications
Oxygen	Operational Mercator Ocean Biogeochemical global ocean analysis and forecast systems (0.25 ºresolution) [1]	WOA (1ºresolution)[2] (used in: a), b), c), d), f)
Dissolved silica		
inorganic phosphorus		
Nitrate		
Phytoplankton	Fixed value [3]	SeaWiFS monthly climatology[8] (used in f); In situ data; analytical results
Diatoms	Fixed value from ocean colour data from Copernicus [4]	
Zooplankton	Fixed value [5]	

1 - CMEMS model results (Julien 2019); 2- WOA2018 monthly climatology (Garcia et al. 2018); 3- Botelho, 2014; 4-Xi et al., 2020a; 5- Carmo et al., 2013b; (a)- PISCES(Kane et al. 2011); (a)-METB(Aumont et al. 2015); (c)-MEDUSA(Yool et al. 2013); (d)-FASHAM(Haney & Jackson 1996); (e)- FENNEL(Rocha et al. 2019);

After initialization, the model runs in continuous mode, assuming a null gradient boundary condition, where the value of a variable is equal to the value at an adjacent interior point, using the results of the previous run as the boundary condition for the next run

Simulation length and frequency

The simulation starts in January 2017, and model was run for two years. Calibration and validation process was performed only after February 2017 (giving 4 weeks of initialization period). After the initialization, the model was run in a continuous mode, without assimilation, with a time step of 120 seconds, and hourly model outputs.

3.3.2.2. Model parameterization

Parametrization process is always necessary when applying a model to a new domain, and is commonly performed by tuning the model within the range of literature parameter values, and by comparing the model results with in situ-data, or other data sources available, until finding the best fit between computed results and observed data (Arhonditsis et al. 2006).

MOHID Water Quality parameterization was based on MOHID default values and adapted considering other biogeochemical model applications and different case studies. Different model applications used on a global and regional scales were considered: PISCES (Aumont 2005), ERSEM (Edwards et al. 2012), Biofenel (Rocha et al. 2019), NEMURO (Yamanaka et al. 2004, Mattern et al. 2017), PlankTOM5 (Buitenhuis et al. 2010) and CCSM-BEC (Moore et al. 2001). Also other multidisciplinary and inter-comparison studies were used in this parametrization (Litchman et al. 2007, Gnanadesikan et al. 2011, Hashioka et al. 2013), as well as different studies in the Azores region (Macedo et al. 2000, Valente 2013, Barcelos Ramos et al. 2017). Some of the main characteristics of these models are summarized in Table 3.5.

Table 3.5- General characteristics of MOHID and other biogeochemical models, considering the biogeohemical cycles, NPZD components, phytoplankton functional types (PFT), and nutrient ratios.

Model	Biogeochemical cycles	Autotrophic PFT	Heterotrophic PFT	Detritus	C:N ratio	C : N : P	Chl:C
MOHID 1)	N, P, Si, O2	Phytoplankton (all excluding diatoms); Diatoms	Zooplankton (with different PFT preferences)	Yes	fixed	106:16 :1	fixed
PISCES 2)	N, Si, PO2, Fe, Ca	Nanophytoplankton, Diatoms	Micro & mesozooplankton	Yes			fixes/variab le
ROMS 3)	N, P	Nanophytoplankton	Zooplankton				fixes
MEDUSA 4)	N, P, Si, Fe, CaCO3, C	Phytoplankton (all excluding diatoms); Diatoms	Micro & mesozooplankton	Yes	Fixed	106:16 :1	variable
HAMOOC 5)	N, P, Fe	Phytoplankton	Zooplankton			122:16 :1	fixed

1)-(Instituto Superior Técnico 2003); 2)- (Aumont 2005); 3)(Peña et al. 2016); 4)(Yool et al. 2013); 5) (Ilyina et al. 2013)

Because different biogeochemical models consider different methodologies, limitation factors, different importance to top-down ot bottom-up processes, and different PFT, the parametrization is not a linear process. Also, for the same model different parametrizations can be found considering different case studies, domains, or environmental conditions (Hashioka et al. 2013, Aumont et al. 2015).

The big aim of this parametrization process was to achieve satisfactory results, able to simulate the known typical dynamics in the Azores.

3.3.2.3. Model calibration and validation

In general, for biogeochemical model applications, the most common approach for model calibration and validation for phytoplankton (or chlorophyll_a) is based on contrasting model outputs with satellite-derived surface chlorophyll (Silva et al. 2013). Several model applications follow similar approach for model assessment, using remote sensing data (Anugerahanti et al., 2021; Capotondi et al., 2019; Costa et al., 2012; Espinoza-Morriberon et al., 2016; Lacroix et al., 2007; Perruche C et al., 2016), or WOA climatology (Espinoza-Morriberon et al. 2016) for model validation.

Ideally, model results should be calibrated mostly with in-situ data, however, regarding the water column in the ocean, this data are scarce. Although research cruises provide valuable data for scientific studies, in situ measurements from vessels and scientific cruises are limited temporal and spatially. This is the case in the Azores region, where In-situ biogeochemical measurements available are scarce, and not able to characterize seasonal patterns or the water column variations in the entire region of study. Recently, argo-profiles data are being used for model assessment in the Atlantic, providing profiles of biogeochemical parameters along with the space, depth and time, (Roemmich et al. 2019), however, the absence of this type of data for the Azores study area and period, doesn't allow this type of validation.

These validation limitations are common in oceanographic and regional models, and to surpass them some models use climatology data like WOA climatology (Espinoza-Morriberon et al. 2016, Gutknecht et al. 2016) for the assessment of model results along the water column (Salon et al. 2019).

The model was initialized in January 2017, calibration tests were performed for the years 2017 and 2018. The model calibration effectiveness is reflected on model results, evaluated by model validation.

3.4. Data available for model calibration and validation

Considering the scarcity of in-situ data for the study area, model calibration and validation were performed using: remote sensing data (weekly based), WOA climatologic data (Garcia et al. 2018), and CMEMS model results (Perruche C et al. 2016)).

Remote sensing data

For the surface layers, remote sensing data was used for phytoplankton model assessment. A Global chlorophyll-a data products, OceanColor-CCI-Merged v5.0, developed by ESA Ocean Colour Climate Change Initiative (Ocean_Colour_cci) was used (Sathyendranath et al. 2021). This product provides chlorophyll_a results, on a weekly based, and available online at https://oceancolor.gsfc.nasa.gov/l3/

Chlorophyll (Chl), is widely taken as a proxy for phytoplankton biomass, due to its distinctive optical properties (Anugerahanti et al., 2021 Werdell and Bailey, 2005;) considering different phytoplankton functional types (including diatoms) (Xi et al., 2020b). Remote sensing data is interpolated on the model spatial resolution.

WOA2014 Climatology

WOA climatologic data (Garcia et al. 2018), with a 1° degree resolution, and a variable resolution along the water column for the parameters Nitrate, Phosphate, Silicate and Dissolved Oxygen.

Global model- CMEMS_Bio

CMEMS_Bio product (Julien 2019), with 0.25 degrees resolution, and a variable resolution along the water column for the parameters: Nitrate, Phosphate, Silicate, Dissolved Oxygen, Phytoplankton and clorophyll.

Table 3.6- Biogeochemical in-situ data available for the Azores region

Source Type/name	Parameter	EOV name	reference	Year	nº of datasets	depth profiles/ resolution
Condor and other Seamounth projects	phytoplankton	Phytoplankton biomass and diversity	b	2009/2010;	7 stations	5, 25, 50, 75, 100 and 150 m
	chlorophyl		b, m	2004; 2009/2010;	>20stations	
	Nitrate	Nutrients	b	2009/2010	7 stations	
	Phosphate	Nutrients	b	2009/2010	7 stations	
	Silicate	Nutrients	b	2009/2010	7 stations	
	Dissolved Oxygen	Oxygen	b, m	2004; 2009/2010;	7 stations	profile
	Carbon	Inorganic Carbon	m	2004	7 stations	
	Conductivity (CTD)	Subsurface Salinity	b, m	2004; 2009/2010;	7 stations	
	Temperature (CTD)	Subsurface Temperature	b, m	2004; 2009/2010;	7 stations	
	chlorophyl		b	2009/2010	7 stations	
	zooplankton	Zooplankton biomass and diversity	b	2009/2010	4 stations	-
	primary production		m	2004; 2009/2010;	7 stations	-
Ocean Transects; Atlantic cruises; site specific projects	Mesozooplankton biomass	Zooplankton biomass and diversity	several (b, c, d, e, f, g, h, i , j)	1976/2011	>20datasets	-
	Nitrate	Nutrients	k, n, q, s	1980, 1993, 1996, 1997, 2003,2011, 2012	< 20 datasets	profile
	Silicate	Nutrients	p	1980,1993, 1996, 1997		profile
	Phosphate	Nutrients	o, q, s	1956, 1980,1993, 1996, 1997, 2011		profile
	Carbon	Inorganic Carbon	k, l, n	1980,1993, 1996, 1997, 2003, 2012		profile
	phytoplankton	Phytoplankton biomass and diversity		1993, 1996, 1997		profile
	chlorophyl		k, l, n	1993, 1996, 1997, 2003, 2012		profile
	Oxygen	Oxygen	o, q, s, t	1980,1993, 1996, 1997, 2011		profile
	Conductivity (CTD)	Subsurface Salinity	o, q, s, t	1980,1993, 1996, 1997, 2011		profile
	Temperature (CTD)	Subsurface Temperature	o, q, s, t	1980,1993, 1996, 1997, 2011		profile
BiogeoArgoBuoys	Oxygen	Oxygen	u	2011;2012;2013;2014;2016;2017;2018	<20[1]	profile
	Conductivity (CTD)	Subsurface Salinity		2012;2013;2014;2016	>20	profile
	Temperature (CTD)	Subsurface Temperature		2012;2013;2014;2016	>20	profile
Remote sense data	Temperature	Surface Temperature	v	continuous	n	4 Kilometers
	phytoplankton	Phytoplankton biomass and diversity	v	continuous	n	
EMSO Azores	Several	Nutrients, Oxygen, Salinity, Temperature	w	Continuous (2016-29021)	n	Surface, bottom
Glider	Conductivity (CTD)	Subsurface Salinity			1	profile
	Temperature (CTD)	Subsurface Temperature		2019	1	profile

a-Boyer, Tim P. et al (2018); b- Carmo et al. (2013);c-Dias et al. (1976); d-Sobral et al. (1985);e-Muzavor (1981);f-Roden, (1987); g-Silva (2000);h-Sobrinho-Gonçalves and Isidro (2001); i-Sobrinho-Gonçalves and Cardigos (2006); j-Santos (2011); k- Christiansen, Bernd, (2015); l-Head, Robert (2013); m- Irwin, Brian (2013);n- Becker, S et al. (2020); o- Vidal, Montserrat, (2016); p- Lochte, Karin; Helder, Wim (2004); q- Swift, James (2006); r- Kähler, Paul; Koeve, Wolfgang (2008); s- IFREMER (2001) ; t- Arhan, Michel (2010); u- https://biogeochemical-argo.org/ ; v- https://oceancolor.gsfc.nasa.gov/ ; w- @IFREMER; [1]- Accessed on May 2022

3.4.1. Model parameterization

General parameters used in MOHID and other biogeochemical models are resumed in the following tables. Tables also include values used in other works and *in-situ* studies. MOHID general parameters are based mainly on a EPA Surface Water Quality model review (Bowie et al. 1985).

Table 3.7- Model parameters for small phytoplankton with their default values in MOHID

Parameter	Description	Units	MOHID
PHYGROWMAXF	Phytoplankton Maximum gross growth rate	d^{-1}	1.2 (1-2)
PHYNSATCONS	Nitrogen half-saturation constant for phytoplankton	mgN/L	0.014(0.07-0.014)
PHYSATCONS	Phosphorus half-saturation constant for phytoplankton	mgP/l	0.001
PHYPHOTOIN	Optimum light intensity for phytoplankton photosynthesis	W m-2	80 (120)
PHYFENDREPC	Endogenous respiration constant for phytoplankton	d^{-1}	0.0175
PHOTORES	Fraction of actual photosynthesis oxidized by photorespiration for phytoplankton		0.125
EXCRCONS	Excretion Constant for phytoplankton	--	0.07
FMORTMAX	Maximum Mortality Rate for phytoplankton	d^{-1}	0.02
FMORTCON	Mortality half-saturation rate for phytoplankton	mgC/d	0.3
ASS_EFIC	Assimilation efficiency of the phytoplankton by zooplankton		0.8
PHOTOIN	Optimum light intensity for phytoplankton photosynthesis	W m-2	110 (120)
TOPTFMIN	Minimum temperature of the optimal interval for phytoplankton photosynthesis	^{o}C	16.5
TOPTFMAX	Maximum temperature of the optimal interval for phytoplankton photosynthesis	^{o}C	26.5
TFMIN	Minimum tolerable temperature for phytoplankton photosynthesis	^{o}C	4
TFMAX	Maximum tolerable temperature for phytoplankton photosynthesis	^{o}C	37
TOPTFMIN	Minimum temperature of the optimal interval for phytoplankton photosynthesis	^{o}C	16.5
FRATIONC	Phytoplankton Nitrogen/Carbon Ratio	mgN/mgC	0.18
FRATIOPC	Phytoplankton Phosphorus/Carbon Ratio	mgP/mgC	0.024
FSOLEXCR	Fraction of soluble inorganic material excreted by phytoplankton	---	0.4
FDISSDON	Fraction of dissolved organic material excreted by phytoplankton	---	0.5

Table 3.8- Model parameters for diatoms with their default values MOHID

Parameter	Description	Units	MOHID
DIGROWMAXF	Diatoms Maximum gross growth rate	d^{-1}	1.2 (2)
DINSATCONS	Nitrogen half-saturation constant for diatoms	mgN/L	0.042
DIPSATCONS	Phosphorus half-saturation constant for diatoms	mgP/l	0.002
DISISATCONS	Silicate half-saturation constant for diatoms	mgSi/l	0.028
DIFENDREPC	Endogenous respiration constant for diatoms	--	0.0175
DIPHOTORES	Fraction of actual photosynthesis which is oxidized by photorespiration for diatoms	--	0.0125
DIEXCRCONS	Excretion Constant for diatoms	--	0.018
DIFMORTMAX	Maximum Mortality Rate for diatoms	d^{-1}	0.08
DIFMORTCON	Mortality half-saturation rate for diatoms	mgC/d	0.3
DIASS_EFIC	Assimilation efficiency of the diatoms by zooplankton	--	0.8
DIPHOTOIN	Optimum light intensity for diatoms photosynthesis	W/m2	110
DITOPTFMIN	Minimum temperature of the optimal interval for diatoms photosynthesis	^oC	16.5
DITOPTFMAX	Maximum temperature of the optimal interval for diatoms photosynthesis	^oC	26.5
DITFMIN	Minimum tolerable temperature for diatoms photosynthesis	^oC	4
DITFMAX	Maximum tolerable temperature for diatoms photosynthesis	^oC	37

Table 3.9- Main biogeochemical model parameters for zooplankton with default values used in MOHID, and calibrated values () , and values from other models and bibliography

Parameter	Description	Units	MOHID	Pisces$_a$*	ROMS$_b$*
INGCONSZ	Half-Saturation Constant for Grazing	mgC/l	0.2	0.24	
ZOOEFFCAPHY	Capture Efficiency of phytoplankton by Zooplankton	--	0.8		
DIZOOEFFCAP	Capture efficiency of diatoms by zooplankton	--	0.8		0.5-23
ZINGMAX	Zooplankton maximum ingestion rate	d-1	2		
ZOPHYASS	Assimilation Coefficient of Phyto by zoo	--	0.8	0.7	0.75
DIZOASS	Assimilation Coefficient of Diatoms by zooplankton	--	0.8	0.7	0.75
PHYRATING	Proportion of phytoplankton in zooplankton ingestion	--	0.5	1	
DIRATINGZOO	Proportion of Diatoms in mesozooplankton ingestion	--	0.5	0.5 (1)	
TOPTZMIN	Minimum temperature of the optimal interval for zooplankton growth	^oC	15		
TOPTZMAX	Maximum temperature of the optimal interval for zooplankton growth	^oC	26.5		
TZMIN	Minimum tolerable temperature for zooplankton growth	^oC	4		
TZMAX	Maximum tolerable temperature for zooplankton growth	^oC	37		

*- PISCES and ROMS consider Phytoplankton and Diatoms together; a)PISCES (Aumont et al. 2015); b)ROMS (Rocha et al. 2019);

Phytoplankton growth parameterization

Phytoplankton growth is limited by nutrient availability, light and temperature (Eq.2.12)There is a wide range of estimated phytoplankton growth rates in oligotrophic regions,from 0.1 to more than $1d^{-1}$ (Marañón et al. 2003, Ward et al. 2013) (see Table 3.6). This variability can arise from the spatio-temporal heterogeneity of phytoplankton dynamics in

oligotrophic regions, but also from the lack of agreement between measurement methods (Cáceres et al. 2013).

To parameterize the phytoplankton growth, besides the growth rates, also the limitation factor, and the top-down control (zooplankton grazing) are calibrated.

Besides the uncertainty around phytoplankton growth rate, also the parametrization of the half-saturation constants is rather difficult as observations show that they can vary by several orders of magnitudes, and the different models' parameterizations and studies in the literature reveal different values, as listed in Table 3.10 and Table 3.11. These dissimilarities results from the intrinsic characteristics of each case study, regarding case-study locations, model resolution, time scales, and specific phytoplankton dynamics (e.g. oligotrophic or high productivity regions), but can be related to different model configurations (Hashioka et al. 2013). In this model parametrization, firstly was calibrate the equilibrium between phytoplankton concentration and nutrients concentration.

Table 3.10- Main biogeochemical model parameters for small phytoplankton (Phy) growth and nutrients limitation constants used in MOHID, and other models and case studies

	Model or Case Study, domain and range in the literature											
Parameter	MOHID	Pisces [a,b]	ROMS [c]	FENNEL [d]	Plank-TOM [e]	Medusa [f]	Ward, et al [g]	Chai et al., [h]	Nemuro [i]	Macedo et al [j]	Maranon, et al [k]	HAMOCC 5 [l]
	Azores	Global	global	--	global	--	North Atlantic	Equatoria Pacific	North Pacific	Azores front, Sping bloom	North Atlantic	global
Phytoplankton Maximum gross growth rate (d^{-1})	1.2	0.66 (0.6)*	0.69	0.69 (0.65-3)	0.4 (0.6)	0.53	0.1-1	2	0.8	0.1-0.85	0.1-1.3	0.6
Phytoplankton Nitrogen half-saturation constant (mgN/l)	0.014	$3.6E^{-3}$ ($3.6E^{-3}$- 0.024)*	0.014 (0-0.021)	0.014		0.015	0.028-0.042	0.007	0.014	0-0.028		0.002
Phytoplankton Phosphorus half-saturation (mgP/l)	0.001	0.012 (0.012-0.074)*			2.4							0.0003

*- PISCES and ROMS consider Phytoplankton and Diatoms together; a)PISCES (Aumont et al. 2015); b)PISCES (Hashioka et al. 2013); c)ROMS (Rocha et al. 2019); d)(Fennel 2009); e)-PLANKTOM(Hashioka et al. 2013);f)-MEDUSA model (Yool et al. 2013); g)- (Ward et al. 2010); h) (Chai et al. 2002); i)-NEMURO (Yamanaka et al. 2004); j)- (Macedo et al. 2000); k)- (Marañón 2005); l)-HAMMOCC5- (Ilyina et al. 2013)

Table 3.11- Main biogeochemical model parameters for diatoms growth and nutrients limitation constants used in MOHID, and other models and case studies

	Model or Case Study, domain and range in the literature								
Parameter	MOHID	Pisces [a,b]	ROMS [c]	Plank-TOM [e]	Medusa [f]	Ward, et al [g]	Chai et al., [h]	Nemuro [i]	HAMOCC5 [l]
	Azores	global	global	global	--	North Atlantic	Equatorial Pacific	North Pacific	global
Diatoms Maximum gross growth rate (d^{-1})	1.2	0.66		0.6	0.5	1-2	3	0.4	0.851
Nitrogen half-saturation constant for diatoms (mgN/l)	0.015	3.6E-3 (3.6E-3-0.024)	0.5		0.01	0-0.028	0.014	0.042	--
Phosphorus half-saturation constant for diatoms (mgP/l)	0.002	0.012 (0.012-0.074)	0.01		0.084				0.003
Silicate half-saturation constant for diatoms (mgSi/l)	0.084			0.1	0.084		0.084	0.17	0.225

*- PISCES and ROMS consider Phytoplankton and Diatoms together; a)PISCES (Aumont et al. 2015); b)PISCES (Hashioka et al. 2013); c)ROMS (Rocha et al. 2019); d)(Fennel 2009); e)-PLANKTOM(Hashioka et al. 2013);f)-MEDUSA model (Yool et al. 2013); g)- (Ward et al. 2010); h) (Chai et al. 2002); i)-NEMURO (Yamanaka et al. 2004); j)- (Macedo et al. 2000); k)- (Marañón 2005); l)-HAMMOCC5- (Ilyina et al. 2013)

Nutrient limitations parametrization

Phytoplankton nutrient uptake rate follows the Monod approach, using a hyperbolic relationship of the form $N/(K_s + N)$, where K is the half-saturation constant. During the model calibration process, while calibrating the phytoplankton growth, when the concentration of the nutrient was too low, it was necessary to reduce the half-saturation constant to have the minimum phytoplankton growth rate to maintain the population. However, this Ks decrease diminishes the nutrient limitation, inducing a higher phytoplankton growth rate that could achieve overstated nutrient assimilations rates, resulting in a too fast (and not real) nutrients assimilation.

A modified Monod's formulation (Eq.3.28) was considered, using a modified half-saturation constant, dependent on nutrient concentration (Eq.3.29)(Sharada et al. 2005).

$$modifiedgrowth = \frac{[NO3]}{[NO3] + Ksmodified} \quad \text{Eq. 3.28}$$

$$Ksmodifeid = \sqrt{\frac{[NO3]}{KsRef}} * KsRef \quad \text{Eq. 3.29}$$

With this modified nutrient uptake, the phytoplankton was able to increase the uptake rate with lower nutrients concentration but reduce it with high concentrations. In this way, the nutrient uptake is not so efficient with higher nutrient concentrations (Figure 3.11).

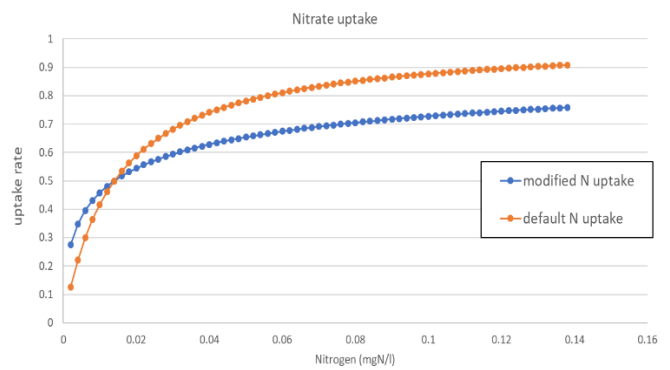

Figure 3.11- Modified and Default nutrients uptake considering the reference Monod formulation (in orange), and the modified formulation (in blue).

This modified nutrient limitation factor, induce a decrease in nutrient uptake, avoiding the extreme nutrient uptake, allowing to achieve a balanced solution between phytoplankton growth rate and nutrients availability, avoiding unreal nutrients depletion.

Zooplankton top-down control calibration

Zooplankton, by grazing, can control the phytoplankton concentration. This top-down control can control the size of the phytoplankton blooms that occurs in the oligotrophic regions (Cáceres et al. 2013). Moreover, the parameterization of zooplankton can also help to control the small phytoplankton vs diatoms dynamics. In MOHID, these parameterizations are performed by balancing the zooplankton maximum ingestion rate (Zingmax), and by changing the zooplankton preference for small phytoplankton (Phyrating) or diatoms (Dirating) Table 3.12

Table 3.12- zooplankton parametrization differences between simulation MOHID_v3 and MOHID_v3_zoo

Parameter	Parameter description	units	MOHID_v3	MOHID_v3_zoo
Zingmax	Zooplankton maximum ingestion rate	d^{-1}	2	2.5
Phyrating	Proportion of Phytoplankton in zooplankton ingestion	--	0.5	0.7
Dirating	Proportion Diatoms in zooplankton ingestion	--	0.5	0.3

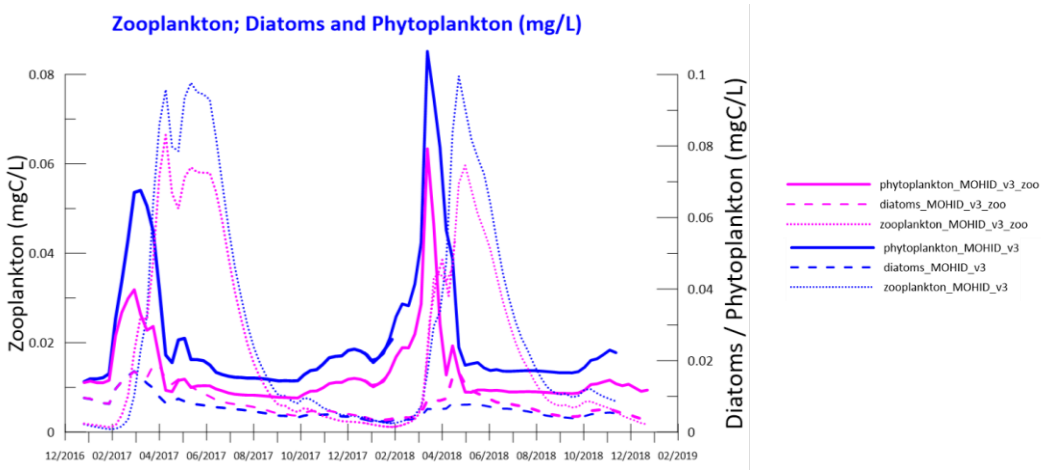

Figure 3.12-Surface weekly average results phytoplankton, diatoms and zooplankton concentration (in mgC/l), from Mohid model simulation "Mohid_v3" in blue; "Mohid_v3_zoo" in pink; All results are weekly averaged, for the entire domain at the surface, represented in mgC/l for 2017 and 2018.

Results represented on the graph in Figure 3.12, show the effect of different parametrization of zooplankton grazing rates on phytoplankton dynamics, revealing how it can control the phytoplankton concentration, limiting the phytoplankton bloom.

With parametrization "MOHID_V3_zoo", , zooplankton has a higher grazing rate, ($2{,}5d^{-1}$, contrasting with $2d^{-1}$ from "MOHID_V3") controlling the phytoplankton concentration by the higher ingestion rate, resulting in a lower small phytoplankton concentration during the entire simulation, comparing with "MOHID_V3". Furthermore, "MOHID_V3_zoo" has a preference for small Phytoplankton rather than Diatoms, which, in this case, allows diatoms to grow. As can be seen in Figure 3.12 where diatoms concentration is higher on simulation "MOHID_v3_zoo" than on the other one. These results show how zooplankton grazing can control the phytoplankton bloom (top-down control (Hashioka et al. 2013)).

Phytoplankton and zooplankton concentrations along the year reveal the importance of the *Zoopreymin* parameter, that establishes a minimum prey concentration (small phytoplankton + diatoms) for zooplankton grazing, to guarantee that prey is not extinguished.

3.4.2. Model validation and assessment

Model validation was performed at the surface and along the water column, comparing MOHID results against the CMEMS model and WOA climatology, for nitrate, phosphate, silicate and dissolved oxygen. At surface model was also validated for phytoplankton, comparing model

results against remote sensing data. Along the water column fixed points distributed along with the model domain were selected for model validation (Figure 3.13). These points are distributed evenly along the domain, along the longitude: 3 points in the North of the domain, 3 in the center and 3 in the South. Also a point in a Seamouth, namelly Gigante seamount. Also a meridional and zonal section were created for model results analysis. In these sections 3-D results are reduced into the x and y dimensions' map by taking a section in a zonal dimensional, and meridional dimension, representing on the YY axis the depth, and along with the XX axis the Longitude, or the Latitude. The selected sections cross the domain at the Pico island in the Central Group (CG) (Figure 3.13- Schematic representation of validation points and domain sections.): Meridional section at: -28.5 º W; and Zonal section at: 38.5ºN.

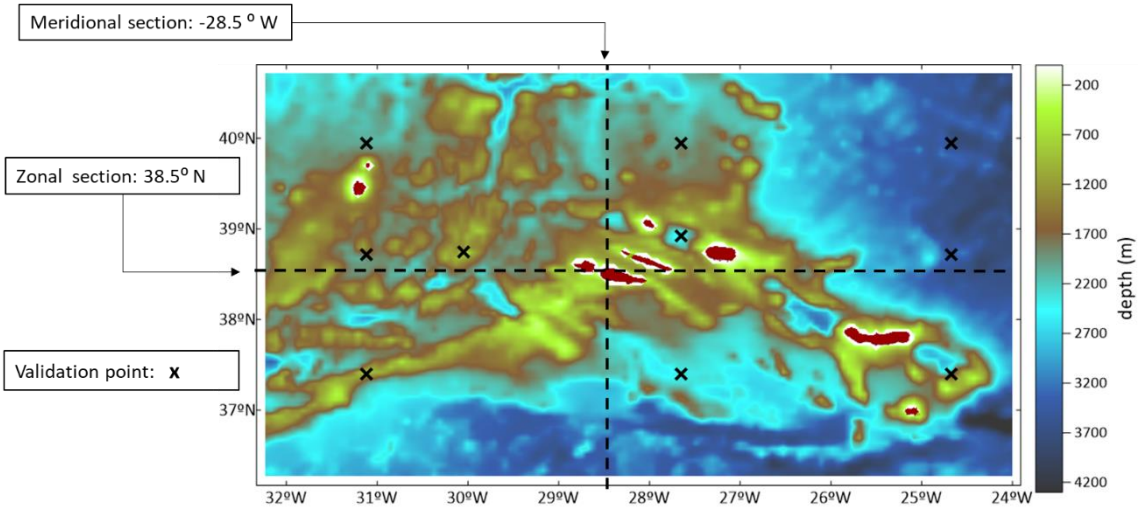

Figure 3.13- Schematic representation of validation points and domain sections.

Phytoplankton validation

Model validation was performed using the product OceanColor-CCI-Merged v5.0, L3, Global product (Sathyendranath et al. 2021). This remote sensing product provides a mass concentration of chlorophyll_a for the surface layer, considering a daily attenuation coefficient of downwelling radiative flux in seawater (kd). The same kd product, developd by NASA's Ocean Biology Processing Group (OBPG), and available at the SeaWiFS Bio-optical Archive and Storage

System (SeaBASS)[3] is used by MOHID. A constant carbon to chlorophyll_a conversion ratio of 0.0125 mgC/l is used (based on other applications for the study area (Fasham et al. 1985, Macedo et al. 2000) as well as global applications (Taylorl et al. 1997, Arteaga et al. 2016) summarized in Table 3.2.

Model skill evaluation was performed by comparing model results with remote sensing data in two ways: First, by comparing the entire model average, to evaluate the temporal evolution of model performance; Secondly, by comparing each grid data point to evaluate the model performance spatially. The validation was done on a weekly basis, as this is the frequency of satellite data.

Nutrients and dissolved oxygen validation

Model results of nitrate, inorganic phosphorous, silicate, and dissolved oxygen, were compared with WOA climatology and CMEMS-bio model, for 2017 and 2018. At the surface, the model was validated considering averages of the entire domain. While along the water column time series of fixed locations were used (Figure 3.13). Validation was performed comparing model results at each layer depth, using the vertical resolution of WOA and CMEMS respectively.

3.4.3. Statistical methods and skill assessment

Different methodologies and statistical indexes are used in 3-D oceanographic models (Stow et al. 2009). The conventional model assessment can be higher subjective (with a side-by-side approach), or can rely on statistical methods. In the present study model assessment was performed using: the root mean square error (RMSE) (eq. 3.30), bias (ep.3.31), and Pearson correlation coefficient (r) (eq.3.32) (Gómez-Zambrano et al., 2017), and Taylor diagrams, (Allen & Somerfield 2009).

In the “side by side” approach spatial maps for several parameters are compared with data spatial maps. This approach is frequently used in 3D oceanographic models, enabling assessing model capability to represent the major seasonal and geographical features, based on visually-oriented qualitative statements (Stow et al. 2009).

[3] - https://oceancolor.gsfc.nasa.gov/atbd/kd_490/

The RMSE error is interpreted as a deviation of the simulated results from the measurements.

$$RMSE = [\frac{1}{N}\sum_{i=1}^{N}(O_i - M_i)^2]^{0.5} \quad \text{eq. 3.30}$$

$$Bias = \sum_{i=1}^{n}\frac{1}{n}(M_i - O_i) \quad \text{eq. 3.31}$$

The correlation Pearson coefficient (referred to as correlation), measures the statistical relationship, or association, between model (M) and data(O).

$$R = \frac{\sum_{i=1}^{n}(M_i - \bar{M}_i) - (O_i - \bar{O}_i)}{\sqrt{\sum_{i=1}^{n}(M_i - \bar{M}_i)^2}\sqrt{\sum_{i=1}^{n}(O_i - \bar{O}_i)^2}} \quad \text{eq. 3.32}$$

Taylor diagrams are an advantageous tool to evaluate model performance, aggregating in the same diagram correlation, standard deviation, the centred RMSE (eq.3.32) and bias, between model and reference data.

Standard deviation (σ_m), defined by, is used to measure the spread of data around the mean.

$$\sigma_m^2 = \frac{1}{n}\sum_{i=1}^{n}(M_i - \bar{M}_i)^2 \quad \text{eq. 3.33}$$

The centred RMSE error (CRMSE) is the mean-removed RMSE, thus calculated as follows:

$$CRMSE = [\frac{1}{N}\sum_{i=1}^{N}(M_i - \bar{M})_i - (O_i - \bar{O}_i)^2]^{0.5} \quad \text{eq. 3.34}$$

Taylor diagrams use the Law of Cosines (Taylor, 2001), where the radial coordinate is r = σ_m and the angle is θ = arccos(R). Centred RMSE then appears as the radial distance from the position of a perfect model (r = σ_0, θ = 0), (eq. 3.34). These diagrams can be normalized, comparing different variables, or variables with different variances, by normalizing (i.e., making dimensionless) their standard deviations (Elvidge et al., 2014).

3.5. Results

3.5.1. Validation at the surface

Phytoplankton

To estimate the reliability of the model, surface phytoplankton results were compared against remote sensing data. Model results simulate a realistic temporal evolution of phytoplankton concentration in the entire domain along the year, reproducing the seasonal phytoplankton dynamics. The model represents the typical spring bloom, and the weak autumn phytoplankton bloom (Figure 3.14). The model is overestimating the phytoplankton concentration, with a positive bias during the entire year, except in winter, when it is close to zero or negative (Figure 3.15). Model overestimation is higher in the North east of the domain (Figure 3.16 to 3.18). The higher values of RMSE occur during the spring bloom. Near the islands model concentration is lower than remote sensing data. (negative bias verified on Figure 3.18). The average correlation is 0.643 (Figure 3.19), with the lowest values occurring in region away from the island and near the domain borders.

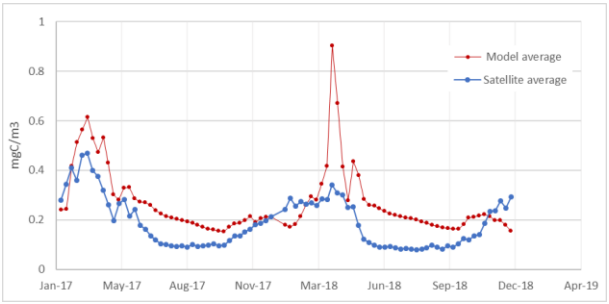

Figure 3.14- Weekly average for phytoplankton concentration at surface, from MOHID in red, and satellite (Chl_a converted to Phytoplankton) in blue, in mgC/l for the year 2017 and 2018

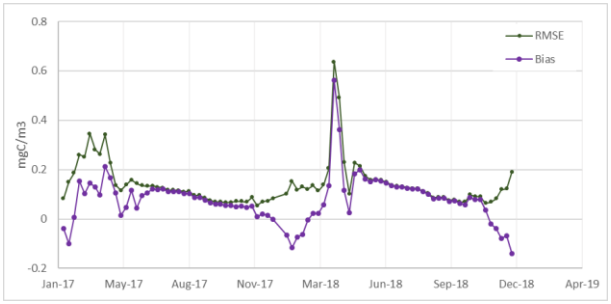

Figure 3.15-Temporal evolution of statistical results for bias and RMSE resulting from the statistical comparison between MOHID and Remote sense data in mgC/l for the year 2017 and 2018, on a weekly based.

Table 3.13- Statistic results for the comparison between MOHID and remote sense data for phytoplankton in (mgC/l) considering model and data average, R^2, BIAS, and Root mean square error (RMSE)

	Model Average (mgC/l)	Data average (mgC/l)	Bias (mgC/l)	R	RMSE (mgC/l)
2017	0.276	0.207	0.069	0.643	0.150
2018	0.258	0.175	0.083	0.43	0.173

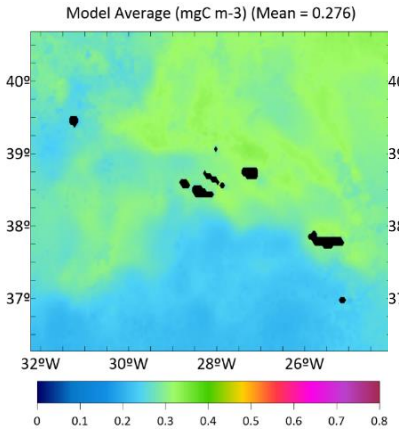

Figure 3.16- MOHID phytoplankton average for 2017 (in mgC/l)

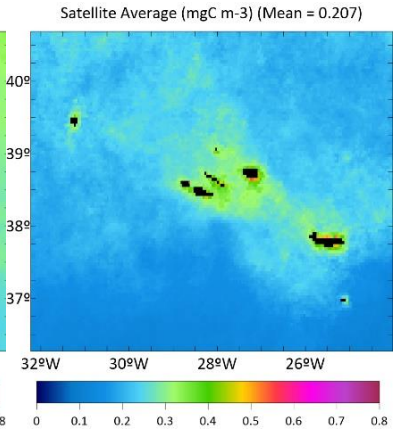

Figure 3.17- Satellite phytoplankton average concentration for 2017 (in mgC/l) (converted from chla_to C)

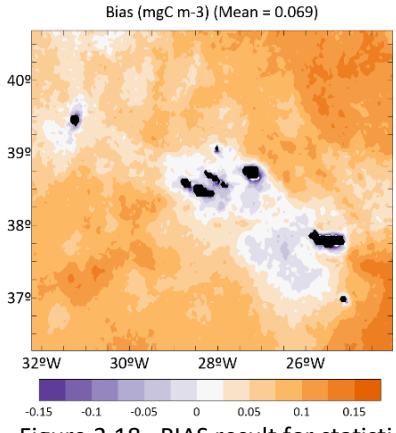

Figure 3.18 –BIAS result for statistical analysis between remote sensing data and MOHID results for 2017 (in mgC/l)

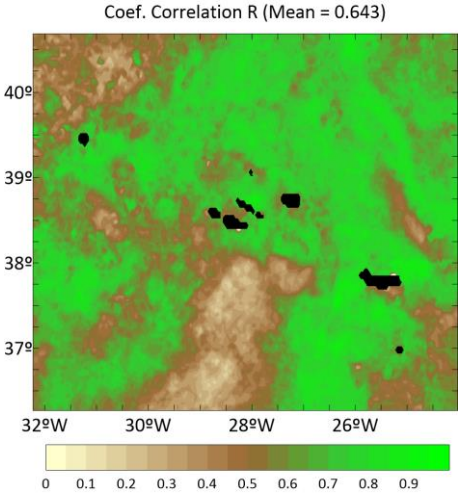

Figure 3.19- Map of correlation coefficient between remot sensing data and model results, for the year 2017

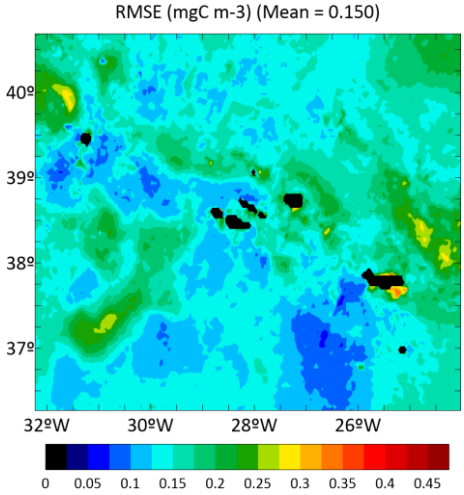

Figure 3.20- Map of RMSE obtain from the statistical analysis for the year 2017

Phytoplankton results show a north-south gradient, with lower concentration in the south part of the domain. Like the remote sensing data MOHID estimates higher phytoplankton concentrations near the islands. Also the highest BIAS and RMSE are located in the borders of the domain, except for a higher RMSE value south of São Miguel island.

Nutrients (N, P, Si) and Dissolved oxygen

Model was validated at the surface also for nutrients and dissolved oxygen. The following graphs represent the surface average results for MOHID, CMEMS, and the monthly WOA climatology in 2017 and 2018. Statistical results are summarised in Table 3.14. Results show that the annual cycle of nutrients at the surface was well reproduced by the model. A correlation of

0.92 and 0.9 was obtained for nitrate and dissolved silica, respectively. The lowest values of correlation were obtained for inorganic phosphorous and oxygen. Mohid can mimic the seasonal variations, and also the minimum and maximum values when compared with the CMEMS model (Figure 3.21). MOHID simulates seasonal oxygen dynamics as CMEMS model. However, both CMEMS and MOHID results are lower than WOA climatology data. This difference can be a sequence of the local interface water-air processes, that are solved by the models and not considered in the WOA climatology. At the surface, the oxygen concentration is very dynamic and temperature-dependent. These processes can be represented with a high resolution by the models. Whereas in WOA the resolution is coarse both spatial and timely. Nevertheless, model represents the same seasonal variation as WOA.

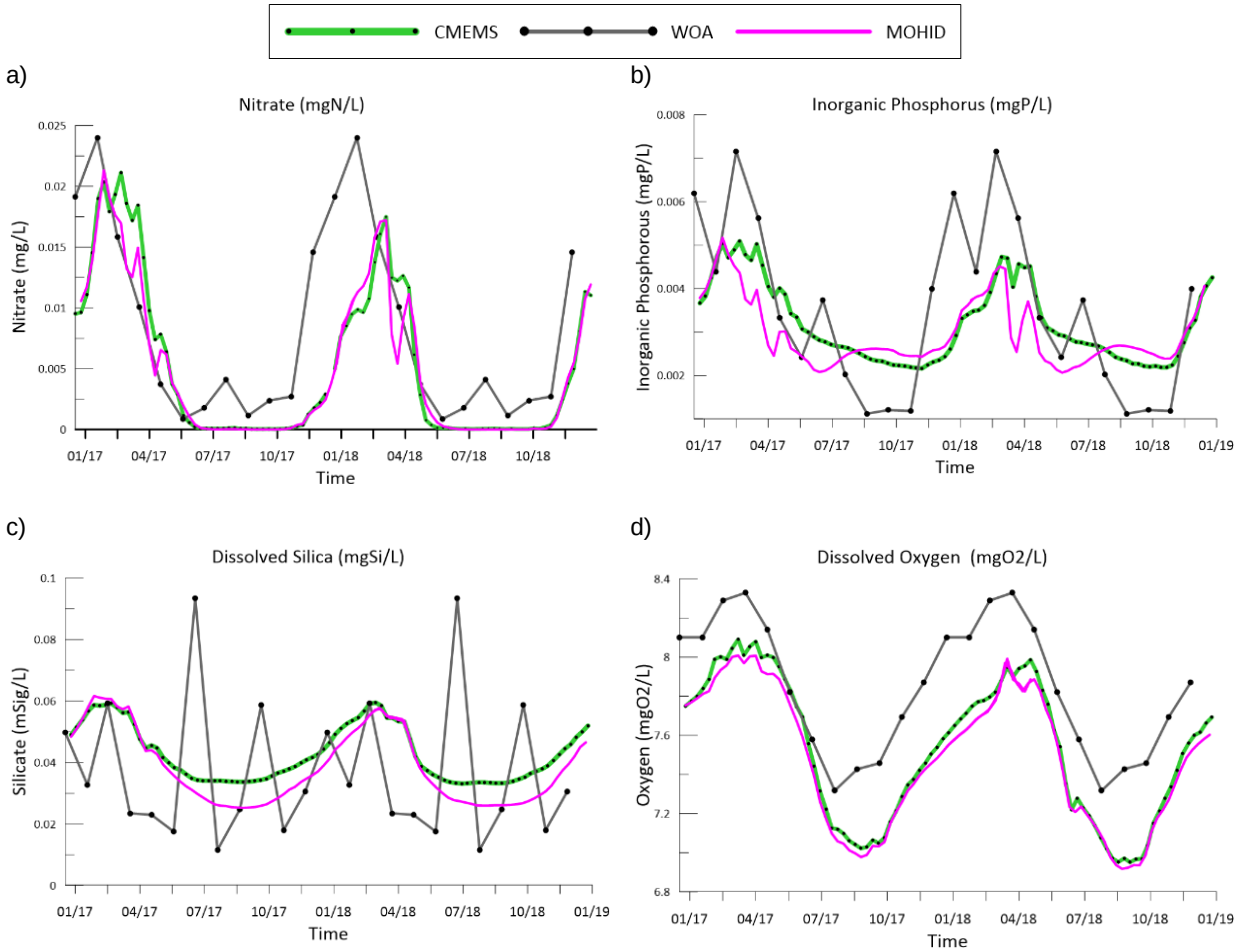

Figure 3.21-Surface average results from Mohid model (in blue); CMEMS model (in green), both weekly averaged; and monthly climatology from WOA is represented in yellow, for 2017 and 2018., for Nitrate a), Inorganic phosphorus b), Dissolved Silica c) and dissolved oxygen d

Table 3.14- Statistic results for the comparison between MOHID with CMEMS model, considering correlation (R), BIAS, Root mean square error (RMSE), for the surface avregae (weekly based) for Nitrate, Dissolved silica, Inorganic Phosphorus, dissolved oxygen

	Nitrate (mgN/l)	**Dissolved Silica (mgSi/l)**	**Inorganic phosphorus (mgP/l)**	**Oxygen (mgO/l)**
Validation MOHID vs:	CMEMS	CMEMS	CMEMS	CMEMS
R	0.92	0.9	0.5	0.68
Bias	9.00E-03	-3.62E-02	9.00E-03	2.52E-01
RMSE (mg/l)	8.3E-01	8.3E-01	8.3E-01	8.3E-01

3.5.2. Validation along the water column (in fixed points)- Nutrients (N, P, Si) and Dissolved oxygen

Model validation for nitrate, phosphate, silicate and dissolved oxygen was performed by comparing the monthly average, at fixed points, along the entire water column. Final statistics are summarized in Table 3.15 and in Taylor diagrams represented in Figure 3.26 and Figure 3.27. Model validation was performed in the entire water column by comparing MOHID, CMEMS and WOA, for the same instant at all the depth layers of CMEMS and WOA. Figure 3.22 to Figure 3.25 show one example of the time series compared, along the water column for the different parameters (Nitrate, inorganic phosphorous, dissolved Oxygen and dissolved silica).

Table 3.15- Statistic results for the comparison between MOHID and WOA climatology data and CMEMS model, considering R, R^2, BIAS, Root mean square error (RMSE), considering 10 points, along the water column, for Nitrate, Dissolved silica, Inorganic Phosphorus, dissolved oxygen and phytoplankton.

	Nitrate (mgN/l)		**Dissolved Silica (mgSi/l)**		**Inorganic phosphorus (mgP/l)**		**Oxygen (mgO/l)**		**Phytoplankton (mgC/l)**
Validation MOHID vs:	WOA	CMEMS	WOA	CMEMS	WOA	CMEMS	WOA	CMEMS	CMEMS
R^2	0.983	0.981	0.971	0.992	0.983	0.983	0.865	0.887	0.941
Bias	-0.007	-0.006	0.0	-0.01	-0.001	-0.001	-0.215	-0.035	0.001
RMSE (mg/l)	0.016	0.014	0.031	0.017	0.002	0.002	0.334	0.166	0.005

MOHID results for nutrients and dissolved oxygen represent the same variation along the water column as CMES and WOA data, with a correlation varying between 84% (to dissolved oxygen) up to 99% (for nutrients). Is visible a distinction between model results (MOHID and CMEMS), and WOA climatology data, for all the parameters, however, the seasonal variations follow the same variations. The model represented adequately the vertical variability), for the different parameters, in the different comparison points (Figure 3.22, Figure 3.23, Figure 3.24,

and Figure 3.25. Water column profiles show an increase of nitrate and phosphate concentrations along the water column, until the 1000 meters depth, like CMEMS and WOA data, followed by a constant maximum value up to the sea bottom. Also for dissolved oxygen MOHID simulates the water column dynamic, with a decrease of oxygen concentration, with a marked minimum oxygen zone followed by an increase of oxygen concentration until the deepest layers.

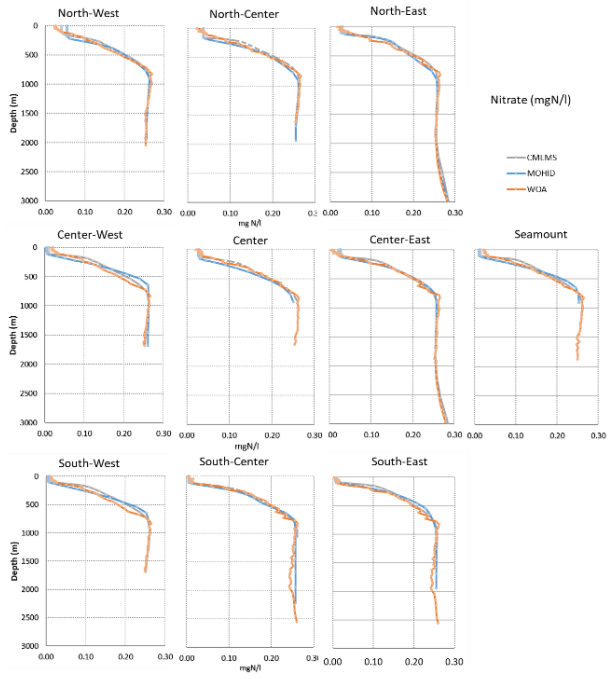

Figure 3.22- CMEMS, MOHID and WOA results of Nitrate in mgN/l, along water column, for the 10 points for the day 15 March 2018

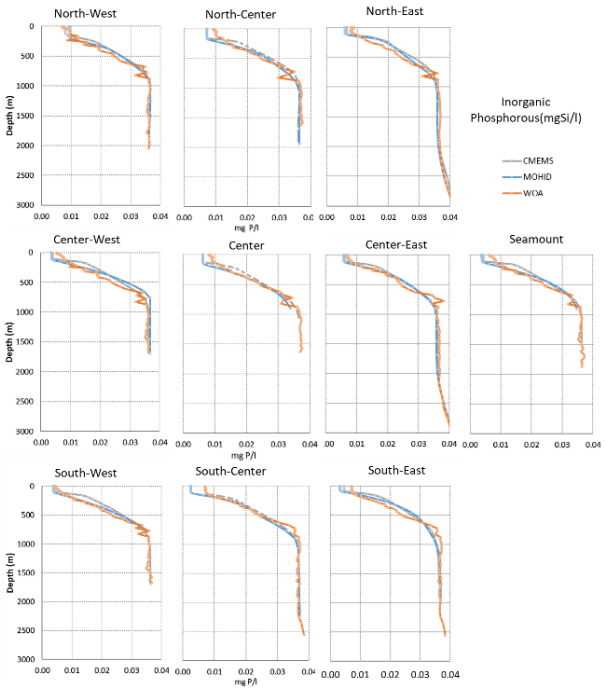

Figure 3.23- CMEMS, MOHID and WOA results of Inorganic phosphorus in mgP/l, along water column, for the 10 points for the day 15 August 2018

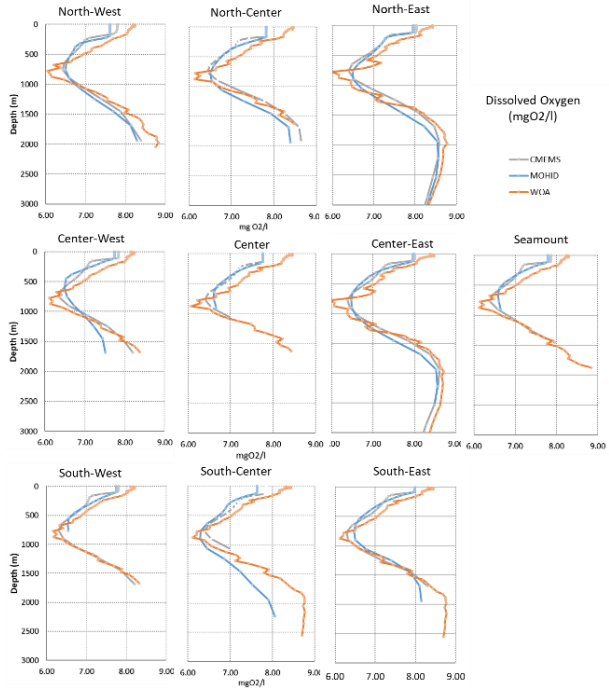

Figure 3.24- CMEMS, MOHID and WOA results for dissolved oxygen in mgO2/l, along the water column, for the 10 points for the day 15 March 2018

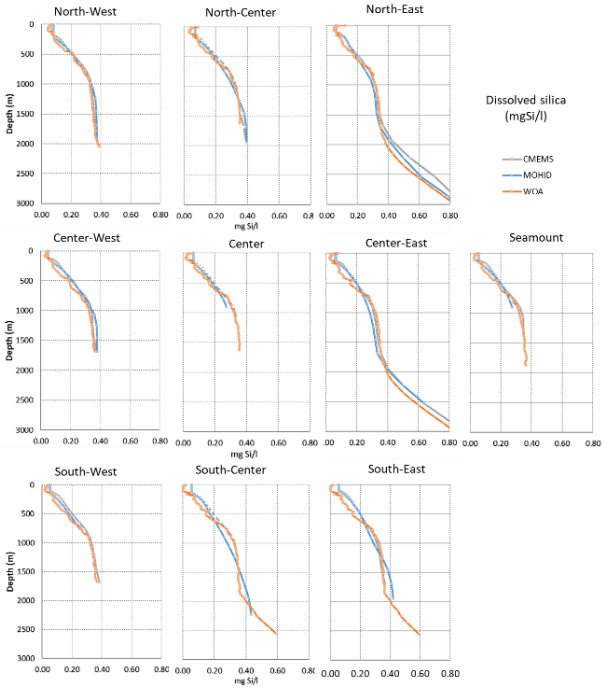

Figure 3.25- CMEMS, MOHID and WOA results for Dissolved silica in mgSi/l, along water column, for the 10 points for the day 15 August 2018

Taylor diagrams in Figure 3.26 and Figure 3.27 depict this good model performance. Dissolved silica, together with dissolved oxygen are the parameters that reflect higher standard deviation and fewer correlations. Nitrate and The comparison against WOA climatology shows higher bias and standard deviation for the dissolved silica concentrations, with bias ranging from -0.5 to 0.5 (Figure 3.27 c)).

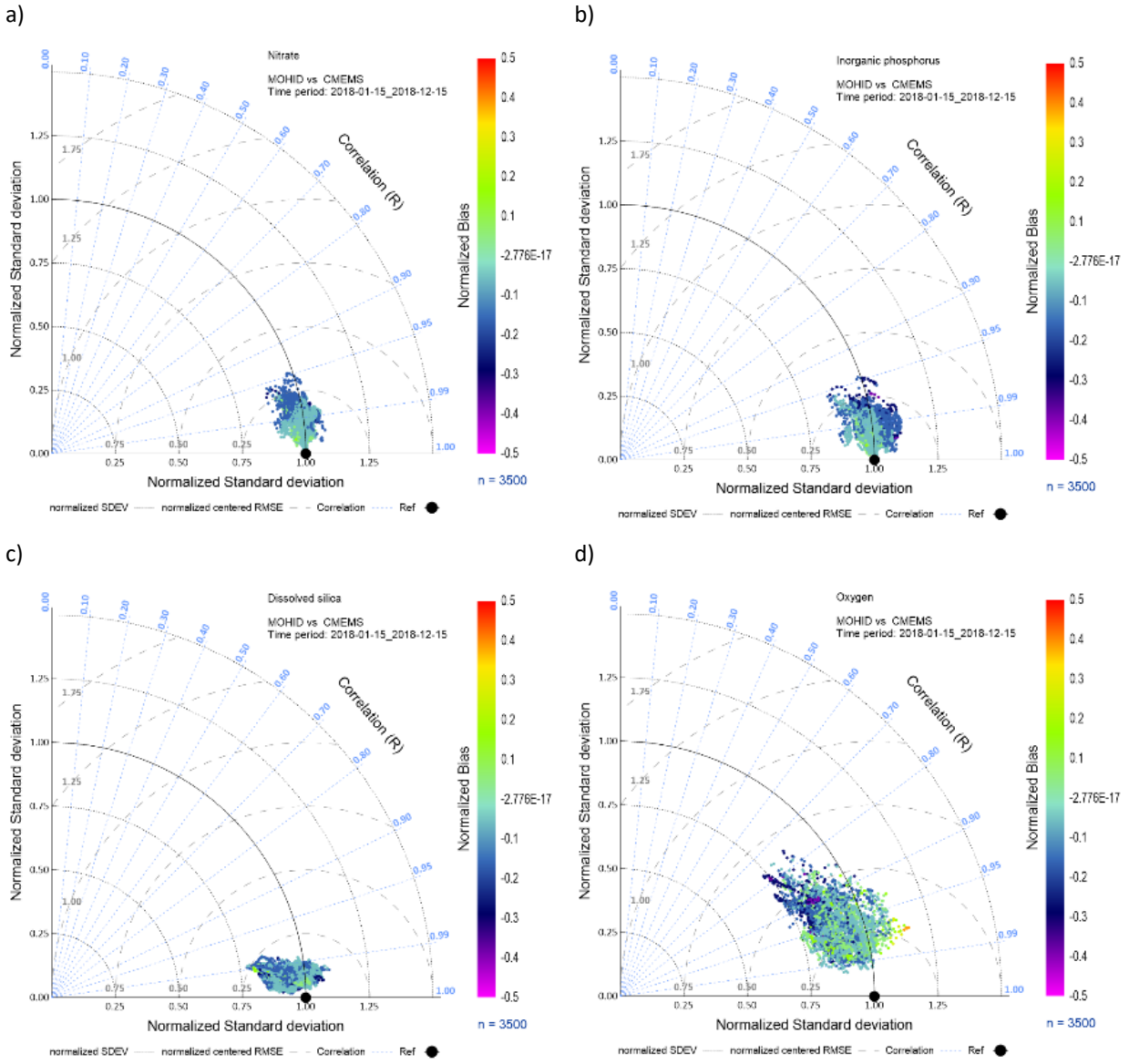

Figure 3.26- Taylor diagrams summarizing statistical results for MOHID validation against CMEMS model for a) Nitrate (top left); b)Inorganic phosphorus (top right); c) Dissolved silica (bottom left); and d) Dissolved oxygen (bottom right).

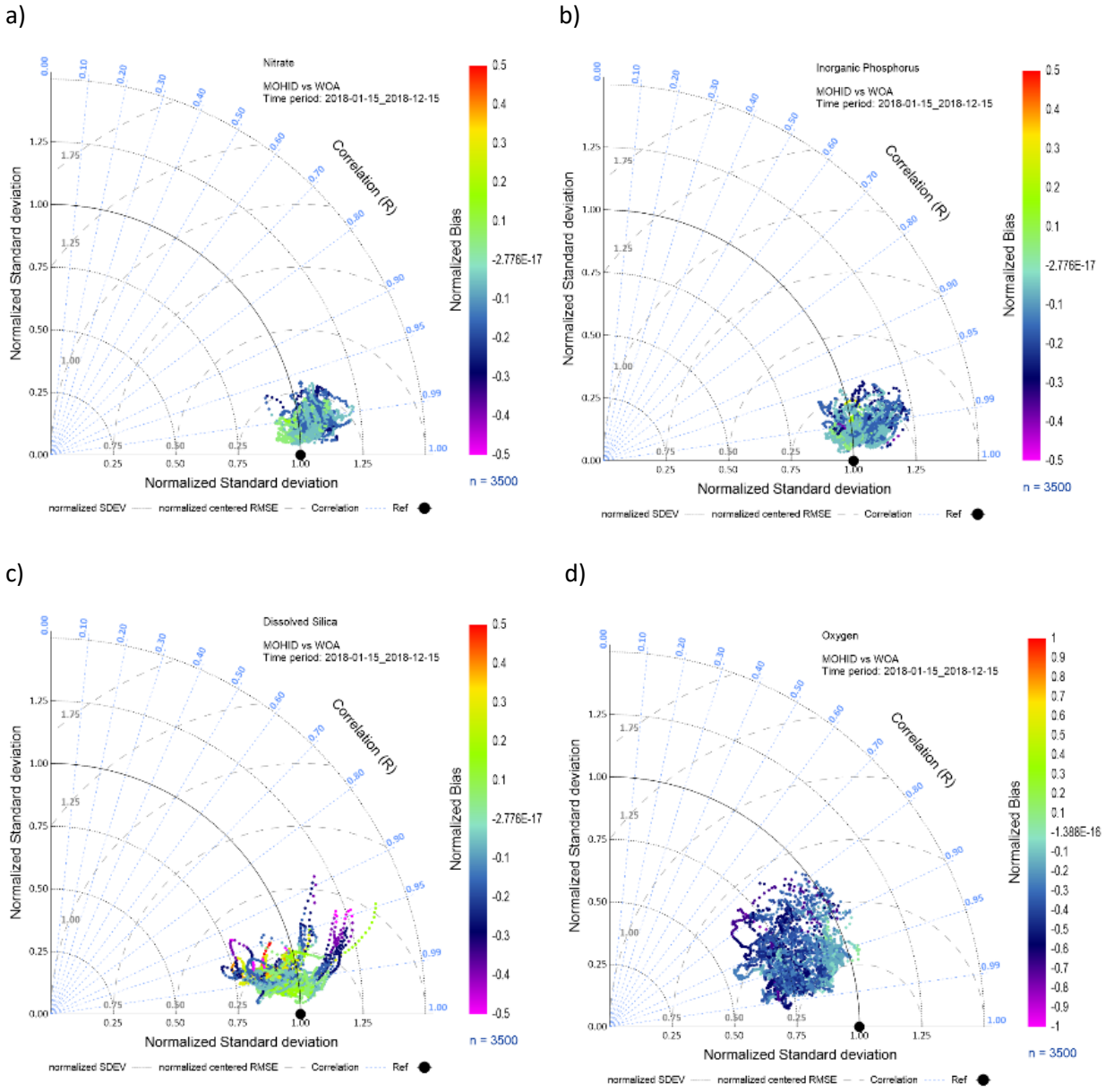

Figure 3.27- Taylor diagrams summarizing statistical results for MOHID validation against WOA climatology for a) Nitrate (top left); b)Inorganic phosphorus (top right); c) Dissolved silica (bottom left); and d) Dissolved oxygen (bottom right).

3.5.3. Seasonal nutrients and phytoplankton dynamics in the Azores

Model validation at the surface and along the water column shows that MOHID can simulate spatial and seasonal variability along with the domain.

MOHID simulates the seasonal winter increase of nutrient concentrations at the surface, with maximum values in March, followed by a decrease during the spring with the lowest values

during summer, for Nitrate, Phosphate and Silicate (Figure 3.21). In the reference years in the study, the maximum nutrient concentration at the surface was in February and March with maximum values of 0.02125 mgN/l and 0.0175mgN/l in 2017 and 2018 respectively. Followed by a nutrient depletion, induced by phytoplankton growth, achieving values of null nitrate concentration at the surface during the summer months (Jully, August and September). Inorganic phosphorous (IP) and dissolved silica (Si) average concentrations have the same seasonal pattern however with a less marked decrease during spring without a total depletion. Maximum of 0.005mgP/l in March, and a minimum of 0.0022 mgP/l in June. And for dissolved silica a maximum of 0.06mgSi/l and a minimum of 0.025mgSi/l. This seasonal variation is representative of the oligotrophic regions (like the Azores), where the low nutrient concentration limits phytoplankton growth. In this case, nitrate concentration can be more limiting than phosphorous, achieving values close to zero in the summer months, while inorganic phosphorous is not depleted. After the summer months, induced by the winter convection, in October, the nutrient concentrations at the surface start to increase, reaching their maximum at the end of the Winter (February/March).

3.5.4. Spatial nutrients and phytoplankton dynamics in the Azores

The phytoplankton model results at the surface show that MOHID spatial resolution allows to simulate of local and regional phytoplankton patterns, with high variability along space and time. Phytoplankton concentration along the domain shows spatial synchrony with nutrient concentration (Figure 3.28, and Figure 3.30 respectively). This relation is highly visible in the northern part of the domain, where higher nutrient concentrations follows the same patterns as phytoplankton concentration. Surface results show how the increase of nutrients is related to the phytoplankton concentration, however, with a one month delay. Results for phytoplankton (Figure 3.28) and zooplankton (Figure 3.29) show a similar seasonal variation, with zooplankton maximum concentrations occurring one month after the phytoplankton maximum. Zooplankton concentration starts to increase in March, after the phytoplankton bloom, with higher values in April, May and June. During June, the phytoplankton concentration at the surface is close to zero in the entire domain except in the top north, justifying the concentration of zooplankton that persist in this area during June, July and August. In October it occurs an increase in phytoplankton

concentration again (autumn bloom), mainly in the northern part of the domain, with higher values during December in the Eastern part of the domain.

For nitrate and phosphate, the model simulates the temporal typical patterns of oligotrophic regions, in values close to zero at the surface. Nutrient concentrations are generally higher in the northern part of the domain (Figure 3.30 for nitrate; for silicate and phosphate, see Annexe I). The similarities in spatial and temporal dynamics of the different nutrients are observable.

At the surface, dissolved oxygen values reveal latitude and longitude gradients, Figure 3.31 reflecting temperature distribution, with richer oxygen areas in the colder regions, and lower oxygen concentration in the southwest of the domain, where sea surface temperature is higher. These surface spatial patterns are closely related to the Mixed Layer Depth (MLD), Figure 3.34, where deeper mixed layers correspond to higher nutrient concentrations (Sverdrup 1953).

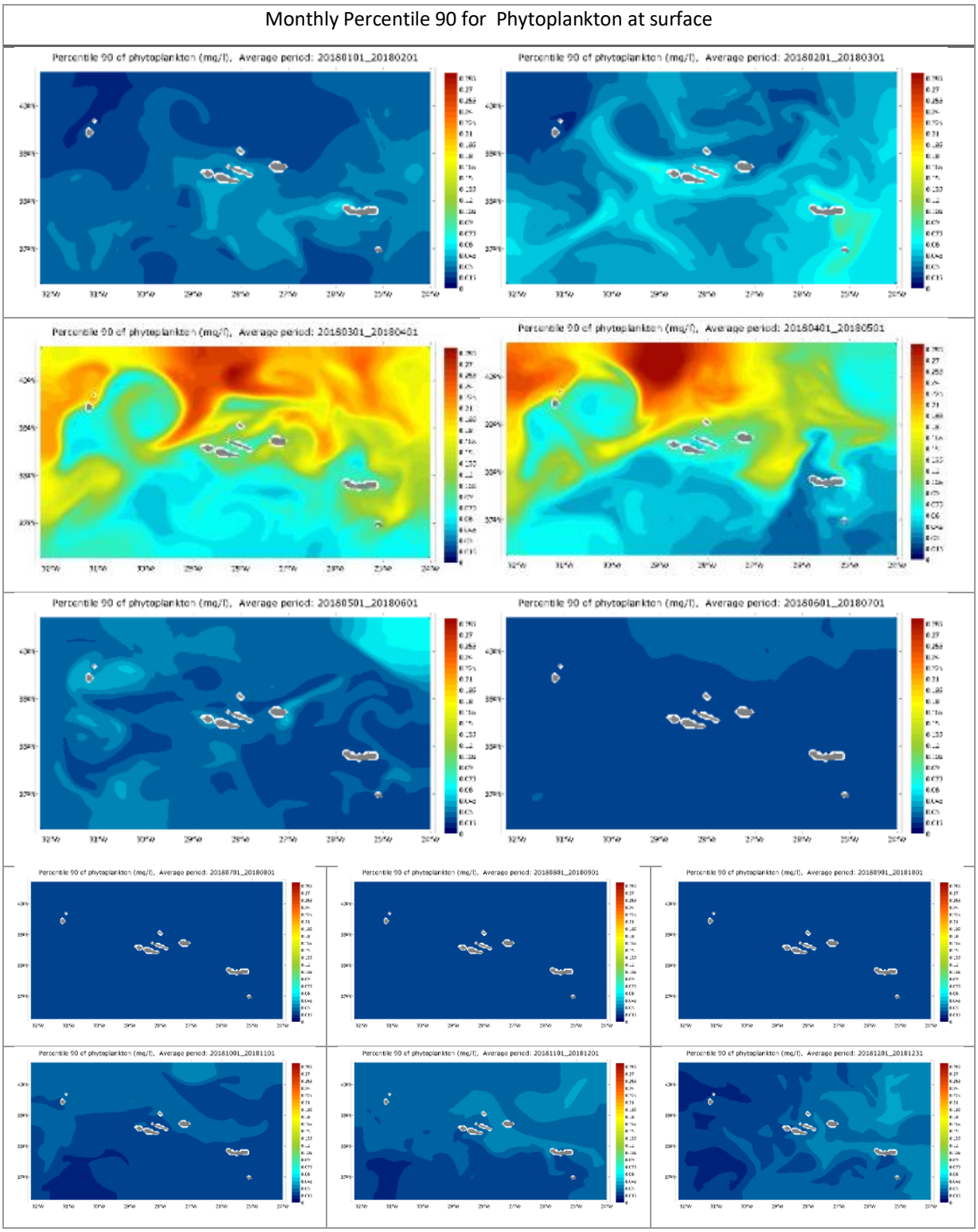

Figure 3.28- Monthly Percentile 90 for phytoplankton model results at surface from January 2018 to December 2018

Monthly Percentile 90 for Zooplankton at the surface

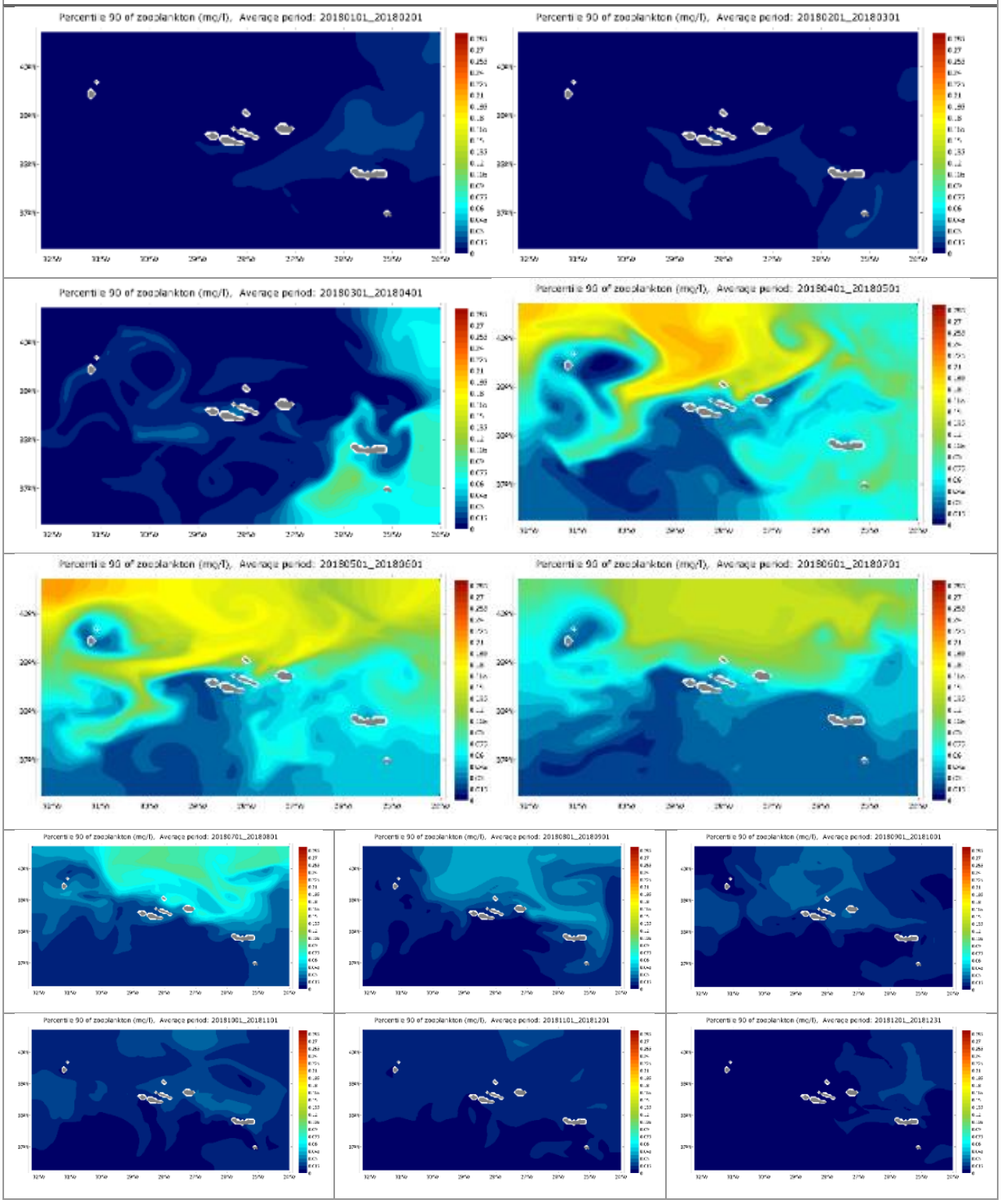

Figure 3.29- Monthly Percentile 90 for zooplankton model results at the surface from January 2018 to December 2018

Monthly Percentile 90 for Nitrate at the surface

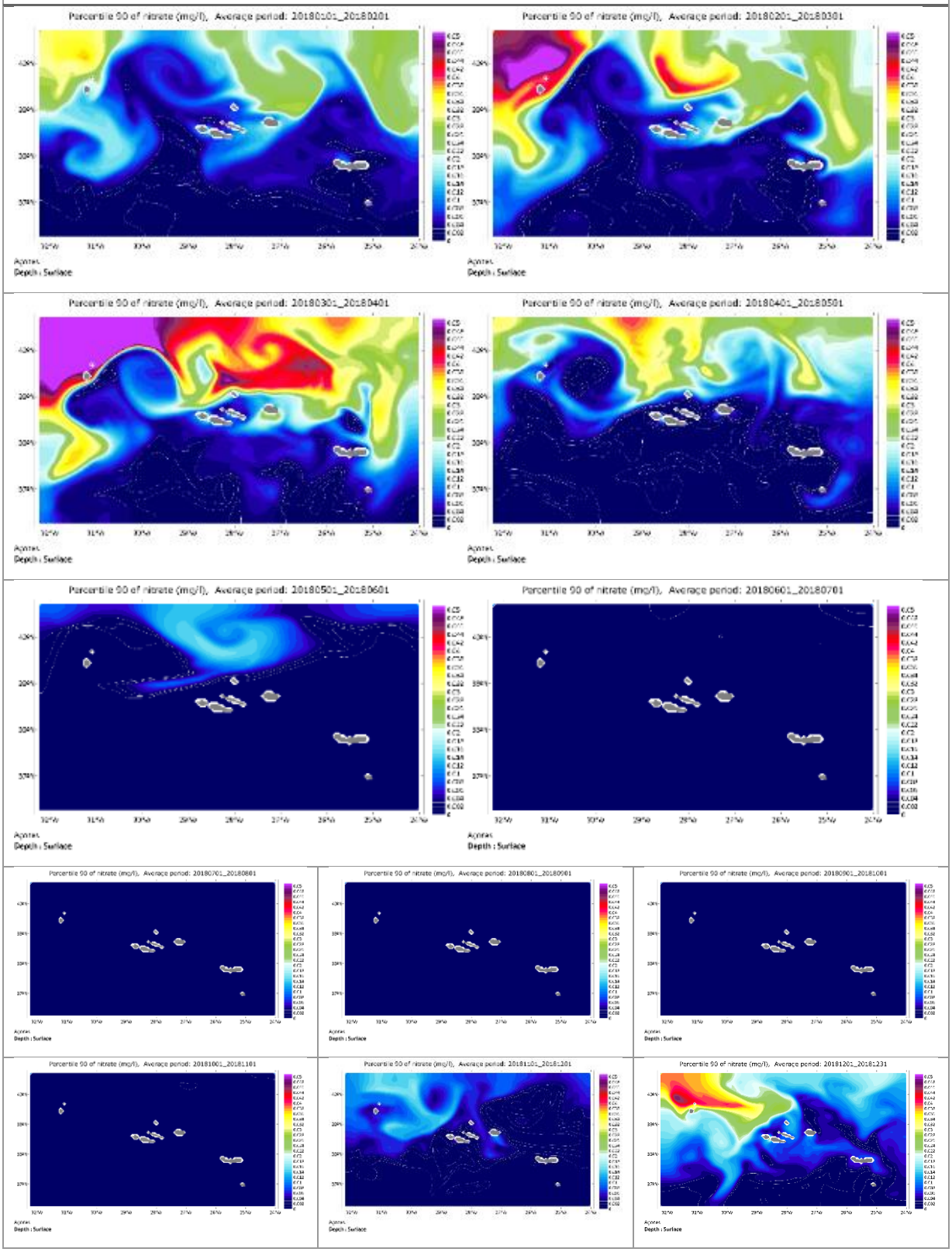

Figure 3.30- Monthly Percentile 90 for nitrate model results at the surface from January 2018 to December 2018

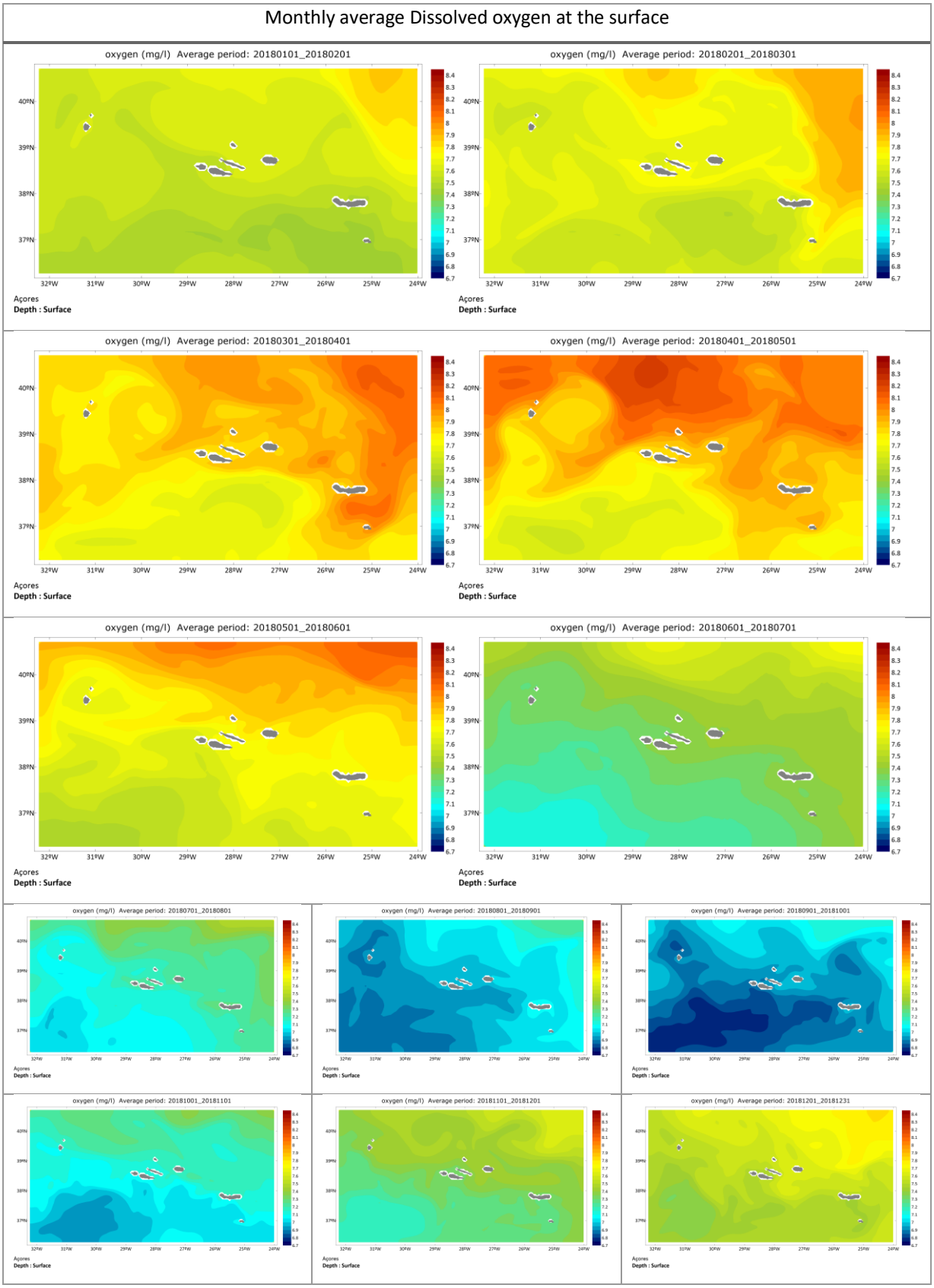

Figure 3.31- Monthly average for dissolved oxygen model results at the surface from January 2018 to December 2018

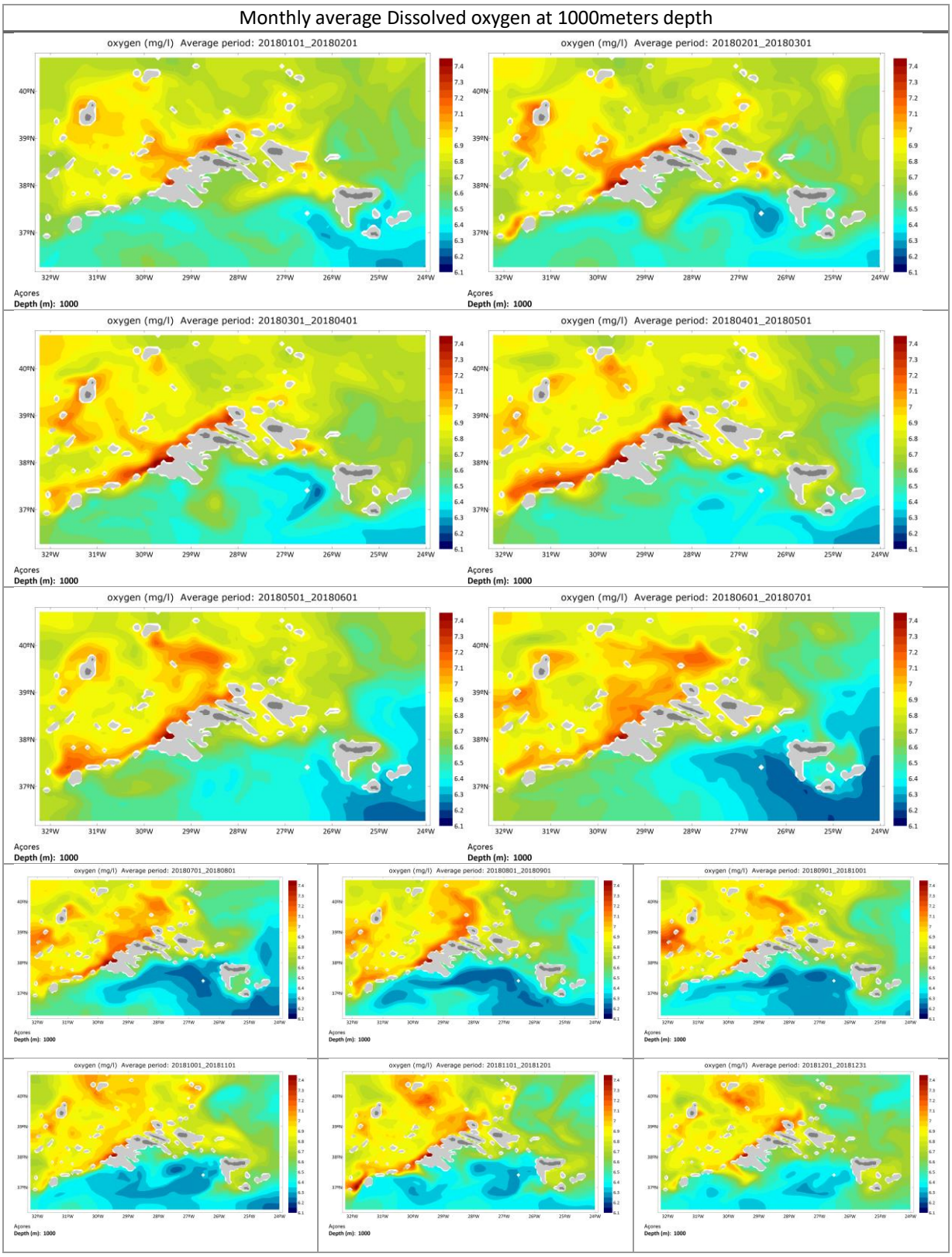

Figure 3.32- Monthly average for dissolved oxygen model results at 1000meters depth from January 2018 to December 2018

3.5.5. Mixed layer depth and nutrients (nitrate) at surface

The mixed layer depth (MLD) is defined as the uppermost layer of uniform density (constant temperature and salinity) (Thomson & Fine 2003). Mixed layer dynamics act directly, on the nutrient supply, on the availability of light, and consequently, on phytoplankton dynamics (Doney et al. 2001).

In the Azores region, the seasonal and spatial dynamics of the MLD are characterized by a typical higher MLD during winter, caused by the stronger wintertime winds, followed by a decrease from spring to summer (Valente, 2013). Model results reflect these dynamics, as it is shown in Figure 3.33 which represents the seasonal dynamics of surface concentration for phytoplankton, diatoms, and nitrate, and the mixed layer depth, during 2017 and 2018.

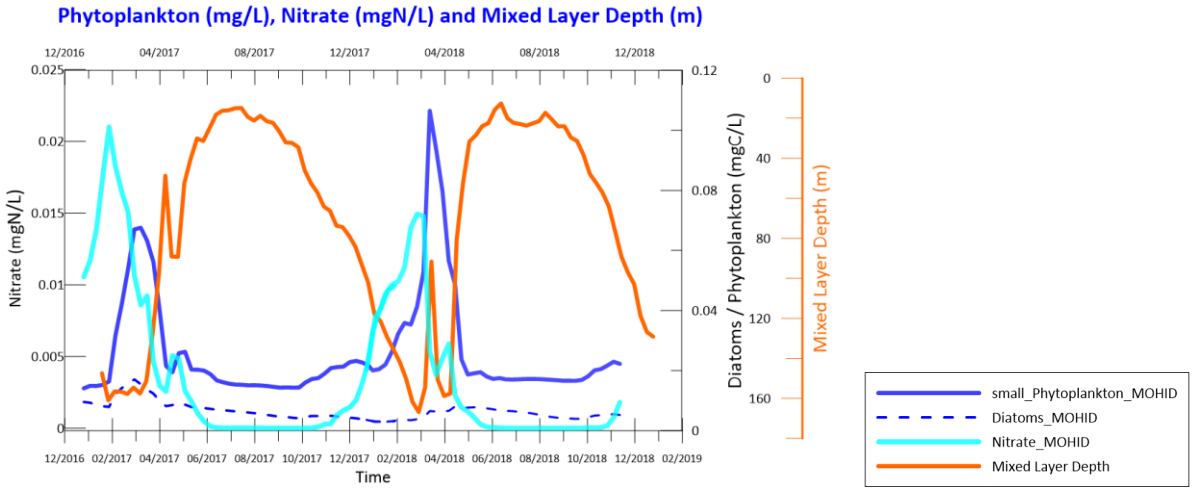

Figure 3.33- Surface average results for phytoplankton, diatoms and zooplankton concentration (in mgC/l), in dark blue; for Nitrate in light blue, and mixed layer depth (meters) in orange. All results are weekly averaged, for 2017 and 2018.

The estimated MLD seasonal variation follows the expected evolution for this region (Valente 2013), with a deepening during winter, achieving the highest values during late February and March, matching with the highest nitrate concentration at the surface. In the winter the average MLD achieves values of more than 160 meters depth on average. During summer the shallowing of the MLD goes up to 20 meters depth. This winter mixing induces a nutrient increase at the surface (Santos et al. 2013) up to the maximum value of 0.02 mgN/l in February. This

highest nutrient concentration, followed by increased irradiance in spring, enhance the phytoplankton growth.

During spring, the shallowing of the MLD diminishes the depth of the euphotic zone, resulting in the development of the seasonal thermocline. This seasonal thermocline tends to confine the phytoplankton in the euphotic zone, which has more nutrient concentration. During the summer, weather conditions induce vertical stratification with the consecutive diminution of the MLD, strengthening the seasonal thermocline (Sverdrup 1953). This thermocline will difficult the nutrients enrichment from deeper layers' depth, resulting in a lower nutrient concentration at the surface. Therefore limiting phytoplankton growth. By August all nutrients are depleted in the mixed layer. At the beginning of autumn, the weather conditions induce the vertical mixing and the MLD deepening, and therefore nutrient entrainment into the MLD. These results corroborate the seasonality reported for the Azores region, showing that nutrient concentrations vary with mixed layer depth (Valente 2013).

This nutrient depletion is a consequence of the phytoplankton nutrients consumption, demonstrating the bottom-up control that phytoplankton takes over the nutrients cycle in the ocean (Hashioka et al. 2013). This relation between nutrients concentration and phytoplankton growth it is a characteristic of oligotrophic waters, like the North Atlantic, and specifically, the Azores region (Giacomello & Menezes 2012, Barcelos Ramos et al. 2017) where the concentration of the nutrient is one of the bigger limitations for phytoplankton growth (Calbet et al. 2009).

3.5.6. Spatial distribution of the Mixed Layer Depth

In the Azores the spatial variability of the MLD is highly dynamic. In the North of the Azores region, the stronger winter winds induce vertical mixing and the MLD can go up to 250 meters depth (Figure 3.35). While in the south of the domain it goes up to 100 meters. Contrasting with these winter months, during summer the MLD can be above the 25 meters depth. During summer the MLD is shallower around the islands (Figure 3.35).In the Central and Eastern groups, the MLD can achieve a depth between 15 and 35 meters depth. Islands from the West group experience more variability, with higher MLD in June. Spatial variation also reveals a longitudinal gradient. During winter, around the islands from the Western Group (WG) the MLD can go up to 250

meters depth, in the CG up to 150m and in the EG around 75 meters. The same regional gradient was verified by (Valente 2013) .

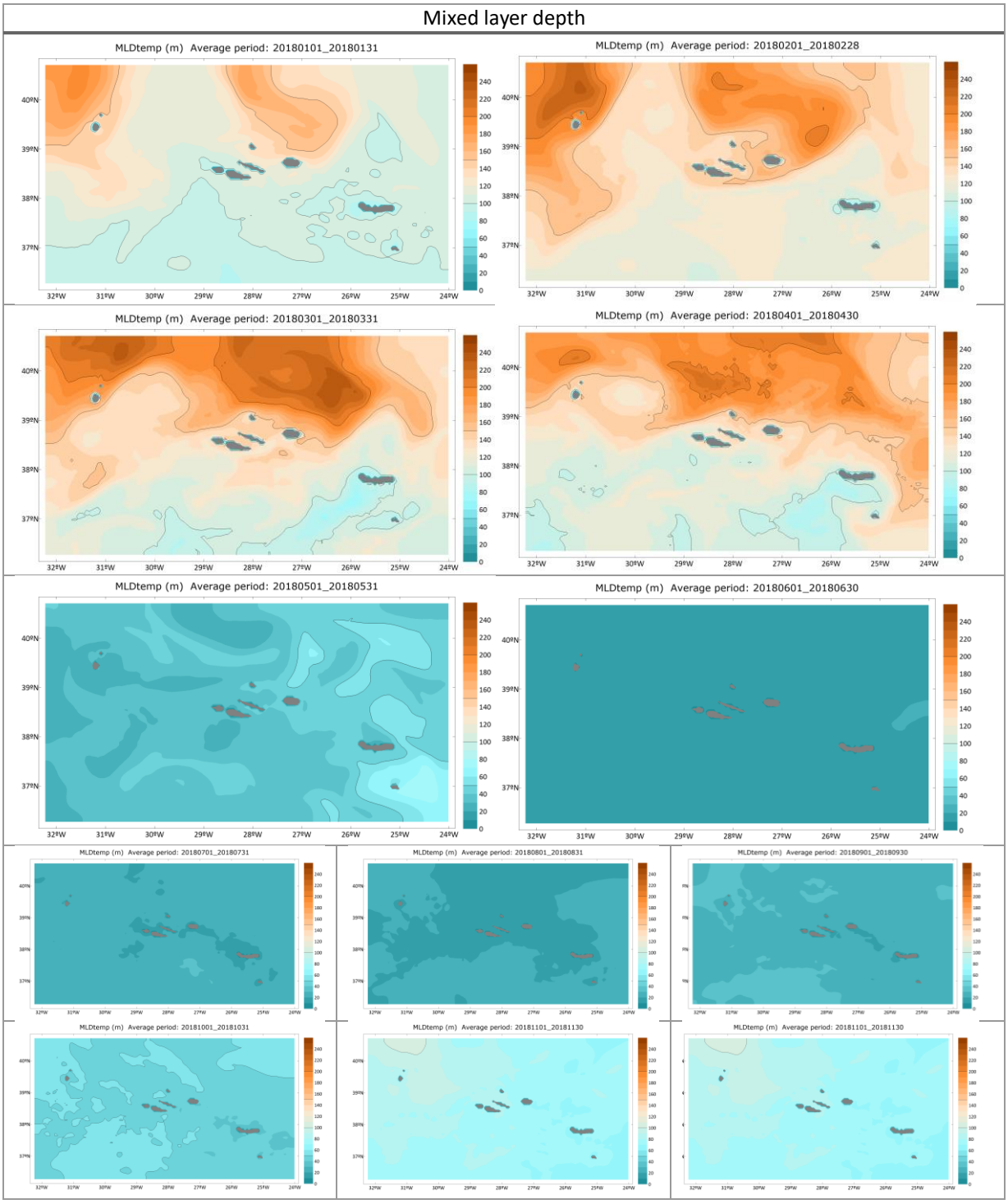

Figure 3.34- Monthly average for mixed layer depth, in meters, from January 2018 to December 2018, using a colour scale between 0 and 250 meters

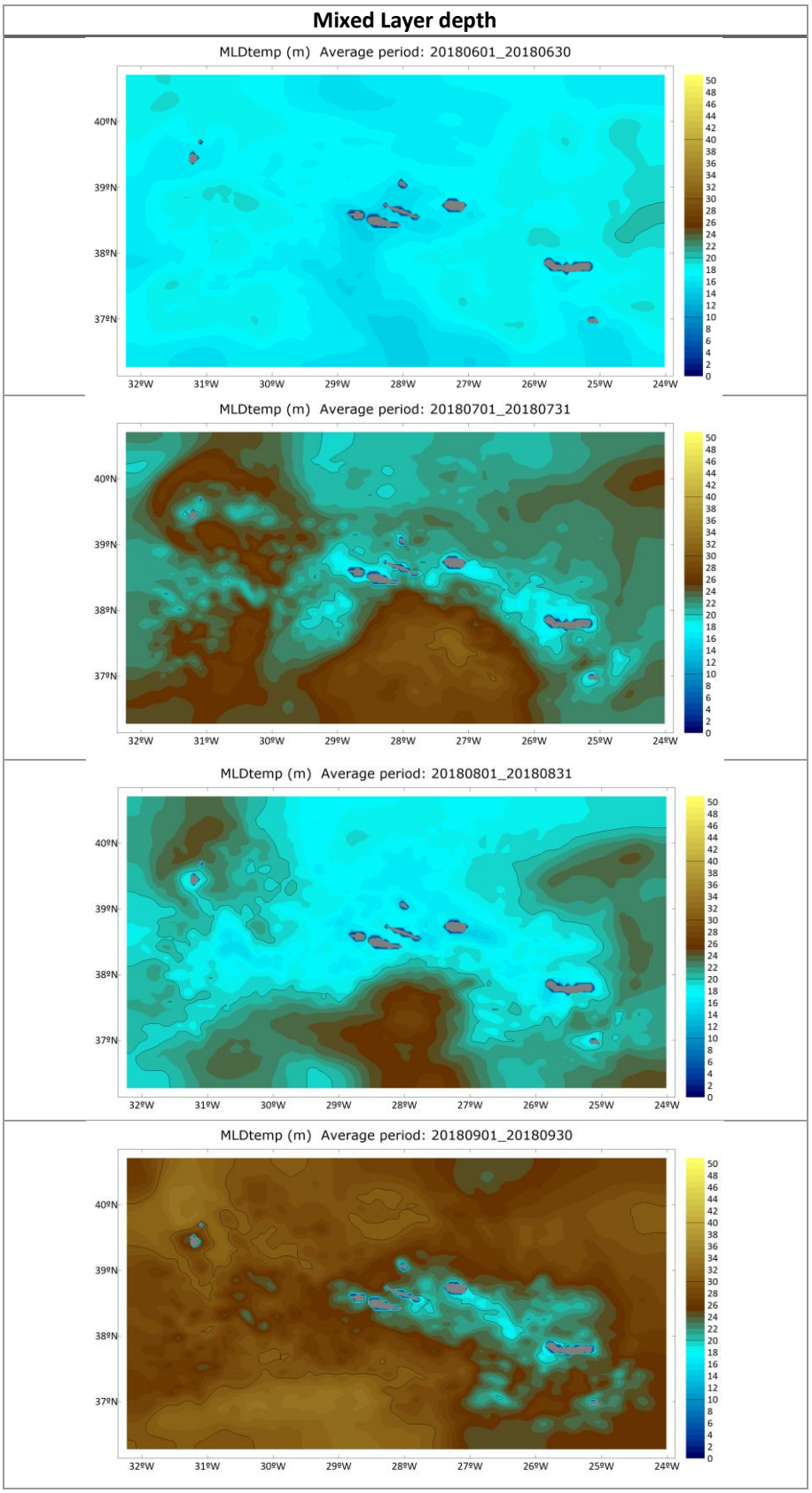

Figure 3.35- Monthly average for mixed layer depth, in meters, from June 2018 to September 2018, using a colour scale between 0 and 50 meters

3.5.7. Deep chlorophyll maximum (DCM)

The deep chlorophyll maximum (DCM), is a well-documented phenomenon, typical of the oligotrophic regions(Cornec et al. 2021). It occurs after the spring bloom, and established below the mixed layer. In the Azores region it can present a south-north positive gradient, by the influence of the Azores current in the South (Macedo et al. 2000).

Analysis of phytoplankton results along the water column Figure 3.36 allows inferring if MOHID can simulate this deep chlorophyll maximum (DCM), which from now on is referred to as deep phytoplankton maximum (DPM).

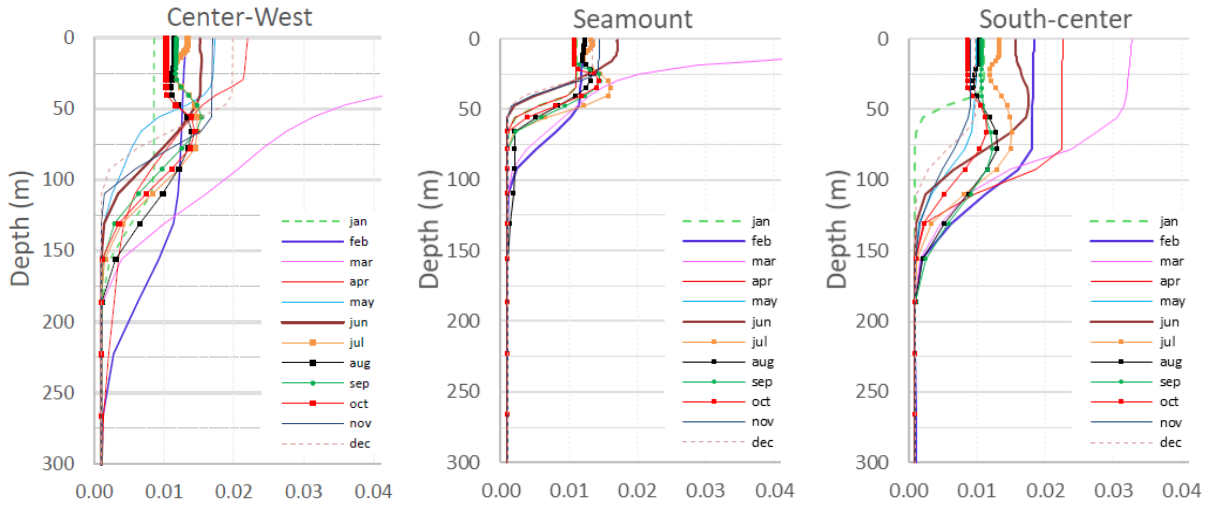

Figure 3.36- Monthly averages for phytoplankton modelled results, along the water column, from the surface until 300meters depth, for three fixed points (Centre-West, Cavala seamount and South-centre points)

Phytoplankton concentrations along the water column show a vertical gradient, with seasonal and spatial gradients (Figure 3.36). The DPM can occur at different depths mostly in the summer months, July, August, September and also in October.

At the seamount location, the maximum phytoplankton concentration occurs between 25 and 50 meters, while in the other points, can occur at 75 meters depth (Center-West), or even deeper. Also at the seamount the gradients are more established than in the other points. In the South-center point, the DPM is also visible in June.

3.5.8. Vertical distribution: Nutrients, phytoplankton, Dissolved oxygen and temperature a

Vertical profiles show similarities between nitrate and phosphate distribution along the water column, with a lower concentration in the first layers, and a slow increase along with the depth until 300 meters depth, followed by an increase up to the sea bottom for both nutrients Figure 3.37 and Figure 3.38. The spring phytoplankton bloom is visible at surface layers, by the higher concentration of phytoplankton and diatoms in February, March and April. From May to September, diatoms concentration is higher from 50 up to 100meters depth, while surface concentration values are close to zero. The small phytoplankton concentration also follows this distribution pattern.

Oxygen concentration at the surface layers is highly dynamic. In the interface water-air layer, the oxygen concentration reveals lower values during the summer months than during the winter. This is a consequence of the increase in surface temperature m that decreases the oxygen solubility hence decreasing oxygen concentration at the surface (Matear & Hirst 2003).

In the euphotic zone, the oxygen concentration is highly related to the phytoplankton concentration. Where, as a result of the photosynthesis by phytoplankton the oxygen concentration increases (Hirose and Kamiya, 2003). Model results show that the maximum dissolved oxygen concentrations match the higher concentration of phytoplankton. Simultaneously the nutrient concentration diminishes by the phytoplankton consumption.

The model represents the typical oxygen patterns along the water column, as the depth increases, dissolved oxygen declines, reaching a minimum concentration between 500m and 1000 meters depth (Bashmachnikov et al. 2015). Below this minimum oxygen concentration occurs an increase o ending up in maximum values at the bottom layer. This increase is related to the increase of pressure and the decrease in water temperature, as stated before inducing oxygen solubility. But is also related to the deep ocean circulation, namely by the influence of the North Atlantic Deep Water, characterised by its lower temperature and higher oxygen concentrations, and observed about 2500 to 3000m and below, in the Azores region (Palma et al. 2012, Bashmachnikov et al. 2015).

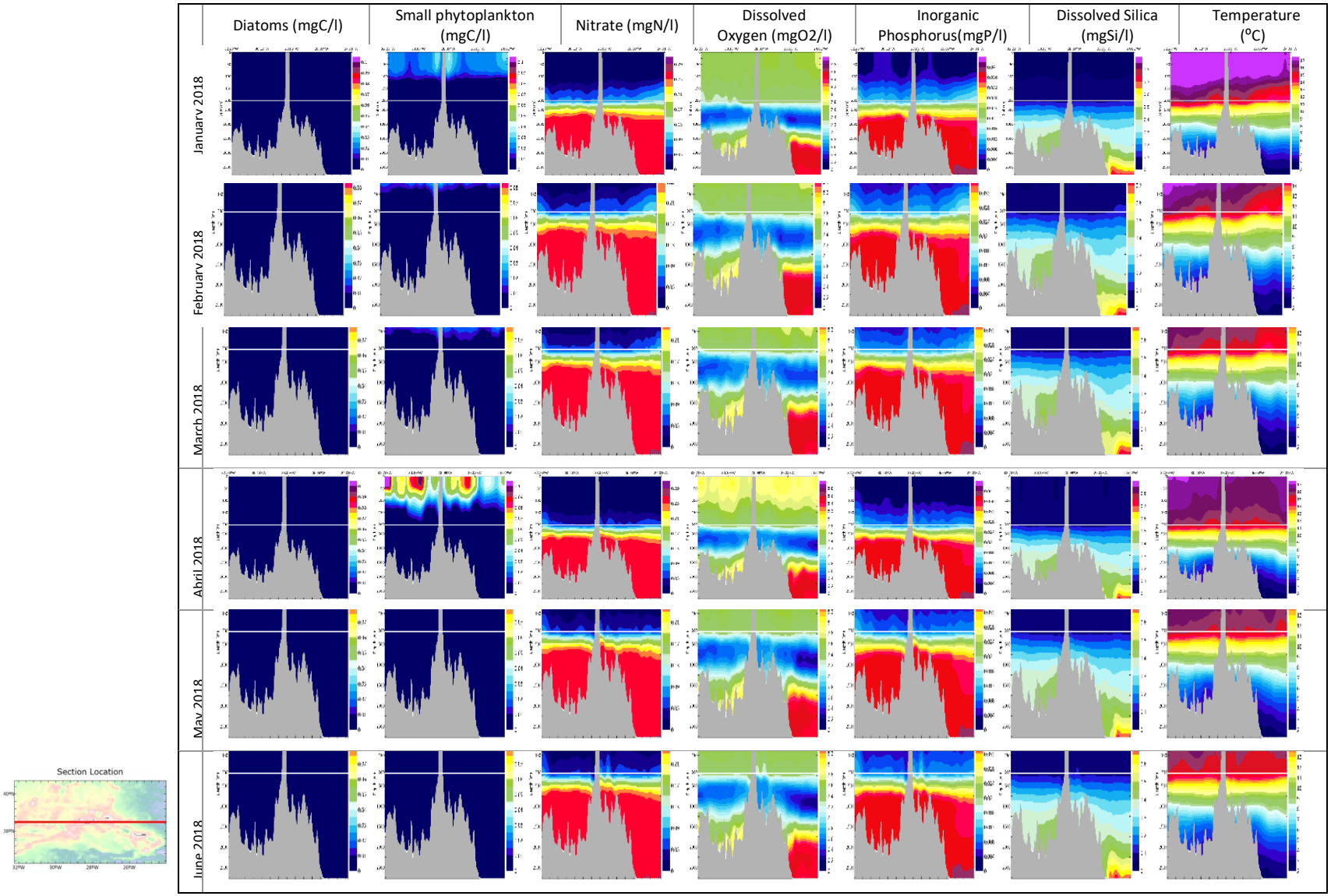

Figure 3.37- Monthly average from January to June 2018 for diatoms (mgC/l), small phytoplankton (mgC/l), nitrate (mgN/l), dissolved oxygen (mgO2/l), inorganic phosphorus (mgP/l), dissolved Silica (mgSi/l), and temperature (ºC) along water column (from surface 3000meters depth), along the meridional section at 38ºN. Depth profiles present a higher resolution until 250meters depth, and less resolution from 250meters until 3000meters depth. The section goes from 32.2ºW on left to 24º

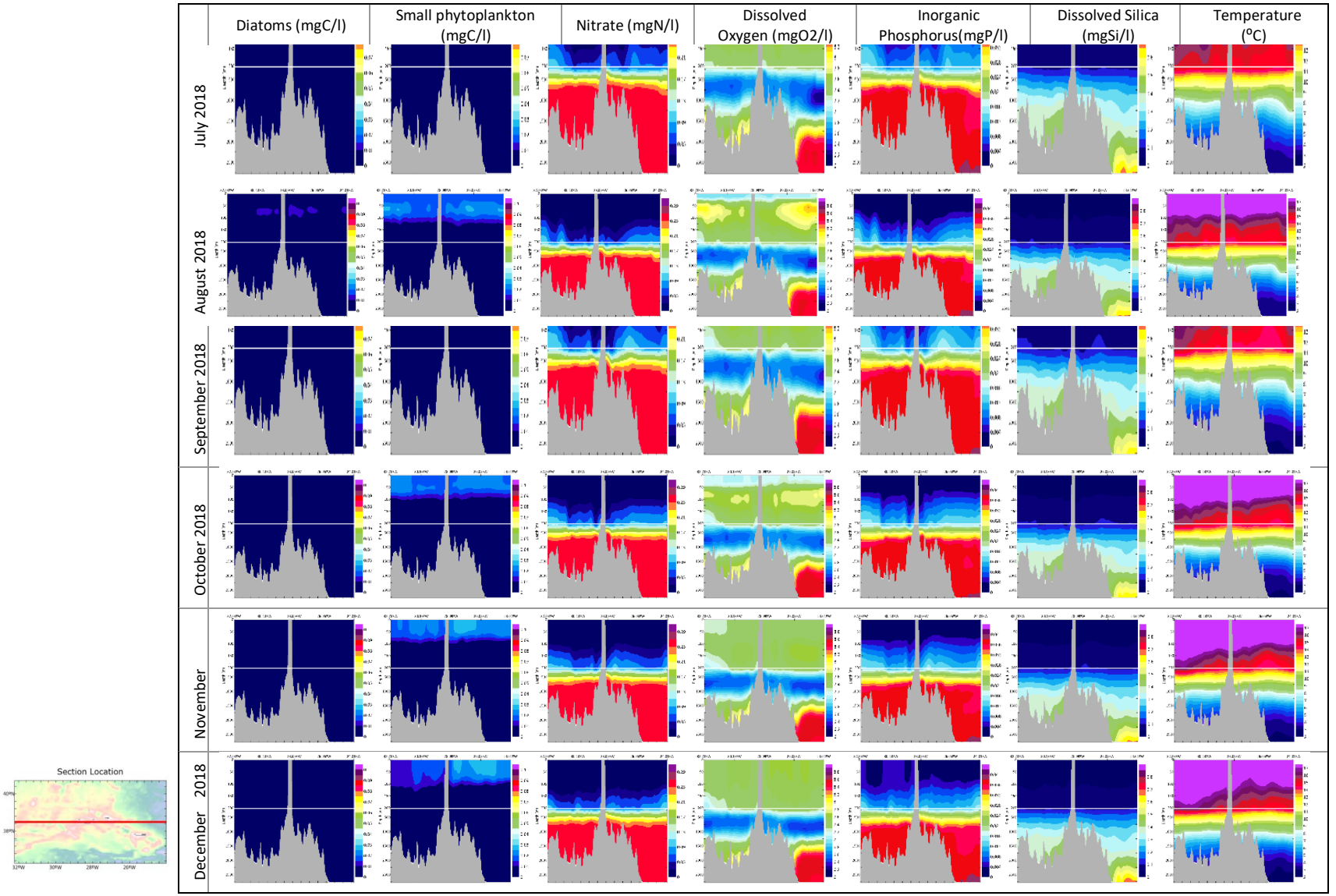

Figure 3.38- Monthly average from July to December 2018 for diatoms (mgC/l), small phytoplankton (mgC/l), nitrate (mgN/l), dissolved oxygen (mgO2/l), inorganic phosphorus (mgP/l), dissolved Silica (mgSi/l), and temperature (°C) along water column (from surface 3000meters depth), along the meridional section at 38°N. Depth profiles present a higher resolution until 250meters depth, and less resolution from 250meters until 3000meters depth. The section goes from 32.2°W on left to 24°W on right.

3.5.9. Hydrodynamic spatial and seasonal patterns

The topography of the Azores region induces a spatial variability of the hydrodynamic patterns. At 500 meters' depth, in Figure 3.39 and Figure 3.40, is visible the effect of the archipelago bathymetry in the currents direction and velocity, with the development of vortices between the islands of the western group, and the central group. The vertical component of the velocity (component w), (Figure 3.41Figure 3.42, third column) reveals higher vertical velocities shaped by the topography.

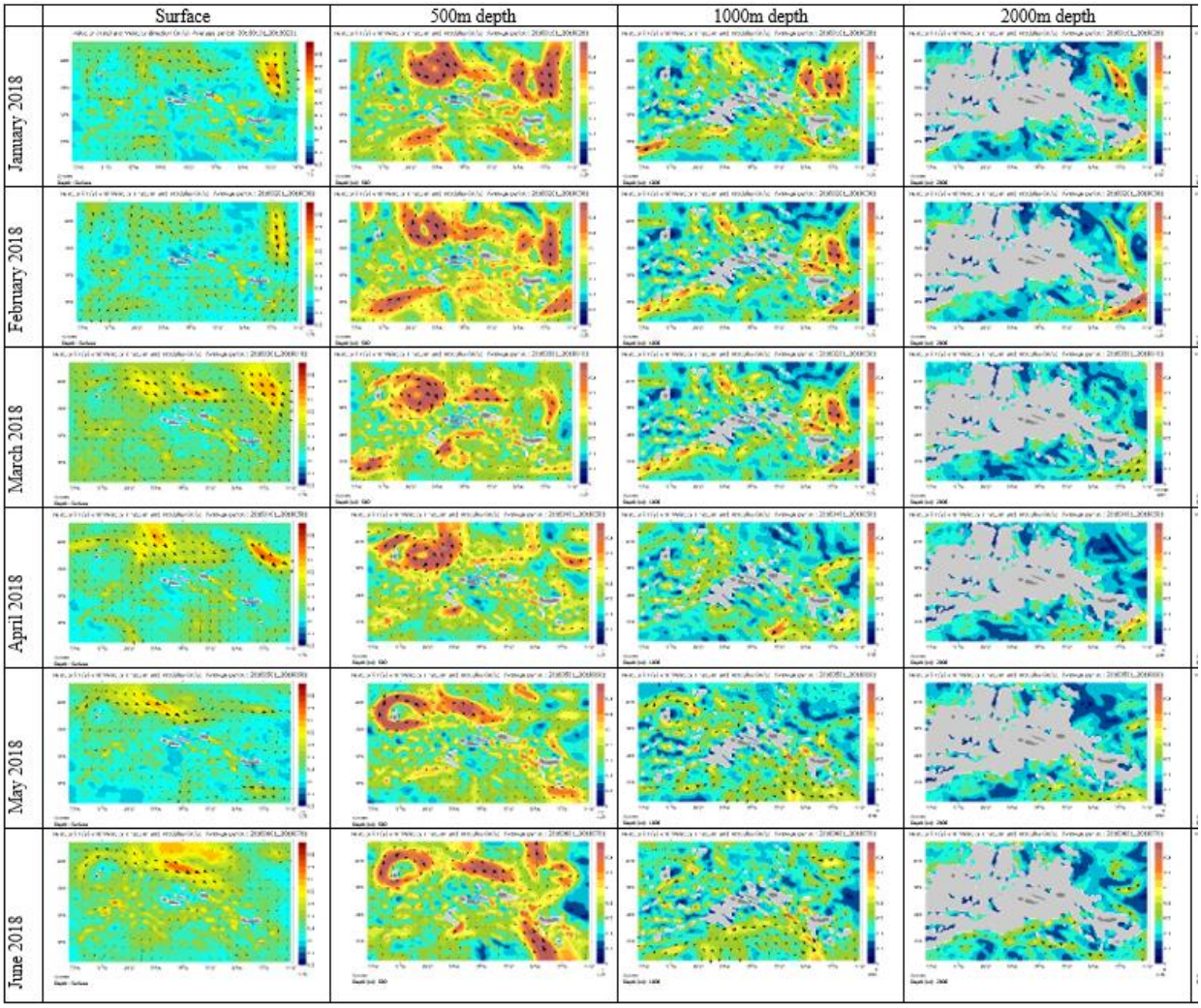

Figure 3.39- Monthly average, from January to June 2018 of velocity modulus and direction at surface, 500m 1000m and 2000m depth. All images are plotted with the same colour scale.

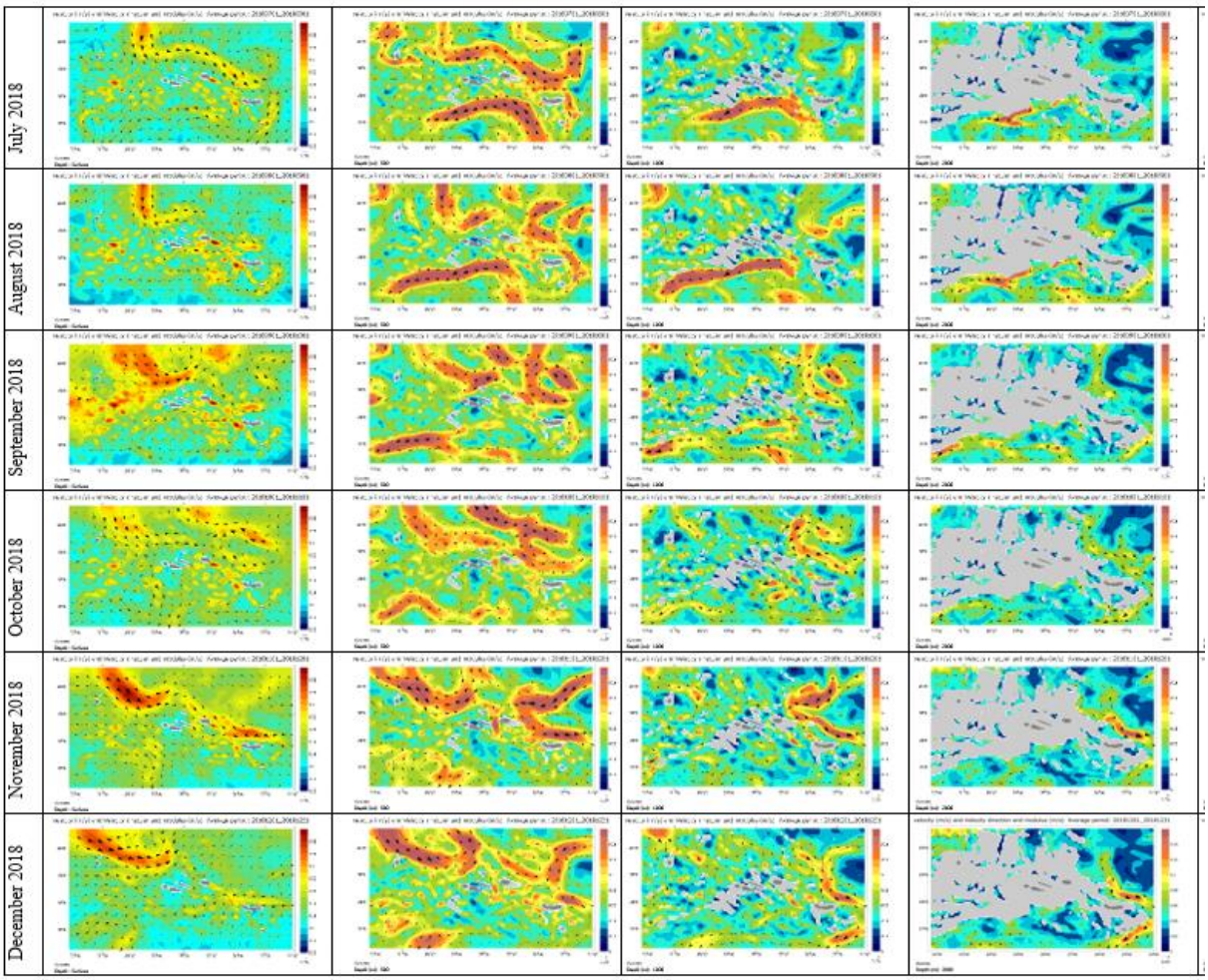

Figure 3.40- Monthly average of velocity modulus and direction at surface, 500m 1000m and 2000m depth. All images are plotted with the same colour scale

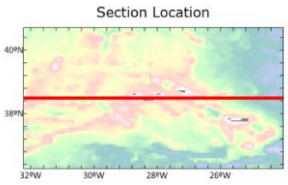

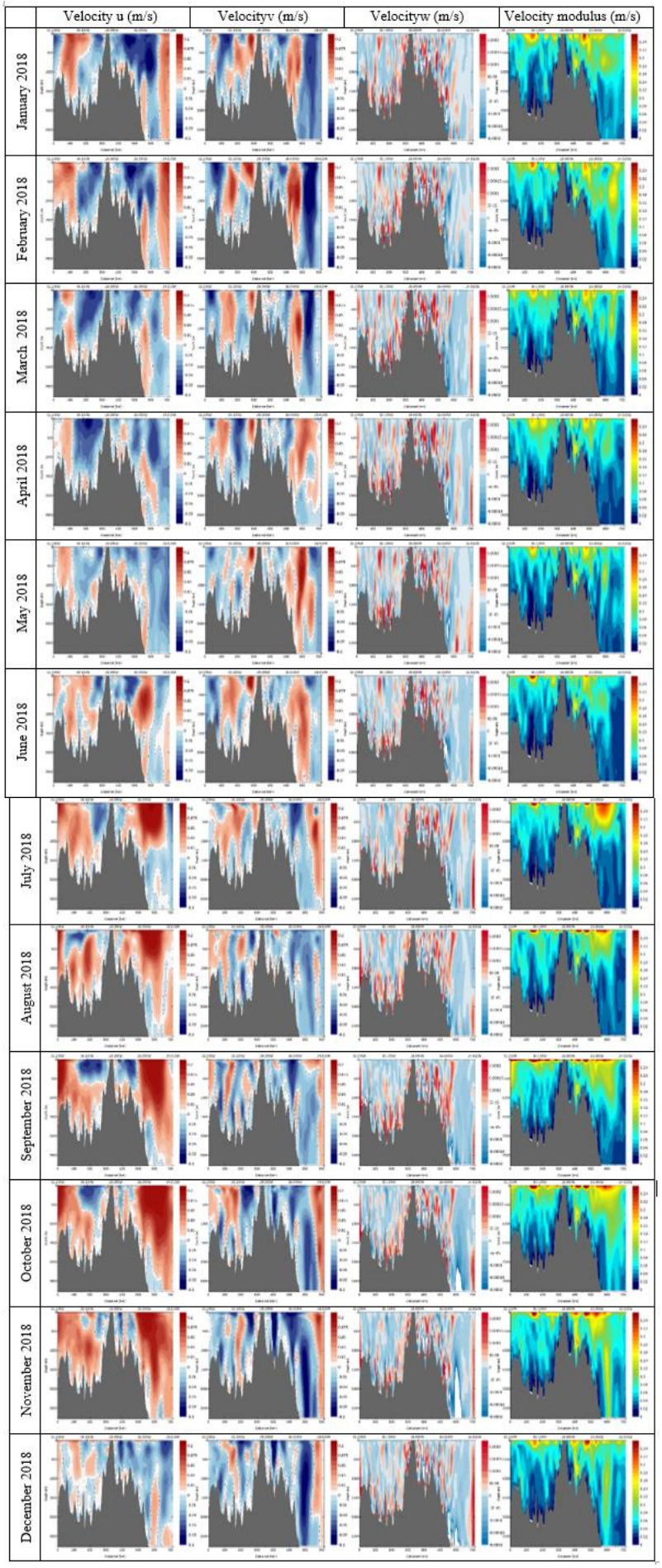

Figure 3.41- Monthly average of velocity u, v, w and velocity modulus in m/s along the water column in the zonal section of 38.5ºN for for January to December 2018

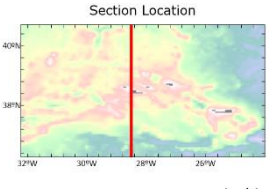

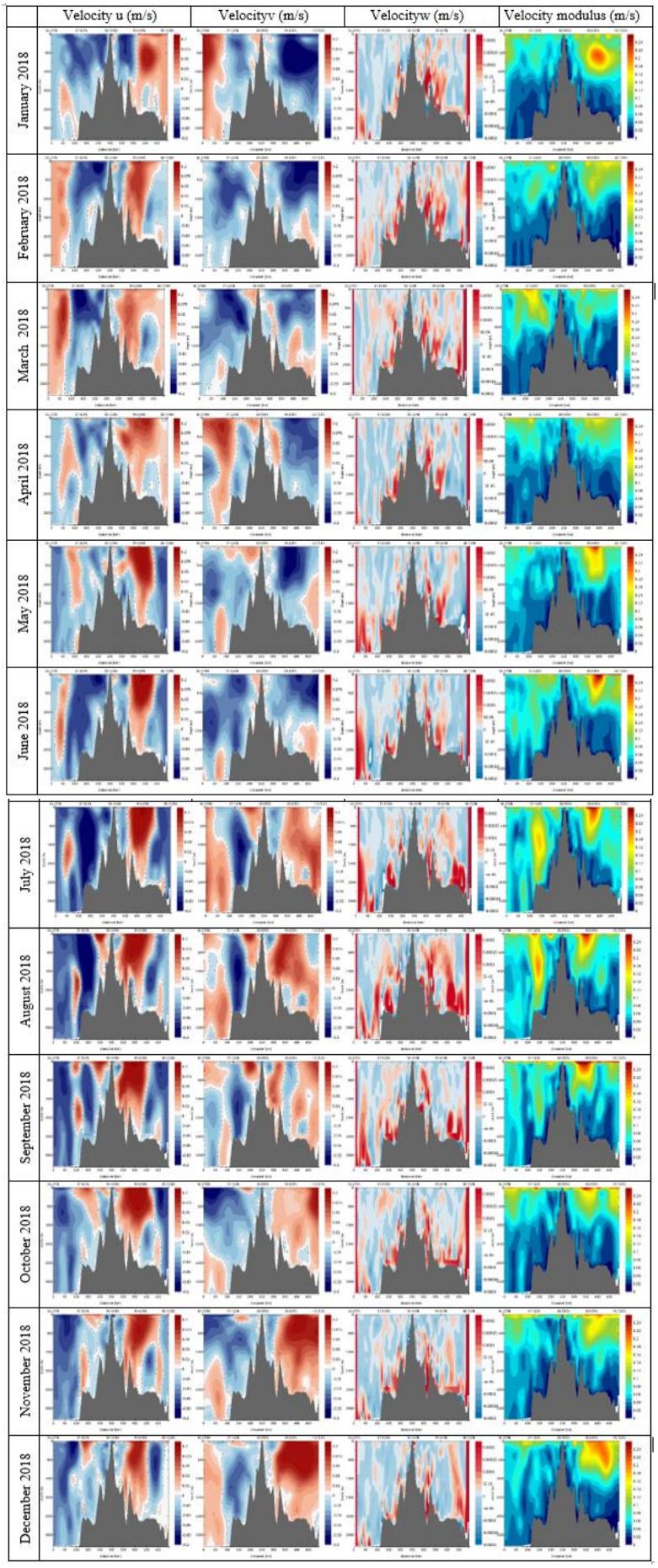

Figure 3.42- Monthly average of velocity u, v, w and velocity modulus in m/s along the water column in the meridional section at -28.5°W, for January to December 2018

Sea surface temperature, salinity and currents velocity at surface

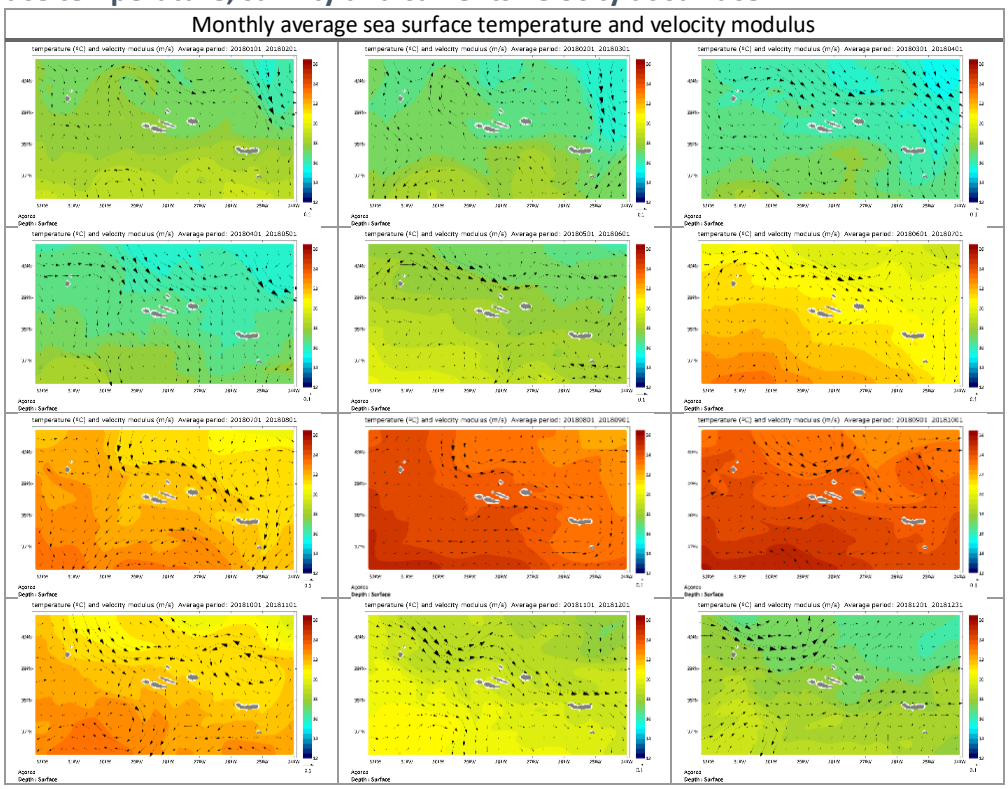

Figure 3.43- Monthly average of sea surface temperature and hydrodynamic vectors for 2018

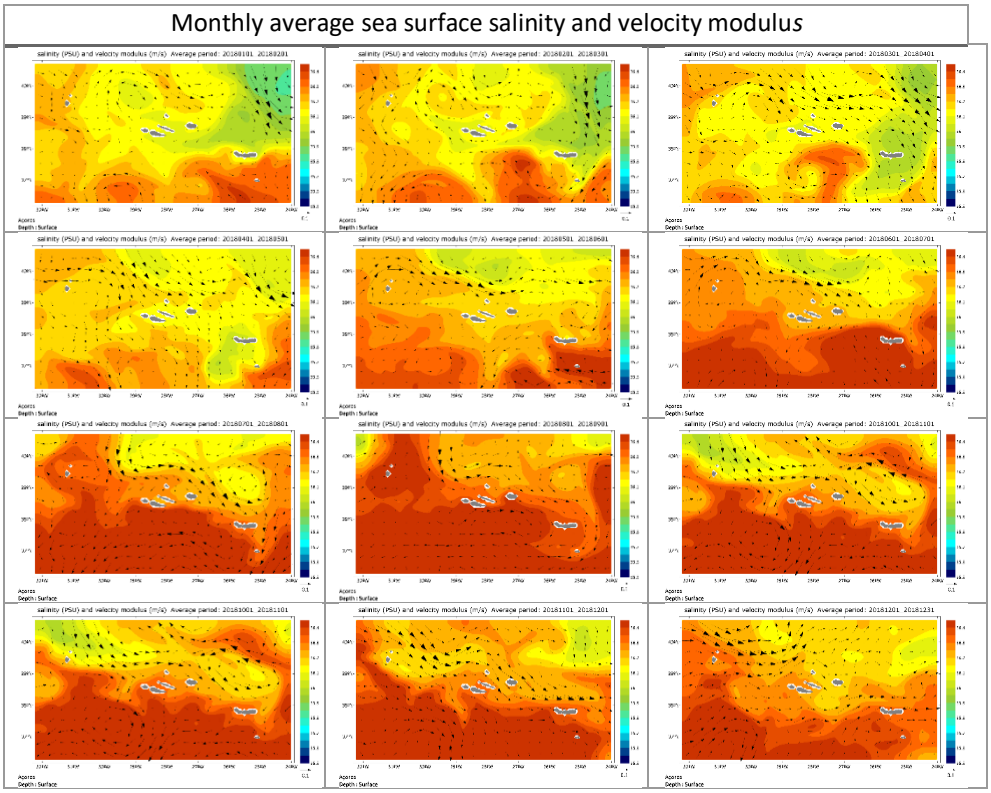

Figure 3.44- Monthly average of sea surface salinity and hydrodynamic vectors for 2018

3.6. Discussion

The leading objective of this work was to implement a biogeochemical model able to simulate the general biotic and abiotic processes in the Azores region. The present configuration of the MOHID biogeochemical model reproduced adequately the dynamics of the main biogeochemical variables (phytoplankton, nutrients and dissolved oxygen) in the Azores.

Parameterization and calibration

The calibration work was processed in a step-by-step approach, with successive model runs, starting with the standard model parametrization values, testing values from other biogeochemical models and case studies, and considering values within the range of literature, until a satisfactory fit was obtained for the Azores region.

Mohid biogeochemical model runs over a hydrodynamic solution that was previously validated for the Azores region (see Chapter2 of this dissertation). This is not, though, a fully coupled model system, that enables feedback between biogeochemical and hydrodynamic processes since the fully coupled solution is very computationally demanding requiring biogeochemistry to be handled on a time-step required by the hydrodynamic model, which is often much shorter than the time step of the major biogeochemical processes (Robson 2014). In MOHID the biogeochemical processes are solved by the “Water quality module”, inside each control volume (domain grid cell). This “offline“ coupling of transport processes and biogeochemical processes is a common approach used on local, regional and global models (e.g. Aumont et al., 2015; Fennel et al., 2006; Hashioka et al., 2013). The biogeochemical model time step can be, and often is, different from the transport model time step. The latter needs, due to numerical reasons, smaller time steps than the biochemical models. In this application hydrodynamic model has a timestep of 120 seconds, while for water quality the timestep is 3600 seconds, increasing computational efficiency.

Since biogeochemical models are more detailed and complex it is important to define modelling objectives, to calibrate the model to pursue those objectives. In this case, the major objective was to simulate biotic dynamics in the Azores region, to provide 3-dimensional results to proceed to further studies, and to support the current scientific needs in the Azores. This application was applied to study biogeochemical processes at a regional scale, to support

other studies, and provide biogeochemical data for the entire Azores region. The model was applied for the years 2017 and 2018, including the calibration and validation.

Because phytoplankton rules the major biotic processes in the water column, the model was calibrated firstly by tuning phytoplankton growth and the different limitation growth factors.

Different model parameterization tests were performed based on other models and case studies, as compiled in Table 3.10 to Table 3.9. Besides the growth rates, also “bottom-up”, and “top-down” processes were studied. The bottom-up control refers to the different limitation factors as nutrients limitation, light limitation and temperature control, and “top-down” control is performed by grazing pressure by zooplankton (Hashioka et al. 2013, Chen et al. 2014, Daewel et al. 2019).

Different growth rates and limitation factors were used for small phytoplankton and diatoms, to find the best fit for the Azores region. Conceptually, smaller phytoplankton have advantages for light and nutrient harvesting by their relatively high surface/volume ratio, which allows more efficient exploitation at low nutrient concentrations, and consequently a higher growth rate. Larger phytoplankton, namely diatoms, have an advantage in utilizing nutrient pulses and exploiting vertical gradients (Sommer et al. 2017). For these reasons, in the Azores, an oligotrophic region (due to the low nutrients concentrations), it could be expected small phytoplankton have higher growth rates. However, several studies show that this statement cannot be considered in all situations (Teira et al. 2005, Barcelos Ramos et al. 2017, Karpowicz et al. 2020). Hashioki et al., 2013, performed an inter-comparison study with different biogeochemical models (PISCES, NEMURO, PlankTOM5 and CCSM-BEC), and shows how different models need different parametrizations to regulate phytoplankton growth, due to the different governing processes and model configurations.

Also, phytoplankton growth is driven by physical and environmental conditions (e.g. currents, wind, upwelling, vertical mixing, solar radiation, temperature, and nutrients availability) (Fasham et al. 1985), which are very dynamic in the Azores region, making this calibration process unique for each location. The same is valid for the half-saturation constants that, in general, increase with the size of the phytoplankton cell as a consequence of a smaller surface-to-volume ratio (Eppley & Thomas 1969). Diatoms should have larger half-

saturation constants than small phytoplankton, however, these constants are very difficult to quantity (Mulder & Hendriks 2014) and can change several orders of magnitude between different models (Table 3.10, Table 3.11). Several tests were performed until achieving a parameterization able to mimic the general phytoplankton dynamics for this case study.

The use of the modified Ks (Nitrate half-saturation factor) allows having better results regarding phytoplankton growth, considering that phytoplankton can adapt nutrients uptake considering environmental concentrations, reducing efficiency under high nutrient conditions, and increasing efficiency under oligotrophic and lower nutrients concentrations (Buchanan et al. 2018).

Finally, to fine-tune the solution, the parameterization process focuses on the "top-down" process. In MOHID this top-down control allows parameterizing the zooplankton preference for small phytoplankton or diatoms, allowing to regulate of their concentrations. Figure 3.12 shows the effect that the top-down processes have on phytoplankton and diatoms concentration, allowing to control of the general concentration, but maintaining the same seasonal patterns. The model considers a minimum threshold for phytoplankton concentration below which grazing ceases.

Model Validation

Surface

All the model parameterization and calibration processes are reflected in the model performance. Model validation for phytoplankton at the surface reveals that seasonal and spatial phytoplankton concentrations are well reproduced. The seasonal cycle of surface phytoplankton is in phase with satellite estimations (for chlorophyll_a). The model can simulate the prevalent seasonal variations, with the prominent spring bloom, and the smoother Autumn bloom. However, the solution is overestimating the phytoplankton concentration at the surface Figure 3.14. Nevertheless, the higher positive bias occurs when the error of the solution (RMSE) is higher, during the spring phytoplankton bloom. This overestimation of phytoplankton concentration during the bloom was also detected in other model applications in oligotrophic regions (Gutknecht et al. 2016).

This difficulty of simulating with precision the phytoplankton bloom is transversal to the general biogeochemical models and is one of the major challenges of biogeochemical modellers (Hashioka et al. 2013).

The constant Chl:C ratio used in MOHID, and the need of using a C:Chl ratio, to compare phytoplankton concentration with satellite chlorophyll_a concentrations, can also contribute to this bias. MOHID uses the simplistic fixed C:Chl ratio, likewise in other biogeochemical models (Table 3.2). However, it is known that this relationship is highly variable and can change with temperature, daily irradiance and nutrient concentration (Cloern et al., 1995; Geider et al., 1997) since phytoplankton tends to adapt their C:Chl ratio to the prevailing environmental conditions. Though, even complex biogeochemical models generally use a constant C:Chl ratio on phytoplankton estimations. This is a typical approach for global and regional models where this empirical Chl:C reveals adequate to simulate oceanographic modelling scenarios, despite the associated error (Ayata et al. 2013).

Analyzing these results on a spatial scale, this positive bias does not occur near the islands, but near the borders, concurrently with higher error values (RMSE) and lower correlation values (Figure 3.19 and Figure 3.20). These statistical results highlight the importance of choosing a model domain bigger than the area of interest, to dissipate the boundary conditions limitations. Results indicate that MOHID can improve the solution from the borders of the domain to the centre. Around the islands is clear an underestimation of phytoplankton values, negative BIAS, that can be a consequence of local islands inputs, that are not considered by the model once that on this model configuration, the nutrients inputs are only from the oceanography general conditions.

Model validation was performed with WOA climatology and CMEMS model results, and remote sensing data. WOA climatology is based on a collection of scientifically quality-controlled oceanographic in-situ data (Garcia et al. 2018). It is a widely used product for ocean model initialization and validation, climate studies, and operational forecasting, with the advantages of being based on thousands of in-situ measurements (with no satellite or model data) providing a climatological mean with global coverage. However, while it is useful as a climatology database, it does not represent small scales (temporal and spatial) variations, which can be limiting for small-scale models (spatially and temporally).

Validation results, for nutrient concentration at the surface and along the water column, are shown in Table 3.14 and Table 3.15 where can be seen that the seasonality of nutrient concentrations (nitrate, inorganic phosphorous and dissolved silica) is well computed by MOHID. The model simulates the expected behaviour for the study area, with an increasing concentration of nutrients in the winter, during December, January, and February, followed by a depletion during spring and summer when the lower values are achieved, typical of this oligotrophic region, to what follows an increase during fall and winter (Valente 2013, Amorim et al. 2017). This suggests that meteorological and ocean physical processes that drive the interannual variability of biogeochemical properties in the Azores region are well reproduced by the model.

The physical processes drive the nutrients supply, and as a consequence of winter vertical mixing, and vertical advection induce nutrients supply for the surface layers (McKinley et al. 2018). This (relative) high nutrient concentration induces the phytoplankton growth, which will consequently consume these nutrients, causing, therefore, their depletion after the phytoplankton bloom. This decrease is very intense in the spring months, starting in March, and achieves values close to zero in June. This nutrient depletion is stronger for nitrate than for inorganic phosphorous in MOHID. This goes in line with the major statement that nitrate should be the most limiting nutrient for the phytoplankton growth in the Azores region (Fasham et al. 1990). However, for WOA climatology, this depletion is higher for inorganic phosphorous. Alike along the water column with a lower correlation for inorganic phosphorous (86.5%) than for the other nutrients.

Surface dissolved silica concentration reveals some mismatch compared with WOA climatology, with higher differences for July. For July, WOA climatology has a concentration value much higher than in the other months that does not follow the seasonal tendency of the following and previous months, nor even the typical silicate patterns in the North Atlantic region (Amorim et al. 2017). Analysing the seasonal WOA nutrients average results (averaged for the entire domain), it is visible a higher variability in dissolved silica values, than for nitrate or phosphate. These results can indicate that, in this case, the WOA concentration at the surface is maybe inaccurate, either a consequence of an error during the data treatment along

the validation process or from any spatial or temporal scale limitation. Another in-situ data source could provide additional data to better understand this mismatch. Also, a longer simulation run could help to understand these results. This simulation was only performed for 2 years, not enough to infer if it is a spatial or temporal limitation that is causing this difference between MOHID results and WOA data. However, a comparison with CMEMS models reveals a good correlation (98.3%) for dissolved silica values.

Monthly average results along the water column at fixed points show that MOHID can simulate correctly the nutrients and oxygen concentrations along the water column (from surface until the bottom), in the different regions of the domain. The lowest correlation results occur against dissolved oxygen (86.8%). Some mismatches can be identified in dissolved oxygen results, whit MOHID overestimating the WOA values. However, CMEMS model results are also lower than the climatology. These differences can be justified by the lower resolution of the WOA climatology, but also because the oxygen concentration at the surface is highly related to the interface of water-air processes. Fluxes between the water surface and atmosphere, influenced by temperature, pressure and wind can cause local and temporal oxygen dynamics (Buchanan et al. 2018), not characterized by the climatology of WOA.

Validation results show that this model application is capable of simulating the general biogeochemical patterns in the Azores region, at the surface, and along the water column where, (in the euphotic zone, as a consequence of the primary producers), nutrients are consumed (dissolved phosphorous, nitrogen, dissolves silica) and oxygen is released (produced), while in the deeper layers, the subsurface remineralization conversely releases/consumes these elements (Matear & Hirst 2003).

The major limitation of this model assessment is the lack of in-situ data. The model is only being compared with a climatology (monthly based) and against another model. CMEMS model is frequently validated (Perruche C et al. 2016) and widely used, however, like any other model, has its constraints.

This limitation of in-situ data scarcity is shared with other biogeochemical ocean models, that also use other ocean models for validation (Hjelmervik 2012). In situ measurements collected

during cruises, can provide a high-quality but very sparse in time and space for validation of biogeochemical results (Lancelot et al. 2005).

Regarding the euphotic zone, the model simulates the general patterns in the Azores region, including the deep phytoplankton maximum, typical of oligotrophic regions, and descript for the Azores region (Macedo et al. 2000, Carmo et al. 2013, Santos et al. 2013), induced from both physical and biologic processes.

The gradients for water temperatures, nutrients concentration and phytoplankton reveal that MOHID can simulate both spatial and temporal variations, with a denoted North-south gradient, more visible for the sea surface temperature (always lower in the north of the domain, influenced by the atmospheric conditions but also by the cooler North Atlantic Water masses influence). This gradient is also visible for nutrient concentration at the surface, but in the deeper layers is not so marked. As a consequence of the higher nutrient concentration at the surface, the phytoplankton concentration is also higher in the north part of the domain in the study.

Along with the domain, at the surface, results reveal that the spring blooms are evident during March and April, with higher values in the north part of the domain. During the smoothest autumn bloom, phytoplankton concentration is higher near the islands than in the upper part of the domain.

Surface analysis along the study area shows that the phytoplankton patterns Figure 3.28), mainly the maximum values, are closely related to the maximum values of nitrate concentration (Figure 3.30), mainly during the spring bloom, with the maximum values occurring in the upper part of the domain. This association is also notorious for the sea surface temperature, during the spring bloom (Figure 3.43), with lower temperatures in the upper part of the domain. However, a major factor inducing these biotic patterns is the mixed layer depth (MLD). The spatial variability of the nutrients concentration is highly related to the MLD (Figure 3.34) and consequently with the phytoplankton concentration.

These results confirm how the physical process is closely related to the biogeochemical processes, and shape the seasonal biotic and abiotic processes in the Azores region.

The model simulates the general seasonal phytoplankton patterns at the surface, however with a general overestimation. This is a limitation shared with other biogeochemical models (Gutknecht et al. 2016). The model is a simplistic approximation of the complex lower trophic levels, considering only 2 Phytoplankton Functional Types, and 1 zooplankton group. This limitation is shared by many other biogeochemical model applications (Yool et al. 2013, Peña et al. 2016, Jung et al. 2020). However, models are always a simplification of the ecosystems chains, and increasing the number of compartments will not necessarily improve the performance of the model given the difficulty of obtaining the necessary observations to guide and validate models (Peña et al. 2016).

The availability of in-situ data for validation is another limitation. MOHID was validated against WOA (a monthly climatology database), and against CMEMS, another model, that has its proper limitations.

New and more *insitu* data and biogeochemical and ecological observation systems will allow for significant advances in model calibration and development. The existence of long time-series data from insitu observatories and fixed stations could be advantageous.

A longer run would help to better understand and calibrate the biotic patterns, these 2 years run are the first approach for this model application.

3.7. Conclusions

The main objectives of this chapter were the implementation, calibration and validation of the MOHID biogeochemical model in the Azores region. Model validation results show that with this parametrization, MOHID can simulate the major biotic and abiotic processes in the region.

Physical processes have a large influence on biogeochemical patterns (Moll & Radach 2003). Phytoplankton growth is driven both by the physical and environmental conditions in the ocean and in the interface with the atmosphere(Fasham et al. 1985). Being the Azores region characterized by a high spatial, and seasonal y of the marine environment (Amorim et al. 2017), and a highly dynamic region, influenced by different ocean currents and water masses (Palma et al. 2012, Sala et al. 2016), this calibration process is very particular for this region.

Different parameterizations as the phytoplankton growth rate, half-saturation constants for nutrients uptake, mortality, zooplankton grazing, were tested, considering the seasonal high variability of the environmental conditions in the Azores (like solar radiation, nutrients availability, etc), until achieving a good model performance.

The model simulates a seasonal evolution of the total phytoplankton concentration reflecting the seasonal variations reported for oligotrophic areas, and specifically for the Azores region.

The model can simulate the general patterns at the surface, along with the depth, with a detectable deep maximum of phytoplankton (DMP). This suggests that meteorological, physical, and biological processes that drive the interannual variability in the Azores region are correctly reproduced by MOHID.

Comparison between MOHID, CMEMS model results, and WOA climatology, at the surface and along the water column, reveals a similar seasonality in nutrients and dissolved oxygen concentration, revealing that MOHID can simulate the biogeochemical dynamics in the study area. Models (MOHID and CMEMS) results and WOA exhibits a difference, which may be due to the different time scale. While WOA has a climatological monthly means scale, models have an hourly scale. However, it is visible that both models, MOHID and CMEMS, follow the same general behaviour as WOA climatology, showing that despite local and seasonal behaviour the ocean biogeochemical dynamics tend to follow a tendency. However, models and high-resolution models have the advantage of identifying and allowing to study of local and temporal behaviour that climatology cannot represent.

MOHID can simulate phytoplankton dynamics along the study area, improving the solution from the borders of the domain, and providing better results near the islands. This statistical results for model validation against remote sensing data for phytoplankton validation show the importance of choosing a model domain bigger than the area of interest, to dissipate the boundary conditions limitations.

A nesting modelling strategy can be applied to study these processes at a local scale, on an island scale or a seamount scale. It would be useful to study the biotic processes, and the physical processes at a higher resolution, allowing the study at a seamount scale, like population connectivity studies.

Chapter 4- **Particle tracking model- Larval dispersal and connectivity**

4.1. Abstract

A biophysical particle tracking model was applied to study larval dispersion and populations connectivity in the deep-sea. This chapter describes the model implementation and calibration, and the application for 2 different case studies: Case study 1- larval dispersion of a sessile organism, a deep-sea sponge- *Pheronema carpenteri*; Case study 2- larval dispersion of a non-sessile organism *Chaceon affinis*. Model results for the two different case studies are discussed.

4.2. Introduction

Connectivity between marine populations is a fundamental process driving its persistence and influencing ecosystems' structure, biodiversity, productivity, dynamics and resilience (Kenchington et al. 2019, Busch et al. 2021). Connectivity in deep-sea habitats is a key for spatial management and conservation plans including Marine Protected Areas (MPA) (Lima et al. 2020, Combes et al. 2021). Benthic species rely on their larval phase for individual species survival, increasing population dynamics and persistence (Hilário et al. 2015). The larval development can be direct (and dispersal through migration) or by larvae that are pelagic or benthic. If larvae have a pelagic phase are advected by ocean currents, being able to "migrate" between geographically separated populations, and colonize new areas, promoting population connectivity and maintenance (Paris et al. 2013).

Though planktonic larval stage and larval dispersal are crucial to understanding population connectivity in the deep-sea (Ross et al. 2020), little is still known about both larval dispersal and connectivity. Difficulties in collecting in-situ data have delayed the progress in deep-sea biology and larval behaviour studies (Kenchington et al. 2019).

Recently, the use of biophysical and particle tracking models has become advantageous due to the previously proven importance of submarine mountains as well as oceanographic features on larval retention and dispersal patterns (Werner et al. 2007, Cowen & Sponaugle 2009, Combes et al. 2021).These biophysical particle tracking models allow the study of particles (larvae) dispersal and populations connectivity by using the physical component (hydrodynamic model), integrating the biological component (e.g. larvae behaviour (passive, swimming, bottom oriented, etc.); pelagic larvae duration, mortality, response to temperature, etc.); and including the definition of recruitment areas and settlement depths (Busch et al. 2021).

Several model applications have been applied to simulate larval dispersal, allowing the study of populations connectivity in vulnerable marine ecosystems (Ross et al. 2017, Kenchington et al. 2019, Wang et al. 2020), including deep-sea sponges aggregations (Ross et al. 2019, Busch et al. 2021). These models also allow assessing the role of larval dispersal on population connectivity regulation and supporting management plans for fisheries and vulnerable marine ecosystems (VME) (Kough 2014, Kenchington et al. 2019, Combes et al. 2021). Several studies highlight the importance of oceanographic features, like seamounts, or hydrodynamic patterns, for larval retention or dispersal (Werner et al. 2007, Cowen & Sponaugle 2009, Combes et al. 2021).

The Azores region is characterized by its complexity of bathymetric features, including 9 islands, more than 460 seamount-like features, and hosting a high diversity of sponge grounds, that may be classified as VME (Pham et al. 2015, Morato et al. 2016a, Somoza et al. 2020). Recently, several areas of Azores were included in the Azores Marine Park (AMP?) due to its vulnerability and ecological relevance. The AMP was implemented in 2011 by a regional law decree (DLR 28/2011/A) and was extended in 2016 to include Condor and Princesa Alice seamounts as MPAs (DLR 13/2016/A). The establishment of these region as MPA, increases its protection, but also creates the need for generating and implementing management plans and measures with well-defined objectives and regulations (Abecasis et al. 2013, Combes et al. 2021). Connectivity in deep-sea habitats is a key element of MPA conservation plans (Lima et al. 2020, Combes et al. 2021).

The objective of this chapter is to apply a biophysical particle tracking model to study larval dispersal and populations connectivity for two different case studies, considering different organisms:

- a deep-sea sponge- *Pheronema carpenteri*, a sessile organism;
- a deep-sea crab- *Chaceon affinis*- a non sessile organism.

4.3. Methodology

4.3.1. Particle tracking model

To study larval dispersal and connectivity, a coupled biophysical particle tracking model was applied to the Azores region. The particle tracking model, CMS- Connectivity Modelling System (CMS v2.0; Paris et al. 2013), was coupled with the 3-D hydrodynamic and biogeochemical model.

The CMS-Connectivity Modelling System is an open-source model, freely available online[4] , it was created at the University of Miami, for the multi-scale tracking of biotic and abiotic particles in the ocean, like complex larval migrations providing probability estimates of populations connectivity (Paris et al., 2013). This particle tracking model has been used extensively in the past to study the dispersal of larvae in the deep-sea, and the connectivity between different organism populations (Metaxas & Saunders 2009, Longmore et al. 2014, Antonio Baeza et al. 2019, Criales et al. 2019, Gary et al. 2020, Ross et al. 2020), also for physical oceanography applications (Sala et al. 2016, van Sebille et al. 2018). This model runs off-line, over a 3D hydrodynamic model, applying its velocity fields (u, v, w) to each particle, using a 4th order Runge–Kutta numerical discretization method to differentiate particle positions through space and time. Thus the model can run with a time step lower than the hydrodynamic solution, ensuring that particles cannot cross a model grid cell in a single time step and allowing for more accurate estimates of particles dispersal (Paris et al. 2013, van Sebille et al. 2018). It's a modular and probabilistic model, allowing to include additional 'behaviours' to the particles. Modules distributed with the code include mortality, vertical

[4] https://github.com/beatrixparis/connectivity-modeling-system

migration, and a connectivity module designed to generate a connectivity matrix output from the source to the final destination of the particles.

CMS allows tracking all the particles (larvae), along the entire study area, computing mortality, and behaviour, providing results along time including particles' location (x, y and depth), water properties, and particle status. CMS also computes the probability of larval exchange (connectivity) between several spawning locations, and recruitment areas.

MOHID hydrodynamic model results were used to provide the hydrodynamic conditions for the dispersal simulations. MOHID provides a 1/16º horizontal resolution (6km), and 50 vertical layers, with hourly outputs, in a 3-D resolution. Besides the velocity vectors, MOHID also provides, among other parameters, temperature, salinity and biogeochemical water properties for further analysis. As described in *Chapter 2* and *Chapter 3* of this dissertation, this model application was validated for the study area (both hydrodynamic and biochemical parameters).

4.3.2. Model implementation

This particle tracking model was used to study larval dispersal and connectivity between different populations. Each population is one release, and larvae are represented by lagrangian tracers. In this implementation, each population is defined as a release location, characterized by a position (longitude, latitude and depth).

For connectivity studies, recruitment areas and settlement areas are defined. Each population is one recruitment area, defined by a polygon. Settlement areas are also defined by a polygon. In this case, all the recruitment areas are settlement areas.

Due to the many uncertainties about deep-sea larvae biology, the modelling approach considers several pelagic larval duration (PLD), and seasonal scenarios to encompass different potential situations (Wang et al. 2020).

Different scenarios were computed considering different spawning seasonality and pelagic larval duration (PLD). Larvae can be passive or assume behaviour. Passive larvae are advected by the hydrodynamic fields, without any behaviour or swimming velocities. Larvae can assume behaviours, like swimming velocity, buoyancy, or swimming surface-oriented or

bottom-oriented. The model can assume different larvae stages, with different durations and behaviours. Swimming velocities can be temperature-dependent.

CMS particle tracking model allows the tracking of all the larvae advected by the hydrodynamics, calculating its travel distance, depth, and settlement positions. Model also considers mortality and different settlement strata. Each release is defined by the following parameters: location, depth, number of particles released, frequency of the release and release date.

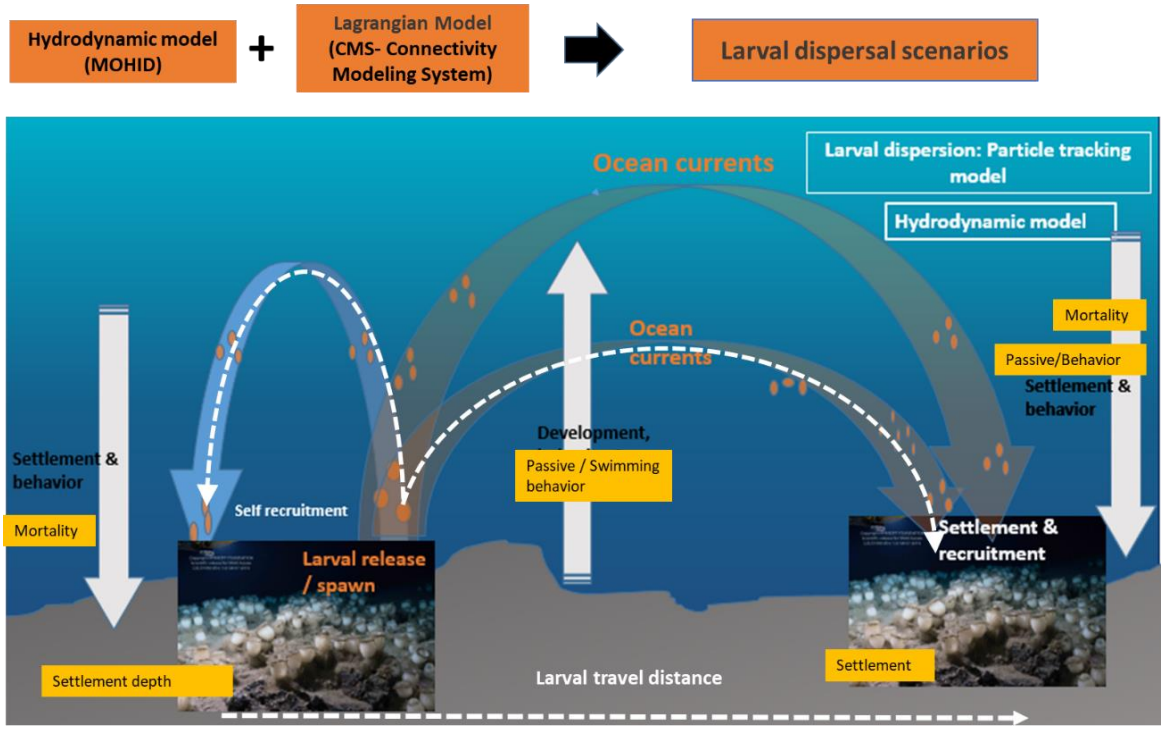

Figure 4.1- Diagram representing larval release and dispersal and model tools to simulate larvae dispersal

Release locations

Release locations should be defined considering the location in the study, and the model domain and resolution (North et al. 2009). The locations should be sufficiently far from the domain limits to avoid boundary effects like massive loss of particles out, which would bring uncertainties on model results; and regarding model resolution, separated by several domain cells, or by bathymetric barriers (e.g. island, seamount). Each release location is therefore defined by a point (longitude, latitude and depth).

Release location and settlement locations

Each release location represents a population in the study. For the connectivity assessment recruitment polygons are defined. Each population is therefore defined by a polygon of 6*6km (model resolution). Each population Is a release location and a settlement location.

Spawning input

Since there is no information about the frequency and seasonality of larvae emission, a hypothetical number must be defined (Cowen & Sponaugle 2009). To standardize this approach the same number of particles for all the locations was considered, assigning the same hypothetical relevance to all the release points, considering the same release size and frequency. Releases were performed with a time step of 1,5 hours, in order to capture a larger number of dispersal scenarios. Moreover, for the correct and most efficient model implementation, the number of particles to release was calibrated to provide an accurate larvae dispersion result, considering the computational efficiency.

4.3.3. Model parameterization and calibration

Lagrangian models have the advantage to be less computational heavy than eulerian models, enabling the use of thousands of particles for dispersal studies. Nonetheless, the number of particles to use is an important statement, that needs to be calibrated for each model application. The hydrodynamic model has a turbulence factor, and the lagrangian model a diffusivity factor, to simulate processes smaller than model resolution. Without diffusivity, all lagrangian tracers released at a specific location in space and time would follow identical tracks (Ross et al., 2016). Though, in reality, this does not happen and the lagrangian models consider the diffusivity parameter to get a more realistic solution.

The number of particles to release in each simulation should be enough to surpass this diffusivity and to provide confident results, and robust larval transport predictions, bearing in mind the random factor that all the dispersal models have. If too few particles are released, trajectories can have statistical outliers and do not satisfactorily represent the desired ensemble average, with a risk to induce erroneous conclusions (North et al., 2009).

Because the number of particles can increase the computational demand, a trade-off between computational time and result accuracy should be established. Sensibility testing should be done to calibrate the correct number of particles, considering different scenarios of hydrodynamic situations, at different release locations (considering longitude, latitude and different depths). The correct number of particles should avoid two typical errors: the number of particles is insufficient to capture the model diffusivity, and the particle release distribution does not adequately sample a subarea of particular importance (Jones et al. 2016).

To estimate the best number of particles, and avoid these accuracy errors, different methodologies can be used by analysing:

- Dispersal pathlength distances saturation;
- Particle density distribution, and the evaluation of the fraction of unexplained variation (Simons et al. 2013).

Dispersal pathlength saturation

One possible method of defining the correct number of particles is by analysing the dispersal pathlength saturation. Following this method, a correct number of particles must create a saturated dispersal path without abrupt variation along with travel distance. An adequate number of particles is achieved when these variations are smoother (Kough et al. 2013).

To apply this methodology, all particle pathlengths are considered. Pathlength is calculated by summing the travel distances during each time step, for all the particles, during the entire particles' lifetime. Dispersal pathlength saturation is analysed by graphing the probability of dispersal pathlength distances binned into small increments (e.g. 2km). (Kough et al. 2013).

Particle density distribution, and the fraction of unexplained variation analysis

Simons et al. (2013), propose a method for testing the best number of particles using the Fraction of Unexplained Variation (FUV) analysis. This method ensures that a simulation closely approximates a reference solution. As particles are released and tracked in three dimensions within the model domain, the vertically-integrated particle distribution at a

particular point in time, is quantified with a two-dimensional Particle Density Distribution (PDD) (Simons et al. 2013).

The PDD is calculated in two steps:

i) Firstly by vertically integrating the number of particles within a grid cell to create a two-dimensional (2-D) distribution;

ii) And secondly dividing the distribution by the total number of particles released up to that date.

Initially, a simulation is computed with a larger number of particles (the reference simulation), and its PDD is calculated. Because this solution is computed for the largest number of particles available, it is considered to provide the best representation of the particle distribution along the study area.

Afterwards, different subsets are tested, calculating the PDD for the different number of particles (n) extracted randomly from the reference simulation. This second step is repeated several times, 100 times in this case, to have a representative subset sampling. Finally, each tested subset is compared with the reference solution by computing the FUV between them.

The FUV is calculated by:

$$FUV = 1 - r^2 \qquad \text{Eq. 4.1}$$

where r is the linear correlation coefficient between two different PDDs.

The third step is to calculate the FUV upper bound for each subset and tracking time. The FUV upper bound was identified where 95% of the FUV distribution lies below the bound.

FUV methodology presents several advantages: i) FUV result is a value between 0 and 1, providing a consistent scale for comparing PDDs which may contain very different numbers; ii) FUV is a conservative measure of difference where the grid cells are independently evaluated. Therefore, it may detect differences in the PDDs even if the particles have the same patterns but slightly shifted in space (something that would be masked when using the typical correlation analysis between patterns of distribution); iii) FUV provides a single number that can quantify the difference between two PDDs.; iv) The use of a squared correlation

coefficient naturally induces a description of the difference magnitude in terms of the residual variance.

In the end, PDDs with a very high FUV are virtually uncorrelated and represent two very different spatial distributions of particles. With this methodology, it is assumed that the number of particles in use is enough to describe the distribution when the FUV is lower than 0.05, considering the 95% confidence level. This cut-off represents the maximum amount of dissimilarity that will be tolerated between the reference and sub-sampled PDDs. For each number of particles to test (from 5,000, 50,000, 100,000, 125,000, 150,000, 190,000), 100 different subsets were tested, and respective FUVs were estimated.

Time length

Larvae particle dispersal and connectivity studies were performed for the year of 2017. Several scenarios were also tested for 2018 to compare dispersal patterns.

4.3.4. Model application and analysis technics

In this work, the results of simulated larval dispersal scenarios were analysed in four different ways: i) by analysing the Particle Density Distribution (PDD); ii) larvae dispersal maps; iii) by studying the particles' depth and travel distance along with the simulation; and, iv) by using connectivity matrices.

Particles density distribution

As previously described, PDD represents the particle density distribution in 2-D vertically-integrated maps. In the 2-D map used in this study, all particles are represented and each domain grid cell (6km x 6km) represents the integrated number of tracers in the entire water column.

Larvae dispersal maps

Particle dispersal maps represent particle distribution. In this maps, particles are not integrated into the water column, and all the particles at each cell are graphed. Some particles can “mask” others, by overlapping. In these maps, each particle colour represents only one category: release’s id, depth, particle’s relative time, or any other property considered by the model. Also, water properties provided by the hydrodynamic model, can be plotted (like temperature, salinity, dissolved oxygen, etc).

Travel distance and depth

Histograms were used to analyse potential travel distances from all the different release points for the different scenarios. These distances were calculated from individual particle trajectories as the sum of straight-line distances between each time step. Also, histograms of particle depths were used to analyse how particles are distributed along the water column.

Connectivity Matrices

Connectivity between 2 locations was assumed when, at least, one modelled particle released from one location (source node) settle in another location (receiving node), after the PLD. When settling on the same location, this is considered self-recruitment. Connectivity is quantified by the percentage of particles that settled upon each location. These matrices represent the percentage of self-recruitment and connectivity between different populations. Source populations are represented as rows (j), and recruitment areas (receive node) as columns (i), self-recruitment in each population is represented in the matrix diagonal. Colours represent the percentage of settled particles in both situations: self-recruitment and connectivity.

4.4. Case Study 1- *Pheronema Carpenteri*

4.4.1. Introduction

Deep-sea sponges are characteristic organisms of the Azores deep-sea (Pham et al., 2015). Dense sponge aggregations, known as “sponge grounds”, are a key component of marine benthic ecosystems, promoting, along with corals, the enhancement of local biodiversity, and are believed to act as feeding, reproductive, nursery and refuge areas for a high number of invertebrates and fish (Pham et al. 2015, Beazley et al. 2021). Due to their vulnerability, and their need for protection, deep-sea sponge grounds can be classified as vulnerable marine ecosystems (VMEs) (FAO, 2009).

Deep-sea sponges are thought to play an important role in the deep-sea nutrient cycle, recycling the nutrients, by their capacity of filtering large quantities of water filtering properties (Leis 2020). Also, they contribute to the biogeochemical cycling of dissolved nutrients, namely carbon and nitrogen, but also for silicate in the case of siliceous sponges (like the sponges of the class Hexactinellida) (Howell et al. 2016, Maldonado et al. 2016, Ross et al. 2019).

4.4.1.1. *Pheronema carpenteri*

Pheronema carpenteri (Thomson, 1869*)* is a hexactinellida sponge from the genus *Pheronema* (Alvarez et al. 2022). They are nest-shaped sponges, up to 25 cm high and 30 cm across, and can be more than 200 g in wet weight. These sponges are anchored in the bottom by rooting tufts of long spicules (Maldonado et al., 2016). and can form aggregations of up to 475 individuals per 1,000 m^2, with peak abundances and wet weight biomass up to six individuals/m^2 (average 1.5 individuals m^2) and 1.1 kg/m^2 (average 372 g/ m^2), respectively (Rice et al. 1990).

P. carpenteri aggregations can occur from south of Iceland and west of Scotland, across the Porcupine Seabight, the Azores, northern Spain, Portugal coast, Canary Islands, and off Morocco forming the most extensive sponge aggregations at 800–1,350m depth (Rice et al. 1990, Barthel et al. 1996, White 2003, Tempera et al. 2013, Maldonado et al. 2016). They can

also be found on the margin of Greenland and Canada, on the south side of the Faroes-Iceland Ridge (Howell et al. 2016).

In the North Atlantic, dense aggregations of hexactinellida were identified in the continental slopes, and some of them are reported to have persistent spicule skeletons after death (Maldonado et al. 2005). These spicule mats created by the senescence and death of hexactinellida sponges like *P. carpenteri* can form biodiversity hotspots (Henry & Roberts 2014), and may even function to reduce sediment erosion in the deep sea (Black et al. 2003).

***Pheronema carpenteri* in the Azores**

In the Azores, sponge aggregations dominated by *P. carpenteri* have been recorded on the Cavala, Condor, and Mar da Prata seamounts, and in the Açores bank, in depths between 700 m and 924 m (Tempera et al., 2013 citing several sources: Pérès et al., 1972; Tempera et al., 2012; Pereira, 2013). In Condor seamount, *P. carpenteri* multispecific aggregations with higher sponge density were found at 700-825 m depth, whereas mixed substrates found approximately between 430-1100 m were the most taxonomically diverse. More recently, a dense aggregation in the South of Pico was identified (Creemers et al. 2019, Colaço et al. 2020). Additionally, data from exploration missions, and collected from observers and bycatch, allow the identification of several sponge aggregations namely in the South of Faial, North of Pico island, in Formigas, Açores bank and more recently in Gigante seamount ((Colaço et al. 2020)). Moreover, during the development of this work, but not included, more sponge observations were reported in the Azores, by multidisciplinary scientific cruises and exploration missions, performed among others, by researchers at the University of the Azores (IMAR 2018, Friedlander et al. 2019, Somoza et al. 2020).

4.4.1.2. Deep-sea sponges' biological traits

The current understanding of deep-sea larval behaviour for deep-sea sponges is extremely limited (Busch et al. 2021), mainly due to the inherent difficulty to assess deep-water habitats (Lopes 2005). During their life cycle, after hatching, sponge larvae are pelagic, drifting in the water column for a limited period (Pelagic Larval Duration, PLD), before settling on the seafloor, in a recruitment area, to become sessile juvenile sponges (Maldonado, 2006).

Hexactinellids are currently assumed to be viviparous with lecithotrophic larvae (Maldonado & Young 1999). Available data about hexactinellida sponges biology, results mainly from studies with shallow-water sponges (Barthel et al. 1996, Boury-Esnault et al. 1999), artic populations (Leys & Lauzon 1998), between other cases (Bett & Rice 1992, Boury-Esnault et al. 1999, Guillas et al. 2019). The available data from these studies indicate that most sponge larvae are anchiplanic, with a short planktonic larval duration of minutes to a few days (usually< 2 weeks) (Maldonado et al. 2016, Ross et al. 2019). However, this short PLD is only reported for shallow-water species and is believed to not be representative of deep-sea water taxa as *P.carpenteri*. Deep-sea species are thought to have longer PLDs than their shallow-water counterparts (Hilário et al., 2015). Furthermore, Vacelet et al, 1999, suggest that unciliated hoptimella larvae sponge may remain in the plankton for longer periods, perhaps months (Maldonado, 2006). Environmental factors like seawater temperature can influence the duration of the reproductive period (Maldonado, 2006).

Information about sponges' spawning periodicity is limited. Previous studies often assume that deep-sea sponges do not experience seasonality, unlike their littoral relatives, because they are too deep to be influenced by light (Barthel et al. 1996). However, further studies pointed out that despite their deep-sea habitat, sponges experience seasonality which influences their growth rates and perhaps reproductive period, which, in turn, may be regulated by patterns of primary production in the photic zone of the ocean and subsequent sinking of the generated production (Leys & Lauzon 1998). Table 4.1 summarize information about deep-sea sponges biological traits found in the literature review.

Spetland et al (2007), collected information about *Geodia barretti* sponge biology, (located at 60–250 meters' depth, in Norwegian fjords), identifying one (Spring) or two (Spring and October) discrete peaks of gamete release over the year cycle. Maldonado et al., 2017, also suggest a synchronization between sinking primary production and deep-sea sponge reproduction (Kenchington et al., 2019).

For applying particle tracking models to study larvae dispersal, it is essential to include information about their biological traits like spawning seasonality, larvae behaviour, and pelagic larval duration (Busch et al. 2021). When and how often marine species release larvae (i.e., spawning window and periodicity) can be determinant for connectivity among sites

(Treml et al. 2012). Therefore, this information, together with other important life history parameters like PLD and larval mortality, is essential to developing dispersal phenotypes to model connectivity (Treml et al. 2012). Larvae mortality can be caused by predation, by advection away from suitable settlement habitats, or it can occur by "physiological stress" caused by an overextended planktonic phase (Maldonado 2006).

Table 4.1- Pelagic larval duration, spawning seasonality, and sexuality of deep-sea sponges organisms, from different locations and depths

Organism	PLD	Spawning season	Organism location	Laboratory /in situ	Reference
all sponges	<14days				1)
generic		phytoplankton blooms (March/autumn)	Several; northwest Atlantic		2)
Hexactinellids	<24h	--	North Atlantic		3)
Hexactinellids	>24h	--	North Atlantic		3)
Most sponges	<2weeks			laboratory	1)
Geodia barretti		Spring & autumn / phytoplankton blooms	Norwegian fjords, deep continental shelf	In situ	4);5)
sponge holobionts	14 days	June (1-30june)	Cantabrian sea		6)
Alectonid sponges (Demospongiae)	>30 days/ months				7)
Hexactinellids		All year round / phytoplankton blooms	Fiords, British Columbia		2)
Oopsaca		All year round	submarine cave, France		2)

1) Maldonado, 2006; 2) Kenchington et al., 2019; 3) Busch et al., 2021; 4) Spetland et al. 2007; 5) Leys and Lauzon et al., 1998; 6) Ross et al., 2019; 7) Vacelet 1999.

In the absence of data and information about *P. carpenteri*, the information about the class hexactinellida, other classes of deep-sea sponges or even another phylum of deep-sea organisms, can be useful to study different scenarios (Maldonado 2006, Ross et al. 2019, Busch et al. 2021).

4.4.2. Model Setup

4.4.2.1. Sponge locations

The *P.carpenteri* sponge aggregations in the study are located along the Archipelago (Figure 4.2), in a batymetric range from 630 to 1000 meters depth (Table 4.2). Location 1 (L#1) and 2 (L#2) are located over the MAR (Mid-Atlantic Ridge), in the Cavala (L#1) and Gigante (L#2) Seamounts, locations 3 to 8 in the central group (CG), and L#9 (Mar da Prata) and L#10 (Formigas), in the Eastern Group (EG).

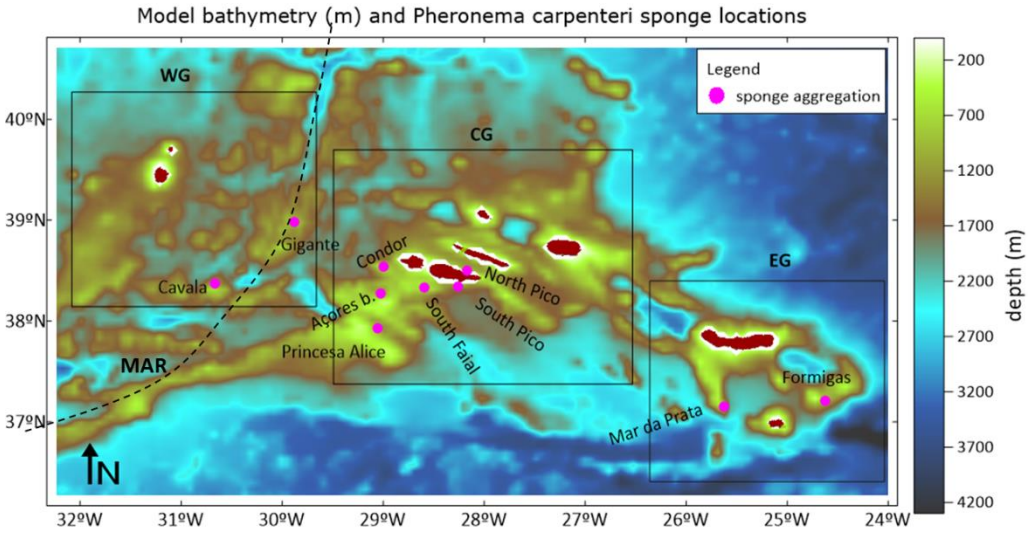

Figure 4.2-Bathymetry of the study area, with the representation of the Mid-Atlantic Ridge (MAR) with a dashed line, the 9 islands of the Azores archipelago in brown, the location of the *Pheronema carpenteri* sponge aggregations in the study with pink circles; black polygons depicts the groups in analysis: WG-Western Group (L#1 Cavala, L#2-Gigante); CG-Central Group(L#3-Princesa Alice, L#4-Açores Bank, L#5-Condor Seamount, L#6-South of Faial, L#7-South of Pico, L#8); EG- Eastern Group (L#9-Mar da Prata, and L#10-Formigas).

Table 4.2- *Pheronema carpenteri* sponge aggregations in the study, their location, depth, source and name/location

Location	Longitude (ºW)	Latitude (ºN)	Depth (m)	Nome/localização	Group	Source
L#1	-30.6701	38.3632	900	Cavala	WG	emodnet[1]
L#2	-29.88809	38.98353	766	Gigante	WG	Exp-Fund.Azul [2]
L#3	-29.06232	37.9183	900	Princesa Alice	CG1	Biodiaz [3]
L#4	-29.02941	38.273	825	Açores Bank	CG2	Sponges-Observer_2017[4]
L#5	-28.99877	38.53281	775	Condor Seamount South	CG3	IMAR-DOP/UAz (CoralFish, Corazon, Condor) [5]
L#6	-28.59288	38.32531	630	South of Faial	CG4	Sponges-observer_2017[2]
L#7	-28.26657	38.33921	1000	South of Pico	CG5	Sponges-Lula[2]
L#8	-28.1735	38.49624	822	North of Pico	CG	Exp-Fund.Azul[2]
L#9	-25.63083	37.14111	780	Oeste West of São Miguel (Mar da Prata)	EG	IMAR-DOP/UAz (CoralFish, Corazon, Condor) [5]
L#10	-24.63	37.205	904	Formigas	EG	Colecta[6]

1-http://ipt.vliz.be/eurobis/resource?r=imagedop_video_annotations; 2-Colaço et al., 2020; 3-Institute of Marine Research (IMAR - Azores), Portugal; 4-Department of Oceanography and Fisheries (DOP) - UAC, Portugal (2016). 5-ImageDOP Bentic Video http://www.vliz.be/en/imis?dasid=4492&doiid=304; 6-DOP/internal unpublished data

4.4.2.2. Model configuration

In this implementation, each sponge aggregation is defined as a release location, characterized by a position (longitude, latitude and depth), and as a recruitment area, defined by a polygon.

Different scenarios were computed considering different spawning seasonality and PLD. Following the most used approach when modelling sponge larvae dispersal in the deep-sea, larvae behaviour was considered passive (Kenchington et al. 2019, Swearer et al. 2019).

CMS particle tracking model allows to track all the larvae advected by the hydrodynamics, calculating its travel distance, depth, and settlement positions. The model contemplates mortality and different settlement strata.

Larvae mortality is computed following the half-life concept (the time it takes half the population to die) likewise in other deep-sea larval dispersal studies (North et al. 2009, Paris et al. 2013). Model configuration is summarized in Table 4.3.

Theoretical "larvae" (passive tracers) were released from the 10 locations in the study, considering the same number of larvae per release. The number of particles released was defined by calibration methods, and it was established to use a total of 150000 particles per release per month.

Particle simulations were performed for the years 2017 and 2018, during monthly releases in March and October (Autumn situation), to consider the spring and autumn spawning situations respectively (Table 4.1). The larvae were released at a regular interval, every 90 minutes, to capture the full range of potential larval trajectories within the spawning period (Ross et al. 2016). Also, a yearly release was performed to cover all the seasonal scenarios within the period. Several PLDs were considered to cover different larval reproductive behaviour (based on literature).

Table 4.3- Biophysical model configuration for case study 1

Model parameter	Parameter description
Hydrodynamic model resolution	6*6km
Model time step	7200 seconds
Number of release points	10
Release depth	Sea bottom
Number of larvae per release	150000/month (calibrated)
Release time step	1.5 hours
Behaviour	Passive (Ross et al, 2019)
Mortality	Half-life (North et al. 2009)
Strata	600 to 1000m (*P.Carpenter*i bathymetric range)
Scenarios	Several considering PLD and seasonality

Scenarios

Table 4.4 summarize the different scenarios studied considering the PLD and seasonal spawning and release length. PDL15 and PDL30 refers to scenarios of 15 and 30 days of Pelagic Larval Duration, respectively.

Table 4.4- scenarios considered in this study, with spawning date and pelagic larval duration

Scenario	PLD (days)	Release date	Release length (days)
PLD15_March_2017	15	March 2017	31
PLD15_October_2017	15	March 2017	31
PLD30_March_2017	30	October 2017	31
PLD30_October_2017	30	October 2017	31
PLD15_year_2017	15	January-December 2017	365
PLD30_year_2017	30	January-December 2017	365
PLD15_March_2018	15	March 2018	31
PLD15_October_2018	15	March 2018	31
PLD30_March_2018	30	October 2018	31
PLD30_October_2018	30	October 2018	31

4.4.3. Model calibration

The number of particles to use in the model was calibrated for this specific case study, considering the 10 release locations, and the scenarios in the study. Two methods were used to calibrate the number of particles: i) the dispersal pathlength saturation; and ii) the fraction of unexplained variation (FUV) analysis. Two different scenarios were analysed: *PLD30_Marchr_2017*, and *PLD30_October_2017*. The longest scenarios were considered to contemplate the worst conditions with the higher dispersal situations, that, in this case, correspond to PLD30. The analysis is performed considering a monthly release, with particles released every 900 seconds during the 30 days. Therefore, by day 30, the last particles are being released, and they will be moving up to 30 (PLD) days more.

Dispersal pathlength saturation

Dispersal pathlength distance (Figure 4.3 and Figure 4.4) shows that a total of 100 000 particles per release per month, provide a saturate movement for all the release locations. Results show that a release of 1000 particles provides a discontinuous result with abrupt changes in the travel distances, with 10000 particles per month, the fluctuations get smoother, but only with 100 000 particles, the dispersal pathlength distance doesn't reveal abrupt changes along with travel distance.

Particle density distribution, and the fraction of unexplained variation analysis

In this calibration step the number of particles tested goes from 5 000 up to the reference value of 200 000 particles released per month at each location. Results show that by day 45 the FUV is above 0.05 for the majority of the releases with 100000 released particles (Figure 4.5). However, by day 60, FUV results show that the number of particles required to achieve a robust PDD (FUV below 0.05 (Simons et al. 2013)) should be 150000 particles per release per month, for both tested scenarios.

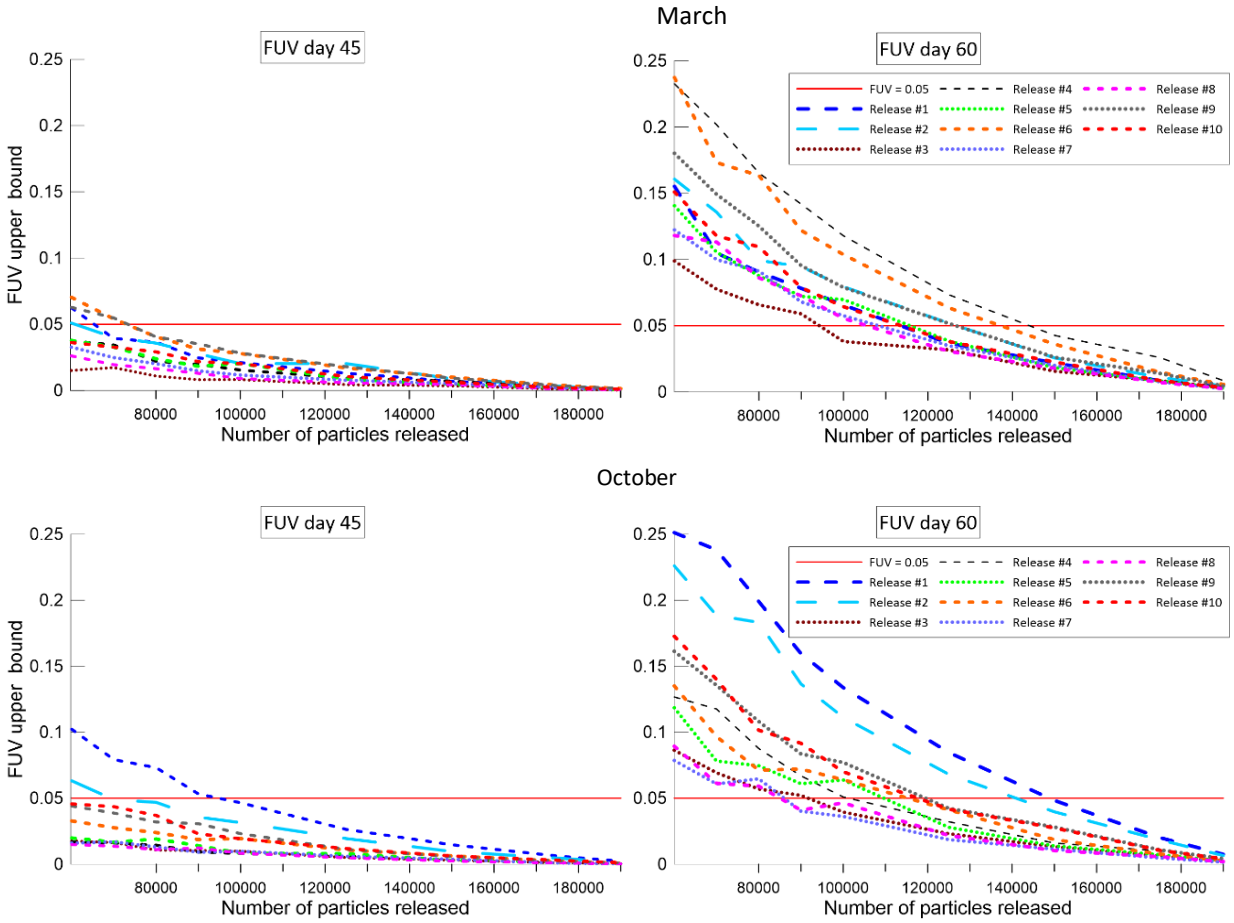

Figure 4.3- Fraction of unexplained variation (FUV) upper bound versus the number of particles released in March (top), and in October (down) with a PLD30 and tracking time of 45 days (left) and 60 days (right) for the different 10 release locations. The horizontal red line is drawn at a FUV upper bound of 0.05. For the reference simulation, (for each situation) it was considered a release of 200000 particles per month, per release. For each number of particles to test (from 5000, 50000, 100000, 125000, 150000, 190000), were tested 100 different subsets, and the FUV upper bound of each test was estimated (Simons et al., 2013.

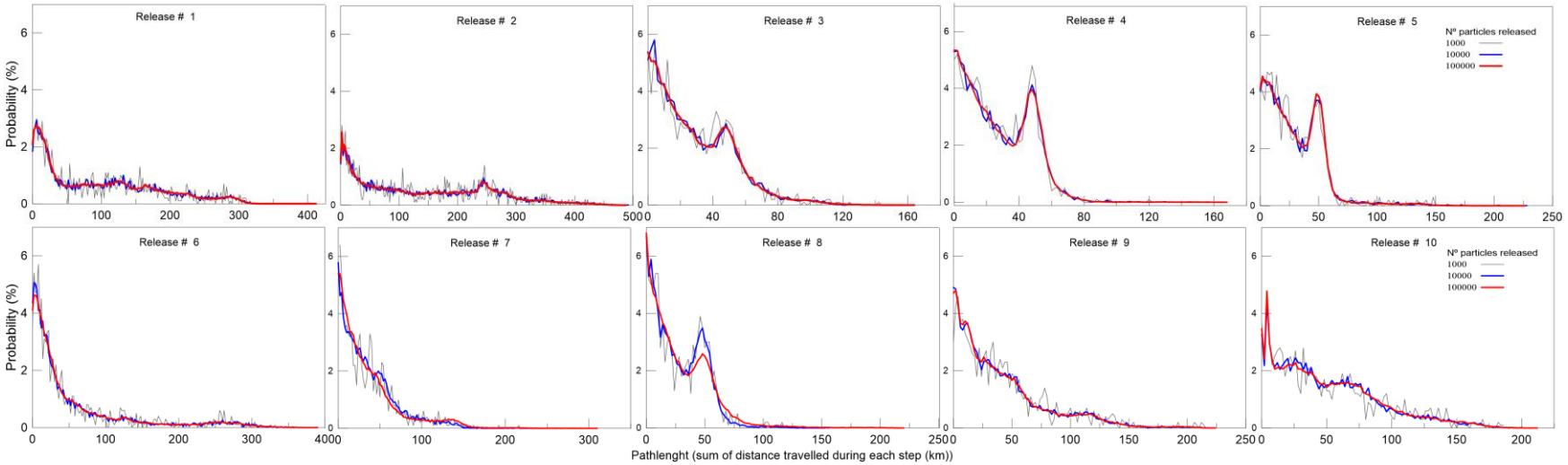

Figure 4.4- Probability of dispersal pathlength distances, for scenario *PLD30_March_2017* (with a considering a PLD30) , with different numbers of particles (1000; 10000; 100000). The X-axis is the pathlength travelled by each particle (sum of distances moved during each time-step) binned into 2km increments, and the Y-axis is the probability.

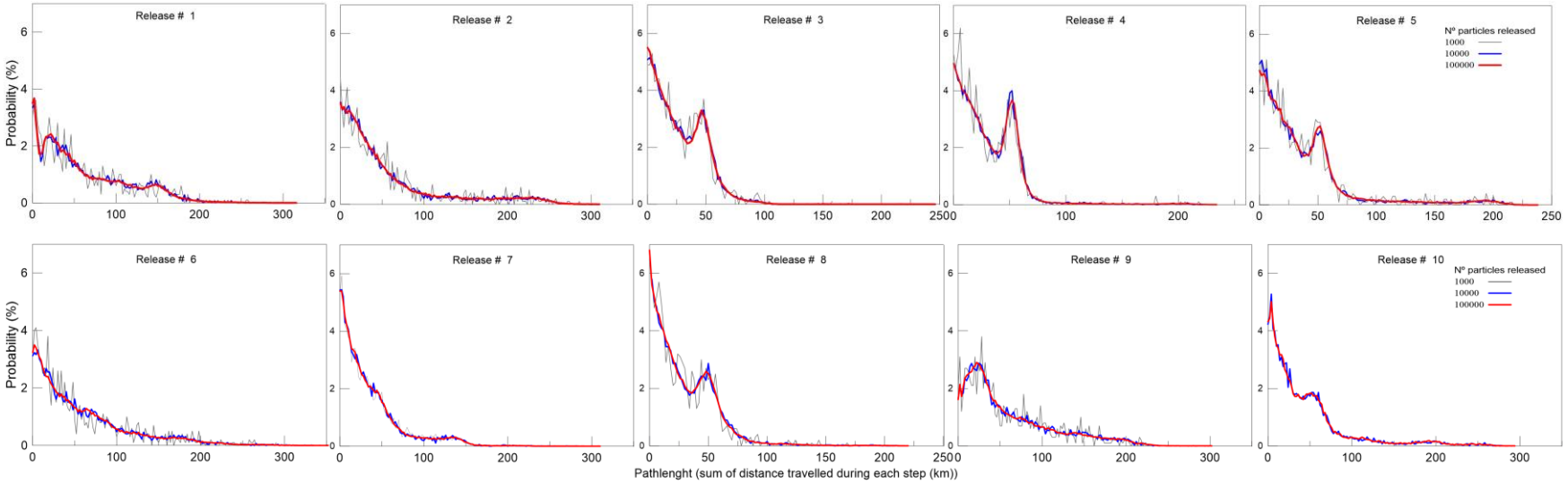

Figure 4.5- Probability of dispersal pathlength distances, for scenario *PLD30_October_2017* (with a considering a PLD30), with different numbers of particles (1000; 10000; 100000). The X-axis is the pathlength travelled by each particle (sum of distances moved during each time-step) binned into 2km increments, and the Y-axis is the probability.

4.4.4. Results

4.4.4.1. Larval dispersal

Particle density distribution- Seasonality

Larvae dispersal was studied for different season scenarios. Larval dispersal shows different spatial and seasonal differences. Larger PLD contributes to a higher dispersion, mainly in the Central Group (CG), with larvae dispersal plumes covering the entire region between Princesa Alice and South of Faial (Figure 4.6 d). Larval dispersal shows different patterns for March and October releases.

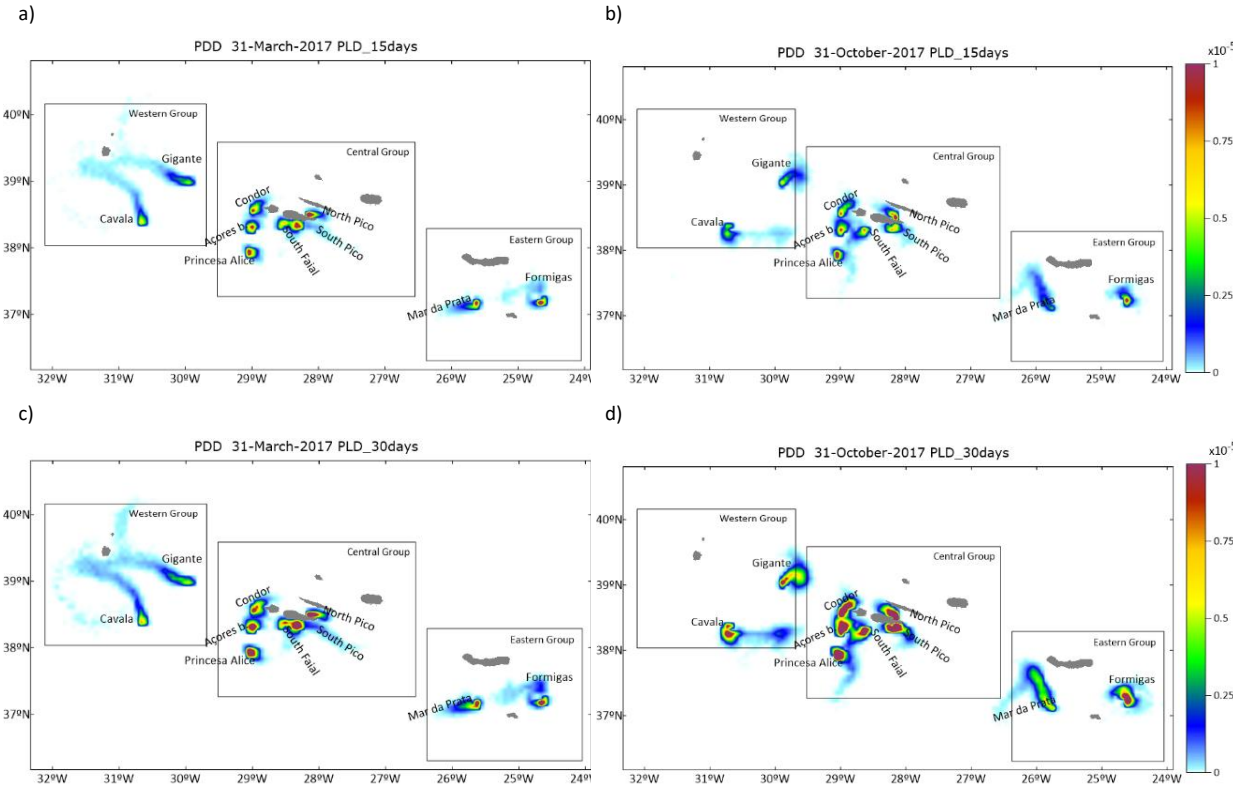

Figure 4.6- Particle density distribution for the scenarios *PLD15_March_2017* (a) top left) and *PLD15_October_2017* (b) top right), for the 31st of March, and 31st of October respectively, and scenarios *PLD30_March_2017* (c) bottom left) and *PLD30_October_2017* (d) bottom right), for the 31st of March, and 31st of October respectively. Black poligons represent the differerent release groups: WesternGroup (L#1-Cavala, L#2-Gigante); Central Group (L#3-Princesa Alice, L#4-Açores Bank, L#5-Condor Seamount, L#6-South of Faial, L#7-South of Pico, L#8); Eastern Group (L#9-Mar da Prata, and L#10-Formigas).

Larvae dispersal from the Western Group (WG), Cavala and Gigante, are advected predominantly towards the West end NorthWest direction in March, surrounding the Flores

and Corvo islands. While in October, the larvae dispersal plume goes in the East direction, towards the CG. Compared with the other releases, the larvae dispersal of L#1 and L#2 show higher travelled distances (median values of 43 and 44 km respectively, (Table 4.5) while the other releases range from 15 to 24km. Values for the March PLD30 scenario). Larvae dispersal plumes in the CG, in October, have a dispersal mainly along the North-South direction, while during March the patterns is diffrent. During March, L#7, in the South of Pico island, shows higher dispersal toward the East. In the Eastern group, the dispersal plume from L#9 shows higher dispersion towards the North in October, and to the West during March.

Particles distribution from each release point

The modeled larvae dispersion shows heterogenic patterns considering the spawning season. During March (Figure 4.8 a) there is no connection between the larvae plumes from the WG and CG. While during October is the opposite, occurring overlay between plumes from these 2 groups. Figure 4.8 shows the particle dispersal of scenarios *PLD30_March_2017* (left) and *PLD30_October_201*7 (right), with different colours representing each one of the release sources. These images depict all the particles during the entire simulation and particle density for a specific instant as represented in Figure 4.7.

In March, larvae from the WG group diverge toward the Northwest, achieving all the region around Flores and Corvo islands. Condor Seamount larvae (L#5), can achieve the North of São Jorge island, being the unique release plume reaching that location. It is only during March that a tracers' corridor is formed between CG and EG, creating a potential connection between these two groups. Açores Bank larvae (L#6) can achieve the EG, around São Miguel island. While in October don't. In October the distribution patterns are different. The connection between the plumes of these 2 groups is very weak. Nonetheless, dispersal pathways show a higher dispersal on the western part of the domain, between the CG and the WG, with larvae from CG, L#5 (Condor Seamount) and L#8 (North of Pico) getting closer to L#2 (Gigante Seamount), and larvae from L#1 (Cavala seamount) achieving the CG region.

Particle distribution along the domain reveals that some particles can be advected out of the domain, mostly from the WG, and EG (L#1 and L#2; and L#9 and L#10 respectively). Nonetheless, this number of particles is negligible, with a maximum of 0.03% from L#10 (Figure A Annexx II).

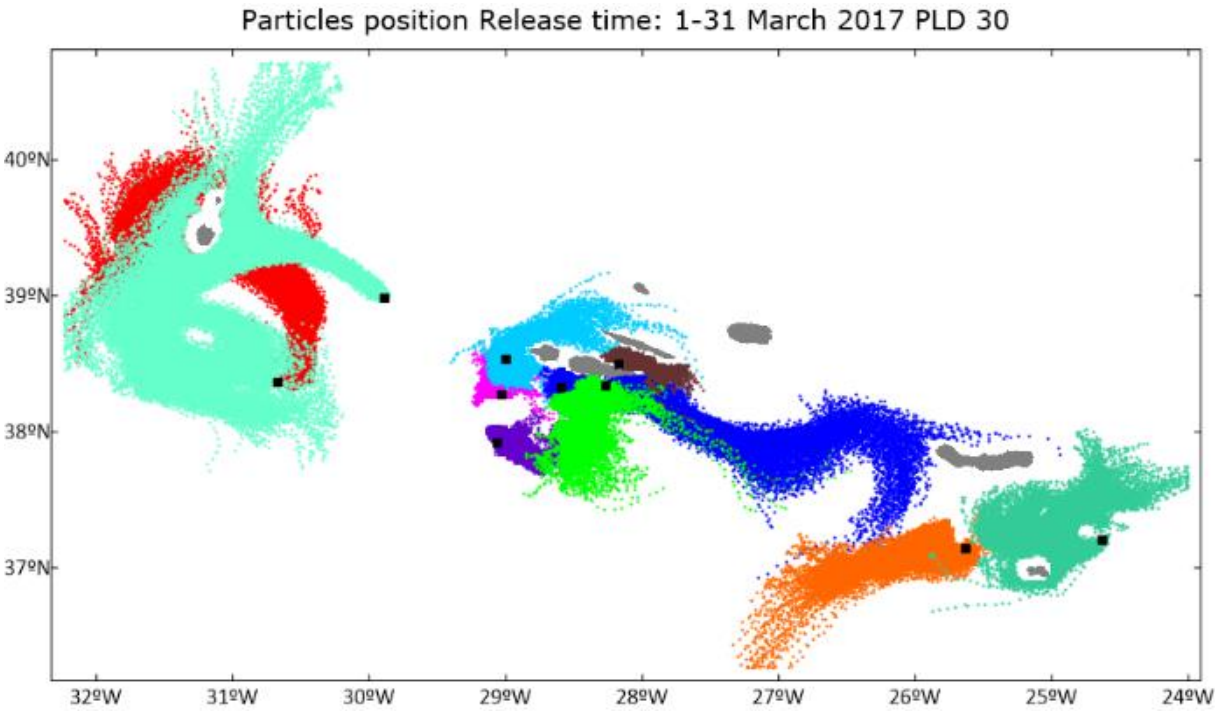

Figure 4.7- Representation of all particles positions along their trajectories, for *PLD_30_March_2017* Different colours represent the different release points. For less overlapping between particles, only 1/10 of the total particles are represented.

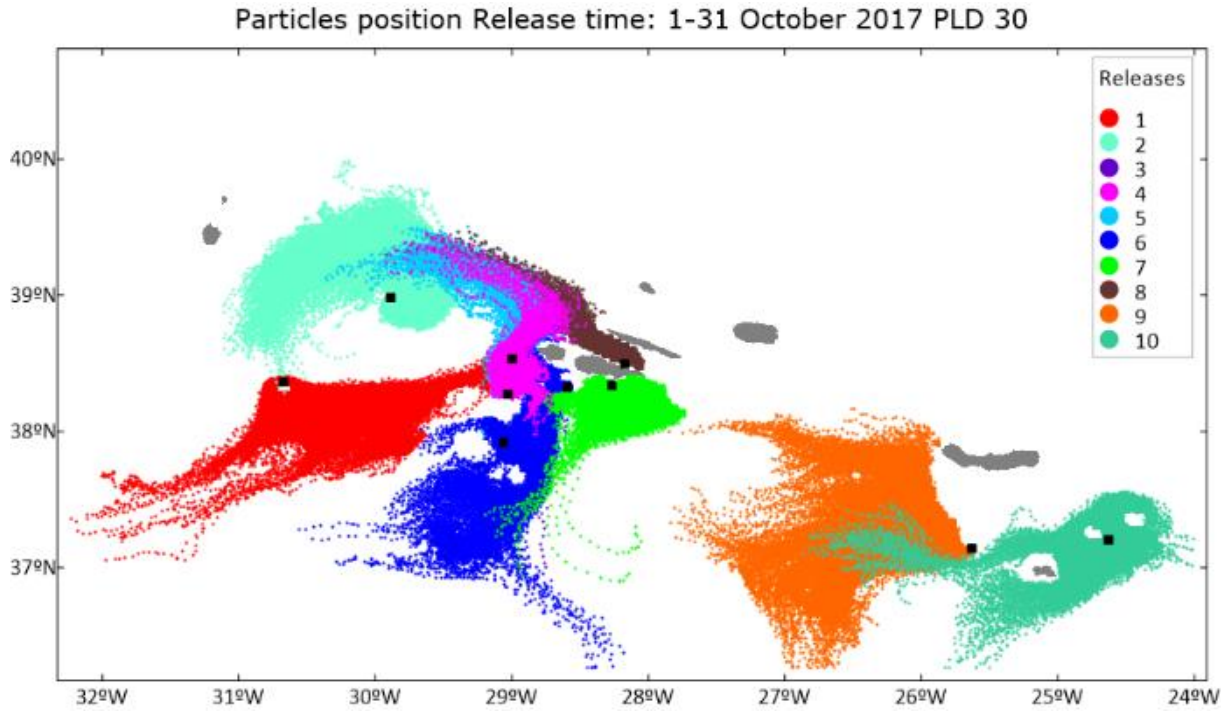

Figure 4.8- Representation of all particles positions along their trajectories, for *PLD_30_October_2017*. Different colours represent the different release points. For less overlapping between particles, only 1/10 of the total particles are represented.

Hydrodynamic and water properties patterns

Larvae are advected by ocean currents. Hydrodynamic results help to understand particle dispersal plumes. Figure 4.9 shows the hydrodynamic patterns (monthly average) for March and October, at 750 meters depth. During March an eddy is formed, between WG sponge locations and Flores island. This eddy is contributing to particle retention in this area. Apart from this eddy, is visible an absence of particles over the most intense currents. For the October case, the major hydrodynamic fields presents another pattern, and again, the higher velocity fields match with the absence or reduced particle density. The higher density of particles occurs at lower hydrodynamic fields.

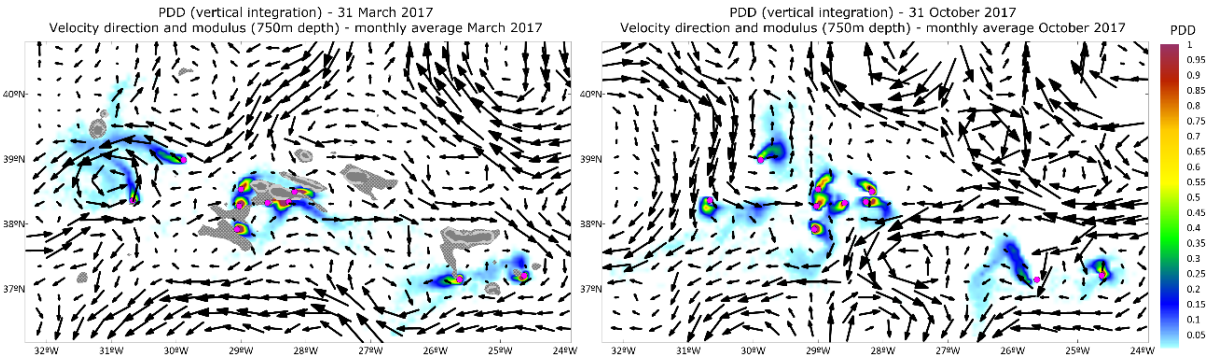

Figure 4.9- Particles density distribution integrated in the water column, represented by a gradient color scale from blue to red, where 0 is white), for 31 March 2017 (left), and 31 October (right), vectors are representing the monthly average of velocity modulus and direction at 750meters depth.

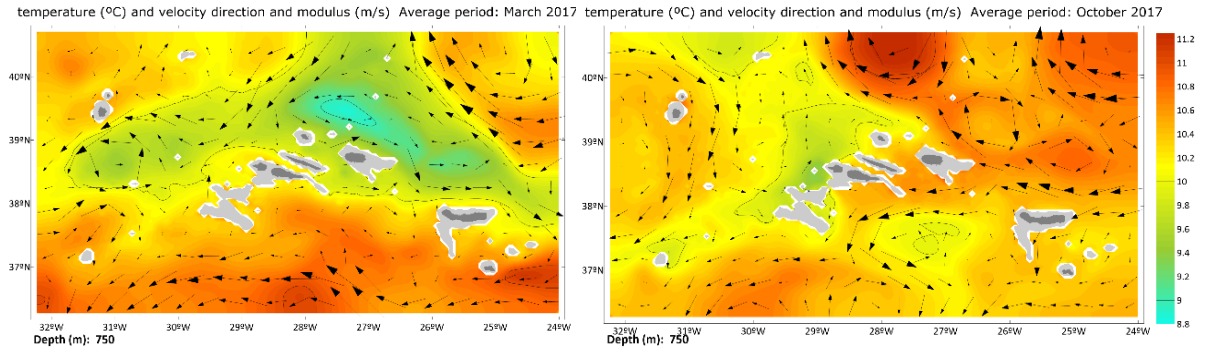

Figure 4.10- Monthly average of sea temperature and vectors representing velocity direction for March (on left) and October (on right).

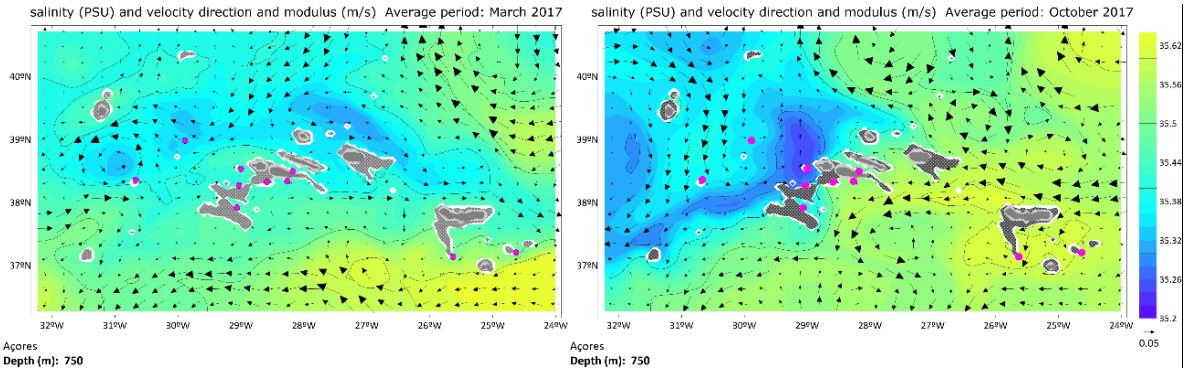

Figure 4.11- Monthly average of sea salinity and vectors representing velocity direction for March (on left) and October (on right).

Monthly averages of temperature and salinity (represented by colour), velocity modulus and direction (represented by vectors), at 750 meters depth, are represented in Figure 4.10, and Figure 4.11 respectively, revealing seasonal and spatial differences in water properties between March and October. During March, at 750 meters depth it is visible a major current from North to South-West, over the MAR. During October this current is less intense and particles are advected from the MAR to the CG. In the Central Group, the averaged ocean circulation consists of highly-variable along-shelf currents that follow bathymetric features, with a less pronounced velocity dynamic near the central group. Between the Central and Eastern Groups, the hydrodynamic patterns go mainly in the Eastwards direction during March, with low intensity, while in October it is clear a strong current coming from East, going South and Westwards.

4.4.4.2. Particles travel distance

Larvae can travel from a few kilometres to more than 400km. As travel distances are highly non-normal, histograms and median and the 95th percentile of dispersal distances are used for this analysis, rather than mean values, (Table 4.5). Maximum total travel distances are one order of magnitude larger than median distances.

Table 4.5- Particles travel distance for the different scenarios. Maximum distance (max); median distance (med) and percentile 95th

	Travel distance (kilometres)											
	PLD_15_March			PLD_30_March			PLD_15_October			PLD_30_October		
	max	med	P95	max	med	P95	max	med	P95	max	med	P95
Location L#1	221	14	126	375	43	207	152	16	73	325	33	138
Location L#2	285	18	107	462	44	220	179	15	77	334	32	195
Location L#3	75	8	36	146	16	58	97	7	34	192	15	51
Location L#4	83	8	39	186	15	53	132	10	43	314	18	71
Location L#5	128	10	55	326	19	80	158	10	61	359	26	168
Location L#6	205	10	50	436	21	132	196	14	61	385	26	128
Location L#7	127	9	40	254	20	87	108	9	42	341	20	98
Location L#8	69	8	38	270	15	55	85	7	39	286	16	63
Location L#9	118	10	47	264	22	97	176	27	86	406	50	148
Location L#10	113	11	59	218	24	96	168	11	55	345	23	162

Across all March and October scenarios, the longer PLD origins higher travel distances. Larvae travel distances can change both seasonality or spatially. During March release larvae from the WG locations (L#1) and (L#2) have higher travel distances than the remaining locations during (p95th of 207 and 200 km respectively).

The overall median particle transport distance In the CG, in all the tested scenarios median travel distances are lower than in the other groups (from 8 to 20km), which can contribute to higher self-recruitment levels. The October release contributes to higher travel distances. Besides the maximum travel distances registered. Most larvae (more than 50%) travel up to 25km with a PLD of 15 days. As is represented in histograms in Figure 4.12 and Figure 4.13. Only larvae from Mar da Prata release (L#9), show different behaviour. With a PLD of 30 days, 50% of the larvae travel up to 50 km (28% are reported in the first bin of 25 km, and 22% in the second bin (25-50 km)). These longer travel distances are related to the strong currents that occur in this region during October (Figure 4.9 b).

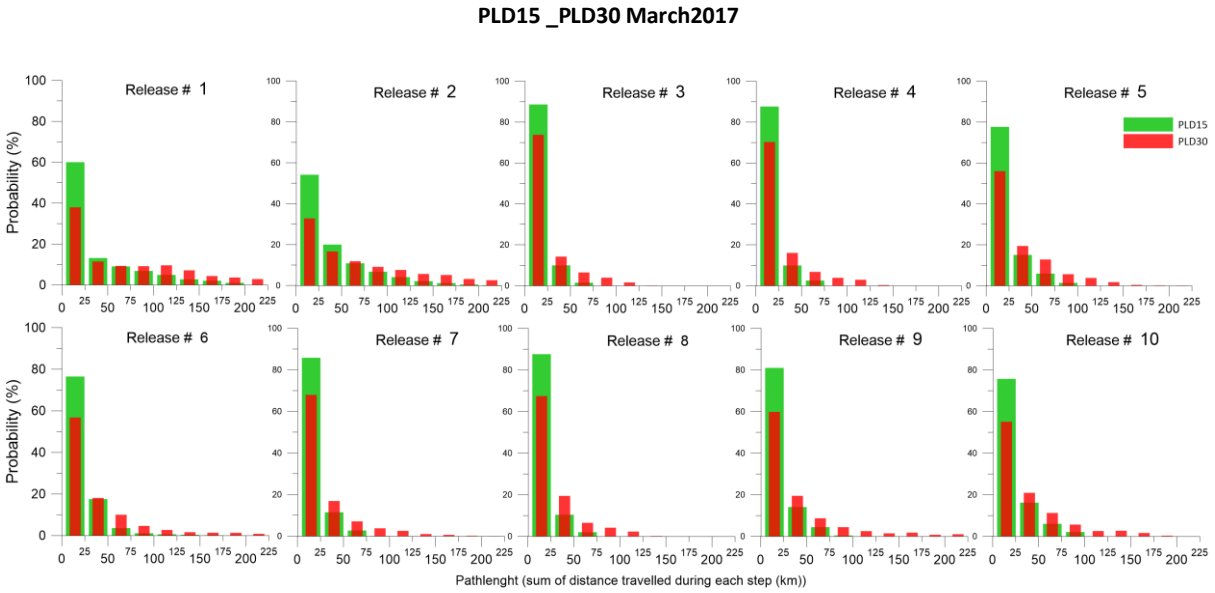

Figure 4.12- Histogram (in %) of the total travelled distance from each particle to the release point, in km, considering a PLD of 15 days in green, and PLD of 30 days in red for March release. Distances greater than 225 km were extremely rare and are not shown.

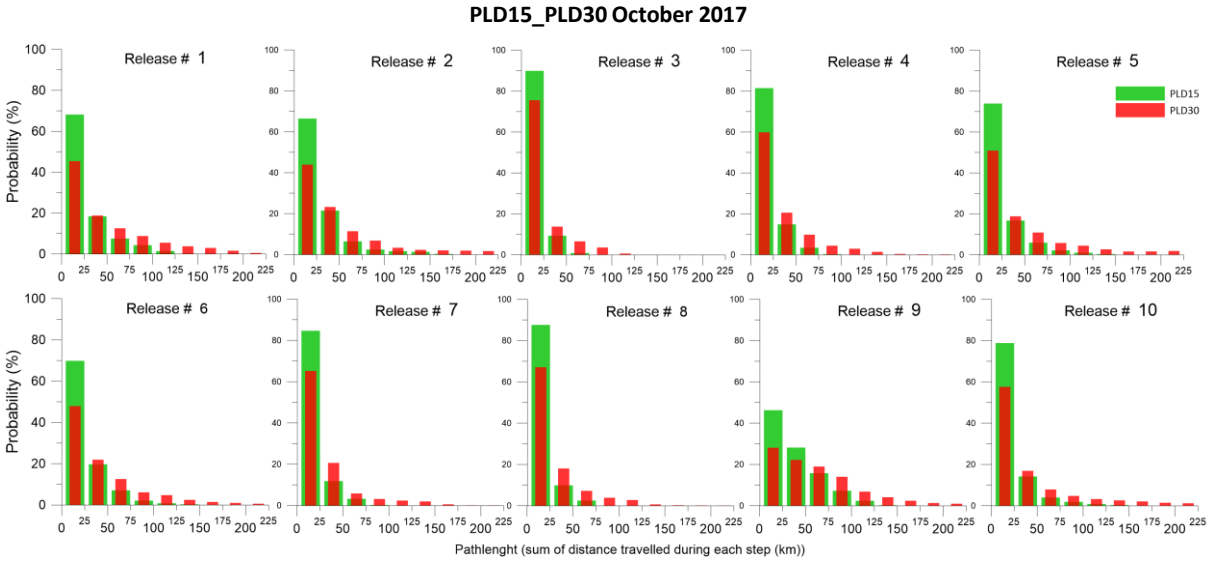

Figure 4.13- Histogram (in %) of the total travelled distance from each particle in km, considering a PLD of 15 days in green, and a PLD of 30 days in red for the October 2017 release. Distances greater than 225 km were extremely rare and are not shown.

4.4.4.3. Particles depth

Despite larvae travelling in different bathymetric ranges, they mostly remain in a bathymetric range near the depth release. In all the locations, except for Location L#1, larvae remain (>40%) in the bathymetric range of the release (Figure 4.15). Histograms of particles' depth along their trajectory are presented in Figure 4.14 for the March release, and

Figure 4.15 for the October release. In all the situations a longer PLD contributes to a wider distribution of particle depth along the water column.

Larvae vertical migration is not related to bathymetry. Can be related to the release location depth, and the local currents at the different seasonal simulations. As can be seen in Figure 4.16 where, at the same location, for the different scenarios particles are in different depths.

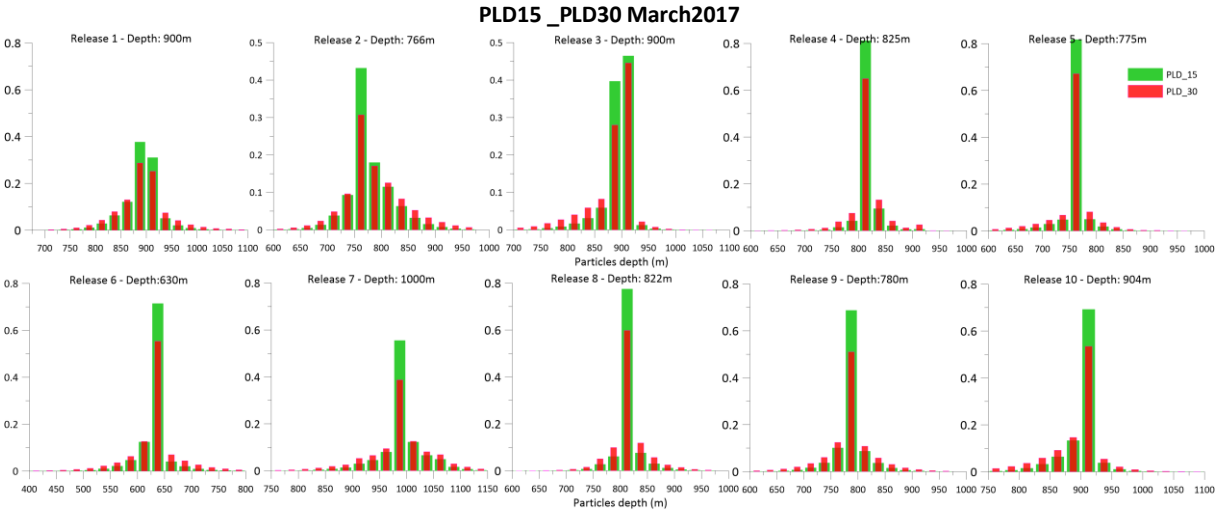

Figure 4.14- Histogram of the particles depth along their trajectory, for each location,for PLD15 days and a PLD30 for March 2017 release. The depth of the respective release is detailed in the top of each graph

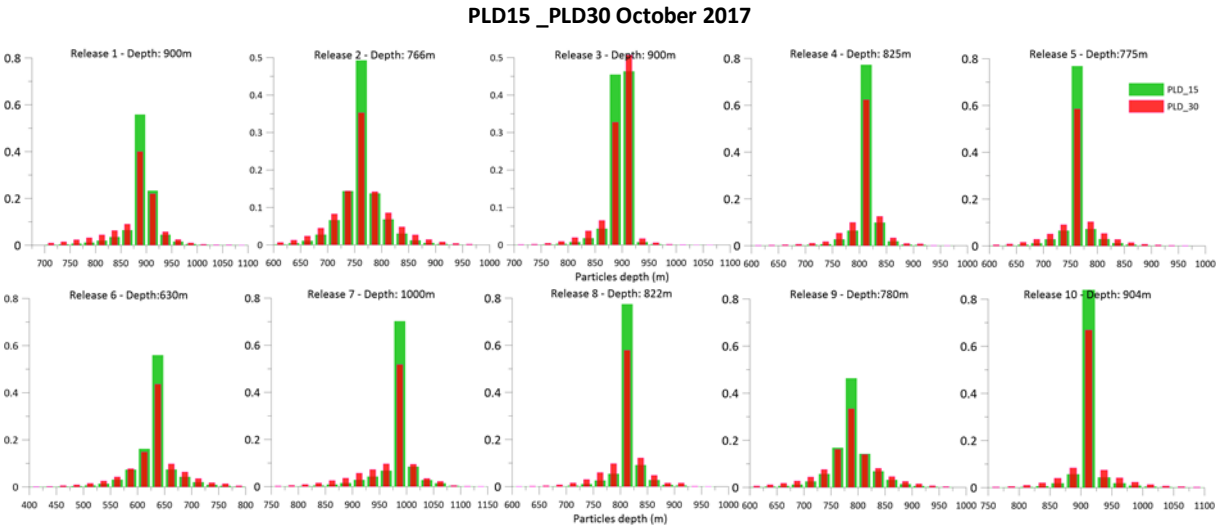

Figure 4.15- Histogram of the particles depth along their trajectory, for each location,for PLD15 days and a PLD30 for October 2017 release. Depth of each respective release is detailed in the top of each graph

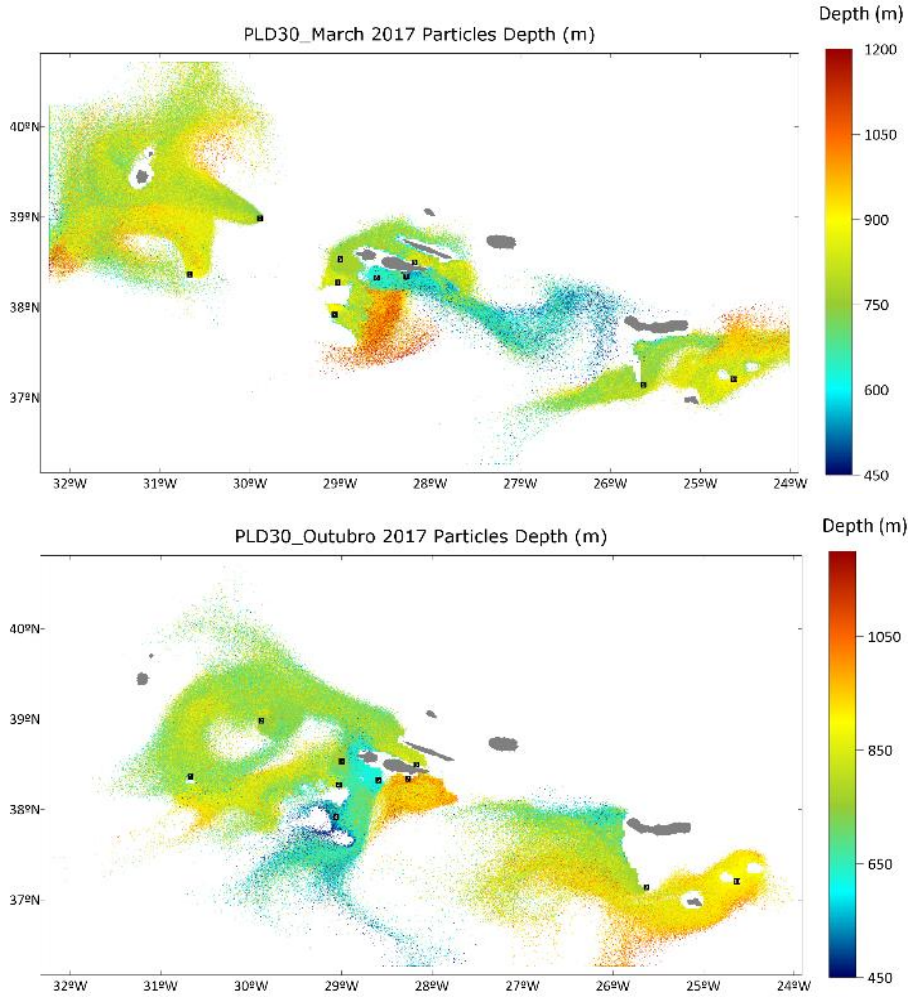

Figure 4.16- Particles depth along the entire release time for PLD 30 in March scenario (left) and October scenario (right), the colour scale represents particle depth ranging from 450 to 1200 meters depth.

This lower vertical migration is visible in particle dispersal between the CG and EG (Figure 4.16). In March particle's depth range from 450 to 750 m (particles from L#6 Figure 4.8), and in October from 600 to 1000m depth (particles from L#9). These particles' depth is related to the release location, and the hydrodynamic patterns at that moment, and not to the bathymetry.

4.4.4.4. Connectivity between sponge aggregations

Larvae dispersal originates different connectivity relations considering the PLD. PLD of 30 days (Figure 4.18) enables more connectivity between the different sponge aggregations than a PLD15 (Figure 4.17). Although, lower PLD (15 days), results in higher self-recruitment levels on L#1 (Cavala Seamount) and L#5 (Condor Seamount). Connectivity is illustrated by connectivity matrices, and also by connectivity arrows represented on the map (Figure 4.17 and Figure 4.18 for scenarios *PLD15_year_2017*, and *PLD30_year_2017* respectively). Matrices depict the percentage of self-recruitment and connectivity between different sponge aggregations.

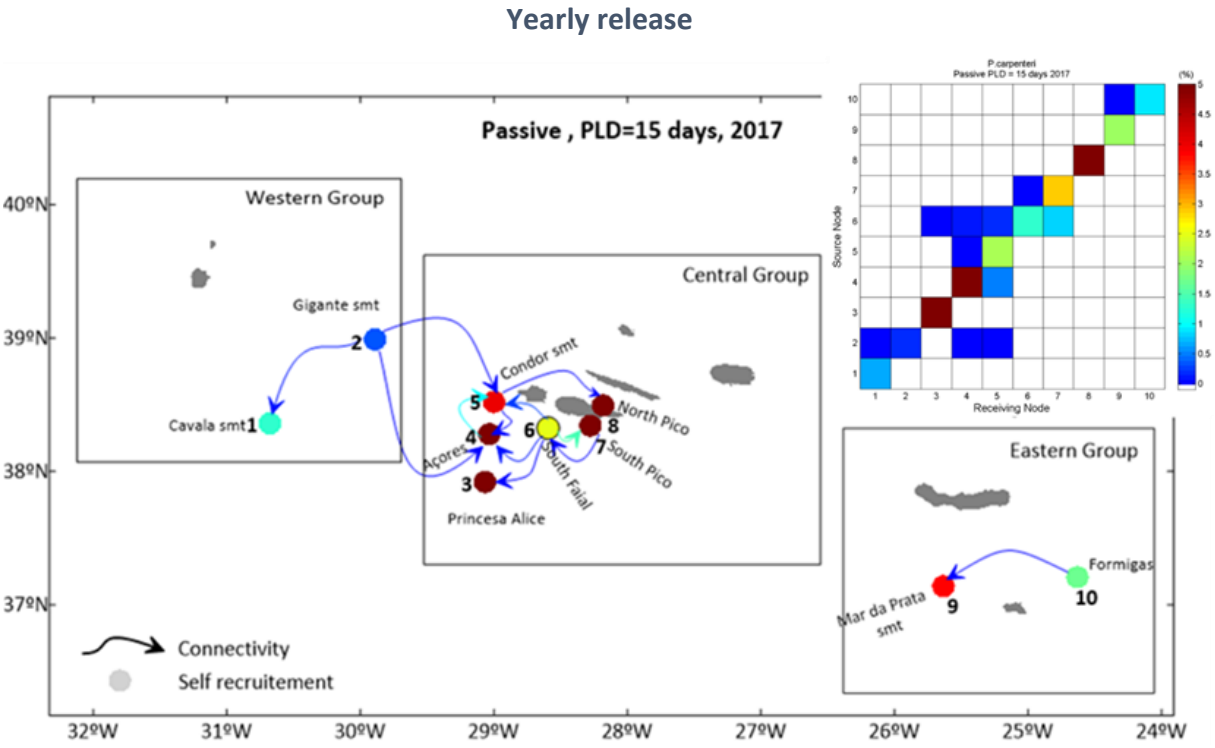

Figure 4.17-Map of connectivity relations, and respective connectivity matrix, for a yearly release (2017) with a PLD 15, connectivity arrows and auto-recruitment circle colours represent the percentage of settled particles.

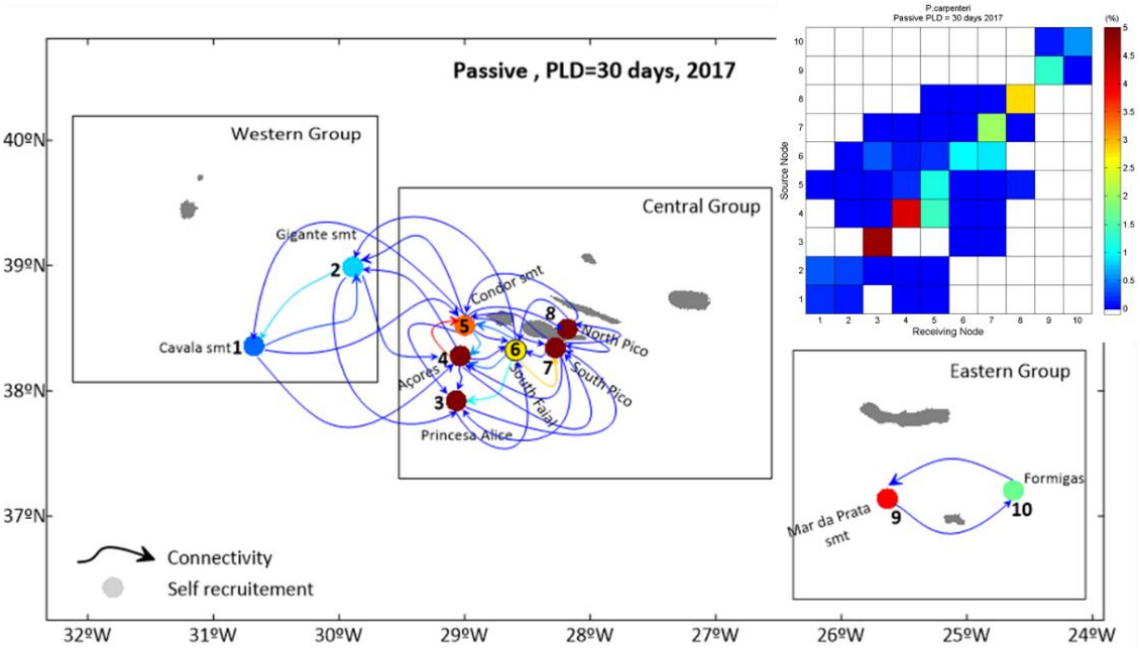

Figure 4.18- Map of connectivity relations, and respective connectivity matrix, for a yearly release (2017) with a PLD 15, connectivity arrows and auto-recruitment circle colours represent the percentage of settled particles.

In the scenario of PLD15, the connectivity among Gigante and Cavala Seamounts (L#1, L#2), is unidirectional, while in the scenario of PLD30 this connectivity is bidirectional. Moreover with PLD 30 Gigante seamount is connected not only with Cavala Seamount but also with sponge aggregations of the CG (Condor Seamount and Princesa Alice and Azores banks). In this scenario, the sponge aggregation North of Pico (#8) only receive larvae from the Condor seamount, while, in a scenario of PLD30 receives larvae from Condor and South of Pico, and its larvae can achieve several aggregations (Condor(L#5), South of Faial(L#6), and South of Pico(L#7)). The sponge aggregation in the South of Pico faces a similar behaviour, while in a PLD15 is only connected with the South of Faial, with a PLD30 it is connected with several sponge aggregations of the central group, but also with Gigante Seamount from the Western Group.

The connectivity between sponge aggregations of the central groups is much higher in a scenario of PLD30 days than in PLD15. There is no connectivity between the EG and the CG or WG, in both scenarios. In the WG the connectivity between Formigas (L#10) and Mar da Prata Seamount (L#9), is unidirectional, with a PLD of 15 days, and bidirectional with a PLD30.

The yearly release allows for analysis of all different spawning and hydrodynamic scenarios. However, deep-sea sponges spawning may have seasonality, related to phytoplankton blooms (Leys & Lauzon 1998). Seasonal analysis was performed for March and October releases.

Seasonal releases (March and October)

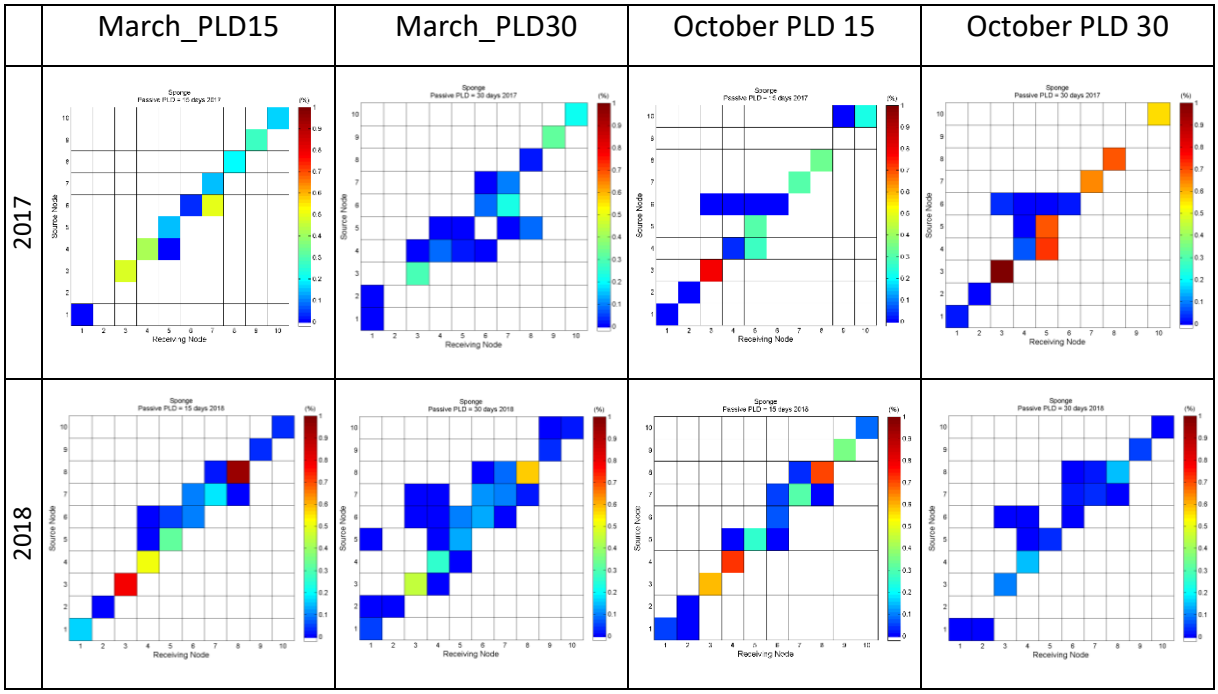

Figure 4.19- Connectivity matrices for the March_PLD15, March_PLD30, october_PLD15 and October_PLD30 for 2017on top and 2018 on bottom, connectivity and auto-recruitment colours represent the percentage of settled particles.

The hypothesis of a seasonal spawning release, occurring only for one month, in March and October, conducts to lower connectivity between the different sponge aggregations (Figure 4.19). Only in the scenario March_PLD_30_2018 was estimated connectivity between larvae from the CG and WG, between Azores bank, and locations L#1 and L#2. In the remaining scenarios, no connectivity was predicted between the different groups. In the CG connectivity between different sponge aggregations face seasonality. Also, the self-recruitment percentage is different from March to October, with the releases from CG presenting the highest self-recruitment percentage in October. The sponge releases from Açores Bank (L#4), Condor Seamount (L#5), and South of Faial (L#6) show connectivity with the other 3 sponge locations, in MarchPLD30 scenarios.

In different situations, Gigante seamount (L#2) doesn't have self-recruitment, nor connectivity with any other release, similarly to Mar da Prata seamount in *October_PLD30_2017*, indicating that this can be more vulnerable locations.

Particles settlement location

Besides the sponge aggregation locations in the study, particles can also settle in other regions of the domain within the defined bathymetric range of 600 to 1000 meters in depth. Seasonal dynamics can induce different settlement positions. This difference is evident in the settlement locations in the EG, and along the MAR, where larvae from different populations settle in different locations (Figure 4.20 for March and Figure 4.21 for October release).

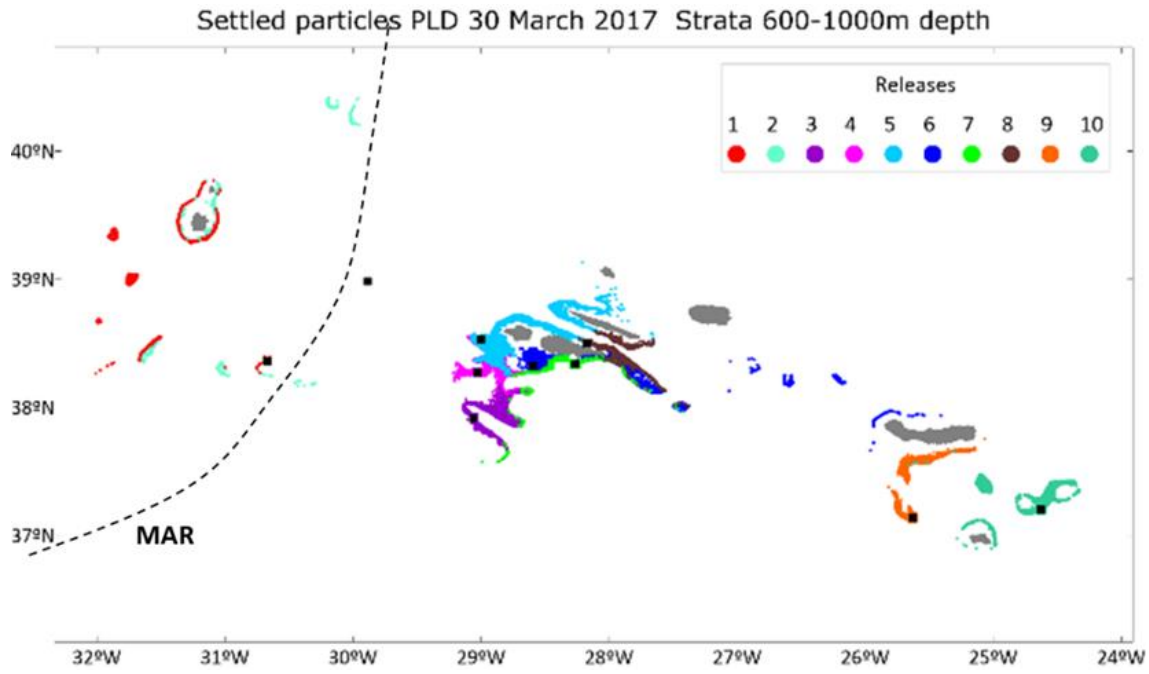

Figure 4.20- Location of settled particles, in the entire domain, in between the bathymetric range of 600 to 1000m depth, for March release. Different colours represent different releases

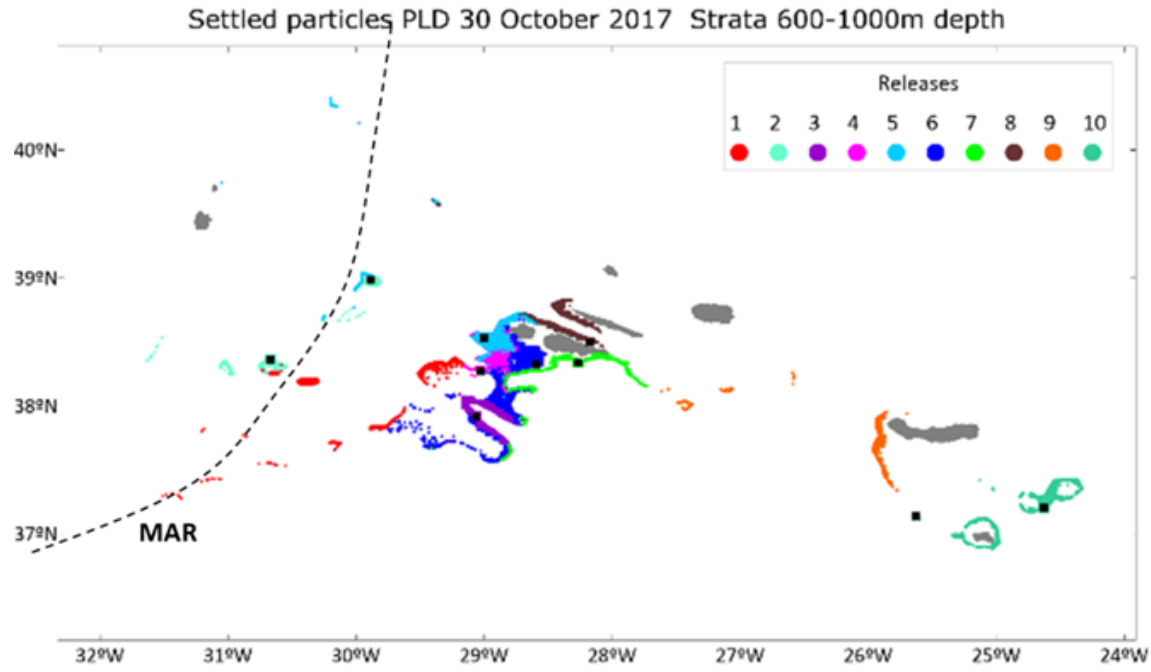

Figure 4.21- Location of settled particles, in the entire domain, in between the bathymetric range of 600 to 1000m depth, for October (right). Different colours represent different releases

In the CG, induced by the higher number of releases, there is a higher number of settled particles. During October there is connectivity between WG and CG. Larvae from Cavala seamount (L#1) can settle in the CG, and from Condor seamount L#5 (in blue) can settle along the MAR, while in March do not. Results also show that between CG and EG exists a location where particles can settle. During March settled particles are from the South of Faial (L#6), while during October from Mar da Prata (L#9).

4.4.5. Discussion

Larval dispersal is an important ecological process (Ross et al. 2020). This is of particular importance for deep-sea sponges, as they are sessile organisms throughout their adult life (Cowen & Sponaugle 2009). *Pheronema carpenteri* rely upon the larval dispersion for colonizing new areas, and for population dynamics and persistence (Ross et al. 2020).

Pheronema carpenteri larvae were modelled as passive tracers, similarly to other modelling studies on deep-sea sponges larvae dispersal (Kenchington et al. 2019, Swearer et

al. 2019). Because particles are advected through the hydrodynamic conditions, it is required an accurate (Ross et al. 2020) high-resolution hydrodynamic solution and a calibrated lagrangian model, to assure that particle dispersal can provide reliable dispersal patterns (North et al. 2009). Regarding this, calibration tests were performed to determine the correct number of particles to use for this case study.

The FUV method (Simons et al. 2013), indicates that the most efficient number of particles was 150000 particles per month, per release. Sponge locations at MAR (L#1 and L#2,) reveal a higher FUV, requiring a higher number of particles to produce a valuable result. This can be a consequence of their higher dispersal travel distance (Table 4.5). Moreover, the dispersal pathlength saturation method indicates 100000 as an efficient number of particles to produce an accurate result. In this situation, the higher number of particles (150000) was chosen. However, this decision is always a compromise between computational time and result accuracy (Jones et al. 2016), and in this case, it was possible to choose the higher number of particles: 150000 per month per release.

The pelagic larval duration (PLD) is one of the most relevant parameters when applying the larvae dispersal model (Henriksen et al. 2003, Howell et al. 2016, Wang et al. 2021).

Results of this study corroborate the common assertion regarding the positive relation between PLD and dispersive capabilities in marine organisms larvae (Holstein et al. 2014). Results show that longer PLDs generate higher dispersal patterns, higher travelled distances and consequently higher particle exchange between different sponge aggregations.

All the hypotheses in the study, PLD15 and PLD30, and different seasonal releases allow the study of a wider range of scenarios and biological hypotheses.

Connectivity and self-recruitment

Model results for seasonal releases (March and October) show that apart from Gigante Seamount (L#2), and Mar da Prata Seamounth (L#9), all the other locations have self-recruitment, locally retaining a proportion of their larvae. Contrariwise, Gigante seamount and Mar da Prata populations can be more vulnerable, by the absence of self-recruitment. Gigante seamount is located in a highly hydrodynamic region, over MAR, under the influence

of strong hydrodynamic patterns (Figure 1.9) that contribute to a higher particle dispersal away from the recruitment area.

Dispersal results show that sponge aggregations at the Eastern Group (EG) are isolated from the others, not revealing any exchange of particles (no connectivity) among other sponge aggregations in the study, due to their distance to the other sponge aggregations in the study. During the October release, the connectivity can also be constrained by the stronger currents between CG and EG.

The yearly release was performed to analyse the potential connectivity between all the sponge aggregations, considering more scenarios than the March and October spawning. This hypothesis can serve as a "big picture" of a potential (optimistic) connectivity scenario. The connectivity matrices for this yearly release, (Figure 4.17)reveal higher particle exchange between the sponge aggregations. In the CG, with PLD30, most of the locations are connected. However, most of these connectivity levels are lower, with less than 0.75% of larvae supply (Table A1 in ANNEXX 2), and the self-recruitment range from 0-4%. When considering PLD15, which is the most consensual PLD for deep-sea sponges larvae (Maldonado 2006, Wang et al. 2020), the yearly scenario shows higher self-recruitment percentages, from 0 to 5.4% (maximum in L#4 Açores Bank) however with fewer particles exchanged between different releases. This self-recruitment maintains the population, but it is disadvantageous if the population is impacted.

Sponge aggregations from CG can also be connected with MAR. This connectivity is bidirectional, between Cavala Seamount, Açores bank, and Condor Seamount. Particles from the Gigante seamount can settle in Princesa Alice, Açores Bank, and in the Condor seamount. These results point out that these 3 locations: Princesa Alice, Açores Bank, and Condor Seamount are sink and source locations.

Scenarios with 15 days of PLD indicate that sponge locations North and South of Pico are not connected in 2017, but they are in 2018. This shows how the system is dynamic, and how the hydrodynamic patterns can have different patterns from one year to another. Nevertheless, this can also be a consequence of model resolution (6km), and the proximity of these two sponge aggregations, considering the model resolution. Maps of particle distribution (Figure 4.8) shows how dynamic is this region. L#7, North of Pico, located in the

channel between Pico and São Jorge islands, reveals high dynamic dispersal patterns, being advected in towards East on March (Figure 4.9), and towards West on October. Only a higher model resolution or a multiyear analysis would provide more information to better study the connectivity between these two locations.

Particles vertical migration

Major circulation patterns promote larvae dispersal in the deeper layers. Larvae, do not achieve the surface layers. This can be related to the lower vertical currents, and lower velocity patterns, typical of the bottom layers (Figure 4.10). This demersal larval behaviour was reported in other deep-sea dispersal studies and might be related to larval behaviour in searching for potential recruitment areas in their suitable bathymetric range (Young et al. 2012).

Temporal and spatial variability

Particle dispersal patterns reveal high variation along space and time, as a consequence of high dynamic oceanographic conditions in the region. During March, the domain is under the influence of a strong current, over MAR, with strong velocities at 750 meters until 1000 meters depth (Figure 4.9). A temperature gradient, with lower water temperatures, is also visible, creating a strong hydrophysical barrier, avoiding any particle to cross between MAR and CG. By the influence of the meanders of this current, particles from Gigante Seamount (L#2) are advected away from this recruitment area, avoiding any self-recruitment in this sponge ground during Spring scenarios. Conversely, these hydrodynamic patterns form an eddy, originating particle exchange between Gigante and Cavala seamounts.

In October, hydrodynamic patterns are different, inducing particle exchange between MAR and CG. Between CG and EG the high-velocity currents, and consequent formation of an eddy, creates a hydrodynamic barrier between these two groups blocking particle exchange. Contrasting with the eddy identified in March over MAR, this eddy does not contribute to particle retention, but the opposite, avoiding particles to cross that area. This eddy is characterized not only by the velocity patterns but also by a demarked gradient of water temperature (Figure 4.10), creating a strong hydrodynamic and physical barrier.

Contrasting with strong currents that can transport particles out of the domain, or for regions without suitable recruitment areas, near the islands and seamounts, the lower velocities induce higher particle retention inducing higher connectivity between different release locations.

Results show that larvae can travel up to 225km distance, with 30 days of drifting duration. However, particles from Princesa Alice seamount don't travel more than 100km. This lower travel distance can be a consequence of the lower velocities in this region, that also induce a higher percentage of self-recruitment.

All these results highlight the seasonal and spatial variability of the hydrodynamic patterns around the archipelago, responsible for the generation of highly spatiotemporally-variable submesoscale patterns that influences larval dispersal, revealing the importance of studying different spawning scenarios.

Model

The model resolution, 6km*6km, does not allow the dispersal analysis at a seamount level, nor how connectivity can change along the slope of one island. This analysis would require a downscaling or a higher resolution hydrodynamic model (North et al. 2009). This limitation is denoted on L#8, North of Pico, but justified by the model resolution. Nonetheless, the model reflects the seamounts and islands' effects on a regional scale, simulating the lower velocities in the seamounts (Giacomello & Menezes 2012, Lima et al. 2020). These lower velocities induce connectivity in these areas, as it is visible in larval dispersal within the region, enhancing particles' retainment, higher levels of connectivity between different sponge aggregations, also higher levels of self-recruitment. The percentage of connectivity depicted on the connectivity matrices (Figure 4.19) reflects these dynamic oceanographic patterns in the regions. Connectivity results show that sponge locations from the central groups are highly connected.

This high exchange and retention of larvae is a particularly important process for ecosystem resilience, also indicating the retention of other deep-sea species like cold water corals (CWC) that inhabit these deep-sea regions in the Azores (Bode et al. 2019, Swearer et al. 2019).

The different larvae exchange between different groups (MAR and CG), contributes to the persistence of these populations, mitigating the risk of recruitment failure (Cowen & Sponaugle 2009, Wang et al. 2021). Furthermore, this higher exchange of larvae would enhance genetic diversity conferring greater resilience to the population (Holstein et al. 2014).

Results point out a higher vulnerability of Mar da Prata, due to the absence of a permanent self-recruitment, and low connectivity patterns between the populations in the study.

Two of the deep-sea sponge aggregations in the study are localized in an MPA, Princesa Alice and Condor Seamount. Particle dispersal results indicate that these two regions are receiving larvae from other locations, being connected with them. This connectivity prompts their persistence and improves the resilience of these habitats (Combes et al. 2021).

Larval dispersal patterns, show the presence of a potential larval connectivity corridor between CG and MAR, Figure 4.8. Furthermore, the distribution of settled particles away from the selected recruitment in the study, shows that between CG and EG, there is a location point where larvae from South of Faial (L#6) settle in March, and larvae from Mar da Prata seamount in October. This location is the Joao de Castro bank, an area also classified as a MPA. This result suggests that this area can be connected with the CG and EG sponge aggregations. However, this exchange of particles depicts a low connectivity potential. A further study considering this location would provide a better analysis.

Also, the use of genetic connectivity studies, and species distribution models can provide a further multi-analysis approach and a better understanding of deep-sea populations connectivity (Kenchington et al. 2019, Swearer et al. 2019, Puerta et al. 2020, Combes et al. 2021). Additional data about these deep-sea organisms and their biology (mortality, larval spawning, and larval behaviour) would contribute to a more detailed analysis.

4.4.6. Partial conclusions Case study 1

The findings of this work estimate the existence of physical connectivity between *Pheronema carpenteri* sponge aggregations in the Azores. The methodology applied, using a

biophysical particle model application, was able to simulate larval dispersal in the Azores region, and to study different scenarios of connectivity among 10 *Pheronema carpenteri* sponge aggregations in the Azores.

Major results indicate that sponge aggregations from the Central Group can represent a significant source and sink larvae locations nursery for *P. carpenteri* sponges in the Azores, by receiving larvae from different sponge aggregations.

Condor Seamount can exchange larvae with Cavala seamount, in MAR Group. Princesa Alice has high particle retention receiving larvae from several sponge aggregations, serving as sink aggregation in the Azores. These results reinforce the importance of maintaining the protection efforts in the MPA (Condor and Princesa Alice), once they are important recruitment areas. Açores bank, South of Faial, and South of Pico also exchange particles among different aggregations, potentially inducing higher resilience through the exchange of larvae from multiple populations.

Nonetheless, Mar da Prata seamount (EG) can be more vulnerable sponge aggregations, because they don't have self-recruitment, as shown in all the tested scenarios., and have low connectivity with the other sponge aggregations in the study.

There is no connectivity between sponge aggregations of EG with CG, however, results show potential connectivity from both groups with João de Castro seamount pointing out a possible interconnection between these groups. Model results also point out some other retaining areas, that might indicate other sponge aggregations not included, and that should be matched with the new data available from recent cruises.

The pelagic larval duration can be crucial for population connectivity. A PLD of 15 days can contribute to a higher fragmentation of the *P. carpenteri* populations in the study area, while the connectivity resulting from a PLD of 30 days would ultimately regulate populations' persistence and recovery after disturbance (Cowen & Sponaugle 2009). More information regarding deep-sea sponges biology or larval behaviour would provide essential data for more detailed studies.

Furthermore, this modelling approach can provide valuable information for the implementation of protection plans and the establishment and prioritization of future management plans.

4.5. Case Study 2- *Chaceon Affinis*

4.5.1. Introduction

Chaceon affinis is a deep-sea red crab (DSRC) that inhabits various substrata on continental slopes, seamounts and deep-water banks in the northeast Atlantic (Castro et al., 2010; Gonzalez et al., 1998). Widespread throughout the world, several DSRC species are species of interest to fisheries such as, e.g., *Chaceon quinquedens* Smith, 1879 and *Chaceon fenneri* (Manning and Holthuis, 1984) (Tuset et al. 2011).

C. affinis has been considered a candidate for further exploitation in European waters (Pinho et al. 2001, Santos et al. 2019). However, despite the growing interest in the exploitation of crab resources, in the Azores fishery exploitation of the *C. affinis* is discouraged (Santos et al. 2019). Further scientific studies to guide management and define sustainable levels for the exploitation of these resources, are necessary. The use of modelling tools to study larval dispersal of this species in the Azores region can provide additional information about recruitment mechanisms, and population connectivity, supporting further scientific studies.

Several studies regarding *C. affinis* were developed in the Macaronesia and other Atlantic areas (Guerao et al. 1996, Weinberg et al. 2003), particularly in Gorringe Bank (Hilário & Cunha 2013) and the Azores region (Pinho M. et al. 2020, Santos et al. 2020), focused mainly on ecological characteristics, fishing dynamics and describing the biology and population dynamics Different reproductive parameters have been studied previously for *C. affinis*, including size at first maturity, sex ratio and fecundity (Abellan et al., 2002; Fernandez-Vergaz et al., 2000; Tuset et al., 2011), but important questions related to mating behaviour, larvae behaviour, synchrony and seasonality remain unanswered.

4.5.1.1. *Chaceon affinis*

C. affinis inhabits continental and island slopes, seamounts, and deep-water banks, at a depth of 400–1500 meters in the northeastern Atlantic, from Iceland to Senegal (López-Abellán et al. 2002; Sampedro et al. 2001), including Macaronesia and other Atlantic areas (Guerao et al. 1996, Pinho et al. 2001, Weinberg et al. 2003, Hilário & Cunha 2013, Landeria & Tamura 2018).

In the Azores, the high abundance of *C. affinis* was reported between 700 and 900 m depths (Pinho et al., 2001). Segregation by sex, related to depth, was reported, with the dominance of males occurring at depths up to 800 m, while females between 800 and 1000 meters depth (Pinho et al. 2001, Biscoito et al. 2015). The presence of females in deeper areas may be related to seasonal downward movements of ovigerous females (López Abellán et al. 2002, Santos et al. 2019). The upper bathymetric distributions of C*. affinis* might also be related to the presence of *Cancer bellianus*, a predator, that inhabits shallower depths, creating a border of competition at around 500–600 m depth, where larger males of *C. affinis* exist maintaining the area of distribution and isolating reproduction and recruitment zones (López Abellán et al. 2002).

In the Azores *C. affinis* shows a clear aggregate distribution ("patches"), possibly reflecting the preference for specific habitats, e.g. muddy bottom with some rocks. (Pinho et al, 2020).

Like most deep-water species, deep-sea crabs present k-strategist life traits, characterized by exhibiting slow growth, long life cycle, late maturity (5–15 years), low fecundity, irregular recruitment and often very low resilience which makes them highly vulnerable to overfishing (Guerao et al. 1996, Da Silva Cortinhas et al. 2022). Therefore, a good knowledge of their early life-history dynamic and reproductive strategies is crucial to better understanding the vulnerability of DSRC stocks, and define strategies for species protection and implementing guidelines for sustainable fishery management (Santos et al. 2019).

Regarding the spawn frequency, studies suggest that females spawn, probably every 2 years (Stevens & Guida 2016). In the Azores, *C. affinis* ovigerous females were found between October to March, with the peak of spawning activity occuring during the autumn and winter (Pinho et al. 2001). In the Madeira islands, ovigerous females were found from October to April, and all year round in the Canarias (Biscoito et al. 2015). Also, Tuset et al. (2011) observed ovigerous females in the last developmental stage during all quarters of the year. These studies suggest that gonad maturation and release of larvae are asynchronous throughout the spawning season (Tuset et al. 2011, Biscoito et al. 2015). The number of eggs in *C. affinis* can range from 200 000 to 600 000 eggs, with six development stages. (Tuset et al. 2011)).

4.5.1.2. Larvae biology

C. affinis larvae are released in the water column (Landeria & Tamura 2018), the larvae phase is pelagic and consists of four zoeal stages and a final megalopa (Tuset et al. 2011). At the end of the PLD, megalopae descend looking for suitable habitat to settle, and recruitment of juveniles takes place in deep waters (~1000 m) (Wigley et al., 1975; Wahle et al., 2008; Stevens & Guida, 2016). Larvae are planktotrophic (Sulkin & van Heukelem 1980), with vertical swimming behaviour (Rivera 2018).

Guerao et al.,1996 described the morphology of the first zoa stage of *C. affinis* evidencing no differences in larval morphology between different species of Chaceon. So, in the absence of more information considering this species, information about other species from the same family can be advantageous. Other species from the same family, namely *C. quinquedens*, which is widely distributed throughout the western Atlantic, from Nova Scotia to South Carolina, have been the object of several studies considering larval behaviour (Kelly et al. 1982, Martínez-Rivera & Stevens 2020). The PLD varies considerably, being as short as 23 days or as long as 125 days (Kelly et al. 1982).

Table 4.6- Location, depth, and biology characteristics (f pelagic larvae duration, spawning seasonality, larval development and number of larvae stages)

Species	Location	Depth range (m)			PLD (days)	Seasonality Ovigerous females	Spawning seasonality	Larval development	Nº larvae stages
		all	Female	Male					
Chaceon Affinis	North/North east Atlantic	140-2000 a)				Spring g); October to May e); All year a); March-April e);	- all year round a); -peak in winter and autumn c); -peak in March and Summer i)	Planktotrophic a)	4 Zoeal + megalopa a)
	Azores	400-1500 b), d), e); higher density:700-900 c)	800-1000; c) ;h)	<800 c), h)					
	Canaries & Madeira	600-1000							
Chaceon quinquedens	Western Atlantic	200 – 1000 h); f)			23-125 h)		Seasonal	Planktotrophic f)	4 Zoeal + megalopa h)
Chaceon bicolour	Western Pacific	200 – 1620 f)					Continuous		
Chaceon fenneri	Western Atlantic	200 – 1500 f)					Seasonal		
Chaceon maritae	Eastern Atlantic	200 – 950 f)					Continuous		

a)- Tuset et al., 2011; b) Biscoito et al., 2015; c) Pinho et al., 2001; d) Biscoito et al., 2015; e) López Abellán et al., 2002; f) Guerao et al., 1996; g) Hilário and Cunha, 2013; h)Kelly et al., 1982; i)Landeria and Tamura, 2018

Despite not inhabiting the Azores region, *C. quinquedens* is a deep-sea crab distributed from 200m to 1500m depth, larvae are hatched in water temperatures from 6 to 10ºC, and can cross thermocline while swimming up to the surface, where can survive in temperatures up to 24ºC. *In-situ* experiments on *C. quinquedens* larval behaviour, performed by Kelly et al., 1982, confirm that in the first development stage larvae show a strong negative response to gravity, with a swimming behaviour able to cross thermoclines (Table 1.8) (Kelly et al. 1982).

Table 4.7-Mean number of days for Chaceon *quinquedens* larvae from hatching to successive moults during larval development at 10º, 15º and 25ºC, values obtained from a study performed by Kelly et al 1982

Stage	Number of days from hatching up to the successive zoe at different temperatures		
	10ºC	15º	25ºC
Zoe I	30	17.2	7.2
Zoe II	60	33.8	11.5
Zoe III	99	52.5	18
Zoe IV	125.4	81	23.3

Table 4.8-Mean swimming rate estimated by Kelly et al 1982, for Chaceon *quinquedens* larvae, during larval stage I zoe, at different temperatures. Kelly et al., 1982

Water temperature (ºC)	Mean swimming rate (cm/s)
11	1.4
11-15	1.7
15	1.7

4.5.2. Model setup

4.5.2.1. *Chaceon affinis* locations

The study area covers the Azores archipelago. The *C. affinis* populations considered in this study, based on different data sources and studies (Santos et al., 2019 and Kaschner et al. 2019), are located in different seamounts, banks, and around the islands (Figure 4.22), Table 4.9.

.

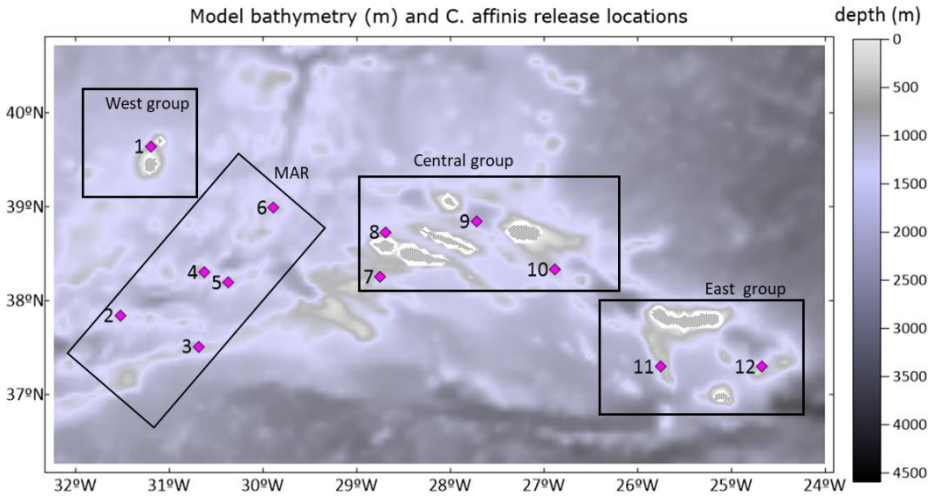

Figure 4.22- *Chaceon affinis l*ocation considered in this case study, locations based bibliography (Santos et al., 2019 and Kaschner et al. 2019), and grouped in different groups for better results discussion.

Table 4.9- Populations considered in this study, Release number, name, group name, location and depth.

Release number	Population name/location	Group	Longitude ºW	Latitude ºN	Depth (m)
L#1	Flores	West group	-31.2	39.64	800
L#2	Menez Gwen	MAR	-31.525	37.8417	950
L#3	Voador Seamount	MAR	-30.69	37.51	820
L#4	Cavala	MAR	-30.63	38.3	800
L#5	Ferradura	MAR	-30.37	38.19	910
L#6	Gigante Seamount	MAR	-29.89	38.99	900
L#7	Açores bank	Central group	-28.75	38.25	900
L#8	North of Faial	Central group	-28.69	38.728	1060
L#9	North of São Jorge	Central group	-27.7738	28.73075	1050
L#	South-East of Terceira	Central group	-26.89	38.33	828
L#11	Mar da Prata	East group	-25.7575	37.295	950
L#12	Formigas	East group	-24.675	37.295	1000

4.5.2.2. Model configuration

In this model implementation, each *C. affinis* population is defined as a release location, characterized by a position (longitude, latitude and depth), being also a recruitment area, defined by a polygon. Particle dispersal are computed with different behaviours and not only with a passive behaviour. Specifically, swimming behaviour surface-oriented, bottom-oriented, with a variable swimming velocity depending on water temperature.

Larval Behaviour

Considering larval behaviour, Chaceon larvae have different behaviours during the 5 larval stages (Tuset et al. 2011), with swimming capability achieving the surface (Tuset et al. 2011, Landeria & Tamura 2018). The biophysical model will simulate this swimming behaviour.

In the absence of detailed information about *C. affinis* larvae behaviours, modelled behaviours were based on, *Chaceon quinquedens*, another deep-sea red crab species, from the same subfamily (Kelly et al. 1982). Larval PLD and swimming behaviour are detailed in Table 4.7 and Table 4.8 respectively.

Lagrangian particles simulate these behaviours at different development stages, with a swimming behaviour surface-oriented during the first development stage (with a swimming velocity water temperature related), and swimming behaviour bottom-oriented in the last development stage and megalopa. In the absence of more detailed data available about larval behaviour, passive behaviour was assumed during development stages II, III and IV, similarly to other model approaches of deep-sea larvae (Ross et al. 2017).

Number of larvae

Based on the number of eggs of this species (199,690–566,956 eggs) (Tuset et al. 2011), a total of 396,800 particles (larvae) were released, per month for each location, within an interval of 800 particles every 90 minutes during 31 days (1 month). This number was tested in the model calibration step and is a representative number of larvae for one unique female specimen, so, substantially lower than the real larvae number. However, in the modelling language, this number represents a proportional rather than complete representation of potential larval dispersal and fate (Ross et al. 2017).

Larvae mortality is computed following the half-life concept (the time it takes half the population to die) likewise other deep-sea larval dispersal studies (North et al. 2009, Paris et al. 2013).

Simulations were set for two different seasonal scenarios in 2017, detailed on **Error! R eference source not found.**, with one monthly release during March, and another during October, to cover different spawning seasons reported for this species (Hilário and Cunha, 2013;

López Abellán et al., 2002; Pinho et al., 2001). The larvae were released at a regular interval, every 90 minutes, to capture the full range of potential larval trajectories within this period (Ross et al. 2016). Several PLDs were considered to cover different larval reproductive behaviours (based on literature

To study the connectivity between populations, each one is defined by a polygon, where larvae can settle. The 12 release locations in this study are also recruitment locations, and the settlement depth was defined between 800m to 1200meters depth (Pinho et al. 2001, Santos et al. 2019).

The general model configuration of this case-study is summarized in Table 4.10.

Table 4.10- Biophysical model configuration for case study 2

Model parameter	Parameter description
Hydrodynamic model resolution	6*6km
Model time step	7200 seconds
Number of release points	12
Release depth	Sea bottom
Number of larvae per release	396800/month (Tuset et al. 2011)
Release time step	7200 seconds
Behaviour	Several behaviours (Table 4.11)
Mortality	Half-life (North et al., 2009; Paris et al., 2013
Strata	800 to 1200m
Scenarios	Several considering PLD and seasonality and behaviours (Table 4.12)

4.5.2.3. Scenarios

Different scenarios were studied considering the PLD and spawning seasonality and different larval behaviours (Table 4.11) reported for this species (based on Guerao et al., 1996; Kelly et al., 1982, Landeria and Tamura, 2018). Table 4.12 summarize the scenarios in the study.

The different behaviours in the study are:

i) **Behaviour_1**- mimics the behaviour reported for *G. quinquedens*, with a swimming behaviour surface-oriented during the first larval stage and a swimming behaviour bottom

oriented in the last stage, with lower activity than during the first stage (Kelly et al. 1982), and a passive behaviour during stages 2, 3, and 4;

ii) **Behaviour_2** differs from Behaviour_1, with a different swimming velocity in the last stage, based on the measured sinking rates (Kelly et al., 1982). Also with passive behaviour during stages 2, 3, and 4;

iii) **Behaviour_3 (Passive behaviour)** larvae are passive during the entire PLD, following the most common approach to deep-sea larvae modelling (Ross et al, 2019).

Table 4.11- Swimming velocity and direction surface-oriented, bottom-oriented or passive) and swimming velocity in the different larval stages and megalopa (* refers to data based on Kelly et al., 1982)

	Behaviour _1			Behaviour _2			Passive_behaviour		
Larvae development stage	zoe1	zoe2 + zoe 3	zoe 4 + megalopa	zoe1	zoe2 + zoe 3	zoe 4 + megalopa	zoe1	zoe2 + zoe 3	zoe 4 + megalopa
PLD- cumulative days	15	90	125	15	90	125	15	90	125
	7	53	81	7	53	81	7	53	81
	7	18	23	7	18	23	7	18	23
Behaviour	surface oriented	passive	bottom oriented	surface oriented	passive	bottom oriented	passive		
velocity (m/s) (15ºC)	0.014	---	0.0014	0.014	---	0.02	---		
velocity (m/s) (11ºC)	0.017	---	0.0017	0.017	---	0.02	---		

Table 4.12- Scenarios considered in this study, for March 2017 (on left), and October 2017 (right), PLD and behaviours

	Scenario	PLD (days)
Release date: March 2017	March_PLD_23_Behaviour 1	23
	March_PLD_81_Behaviour 1	81
	March_PLD_125_Behaviour 1	125
	March_PLD_23_Behaviour 2	23
	March_PLD_81_Behaviour 2	81
	March_PLD_125 Behaviour 2	125
	March_PLD_23_Passive	23
	March_PLD_81_Passive	81
	March_PLD_125_Passive	125

	Scenario	PLD (days)
Release date: October 2017	October_PLD_23_Behaviour 1	23
	October_PLD_81_Behaviour 1	81
	October_PLD_125_Behaviour 1	125
	October_PLD_23_Behaviour 2	23
	October_PLD_81_Behaviour 2	81
	October_PLD_125_ Behaviour 2	125
	October_PLD_23_Passive	23
	October_PLD_81_Passive	81
	October_PLD_125_Passive	125

4.5.2.4. Model calibration

The number of particles to use in the model was calibrated using the dispersal pathlength saturation method. Calibration results show that a release of 360 000 particles, the percentage

of particles in each 2km bin doesn't reveal any abrupt fluctuation, resulting in a smoother line, representative of a dispersal pathlength saturation for all the release locations (Figure 4.22). Therefore it was considered a total number of 360000 particles per location per month.

4.5.3. Results

4.5.3.1. Larval dispersal

To study *Chaceon affinis* larval dispersal different scenarios were tested, considering swimming behaviour surface-oriented, and passive behaviour. Results show that larval can be advected in the entire study area, except in the North-East part of the domain (Figures 4.23 and 4.24). Larval with simulated swimming behaviour have a more dispersive path than passive larvae (Figures 4.23 and 4.24, where the passive behaviour is on the right column). Throughout the simulation, particle density is decreasing, due to the higher dispersion over time. Different patterns along time and space can be identified in the different scenarios. On the last month of simulation (day 123), it is clear a higher particle density in the passive behaviour than in the other scenarios. In the March release, this higher density occurs mainly near the release points of the CG and WG (Figure 4.23) contrasting with the absence of particles between MAR and the CG. In the Passive scenario (on the right in Figure 4.23), different patterns can be distinguished: i) a North-South larvae pathway along the WG and MAR locations; ii) the absence of particles between MAR and the CG; iii) larvae density in the CG and the WG. With the larvae swimming behaviour, a higher dispersal occurs longitudinally over the south part of the domain. Contrariwise, in the October release, article density is higher between the MAR and the CG. A North-South larvae pathway in between MAR and the CG is formed (Figure 4.25). In the 3rd month of simulation, the higher particle density occurs away from the release points. Dispersal patterns reveal higher particle distribution between the CG and the WG, in March than in October.

The higher dispersal on Behaviour_1 and Behaviour_2 scenarios is a sequence of tracers' swimming behaviour. With the surface-oriented swimming behaviour when achieving the surface layers tracers are advected by the surface currents, characterized by higher velocities, than the deeper currents. Behaviour_2 reveals the same density distribution as Behaviour_1.

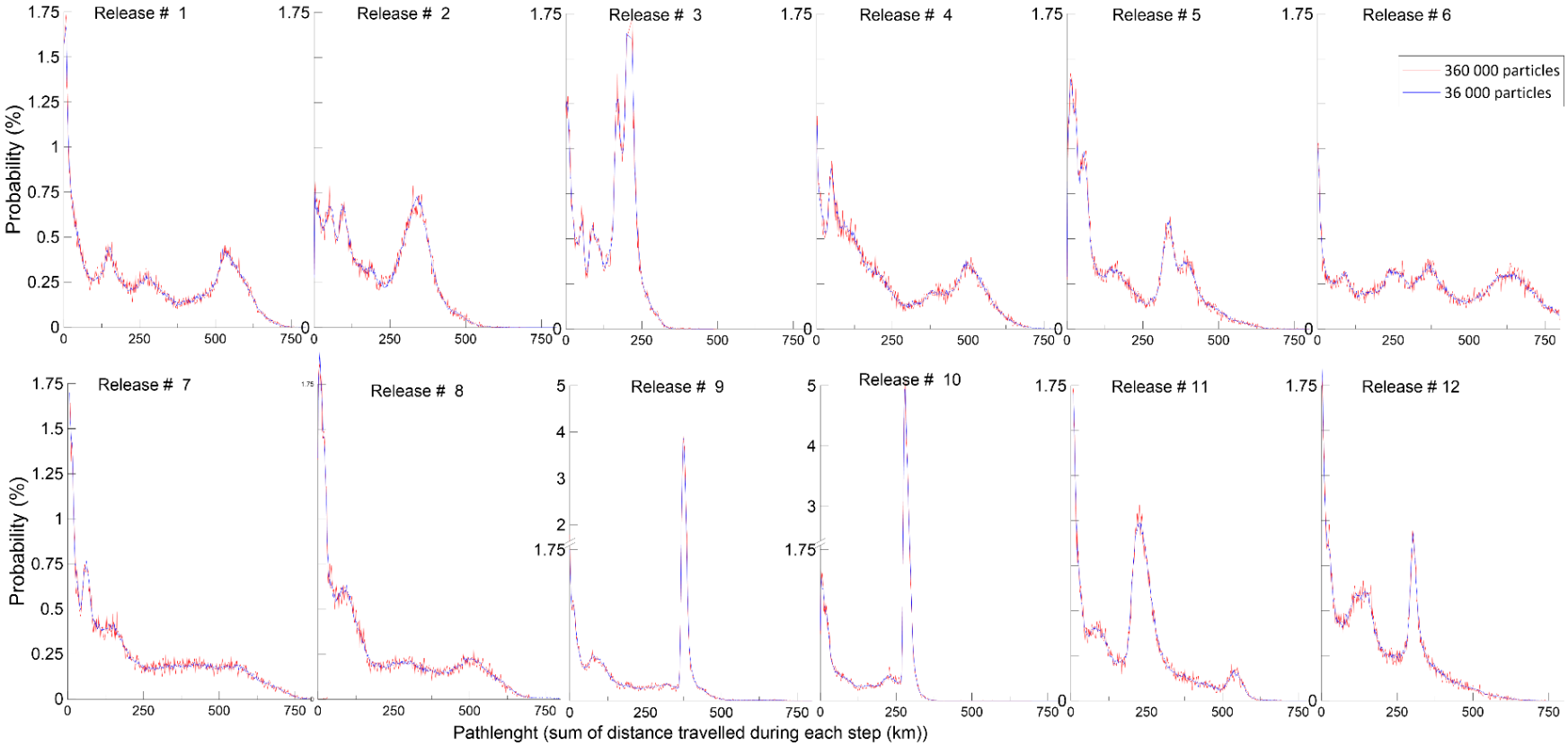

Figure 4.23- Probability of dispersal pathlength distances, for scenario *PLD_81_March_Behaviour_1_2017* , with different numbers of particles (360000 and 36000). The X-axis is the pathlength travelled by each particle (sum of distances moved during each time-step) binned into 2km increments, and the Y-axis is the probability.

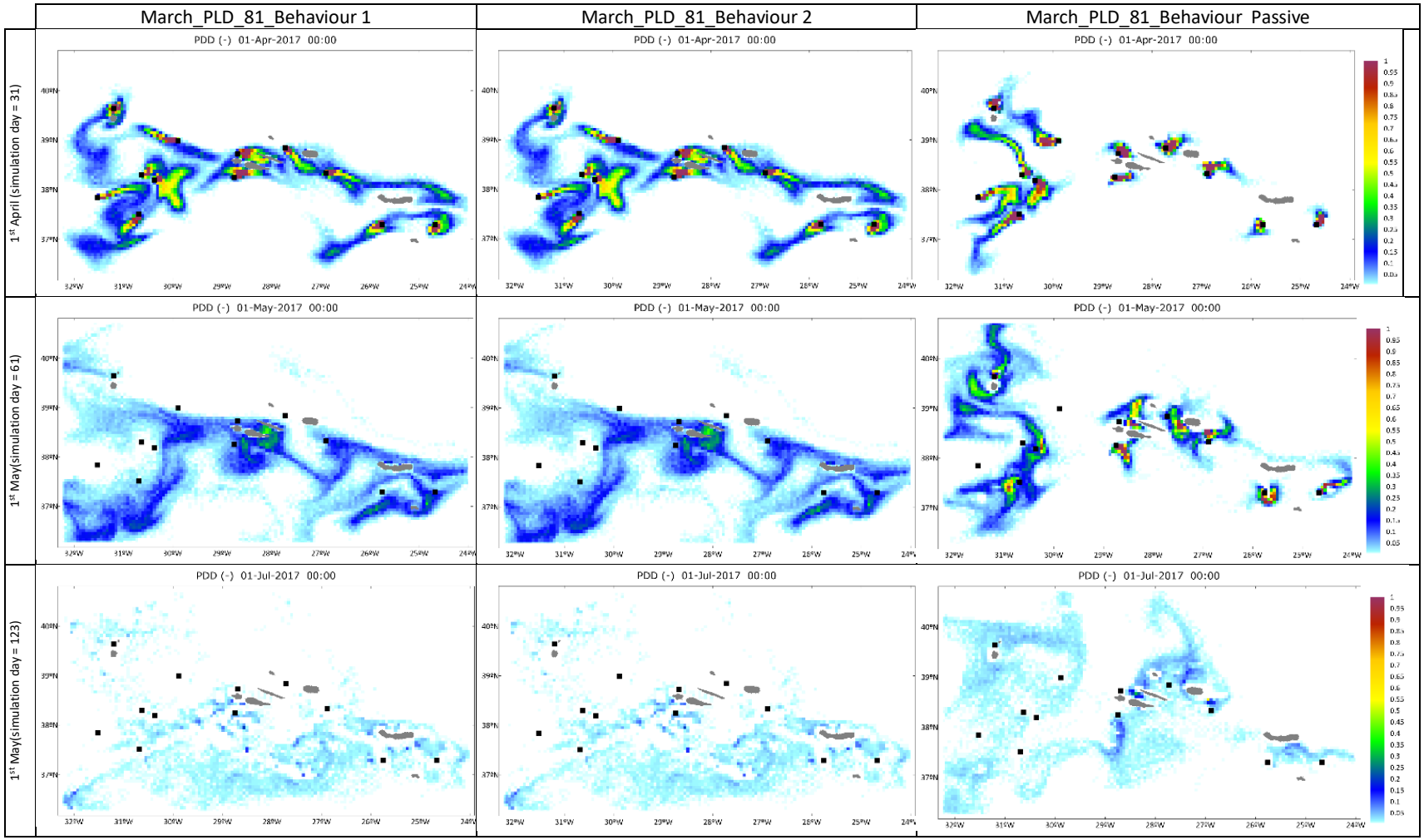

Figure 4.24- Particles density distribution for March release, with PLD of 81 days, with different behaviours, on the left "March_PLD_81_Behaviour_1", "March_PLD_81_Behaviour_2" in the middle, and "March_PLD_81_Behaviour_Passive" in the right, for day 1st April (1 day after the last particle release (simulation day = 31)) (top), 1st May (second row) (simulation day = 61)) and 1st July 2017 (bottom row) (simulation day = 123). The colour legend (from blue to red) represents the particle density distribution integrated with the water column, for each domain cell

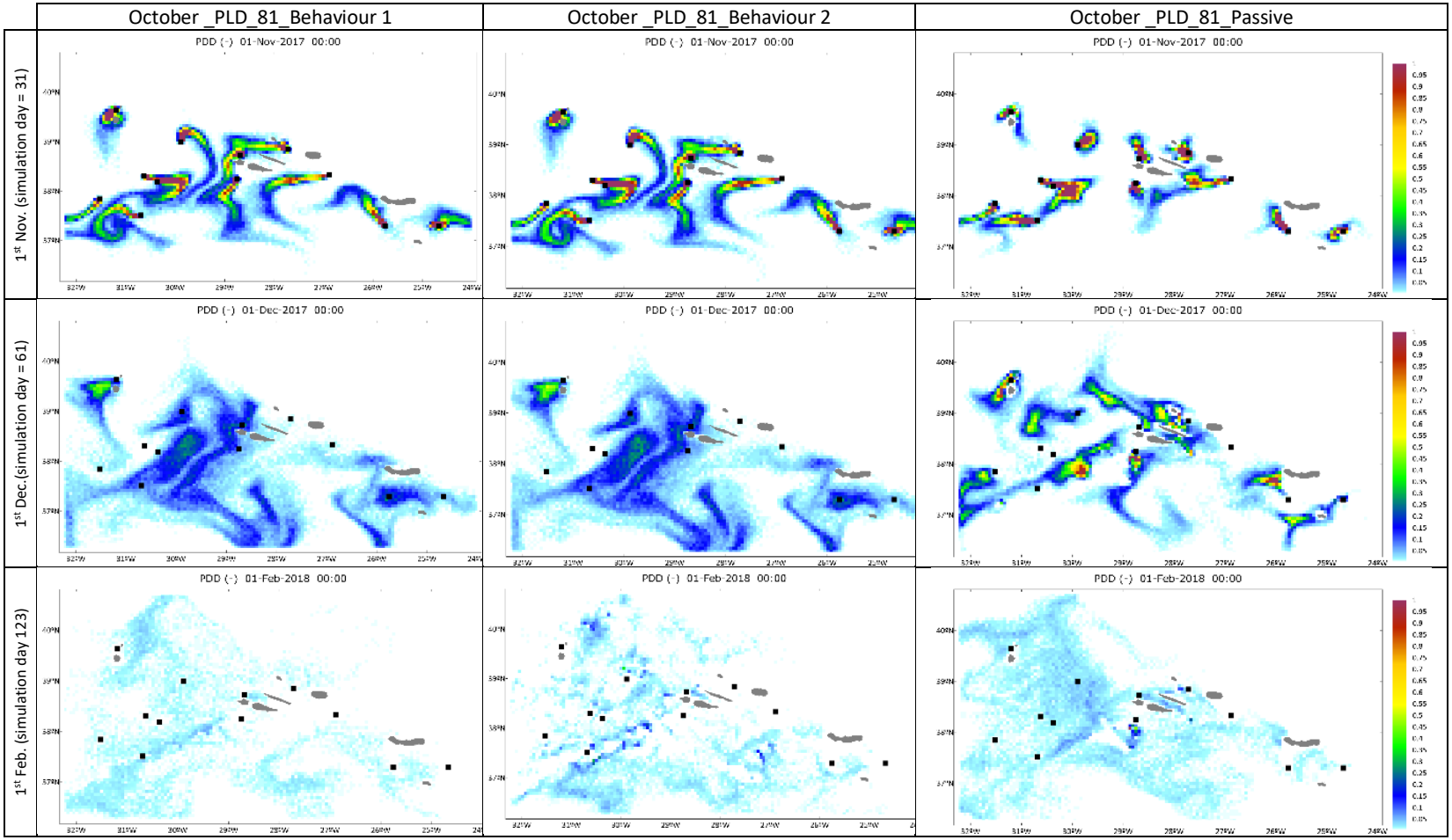

Figure 4.25- Particles density distribution for scenarios with a PLD of 81 days, and different behaviours, for October release, with different behaviours Scenario "October_PLD_81_Behaviour 1" on the left, "October _PLD_81_Behaviour 2" in the middle, and "October _PLD_81_Behaviour_Passive" in the right, for day 1st November (1 day after the last particle release (simulation day = 31)) (top), 1st December (second row) (simulation day = 61)), and 1st February 2018 (bottom row) (simulation day = 123). The colour legend (from blue to red) represents the particle density distribution integrated with the water column, for each domain cell.

4.5.3.2. Particles vertical migration

According to different studies DSRC larvae have a swimming behaviour and can achieve the ocean surface (Kelly et al. 1982, Landeria & Tamura 2018). This swimming behaviour was simulated in this study. Particles (larvae) were able to achieve the most surface layers, as can be seen in histograms in Figures 4.25 and 4.26. In contrast, particles with passive behaviour stay mostly in the deeper layers. Particle's vertical migration is similar for March and October scenarios, not demonstrating any seasonal or spatial patterns. In all the scenarios particles can diverge to areas deeper than 1000 or 1200 meters depth, mostly for particles with passive behaviour. Only releases L#1, L#2 and L#12 show a distinct distribution of particle depths. These differences are a consequence of the percentage of particles that are advected out of the domain. As particles achieve the most surface layers, are consequently exposed to stronger currents (Figure 1.27), which induce a higher dispersion.

The surface layers have stronger velocities, with average values reaching 0.25 m/s, while the deeper layers lower velocities. The vertical decrease of velocity modulus occurs mostly in the entire domain.

Passive vs Behaviour- March_PLD_81

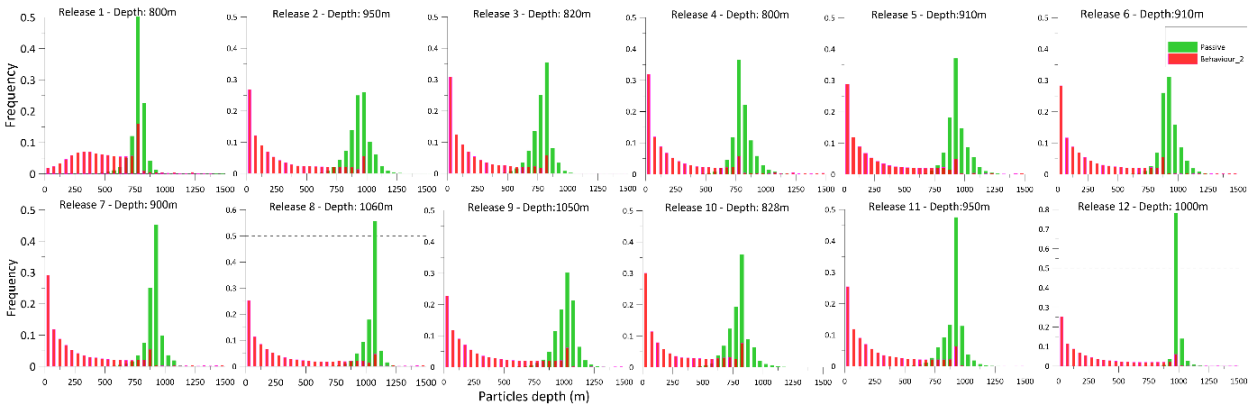

Figure 4.26- Histogram of the depth of the particles along their trajectory, for each release point, considering the passive behaviour (green), and Behaviour_2 (red). The depth of the respective release is detailed at the top of each graph

March vs October for PLD_81 Behaviour_1

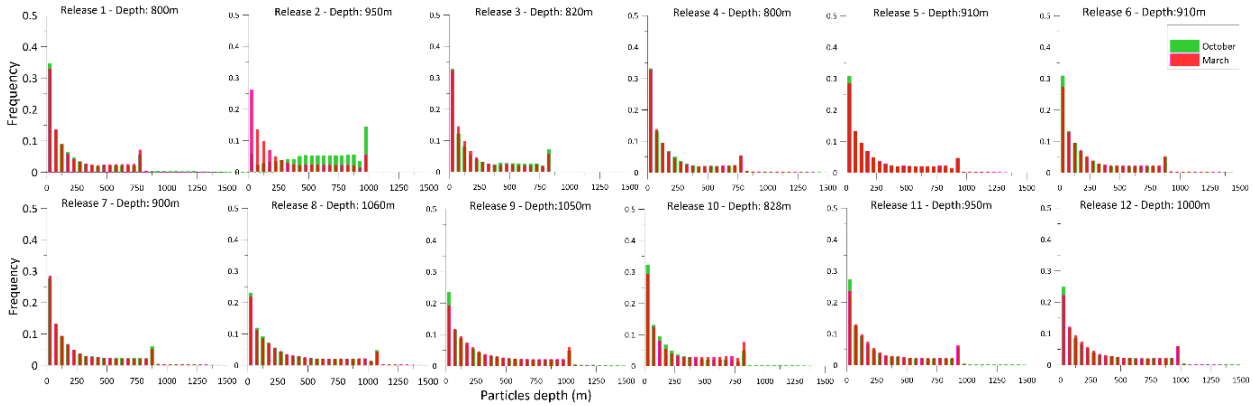

Figure 4.27- Histogram of particles depth along their trajectory for each release, for Behaviour_1 PLD_81 for March (red), and October release (in green). The depth of the respective release is detailed at the top of each graph

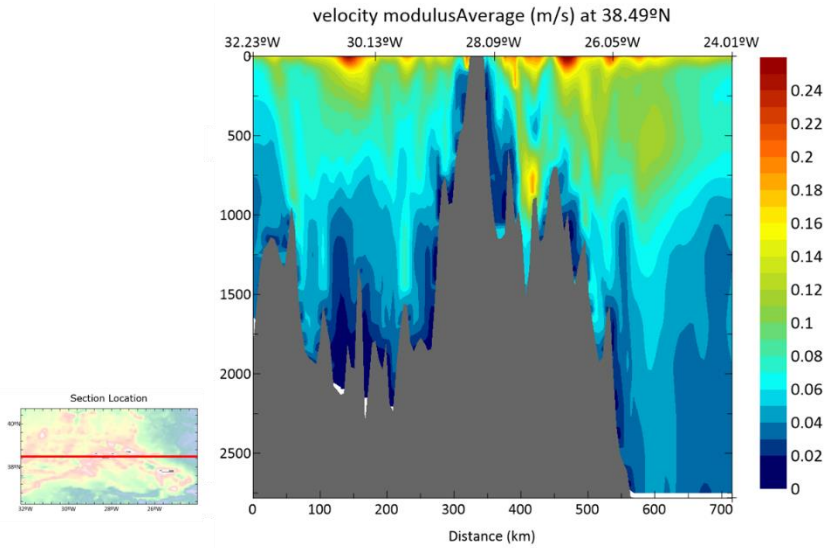

Figure 4.28- Annual average (2017) average of the velocity modulus along the water column for longitudinal section of the study domain. Map on the left shows a representation of the section.

As a result of the different hydrodynamic conditions along the water column, particles in the deeper layers have different dispersion than the ones in most surface layers.

Different particle distributions are identified in the different depths (Figure 4.29). At the surface, the dispersal is higher. For March release, particles from different locations (L#1 (red), #6(orange) and #4(light blue)) achieve the W. In contrast, between 400 and 800 meters depth, few particles are present, and almost none at the deeper layers (800-1200 meters). In the October release, a higher quantity of particles from different locations can be found on the West part of the domain.

At the surface, in October, particles are advected also for the North part of the domain, over the CG and WG. Images of particle dispersal, Figure 4.29, show that particles are advected for regions out of the domain, leaving the domain mainly in the Western and South boundaries.

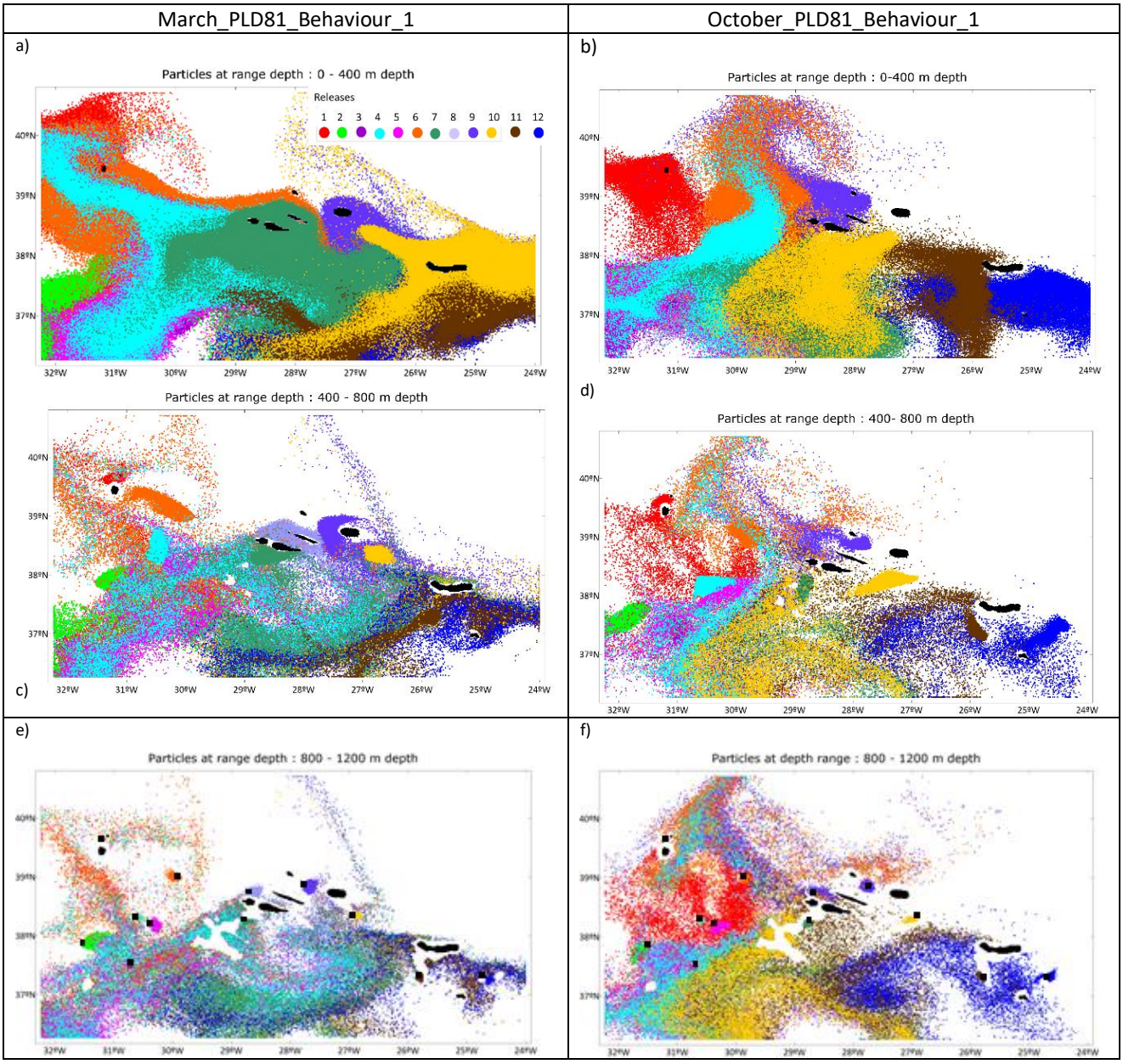

Figure 4.29- Representation of all particles' positions along their trajectories (during the entire simulation period) for scenario "March_PLD_81_Behaviour_1" on left, and "October_PLD_81_Behaviour_1", on the right, at different depth ranges, from the surface until 400 meters depth on the left, between 400 and 800 meters depth in the middle, and from 800 to 1200 meters depth on the right. Different colours represent the different release points. (Only 1/25 of the total particles are represented)

Travel distance

Larval dispersal as a consequence of the swimming behaviour and longer PLDs have diverse dispersive patterns. Median travel distances can range from few kilometres (<15 km for release L#1), to more than 200km (276km for L#6) (Figure 4.31). The total travel distance can be more than 1000 km, for L#10. However, considering the highly non-normal particle dispersal (Phelps 2015), median and percentile 95th dispersal distances are used, rather than maximum travel distances. The percentile 95th travel distances are generally one order of magnitude higher than the median distances in all the releases. As expected, for higher PLDs.

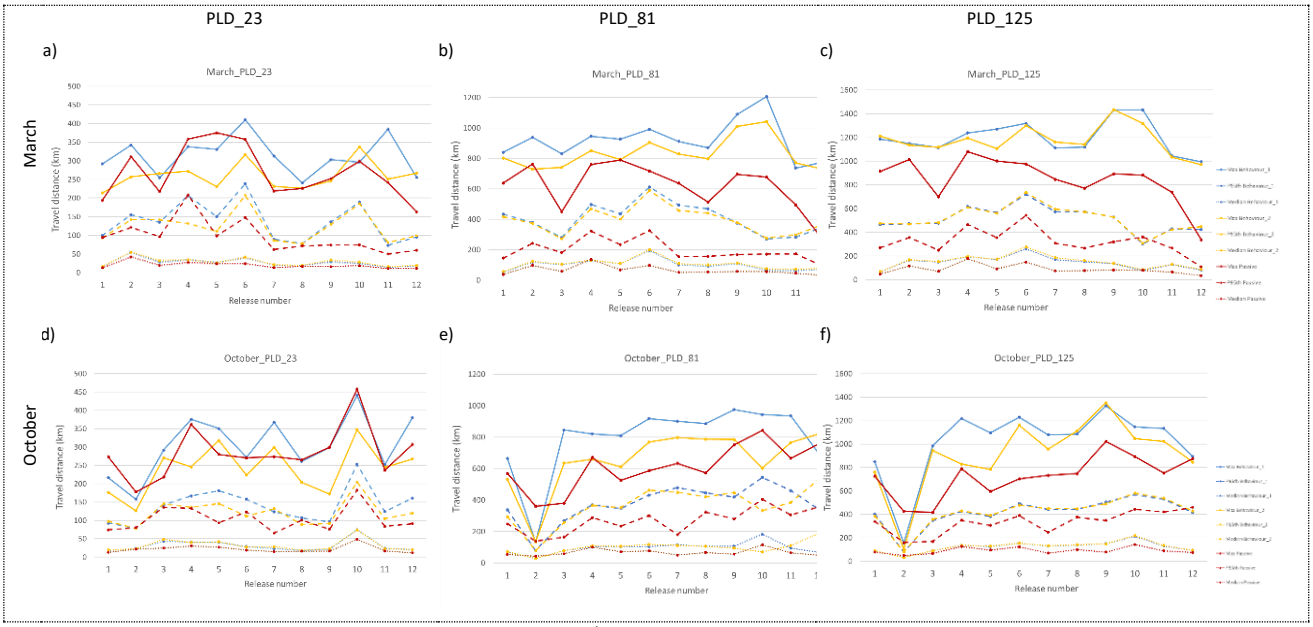

Figure 4.30- Median (Med), maximum (max), and 95th percentile (P95), of total travel distances (km) for all the particles released at each location, considering the different behaviours (Behaviour_1, Behaviour_2, Passive behaviour), for scenarios with spawning in March (top), and October (bottom), for PLD23, (left) PLD81(middle) and PLD125 (right).

The lower median and percentile 95th travel distances are associated, generally, with higher percentages of tracers advected away from the domain (Table 1.14).

On average, 30 to 40% of particles from releases L#1 (Flores island), L#2 (MenezGwen), and L#3 (Voador Seamounth), are advected out of the domain (Figure 1.30). Furthermore, the maximum values can achieve 90% for L#2, and 57% for L#3 during scenario October_PLD125 with Behaviour_1. These higher percentages are reflected in the travel distances, that achieve

anomalous lower values represented on Figure 4.30. These locations are sited in the WG and in the MAR, closer to the domain borders than the others.

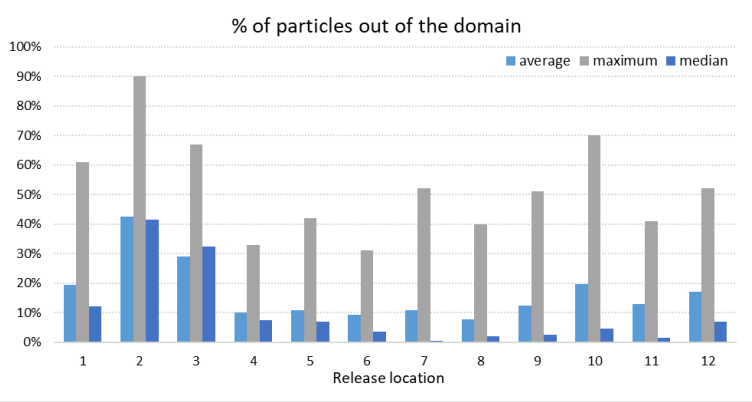

Figure 4.31- Average, maximum and median values of percentage of particles that went out from the domain over all the scenarios in the study for each location.

The percentage of particles that are advected out of the domain is higher for simulations with swimming behaviour and longer PLD (Table 4.14). Particles from the WG, MAR, and EG can leave the domain in different scenarios. In the October scenarios with PLD125, 90% of L#2 particles', are advected out of the domain, while in March about 47% (Table 4.14). This percentage of particles leaving the domain can underestimate particles' travel distances. This is reflected in the histograms of Figure 4.32, depicting that L#2 particles only travel up to 150km during the October release. In this case, 89% of the particles left the domain, and the median travel distance is 29km, while the maximum is 135km.

The simulated swimming behaviour induces higher travelled distances (median from 17 – 259km) than passive behaviour (median from 12-75 km). This difference increases with the higher PLD. , Travel distances from Behaviour_1 and Behaviour_2 are similar. The major differences occur in the release points near the domain limits, L#1, L#2, and L#3, on the West, and releases #9, #10, #11 and #12 with their particles leaving the domain by the South boundary.

Table 4.13- Median (Med), 95th percentile (P95), and maximum(max) travel distance (km) for simulations with Behaviour_1, for March and October with PLD23, 81 and 125. Minimum and maximum values for each scenario are underlined. Column "Out (%)" indicates the % of particles from each release that went out from the domain.

	a)	Behaviour 1_Travel distance (km)																							
		March_PLD 125				March PLD_81				March PLD 23				October PLD_125				October PLD_81				October PLD_23			
		Med	P95	Max	Out (%)	Med	P95	Max	Out (%)	Med	P95	Max	Out (%)	Med	P95	Max	Out (%)	Med	P95	Max	Out (%)	Med	P95	Max	Out (%)
WE	Location_1	63	465	1186	61	53	434	841	46	16	100	292	2	90	402	847	39	72	338	664	20	19	93	217	0
MAR	Location_2	165	472	1149	47	120	378	938	37	55	155	342	0	30	80	153	90	29	79	133	84	23	79	158	45
	Location_3	149	477	1115	46	103	280	830	42	27	135	255	2	89	347	985	67	80	268	846	56	43	142	292	7
	Location_4	194	618	1238	23	130	497	946	12	34	207	338	1	134	426	1217	33	103	370	820	20	41	167	376	0
	Location_5	171	566	1270	24	109	436	927	16	27	150	331	0	126	381	1095	42	102	346	810	24	40	181	351	1
	Location_6	259	719	1319	31	194	612	991	14	40	239	410	2	153	490	1230	24	105	431	918	15	29	158	272	0
CG	Location_7	169	573	1111	29	99	493	912	11	20	90	313	0	129	442	1078	52	115	479	901	31	23	124	368	0
	Location_8	152	573	1119	21	91	469	870	5	19	78	241	0	137	444	1084	40	106	446	885	25	18	107	261	0
	Location_9	136	528	1433	51	108	376	1090	35	29	136	303	0	149	504	1325	22	108	419	975	6	21	96	299	0
	ocation_10	79	303	1432	70	64	271	1207	58	24	189	297	2	212	569	1146	38	183	544	943	16	75	253	441	0
EG	ocation_11	126	430	1044	41	62	284	737	38	14	74	384	0	130	530	1133	33	93	461	936	20	24	124	252	0
	ocation_12	81	423	995	52	71	353	780	31	18	95	256	1	93	415	894	41	68	341	695	26	20	161	380	0

	b)	Behaviour 2_Travel distance (km)																							
		March_PLD 125				March PLD_81				March PLD 23				October PLD_125				October PLD_81				October PLD_23			
		Med	P95	Max	Out (%)	Med	P95	Max	Out (%)	Med	P95	Max	Out (%)	Med	P95	Max	Out (%)	Med	P95	Max	Out (%)	Med	P95	Max	Out (%)
WE	Location_1	69	476	1212	58	57	417	803	44	17	93	214	0	90	385	761	35	72	294	531	19	20	98	177	0
MAR	Location_2	168	469	1135	45	125	373	729	38	55	142	257	0	30	80	103	87	29	79	135	89	23	78	126	51
	Location_3	153	482	1118	43	106	272	741	42	32	142	266	1	90	357	944	65	79	258	634	61	49	146	271	2
	Location_4	196	610	1195	18	132	469	852	8	35	132	272	0	135	430	829	29	108	366	660	12	40	136	246	0
	Location_5	174	561	1107	19	109	402	793	15	26	111	231	0	129	391	785	37	106	352	611	17	42	146	318	0
	Location_6	276	735	1300	24	201	589	905	9	42	207	317	0	154	478	1159	22	118	462	769	30	28	112	224	0
CG	Location_7	187	595	1161	24	109	458	829	6	21	86	232	0	133	448	957	49	112	450	798	23	29	132	299	0
	Location_8	161	572	1141	15	100	440	797	3	20	78	227	0	141	447	1111	38	106	420	787	10	18	89	204	0
	Location_9	139	528	1434	50	114	379	1010	35	33	129	246	0	149	489	1351	21	95	447	785	19	23	92	172	0
	Location_10	85	309	1318	68	75	276	1042	57	28	185	338	0	219	581	1046	34	71	333	602	25	74	204	348	0
EG	Location_11	129	423	1035	40	72	299	771	36	16	81	251	0	134	537	1023	28	111	385	765	2	23	105	245	0
	Location_12	88	448	971	48	79	371	725	28	19	99	267	0	93	428	847	40	188	532	821	9	21	120	267	0

	c)	Passive behaviour_Travel distance (km)																							
		March_PLD 125				March PLD_81				March PLD 23				October PLD_125				October PLD_81				October PLD_23			
		Med	P95	Max	Out (%)	Med	P95	Max	Out (%)	Med	P95	Max	Out (%)	Med	P95	Max	Out (%)	Med	P95	Max	Out (%)	Med	P95	Max	Out (%)
WE	Location_1	48	270	913	41	38	145	638	33	13	94	194	3	77	340	725	8	55	249	569	5	13	75	274	0
MAR	Location_2	117	356	1013	25	97	242	763	14	42	121	311	1	49	160	427	69	43	138	360	67	22	80	178	31
	Location_3	71	249	699	35	58	181	450	23	19	96	218	1	67	168	416	57	59	164	380	48	25	136	218	7
	Location_4	178	465	1080	33	136	323	760	24	27	208	358	2	126	349	790	17	100	288	670	7	30	133	362	0
	Location_5	92	355	1001	20	69	235	790	11	24	98	375	0	94	306	596	9	72	235	525	3	27	94	280	0
	Location_6	149	542	976	7	98	326	717	5	24	148	357	0	122	389	701	1	77	301	587	0	19	123	271	0
CG	Location_7	76	307	846	3	51	155	637	0	13	62	219	0	68	247	733	4	51	181	633	1	15	65	274	0
	Location_8	78	267	772	10	55	156	513	1	16	72	226	0	98	376	748	14	66	323	572	4	16	101	265	0
	Location_9	82	320	893	10	57	168	695	1	16	74	252	0	77	347	1022	11	56	280	751	4	17	76	300	0
	Location_10	80	361	883	8	57	171	678	2	19	75	299	0	142	443	892	15	115	405	842	7	48	183	458	0
EG	Location_11	64	266	738	16	46	173	494	10	11	50	242	0	88	420	753	5	65	305	665	1	17	84	237	0
	Location_12	35	108	338	53	31	87	247	41	12	60	164	3	74	459	876	10	49	357	757	5	12	91	307	0

Same PLD and behaviour, different release month: March_PLD 81 Behaviour_1 vs October_PLD 81 Behaviour_1

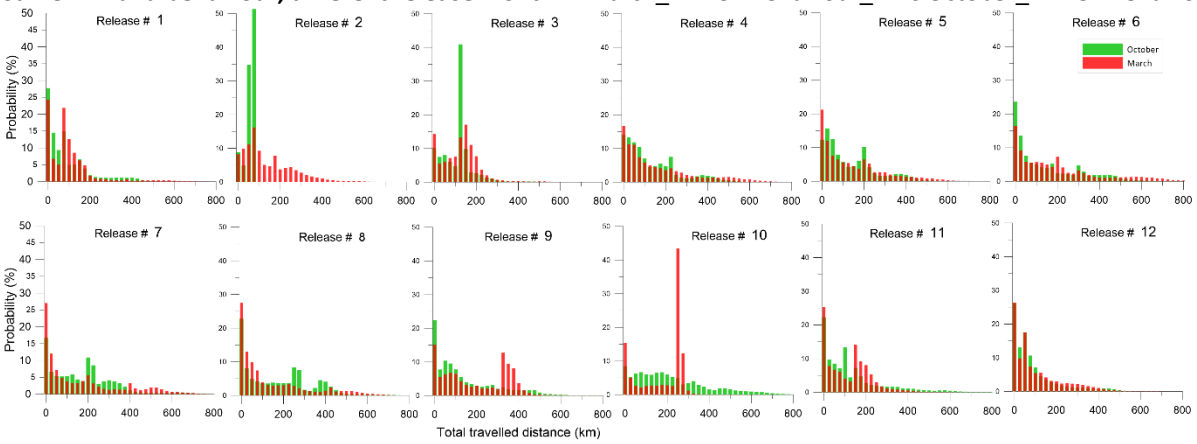

Figure 4.32- Histogram (in %) of the total travel distance from particles from each release, in km, considering a PLD of 81 days, for the October release in green, and the March release in red.

Same release month and PLD, different behaviours: October_PLD_81 Passive vs October_PLD_81 Behaviour 2

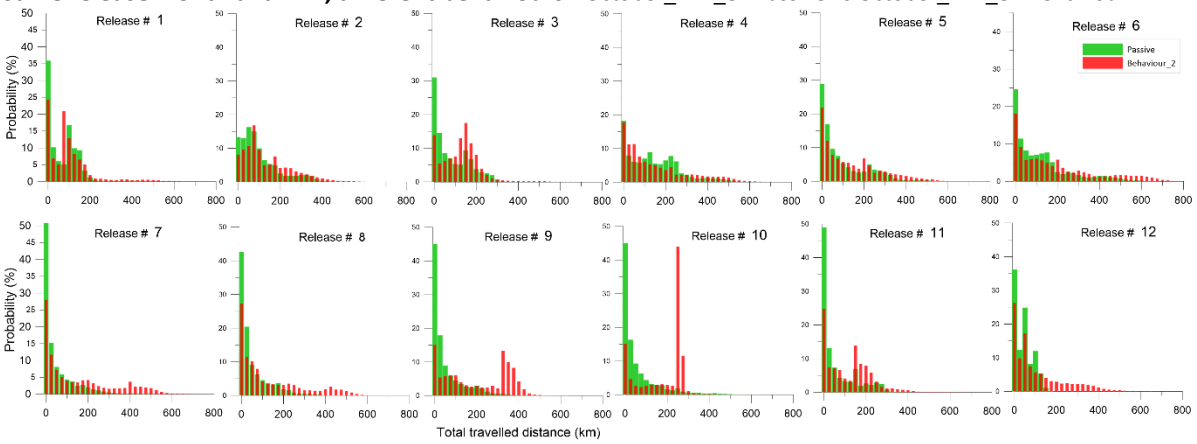

Figure 4.33- Histogram (in %) of the total travel distance from particles from each release, in km, for the October 2017 release, considering a PLD of 81 days, for the Passive behaviour in green, and Behaviour_2 in red.

Same release month and PLD, different behaviours: March PLD_23 Passive behaviour vs March PLD_23 Behaviour 2

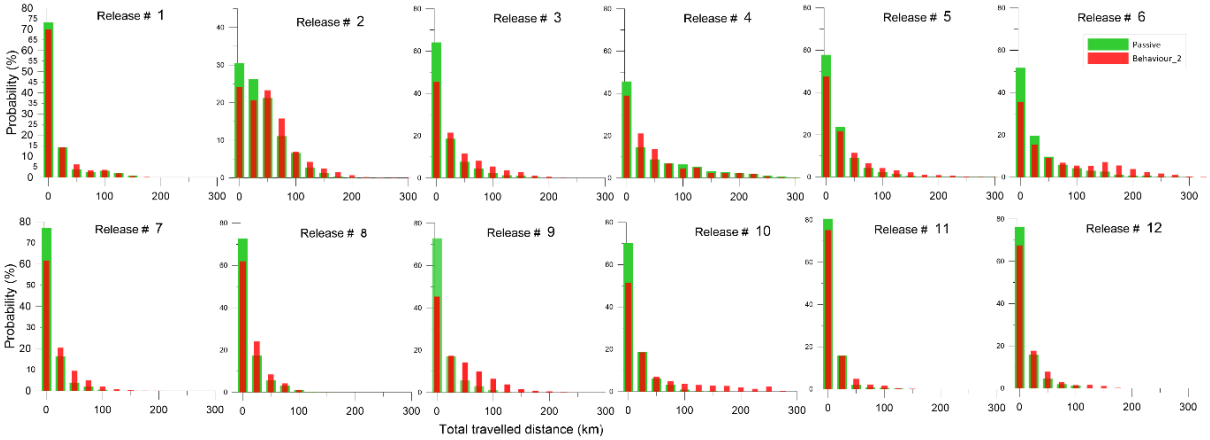

Figure 4.34- Histogram (in %) of the total travel distance from particles from each release, in km, considering a PLD of 23 days, for the Passive behaviour in green, and Behaviour_2 in red, for the March 2017 release.

4.5.3.3. Connectivity between *C. affinis* populations

Larvae dispersal gives rise to different connectivity patterns among the different locations, however with a lower fraction of particle exchange (Figure 1.34). Results show higher self-recruitment in scenarios with the lowest PLD, 23 days, however, less connectivity between different populations. Larval spawning during March prompts a higher exchange of particles between different populations. In general, the percentage of larvae that settle in any recruitment polygon is lower than 0.03%.

Populations located in MAR (L#2 to L#6) have a higher exchange of particles during March than during the October release. The same for the populations in the CG. For PLD81, these populations have more connectivity relations between them and also with the EG.

Larvae that present behaviour_2 shows lower connectivity than the ones that present behaviour_1. In behaviour_2 the simulated larvae velocity during the last larvae stage is higher than on behaviour_1. Possibly this velocity is inadequate and too fast, conducting particles to the bottom of the sea, without time to search for suitable recruitment locations. Connectivity between the different populations is represented in the connectivity matrices in Figure 4.35, Figure 4.36, Figure 4.37. With behaviour_1, the simulated larval dispersal during March results in higher connectivity among populations over the entire archipelago than during October. In all the connectivity situations the percentages of settled particles is reduced, lower than 0.1%. During March, populations from the CG receive particles from the WG, MAR, CG and EG. Nevertheless, during October, for PLD125, populations receiving more particle exchange are located in the MAR, receiving particles from MAR, CG and also from the EG. For PLD81, it is clear a higher number of connectivity relations, in the entire archipelago, during the March release than in the October one.

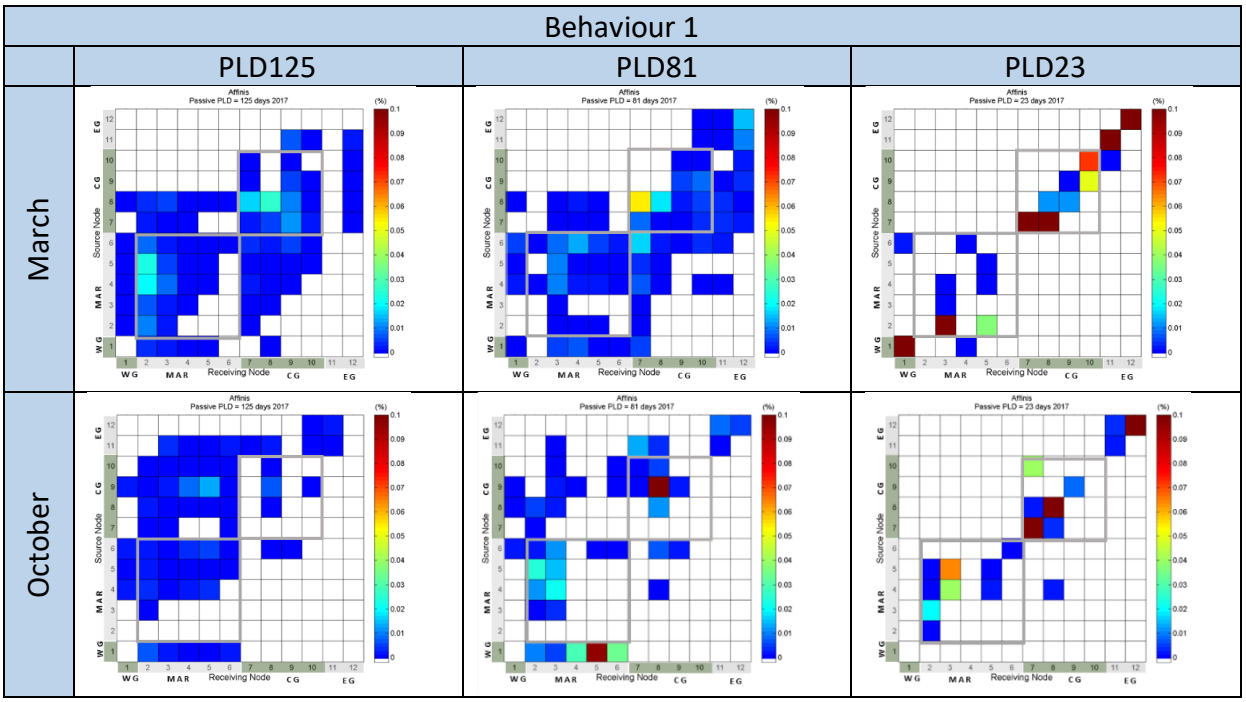

Figure 4.35- Connectivity matrices for Behaviour_1, for PLD125, PLD81 and PLD23, from left to right, for Spawning in March on top, and in October, down. Colours represent the percentage of modelled particles from each population (source node) in vertical axes, that settled in a recruitment area (receiving node) in horizontal axes. Diagonal cells represent auto-recruitment. Each release point is a recruitment area: WG:L#1; MAR: L#2 to L#6; CG: L#7 to L#10; EG:L#11 and L#12).

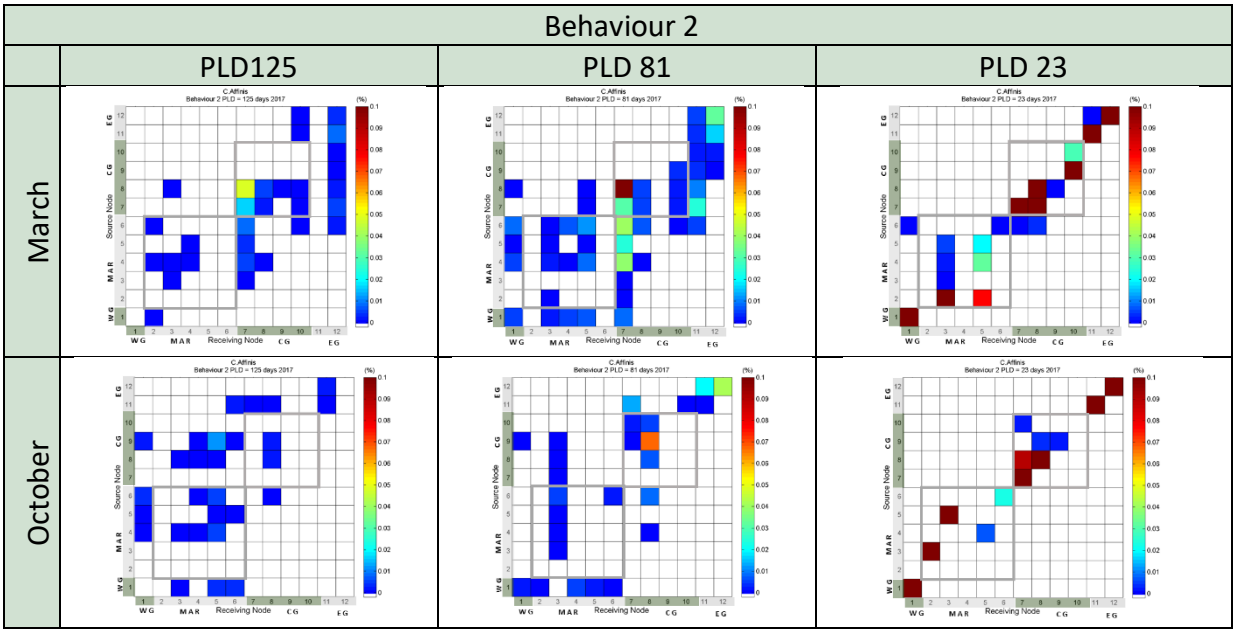

Figure 4.36- Connectivity matrices for Behaviour_2, for PLD125, PLD81 and PLD23, from left to right, for Spawning in March on top, and in October, down. Colours represent the percentage of modelled particles from each population (source node) in vertical axes, that settled in a recruitment area (receiving node) in horizontal axes. Diagonal cells represent auto-recruitment. Each release point is a recruitment area: WG:L#1; MAR: L#2 to L#6; CG: L#7 to L#10; EG:L#11 and L#12).

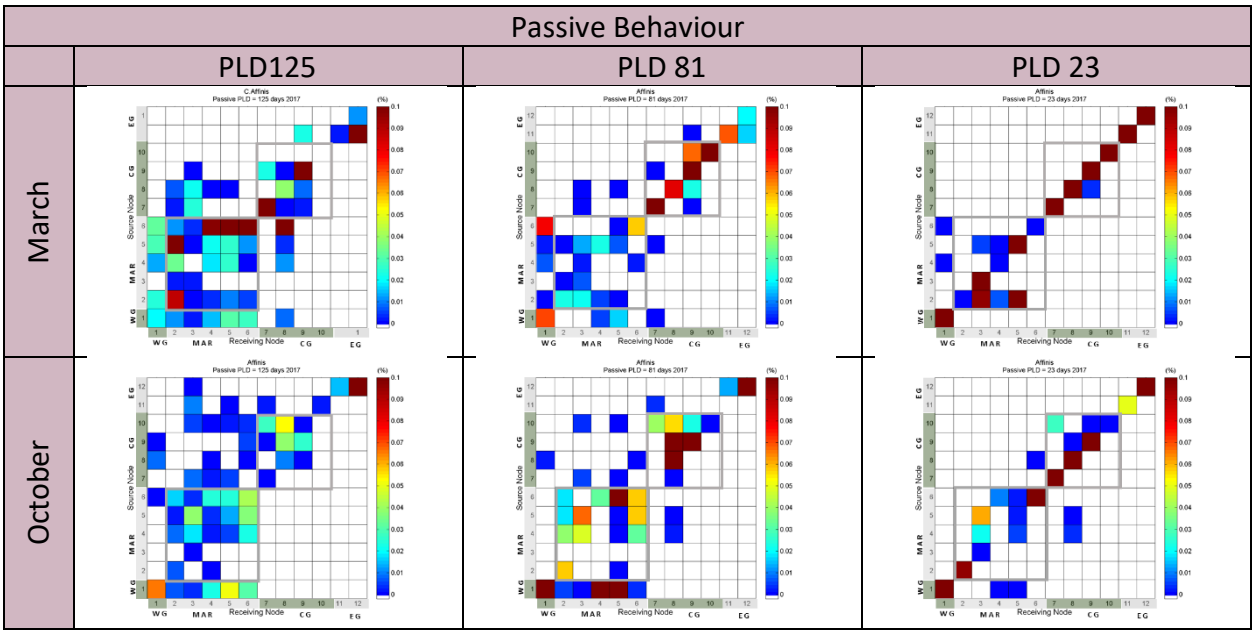

Figure 4.37- Connectivity matrices for Passive_behaviour, for PLD125, PLD81 and PLD23, from left to right, for Spawning in March on top, and in October, down. Colours represent the percentage of modelled particles from each population (source node) in vertical axes, that settled in a recruitment area (receiving node) in horizontal axes. Diagonal cells represent auto-recruitment. Each release point is a recruitment area: WG:L#1; MAR: L#2 to L#6; CG: L#7 to L#10; EG:L#11 and L#12).

4.5.4. Discussion

A biophysical particle tracking model was applied to study the connectivity between different *Chaceon affinis* populations in the Azores. This model allows the simulation of different spawning and larval behaviour hypothesis, to study the dispersal of these deep-sea red crab larvae and population connectivity in the Azores. Although being a benthic moving organism, *C. affinis* also benefits from the larvae dispersal for population dispersal. Populations of this species in the NE Atlantic may be isolated in several coastal groups and seamounts (Santos et al. 2019). In Madeira islands, tagged specimens were found in the same location 3 years later (Biscoito et al. 2015). Therefore, relying upon the larval migration for species resilience. This kind of model has been used to support fisheries decision-making (Swearer et al. 2019)

Model implementation and calibration

In this case study, 12 populations are considered, based on available data. Localized over the entire archipelago, from the most Western island (Flores island (L#1), through MAR, the Central Group, up to the most Eastern location (EG).

Particle tracking results show that particles can be advected out of the domain, induced by the long PLD (from 23 to 125 days). This is a common model limitation of larvae dispersal model applications, specifically in oceanic regions, where the influence of strong currents advect tracers out from the domain (Kenchington et al. 2019, Busch et al. 2021, Wang et al. 2021). The Azores region is under the influence of several water masses and currents that originate highly dynamic dispersal patterns. A bigger model domain could minimize this particle's loss, however, due to the strong currents, it would require a much higher domain, out of the scope of this study. It would also require a higher computational effort. A compromise between model domain, resolution, and computational efficiency, must always be achieved.

One way to surpass this domain size limitation is by increasing the number of tracers in use, ensuring that during the simulation, the tracers' trajectory is representative of the real dispersal scenarios (Simons et al. 2013). For this case study, a total of 396800 particles per month, per release was used, totalizing more than 4.7 million particle trajectories being simulated in each scenario. Calibration tests show that this number of particles can produce saturated dispersal pathlengths. Furthermore, this number of particles is one order of magnitude bigger than other applications, like the one explained in Case study 1 for *P. carpenteri*.

In this model calibration, the FUV method, (Simons et al. 2013) was not performed because it requires the first simulation with a higher number of particles, and subsequent subsample pools of trials to estimate the variability (and the fraction of unexplained variability), which was very computationally demanding. Also, this number of particles is in line with other model applications for ocean regions (Ross et al. 2017, Kenchington et al. 2019). A review study about the state of the art of biophysical models of marine larval dispersal report that in studies with multiple releases, the number of particles released from each location ranged from 1 to 4.2×10^7, with a median of 178, while for a single release from 1 to $1x10^7$ with a median of 1000 particles (Swearer et al. 2019).

Simillarly to other model aplications it was assumed this limitation of particles loss out of the domain, and it was taken into consideration when interpreting connectivity results (Swearer et al., 2019; Wang et al., 2021).

Scenarios and behaviours in study

The different scenarios tested consider different PLD, and spawning seasonality, larval behaviours, based on the information available (Table 4.6). In this case, in the absence of detailed information about *C. affinis* larvae, it was used the available information about other deep-sea red crabs from the same subfamily. To simulate the swimming behaviour it was used data obtained in laboratory, by Kelly et al (1982), for *C. quinquedens*. In terms of modelling, is a common and acceptable approach to use behaviour data from other a congener or confamilial, although it should always bear in mind that behaviours can differ among close relatives (Leis 2020). When using these scenarios several assumptions have been made, which should be taken into consideration when interpreting connectivity results (Young et al. 2012, Swearer et al. 2019, Wang et al. 2021).

Besides the swimming behaviour surface-oriented in the first larvae development stage, also swimming behaviour bottom oriented is considered in the last development stage. In the absence of data about the velocity in the last stage, two different hypotheses were tested. The first bearing in mind the gradual reduction of larva activity during the late stages reported for deep-sea larva (Leis 2020), also observed by Kelly et al., 1982, where it was assumed a velocity 10 times lower than the velocity in the first stage. The second hypothesis was based on the sinking rates measured for these larvae, that increase from the first to the last development stage (2.2cm/s) (Kelly et al. 1982).

The settlement velocity is the unique difference between behaviour_1 and behaviour_2, and it is inducing different connectivity patterns. The simulated higher settlement velocity in behaviour_2 reduces the probability of the larvae (tracers) settling in a suitable recruitment area. Therefore reducing the probability of larvae exchange among different populations. Because tracers are instructed to settle in between a bathymetric range from 800m to 1200meters depth, the lower bottom-oriented velocities of Behaviour_1 larvae have higher chances to be advected to suitable recruitment areas before settling. This result shows that downward velocity is relevant for particle settlement locations, and consequently for connectivity estimates.

This model application also can adapt the swimming behaviour considering the environmental conditions, as in this case, the water temperature. The swimming velocity ranges

from 1.4 at 11ºC, to 1.7 cm/s at 15ºC depending on the water temperature. This increase allows us to better simulate the original conditions, where these larvae can cross the environment thermocline that exists in the Azores from the deeper layers up to the surface.

Model results showed that in this model configuration, using the swimming behaviours, larvae were able to achieve the surface layers, simulating the behaviour observed in the different in-situ studies, where *C. affinis* larvae were collected at the surface (Guerao et al. 1996, Landeria & Tamura 2018). Contrarily, with the passive behaviour, the larvae never achieve the surface layers, not even with the larger pelagic durations.

Particles dispersal

Estimates of particle trajectories reveal that particles can travel up to 1400km in the study area, indicating the potential for *C. affinis* larvae to travel across the entire archipelago during the PLD. Although, the maximum travel distances are one order of magnitude higher than the median values, revealing a higher dispersive system. This distance magnitude is in line with other DSRC dispersal estimates (Kelly et al. 1982), and deep-sea larvae with long PLD (Wang et al. 2021). It is a consequence of vertical swimming behaviour, but mainly due to the residence time near the surface (Figure 4.26), which has a large impact on theoretical travel distances (Gary et al. 2020). Particle dispersal distribution maps (Figure 4.29) substantiate these results, showing high dispersal patterns at the surface.

These higher dynamic currents at the surface layers justify the differences between the travel distances between the passive behaviours and the particles with a swimming behaviour. It is important to denote that this swimming behaviour is imposed by the model only during the first development stage.

Particles simulated with a passive behaviour don't achieve the most surface layers and are advected mainly in the deeper layers. They can be advected in both surface or deeper directions, in a bathymetric range of approximately 500-meter depth (as is depicted in the histograms of particle depth in Figure 4.26). Given the weaker currents in the deeper water layers, the passive behaviour results in lower total travel distances (Figure 4.33). Similar results have been obtained in deep-sea larvae dispersal studies revealing the impact of vertical migration on larvae dispersal and travel distances away from the release location (Young et al. 2012, Kool et al. 2013).

Moreover, model results show that this passive behaviour with lower vertical movement and travel distances induces higher self-recruitment levels, and lower connectivity between different populations, as is depicted in the connectivity matrices of Figure 4.37.

Even with these general lower travel distances, the passive behaviour reflects the different hydrodynamic patterns in the deeper layers, resulting in different connectivity between populations. With a passive behaviour, connectivity can occur between release#12, in the EG, with the populations of the MAR group. Namely, larvae from Formigas can settle in Voador seamount, with a PLD of 125 days and for the October release. This connectivity relation is not present in any other scenario tested.

The highly dispersive scenarios contribute to a large percentage of particles advected out of the domain. The population with a higher percentage of "lost" particles, L#2, Menez Gwen, the most western population in the study, is located in the MAR (Figure 4.22). This higher percentage of lost particles justifies the lower particle exchange with the other populations, mainly in the October scenarios. Connectivity matrices only reveal self-recruitment and connectivity in the Passive behaviour scenarios and for the scenario *October_PLD_23_Behaviour_1*. This result is, therefore, an underestimation of the potential particles exchanged from Menez Gwen populations with other recruitment locations. Once out of the domain, particles are "lost" for the model. However, because currents are very dynamic in the Azores, these larvae in a "real situation" can be advected again for the Azores region. The same for the other locations in the study. Also, these larvae that drift to other regions can be able to settle in other recruitment zones, furthermore, this region can receive particles from remote regions.

Larvae dispersal, even with a swimming behaviour, is mainly induced by hydrodynamic patterns (Wang et al. 2021). The model reveals different seasonal dispersal results, reflected in particle density distribution and lately in the connectivity between populations. Particle density distribution results (Figure 4.24 and Figure 4.25) show a decrease in PDD along time, but also depict the formation of "larval corridors", that might induce particle exchanges between different populations.

For March release with PLD81, a “larvae corridor” is formed between CG and MAR, and also between WG and CG, likely forming a longitudinal larval corridor. In October, the PDD is more intense mostly between CG and MAR, with a North-South larvae corridor more evident than the longitudinal exchange. This dispersal is reflected in the connectivity matrices. After the March release, the exchange between the different groups is multiple, with exchanges between EG and CG, CG and MAR, and MAR and CG with the WG, while in October, the exchange is mostly unidirectional to the MAR populations, with lower connectivity with the populations located in the CG and EG. These seasonal dispersal patterns can be useful to support studies of fisheries planning and management, by providing information on seasonal and spatial dispersal behaviours.

Passive behaviour is the most unlike. The Behaviour_1 seems the most possible scenario for this species, simulations the presence of larvae at the surface, and a patchy connectivity between different populations.

Connectivity between different populations

Major results show multiple connectivity relations between the different groups. This is a positive feature, that can be indicative of higher resilience of these populations mitigating the risk of recruitment failure (Holstein et al. 2014, Pata et al. 2021). It can also compensate the absence of self-recruitment that occurs in these most dispersive scenarios. This result can indicate high levels of connectivity between the different populations of *C. affinis* in the Azores. However, it should be noted that the percentage of particles exchange is lower, mostly less than 0.1%.

Results show that Voador Seamount (L#3), located in MAR, is a major sink area, receiving larvae from all the groups, including from the Formigas (L#12) population from the EG. Also Gigante Seamount, in the MAR group, exchanges particles with populations from all the groups, in the majority of the scenarios in the study, including the passive behaviour. North of Faial population, (L#8), reveals a higher connectivity exchange with the other groups, settling in all the other populations (considering the different scenarios) but receiving fewer larvae from other populations. These results can support the higher abundance of *C. affinis* found in these two seamounts when compared with the coastal zones of the Azores (Santos et al. 2021).

Menez Gwen (L#2) also has a higher abundance of this species in the Azores. Recent studies, after the identification of a new hydrothermal vent in Gigante Seamount, suggest the hypothesis of a higher abundance of this species near hydrothermal vents (Santos et al. 2021). Model results show connectivity with different locations, including Açores bank in the CG, but mainly serving as a potential nursery area, receiving larvae from different releases in MAR, WG and CG. However, model domain limitations constrain the analysis of this location. L#2 is located near the domain borders, and a higher percentage of larvae are advected out of the domain, so these results may be underestimated. However, when analyzing the results of the passive larvae behaviour, this population reveals higher levels of connectivity, being the one with higher connectivity relations with a PLD of 23 days. The model domain limitation restricts the correct analysis of this population larval dispersal. However, it confirms that this location can receive larvae from different populations, and even with the underestimation caused by the domain limitation it reveals also potential as a sink area.

Seasonal spawning is determinant for population connectivity. Simulated larvae from the Formigas population (#L12) don't settle in any other population in the October scenarios. Also population L#10, in the East of the CG, receives fewer particles in October than in the March scenarios. This is a consequence of the hydrodynamic patterns, characterized by strong currents during October, at L#10 location dispersion particles, instead of retaining. The October spawning scenarios reveal fewer connectivity relations than the March scenarios. Several populations in the MAR group, namely Cavala, Ferradura and Gigante seamount (L#4, L#5 and L#6), don't receive any larvae from the other groups. Furthermore, Menez Gwen (L#2), Cavala (L#4) and Ferradura (L#5) don't reveal any self-recruitment. However, in the March spawning scenarios (except for behaviour_2) the populations from MAR receive particles from more populations than in October. It is clear a higher particle exchange from East to West in the October release, with larvae from the Eastern Group settling in the MAR populations. And from West to East, in the spawning release March. The dispersal patterns, in Figure 4.29, reveal a higher number of particles in the deeper layers, in the Western part of the domain, after the October release. The opposite happens in March, with a higher number of particles between CG and EG than in October. This is a sequence of the different hydrodynamic patterns in the middle of the water

column, around 700m depth. As was shown in section 1.3, during spring a strong current with higher velocities occurs between MAR and CG, inducing larval dispersal in this region, and during October, between CG and the EG.

The scenarios tested in this study indicate that the March spawning season and longer PLD can conduct to higher connectivity relations than the October scenario. However, the shorter PLD induces higher self-recruitment levels in all situations.

Model results show how larvae biological characteristics like the PLD and larvae behaviour, including vertical swimming activity, can have a large impact on larval dispersal patterns (Metaxas & Saunders 2009, Ross et al. 2020). Model results also suggest that the settlement velocity during the last development stage can be crucial for connectivity estimates. For this model application the velocity assumed for Behaviour_2, was based on the sinking rate measured by Kelly et al. 1982, in laboratory conditions, which may not reflect the real sinking rates in the environment, and results in lower connectivity patterns than for behaviour_1 and passive behaviour. No information was found in the literature about the settlement stage velocities for DSRC or other deep-sea species (Leis 2020). However, this model results suggest that the assumption of this velocity in this model configuration can incur low connectivity patterns.

The modelled larvae dispersal results for *Chaceon affinis* show a high dynamic connectivity among different locations. However with a low percentage of larvae exchange (when comparing with case-study 1, using the same methodology but with different biological traits, the percentage of larvae exchange is one order of magnitude lower). Although an adequate flow of larvae among sub-populations is crucial for the sustainability of marine resources (Phelps 2015), larvae reaching a site does not necessarily equate to successful recruitment. Furthermore, the transition from pelagic larva to benthic juvenile and on to adulthood is dependent on a variety of post-settlement processes, not considered in this study (Cowen & Sponaugle 2009, Kough 2014).

All these scenarios must be analysed considering the inherent model limitations and bearing in mind all the theoretical assumptions taken, in the absence of detailed biological traits and larval behaviours (Bode et al. 2019). Nevertheless, this methodology shows capabilities to assess larval dispersal with swimming behaviour, and can be used to support multidisciplinary studies on population stock assessment, and, in particular for the *Chaceon affinis* species.

4.5.5. Conclusions – Case study 2

The modelling methodology taken in this study was able to simulate the swimming surface-oriented behaviour, enabling tracers to achieve the surface layers, and mimic the behaviour observed for these deep-sea larvae, that were collected at the surface in different studies (Tuset et al. 2011, Landeria & Tamura 2018). This approach represented an initial step to understanding the factors determining larval dispersal patterns of this species in the Azores.

Model results show how the hydrodynamic patterns in the region have a strong influence on particle dispersal, producing different connectivity results for the different seasonal scenarios (March versus October), and for the different simulations time (reflecting the PLD) and larvae behaviours. Moreover, the uncertainties about larvae swimming behaviours can originate from different connectivity relations.

General results of this biophysical model application suggest that populations of *Chaceon affinis* in the Azores may be connected. Simulated larvae from the WG (Flores island), and larvae from the EG settle in the CG and in the MAR populations. Populations in MAR, namely Voador Seamount are important sink and source of larvae for the Azores region.

The low percentage of larvae exchange also indicates that the populations might be isolated and that despite the populations being connected, caution should be made in the management of the populations confirming the reserves' before their exploitation.

This particle tracking model approach can be valuable for supporting decision-making regarding the establishment of protected areas and fisheries assessment studies for this DSRC species. Further studies in distribution and population dynamics, that this species might require in the Azores, can also be supported by this approach in order to guarantee the protection of this species, before the development of any fishery activity (Santos et al. 2019). Nevertheless, a multidisciplinary approach, must always be used together with ecological and biological studies, and if possible including population genetics (Swearer et al. 2019, Busch et al. 2021). Different habitats can have different species-specific effects on movement (Kool et al. 2013). A further

study should also consider the deep-seabed and neighbourhood characteristics, as well as local landscape aspects, providing a better understanding on larval dispersal (Combes et al. 2021).

The biophysical model provides predictions of the presettlement distribution of larvae, but it does not account for post-settlement processes such as predation and competition, which will reduce recruitment success. A comprehensive study of hydrologic data, particle motions, genetic data sets (Feng et al. 2017), and correction for natural mortality and habitat suitability would also aid the understanding of the dynamics involved.

4.6. Final discussion

Larval dispersion is fundamental to population dynamics, and an important topic regarding deep-sea management and conservation plans (Cowen & Sponaugle 2009, Gary et al. 2020, Combes et al. 2021). Many benthic organisms, not only sessile like deep-sea sponges, but also moving organisms like DSRC, rely on the larval stage as the only opportunity for any significant migration between local populations, and population resilience (Wang et al. 2021). Therefore, understanding the drivers of larval dispersal, and their spatial and temporal constraints is of the utmost importance to for marine managers and ecologists (Ross et al. 2020).

This study used a 3-D biophysical particle tracking model to simulate larval dispersal of two different organisms, to assess population connectivity.

The findings of this work show how the regional patterns of the currents drive the larval dispersion. Due to the dynamic temporal and spacial hydrodynamic patterns in the region, the spawning time and the PLD are determinant factors for larval dispersion and population connectivity.

Model results indicate the existence of connectivity between *Pheronema carpenteri* sponge aggregations in the Azores. Central Group seems to have well-connected populations including the MAR. The East Group populations are isolated. The West Group has connectivity with the Central Group. East populations shall be preserved, as also the Central Group populations as source populations for several locations. These results reinforce the importance of maintaining the protection efforts in the MPA (Condor and Princesa Alice), once they are important source populations.

In what regards *Chaceon sp.* Despite the high connectivity of the most plausible scenario, the low percentage of successfully settled larvae demands caution towards any future exploitation.

Larvae behaviour

Deep-sea sponge larvae are Lecithotrophic (non-feeding) (Maldonado & Young 1999), typically associated with shorter planktonic larval duration (PLD) (Yearsley & Sigwart 2011). In contrast with the planktotrophic larvae from the DSRC (Tuset et al. 2011), which are believed to have longer PLD from 23 to 125 days (Kelly et al. 1982). Simulated dispersion patterns reveal the importance of the PLD on larval dispersion and population connectivity. Model results reveal higher dispersion potential, with longer PLD. Therefore more connectivity among different populations. However, lower self-recruitment in larger PLD scenarios.

In the case of *P. carpenteri* larger PLD scenarios conduct in higher connectivity relations, however, lower self-recruitment in the different populations. The longer PLD studied in the *C. affinis* case study conducts to higher travel distances and dispersion patterns. However, with less percentage of particles exchange. Results of these two case studies show how larval behaviour influences dispersal and travel distances ((Cowen & Sponaugle 2009, Kough et al. 2013)).

Considering passive behaviour, travel distances can vary one order of magnitude when considering a PLD of 23 or 125 days, and when adding a swimming behaviour even more. The swimming behaviour estimated for *C. affinis* larvae increases travel distances up to to hundreds of kilometres allowing the potential connectivity between populations in Mar da Prata and Flores islands.

Different studies show the relevance of investigating a range of possible behaviours to assess different dispersal and connectivity patterns between different populations (Kough et al. 2013, Paris et al. 2013, Holstein et al. 2014, Gary et al. 2020).

In this work, different behaviours are tested (PLD, spawning seasonality, swimming behaviour). And the swimming behaviour reveals to have a large impact on larvae travel distance. Although, concerning mortality, this model uses a fixed half-life concept, with no time-varying mortality. Which is believed to occur in the sea (Connolly & Baird 2010, Leis 2020).

Behaviours in this study are not constrained by the limits of larvae energy stores. However, longer PLD increase the probability of planktonic mortality, reducing post-settlement growth or survival (Metaxas & Saunders 2009).

MPA and the importance of larval dispersal for the resilience of populations

Connectivity among different benthic populations promotes their increasing their genetic diversity (Busch et al. 2021, Wang et al. 2021), and the resilience of the species (Bracco et al. 2019), contributing to their ability to adapt to environmental changes and anthropogenic stressors (Connolly & Baird 2010, Foster et al. 2012, Holstein et al. 2014).

Larval dispersal models can be used to generate a dispersal assessment of an existing MPA network (Ross et al. 2017). A study from Fox et al (2016) demonstrated significant climate-driven alterations in the connectivity of sessile organisms (specifically for CWC). Morato et al. (2020) predicted a large reduction in a suitable habitat of selected deep-sea species (CWC and deep-sea fishes) in the North Atlantic, under future climate change scenarios. Therefore, these connectivity patterns remain to be tested for future climate scenarios. The use of this biophysical model can be used to support these studies, together with habitat suitability modelling and species distribution modelling.

Model application constraints and limitations

Quantitative versus qualitative approach

In this study, a quantitative approach, considering population size or reproduction rate, was not used. Al the populations are simulated with the same number of particles, not reflecting population abundancies. However, once calibrated all the particles simulated are valid. This calibration was performed. Therefore all connections that occur are considered valid. Even if the model estimates that only one particle has settled, this is a valid and potential connection. In nature these unlikely events can happen, long-lived species colonies that live for hundreds of years need a single larva to become established (Botsford et al. 2009).

Model connectivity results may indicate potential qualitative, but not quantitative connectivity. So, when extrapolated for a more complex study, including population abundancies or other

fisheries relevant features, these findings might be even more relevant. Despite all the model limitations, these applications provide a useful tool for decision-making and are a powerful tool for testing hypotheses about marine dispersal.

The major limitation of larval dispersal models is the lack of validation and the difficulty of doing it in the deep-sea (Swearer et al. 2019, Leis 2020). This enforces the necessity of using an accurate and validated hydrodynamic model is crucial. In this study, the hydrodynamic model was previously validated for the entire water column (see CHAPTER 2). However, this model, like many other oceanographic models was not validated for the bottom currents. The complex topography of the Azores (Morato et al. 2008, Peran et al. 2016) can induce local mesoscale activity (Holliday et al., 2000) which likely promotes greater local retention therefore differences in modelled predictions (Ross et al. 2020). The calibration of the model at the deep-sea bottom layers, and also the better bottom resolution would minimize these limitations.

Furthermore, deep-sea particle tracking models is neither validated nor their predictions (larvae trajectories) can be tested or proved (Leis 2020). Empirical data required for model assessment is costly to obtain. These costs increase for the deep-sea, and over broad scales (Kough et al. 2013, Bode et al. 2019). However, different studies using coupled biophysical particle tracking models, for assessing marine dispersal reveal confident results on these modelling tools. Mainly verifying model dispersal and connectivity results comparing results against genetic studies (Selkoe & Toonen 2011), and specifically deep-sea sessile organisms (e.g. for corals (Wood et al. 2014) (Ross et al. 2017)).

Biophysical model sensitivity analysis for parameters like mortality, age of competency, swimming velocity, age of competency, among others for which empirical data are scarce could improve model accuracy (Paris et al. 2013)

4.7. Final Remarks

The findings of this study represent an important development in assessing deep-sea larvae connectivity using modelling tools. Model results show how the hydrodynamic patterns in the region have a strong influence on particle dispersal, producing different connectivity results for

the different seasonal scenarios and the different larvae behaviours (PLD, swimming behaviour, settlement and recruitment).

The differences obtained in the larval dispersal and connectivity responses over the years 2017 and 2018, highlight the model's capability to simulate the hydrodynamic patterns of the region, characterized by a high variability from the surface up to the deep-sea (Sala et al. 2013, Lima et al. 2020). This model application was able to simulate important eddies, and major currents, and identify temporal features that form hydrodynamic barriers or contribute to particle retention or dispersal. and hydrodynamic patterns allow achieving the proposed objectives of studying larvae dispersal over the archipelago, at a regional scale.

It is also worth mentioning that the hydrodynamic model was able to simulate the seasonal and spatial variability of the current system around the archipelago in the entire water column, responsible for the generation of highly spatiotemporally-variable submesoscale patterns that drives these deep-sea larvae dispersal.

Major results indicate that sponge aggregations can present physical connectivity. Sponge aggregation from the Central Group can represent a significant sink and source for *P. carpenteri* sponges in the Azores, by receiving larvae from different sponge aggregations. Results reinforce the importance of maintaining the protection efforts in the MPA (Condor and Princesa Alice), once they are important recruitment areas. Despite no estimated connectivity between the sponge aggregations of EG with CG, model results show potential connectivity from both groups with João de Castro seamount pointing out a possible interconnection between these groups.

Conversely, the longer PLD considered in the *C. affinis*, as well as the swimming behaviour, conducts to higher travel distances and dispersion patterns, creating more patchy connectivity patterns all over the Archipelago. However, with less percentage of particles exchange. Populations from the Western group, in Flores island can be connected with the populations from the central group. Also, larvae from the EG can settle in the MAR locations. Model results indicate that the populations in MAR, namely Voador seamount may be an important recruitment area and nursery for the Azores region.

A limitation of this model application is the temporal scale of the entire simulation, a multiyear study can provide more detailed information on population connectivity. Another caveat

concerns to the model resolution. The model simulates the larval dispersal at a regional level, but not at a seamount scale. However, it is worth saying that this methodology proves to be suitable for larval dispersal assessment, and easily can be applied in a nested model and a high-resolution model. Furthermore, this modelling approach can provide valuable information for the implementation of protection plans and the establishment and prioritization of future management plans.

Chapter 5

Environmental characteristics at deep-sea sponge locations in the Azores

5.1. Abstract

Taking advantage of the 3-D hydrodynamic and biogeochemical models implemented for the Azores region, the environmental conditions were studied at the sponge aggregation locations. A spatial and seasonal analyses was performed at the sponge ground locations, and along the entire water columns. The objective is to better characterize the environmental conditions at this specific *Pheronema carpenteri* sponge grounds.

5.2. Introduction

Deep-sea sponges are often widely distributed as isolated specimens, patchily distributed across space, and as dense sponge aggregations in the North Atlantic (Maldonado et al. 2015, Pham et al. 2015, Wang et al. 2021).

Mainly forming monospecific populations, *Pheronema carpenteri* aggregations were documented in the Porcupine Seabight (Rice et al. 1990), on the continental slope of Morroco (Barthel et al. 1996), and in the Azores, at different locations and seamounts (Xavier et al. 2015, Friedlander et al. 2019, Water & Water 2019, Colaço et al. 2020, Somoza et al. 2020). Although they are believed to support a high biological diversity (Henry & Roberts 2014), the ecological importance of the deep-sea sponges is greater where they form dense aggregations, known as "sponge grounds" (Wang et al. 2021). Due to their functional significance and perceived vulnerability to disturbance, and environmental change, sponge grounds have been classified as a 'habitat under immediate threat and/or decline' by the OSPAR Commission (Ospar 2010), and a vulnerable marine ecosystem (VME) by the FAO (FAO 2008) (Roberts et al. 2021).

Deep-sea sponge aggregations can play an important role in primary productivity and in the biogeochemical cycles (Cathalot et al. 2015). Specifically the hexactinellid sponges like *Pheronema carpenteri* are also characterized as biodiversity hotspots, not only by their high three-dimensional structural complexity but also due to the role of spicule mats created by their senescence and death(Henry & Roberts 2014). *P. carpenteri* aggregations serve as a sink in the marine silicon cycle which is thought to influence primary productivity and the carbon cycle (Maldonado et al., 2005; Hendry et al., 2019), and also by acting as a silicon reservoir (Maldonado et al., 2011).

Several studies have looked at the environmental and biogeochemical deep-sea characteristics that may explain their distribution (Rice et al. 1990, Bett & Rice 1992, Barthel et al. 1996, White 2003, Howell et al. 2016, Vieira et al. 2020). Rice et al. (1990) suggested that *Pheronema* aggregations might be located close to, but not within locations where the bottom topography can induce an increase of near-bottom tidal current velocities. However, because they may not be able to support strong current velocities, sponges would rather benefit from the resuspended or undeposited organic matter carried by these higher currents (Rice et al., 1990). Howell et al. (2016), used environmental parameters, Maximum Entropy Modelling and presence/absence data, to study the drivers for *P. carpenteri* distribution, indicating that water depth and bottom water temperature could be predictors of the distribution of *P. carpenteri* aggregations. Besides being siliceous sponges, silicate was not the most relevant parameter. Although, current speed, or rather hydrography, is also thought to play an important role in driving the distribution of *P. carpenteri* sponge habitat (Howell et al. 2016). There are no existing data on their temperature tolerance and they can be found in a temperature range of 2.73–20.9 °C, and with silicate values ranging from 0.42 to a maximum of 0.62 mgSi/l (Howell et al. 2016). In the Porcupine Seabight (Bathyal NE Atlantic), to study the importance of deep-sea currents, White et al. (2003) use bottom currents measurements at two different locations, with and without *P. carpenteri* aggregations, revealing higher current velocities in the second one. At a north Atlantic scale, Roberts et al (2021), studying deep-sea sponges' distribution (and not specifically *P. carpenteri*), concluded that water masses and major currents constrain the distribution of deep-sea sponges on a basin-scale (Roberts et al. 2021).

In the Azores, several sponge aggregations have been identified, as previously referred on Chapter 4. From these sponge aggregations, the ones in the South of Pico, Princesa Alice, and Condor Seamount were reported as the a dense sponge grounds in the Azores (Figure 5.1) (Colaço et al. 2020).

Figure 5.1- *P. carpenteri* aggregation im South of Pico and individual sponge sample (a), and individual sponge sample from Princesa Alice Bank. Photo credits from: a) REBIKOFF FOUNDATION, and b) (Colaço et al. 2020).

The Azores region is under the influence of different oceanographic processes and water masses (Caldeira & Reis 2017). Characterized by a high spatial, seasonal, and inter-annual variability of marine climatology (Amorim et al. 2017), the understanding of the environmental factors that contribute to the deep-sea benthic organisms' distribution is an issue under research.

In this chapter spatial and temporal biogeochemical properties at specific sponge grounds of the species *Pheronema carpenteri*, are studied taking advantage of the 3-D biogeochemical model built in Chapter 3.

5.3. Methodology

5.3.1. Study site

The *Pheronema Carpenteri* sponge aggregations considered in Chapter ## of this dissertation were used for this study. (Figure 5.2 and Table 5.1).

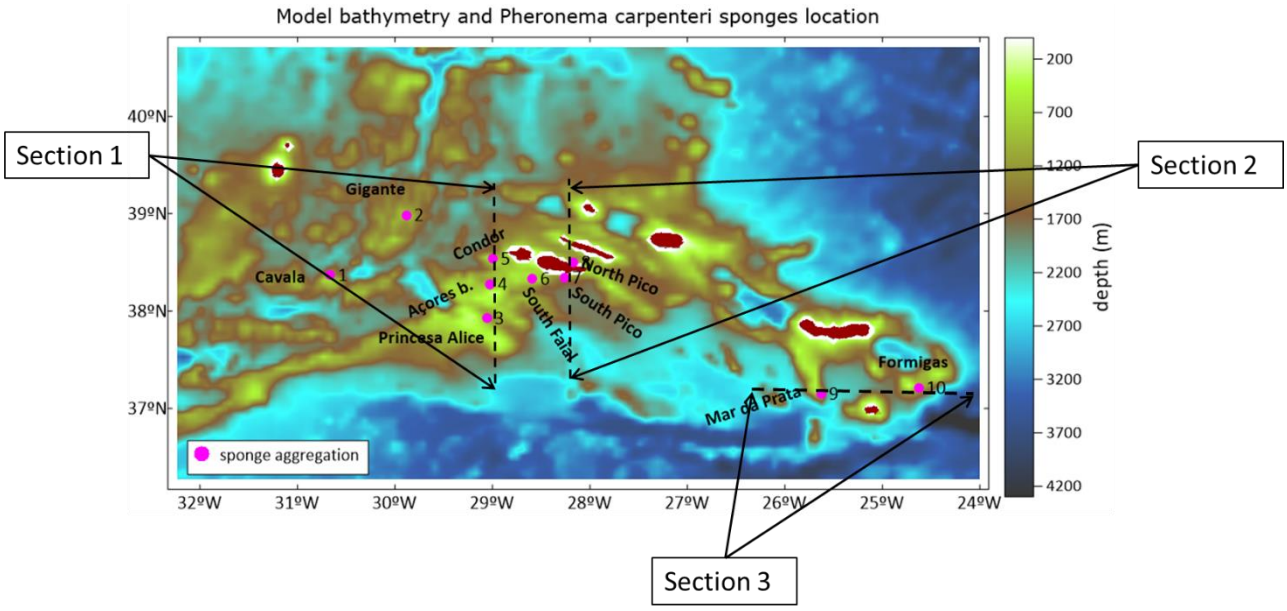

Figure 5.2 Representation of sponge aggregations, with pink circles, and the different sections used to analyse model results

Table 5.1- *Pheronema carpenteri* sponge aggregations in the study, their location, depth, source and name/location

Sponge location	Longitude (◦W)	Latitude (◦N)	Depth (m)	Nome/localização	Group
1	-30.6701	38.3632	900	Cavala	MAR_1
2	-29.88809	38.98353	766	Gigante	MAR_2
3	-29.06232	37.9183	900	Princesa Alice	CG_1
4	-29.02941	38.273	825	Açores Bank	CG_2
5	-28.99877	38.53281	775	Condor Seamount	CG_3
6	-28.59288	38.32531	630	South of Faial and Pico	CG_4
7	-28.26657	38.33921	1000	South of Pico	CG_5
8	-28.1735	38.49624	822	North of Pico	CG_6
9	-25.63083	37.14111	780	Oeste São Miguel (Mar da Prata)	EG_1
10	-24.63	37.205	904	Formigas	EG_2

Table 5.2. Sections used for model results analyses, type of section (meridional or zonal, location, limits and sponge locations across de section

	Zonal/Meridional	Coordinates (◦)	Limits	Sponge Locations
Section 1	Zonal	-29.05◦W	37.5 to 39◦N	Princesa Alice, Açores Bank and Condor
Section 2	Zonal	-28.23 ◦W	37.75 to 39◦N	South of Pico and North of Pico
Section 3	Meridional	38.5◦N	36.2 to 40.8 ◦W	Mar da Prata and Formigas

5.3.2. Biogeochemical model results

Biogeochemical data obtained from MOHID biogeochemical model implemented in the scope of this PhD work were used in this study. The variables used are those shown in Table 5.3. Model results are provided on an hourly based, with a 6km resolution, and a vertical variable resolution. Model results were quantified at the sponge aggregation locations, and along different sections of the domain. Sections and the locations in the study are represented in Figure 5.2 and described in

Table 5.2. for the years 2017 and 2018. Phytoplankton was considered for the sponge location but at the surface.

Table 5.3- State MOHID variables used

Variable	Description	Units	Dt	Details
ϕPhy	Phytoplankton concentration	mgC/l	Hourly	3D
ϕNO3	Nitrate concentration	mgN/l	Hourly	3D
ϕIP	Inorganic phosphorous concentration	mgP/l	Hourly	3D
ϕDissSi	Dissolved silica concentration	mgSi/l	Hourly	3D
ϕOxy	Dissolved Oxygen concentration	mgO2/l	Hourly	3D
ϕTemp.	Temperature	ºC	Hourly	3D
ϕSal.	Salinity	PSU	Hourly	3D
Velocity mod	Velocity modulus	m/s	Hourly	3D
Velocity w	Velocity vector w (vertical velocity)	m/s	Hourly	3D
Depth	Depth	m	--	--

5.3.3. Data processing and statistical analysis

Biogeochemical model results are analysed at the sponges' aggregation locations, at the bottom depth, and also along the water column. Firstly, to avoid the redundancy of information in the variables, a correlation analysis was carried out between them using Spearman's rank correlation coefficient, eliminating variables with a redundancy greater.

For analysing biogeochemical data boxplots representing the median, the upper and lower quartiles, and the minimum and maximum data values were generated for the sponge aggregation points. Different sections were defined to analyze model results (Figure 5.2). These sections are defined over a fixed longitude or latitude, so, they cross different sponge aggregations, and pass near others. For this reason, some mismatch can exist between the representation of the sponge aggregation and the represented bathymetry. Figure 5.2 shows the representation of the different sections crossing different sponge locations. Details of each section are described in Table 5.2. Results were analysed for the entire period of 2017 and 2018 (average values).

5.4. Results and discussion

The Spearman rank correlation coefficient (ρ), obtained between the different variables was greater than 0.7 for Salinity and Temperature (ρ=0.74), and between the nutrients. Phosphate is highly correlated with Nitrate and Silicate (ρ=0.89 and ρ=0.83. Both salinity and Phosphate parameters were excluded from this analysis.

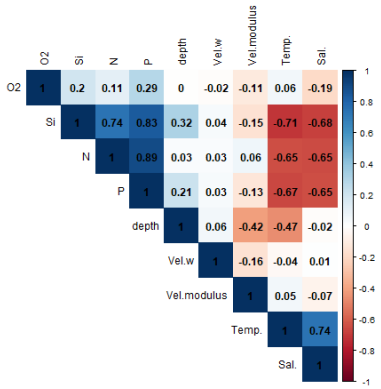

Figure 5.3- Spearman's rank correlation coefficient for the biogeochemical parameters in the study: Oxygen (O2), Dissolved Silica (Si), Nitrate (N), Phosphate (P), Velocity w (Vel.W), velocity modulus (Vel.modulusmod), temperature (Temp.) and salinity (Sal.) at the sponge locations.

5.4.1. Environmental data at *Pheronema carpenteri* locations

Environmental conditions at the sea bed show variability between the different sponge locations (Figure 5.4). A longitudinal gradient is denoted for the nutrients.

Nutrient concentrations (nitrate, phosphate and silicate) are closely related, with, higher concentrations at most Western locations (from Cavala to Condor Seamount), and lower in East. Apart from South of Faial. For temperature, the higher temperatures are at the sponge locations ner Faial and Pico islands, namely South of Faial, South of Pico, and North of Pico.

Nitrate concentrations range from 0.21 to 0.262 mgN/l (standard deviation 0.012). With low variation at sponge locations from Cavala to Condor. Contrasting with the location from South of Faial to Formigas. For Inorganic phosphorous and dissolved silica more variation is identified. Dissolved silica concentrations varies from 0.191 to 0.322 mgSi/l (maximum standard deviation 0.028), and phosphate from and 0.027 to 0.037 mgP/l (maximum standard deviation 0.0019). Dissolved silica concentrations present higher variation at the locations at Princesa Alice, Açores bank, Condor and South of Faial.

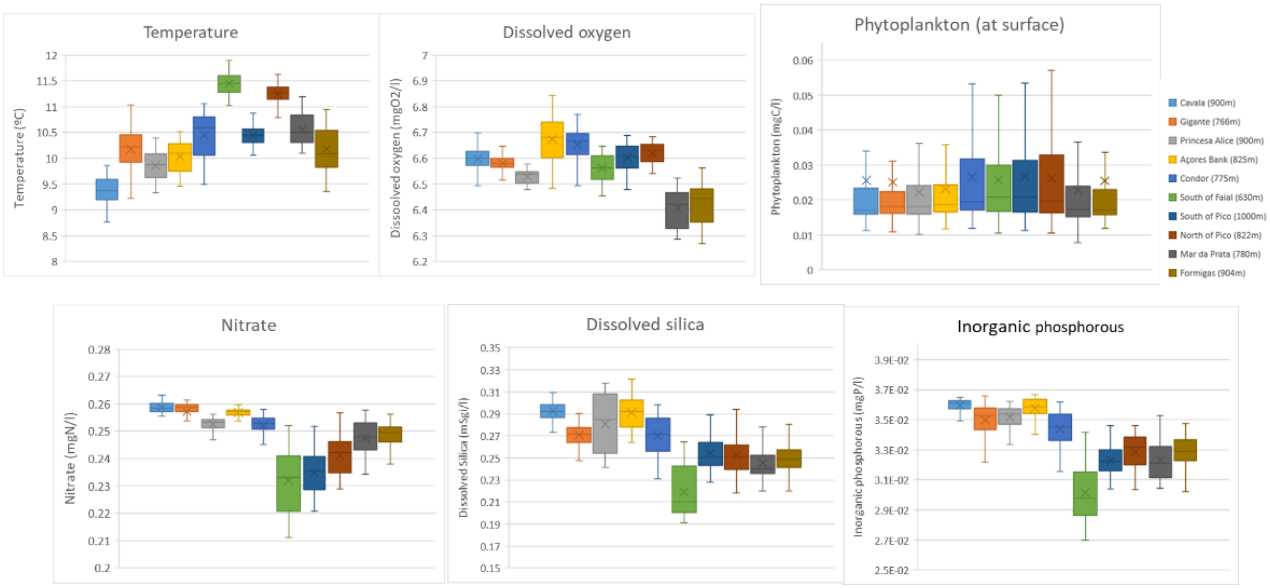

Figure 5.4- Boxplots of biogeochemical parameters (temperature, dissolved oxygen, nitrate, dissolved silica and inorganic phosphorous) for the sponge aggregation locations in the study. Boxplots are created using the first and third quartile, whiskers represent the minimum and maximum values.

Table 5.4- Biogeochemical model results at sponge aggregations, maximum, minimum and standard deviations for temperature, nitrate, dissolved silica, dissolved oxygen, inorganic phosphorous and salinity, for the period 2017-2018.

	Temperature (◦C)		Nitrate (mgN/l)		Dissolved Silica (mgSi/l)		Dissolved Oxygen (mgO2/l)		Inorganic Phosphorous (mgP/l)		Salinity		Phytoplakton (mgC/l)	
Station	Min-max	StDev	Min-max	StDev	Min-max	StDe v	Min-max	StDev	Min-max	StDev	Min-max	StDev	Min-max	StDev
Cavala	8.77 - 9.22	0.30	0.260 - 0.262	0.0005	0.285 - 0.300	0.004	6.55 - 6.58	0.01	0.035 - 0.036	0.0002	35.35 - 35.38	0.01	0.011-0.0169	0.021
Gigante	9.22 - 11.04	0.37	0.242 - 0.261	0.0039	0.248 - 0.290	0.009	6.44 - 6.65	0.03	0.032 - 0.037	0.0010	35.22 - 35.62	0.08	0.0110-.014	0.018
Princesa Alice	9.34 - 10.40	0.28	0.244 - 0.256	0.0027	0.242 - 0.318	0.028	6.48 - 6.58	0.03	0.033 - 0.036	0.0007	35.43 - 35.55	0.04	0.0100-.064	0.009
Açores Bank	9.46 - 10.52	0.3	0.248 - 0.260	0.0015	0.26 - 0.322	0.015	6.48 - 6.85	0.09	0.033 - 0.037	0.0007	35.32 - 35.51	0.05	0.0120-.075	0.011
Condor	9.49 - 11.06	0.42	0.238 - 0.258	0.0034	0.231 - 0.299	0.017	6.47 - 6.77	0.07	0.032 - 0.036	0.0012	35.25 - 35.55	0.08	0.0120-.083	0.014
South of Faial	11.03 - 11.90	0.22	0.211 - 0.252	0.0115	0.191 - 0.265	0.023	6.45 - 6.65	0.05	0.027 - 0.034	0.0019	35.48 - 35.61	0.03	0.0110-.105	0.014
South of Pico	10.05 - 10.87	0.18	0.221 - 0.252	0.0074	0.228 - 0.289	0.015	6.48 - 6.69	0.05	0.030 - 0.035	0.0009	35.44 - 35.60	0.04	0.0110-.106	0.015
Nort of Pico	10.70 - 11.63	0.19	0.229 - 0.257	0.0066	0.218 - 0.298	0.021	6.54 - 6.68	0.04	0.030 - 0.035	0.0011	35.45 - 35.62	0.04	0.0110-.095	0.013
Mar da Prata	10.09 - 11.20	0.29	0.234 - .258	0.0064	0.220 - 0.279	0.014	6.29 - 6.52	0.07	0.030 - 0.035	0.0013	35.43 - 35.76	0.08	0.0080-.111	0.015
Formigas	9.36 - 10.95	0.4	0.233 - 0.256	0.0043	0.220 - 0.284	0.013	6.24 - 6.56	0.08	0.030 - 0.036	0.0010	35.42 - 35.79	0.07	0.0120-.187	0.021

The lower dissolved oxygen concentrations are at Mar da Prata and Formigas aggregations, ranging from 6.29 to 6.52 and 6.24 to 6.56 mgO_2/l respectively. However, with higher standard deviation values (0.7 and 0.8 respectively). South of Faial is the aggregation exposed to higher temperatures, ranging from 11.03 to 11.90◦C. This is the shallowest sponge aggregation, at 630 meters depth. Contrasting with South of Pico aggregation, at 1000 meters depth. Princesa Alice distinguishes from the other locations by the higher variation of dissolved silica values. Alike Açores bank, this location presents the maximum dissolved silica values. Princesa Alice with 0.318 and Açores Bank with 0.322 mgSi/l.

Regarding the densest sponge aggregations in the study: Princesa Alice, Condor and South of Pico. Princesa Alice has higher dissolved silica concentrations and low oxygen concentrations. South of Pico, distinguish from the others by the water temperature, which faces the lower variances. At this location, the nitrate and the inorganic phosphorous have lower median values.

Phytoplankton concentration at the surface is higher in the sponge aggregations near the islands of the Central Group (Condor, South of Faial and South and North of Pico).

5.4.2. Environmental conditions along sections and bottom layer

The biogeochemical water profiles were analysed at the sponge locations along different sections of the domain. Sponge aggregations are located at the bathymetric range of the

minimum oxygen concentration values (Figure 5.5 and Figure 5.6). Zonal sections 1 and 2 have higher nutrient concentrations than meridional section 3.

Nutrient concentrations changes along the water column, with the characteristic increase from the surface up to the sea bottom (Amorim et al. 2017). At the sponges' depth, nutrient concentration achieves the maximum values, and the spatial and seasonal nutrient gradients are low. Only for the dissolved silica concentrations, some gradients can be identified at the different sponge locations. Sponge aggregations are located near the nutricline of 0.03mgSi/l. Results of average dissolved silica at the bottom layer (Figure 5.11**Error! Reference source not found.**), show the sponge location near this nutricline. For the temperature at the sponge locations, (Figure 5.12), it is clear a meridional gradient, with higher temperatures at western sponge locations. The lower oxygen concentrations are at Mar da Prata and Formigas sponge locations. This may be a consequence of the Mediterranean Water Mass, characterized by the lower oxygen concentration (Bashmachnikov et al. 2015), that influences the Azores region between 500 and 1200 meters depth (Palma et al. 2012).

The nutrient concentrations at the bottom depth is higher during the winter months (Figure 5.7). As a sequence of the nutrients input by the winter convection (Berline et al. 2007). However, the seasonal gradient verified at the sponge locations is very low. In the Meridional section, located across Mar da Prata and Formigas, the nutrient concentrations are lower, and the sponges' aggregations are located in the lower oxygen regions.

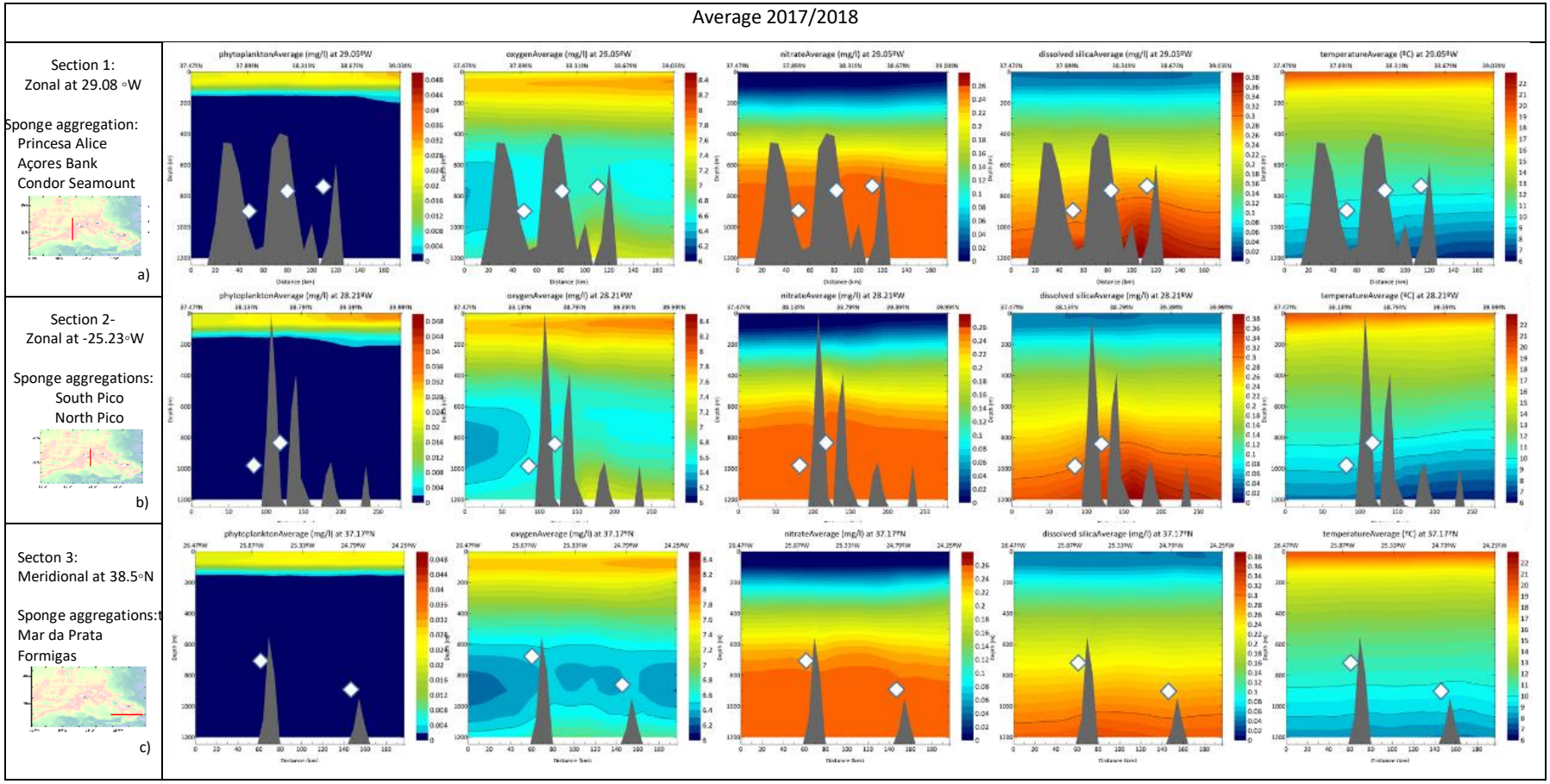

Figure 5.5 - Average model resuls for the period February 2017 to December 2018 for phytoplankton, dissolved oxygen, nitrate, silicate and temperature for 3 sections across different sponge aggregations, and selected locations in the study.

Average 2017/2018

Section 1:
Zonal at 29.08 ◦W

Sponge aggregation:
Princesa Alice
Açores Bank
Condor Seamount

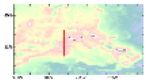

a)

Section 2-
Zonal at -25.23◦W

Sponge aggregations:
South Pico
North Pico

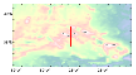

b)

Secton 3:
Meridional at 38.5◦N

Sponge aggregations:t
Mar da Prata
Formigas

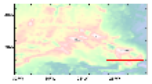

c)

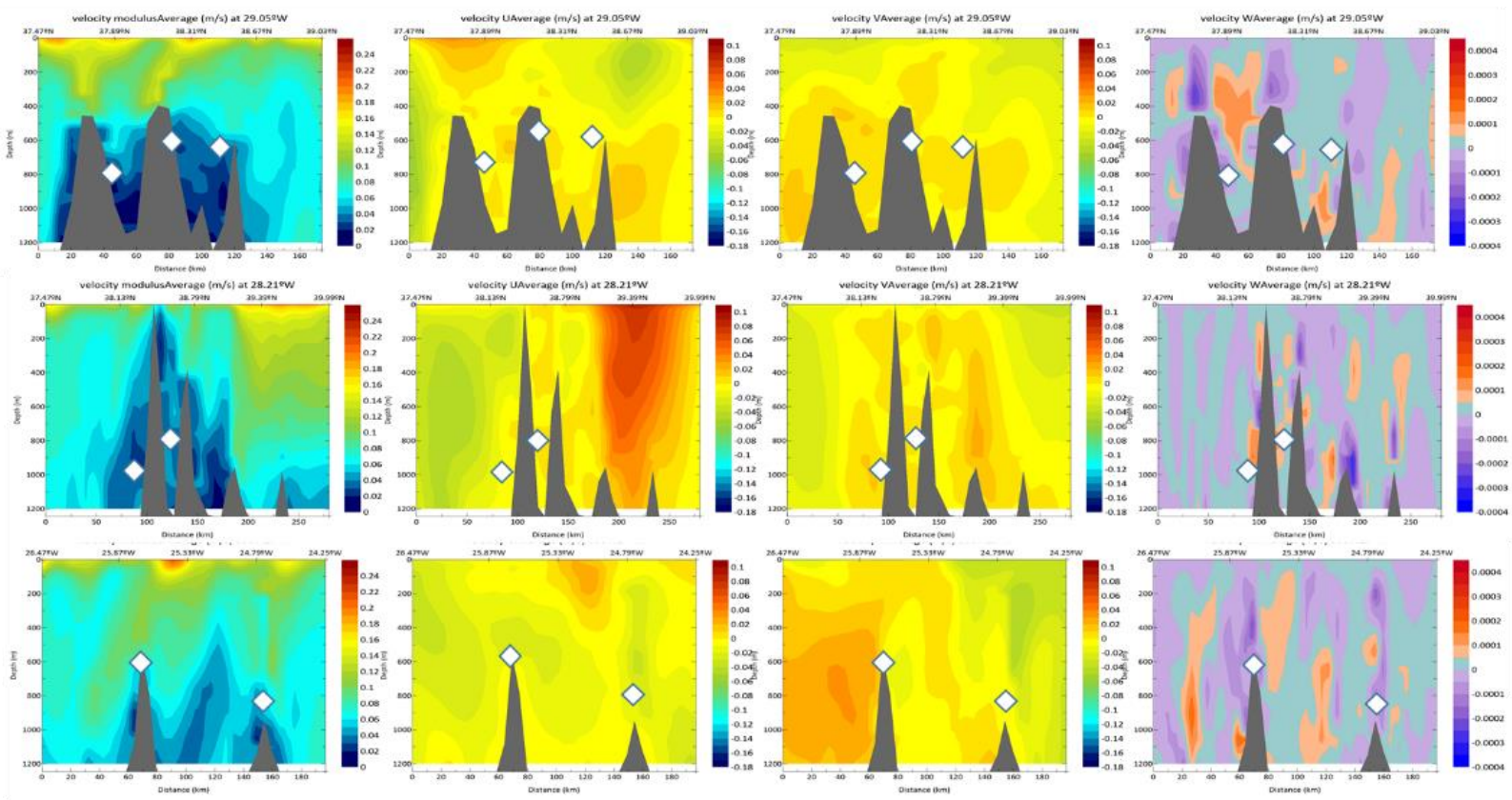

Figure 5.6- Average model results for the period February 2017 to December 2018 for velocity vectors u and v, velocity modulus, and velocity vector w, for 3 sections across different sponge aggregations, and selected locations in the study.

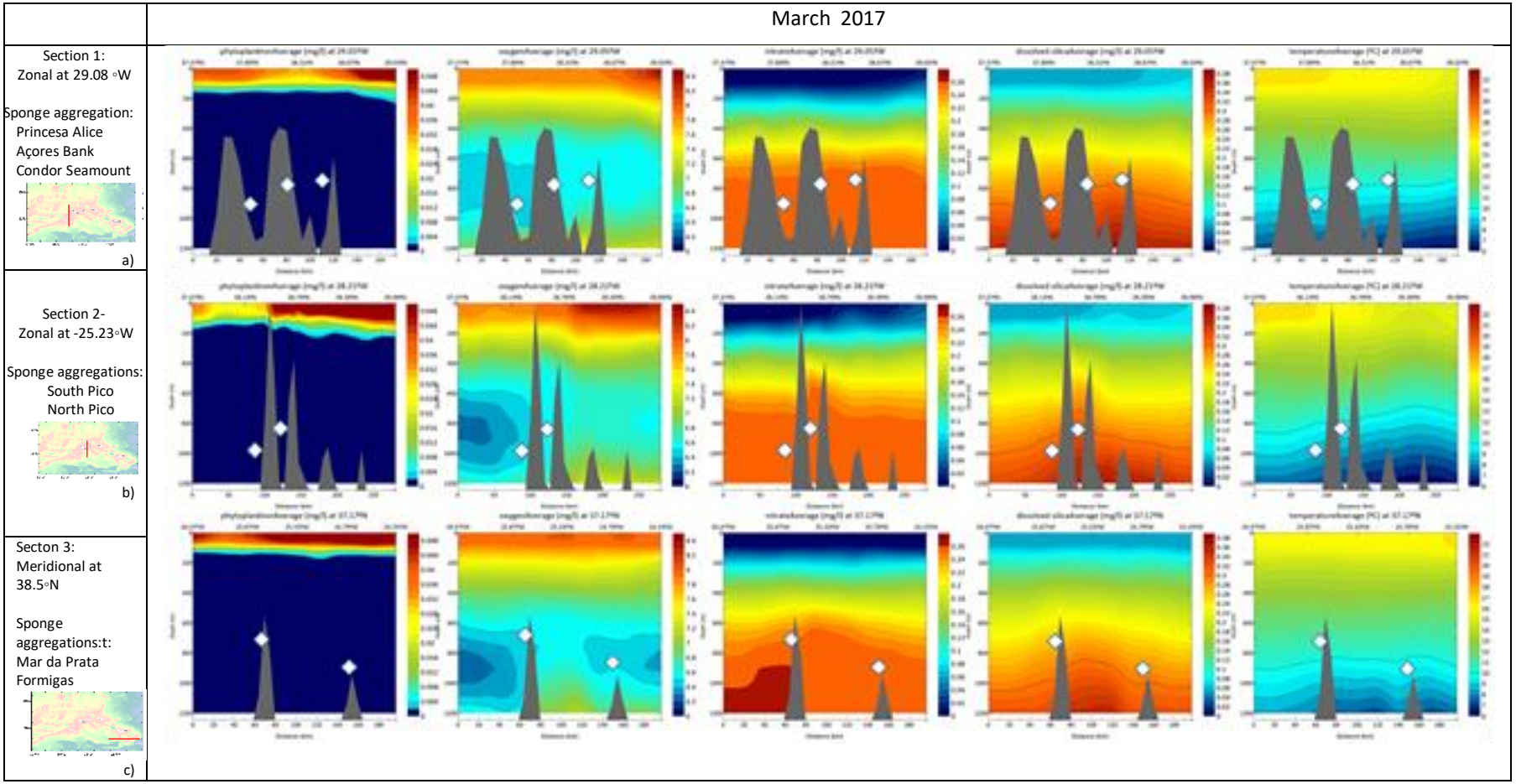

Figure 5.7- Monthly average of model results for March 2017, from the surface up to 1200 meters depth, for dissolved oxygen, nitrate, silcate and temperature, for sections 1, 2, 3 and 4 (top to down respectively). White mark represents sponge location. Bottom topography is represented in grey.

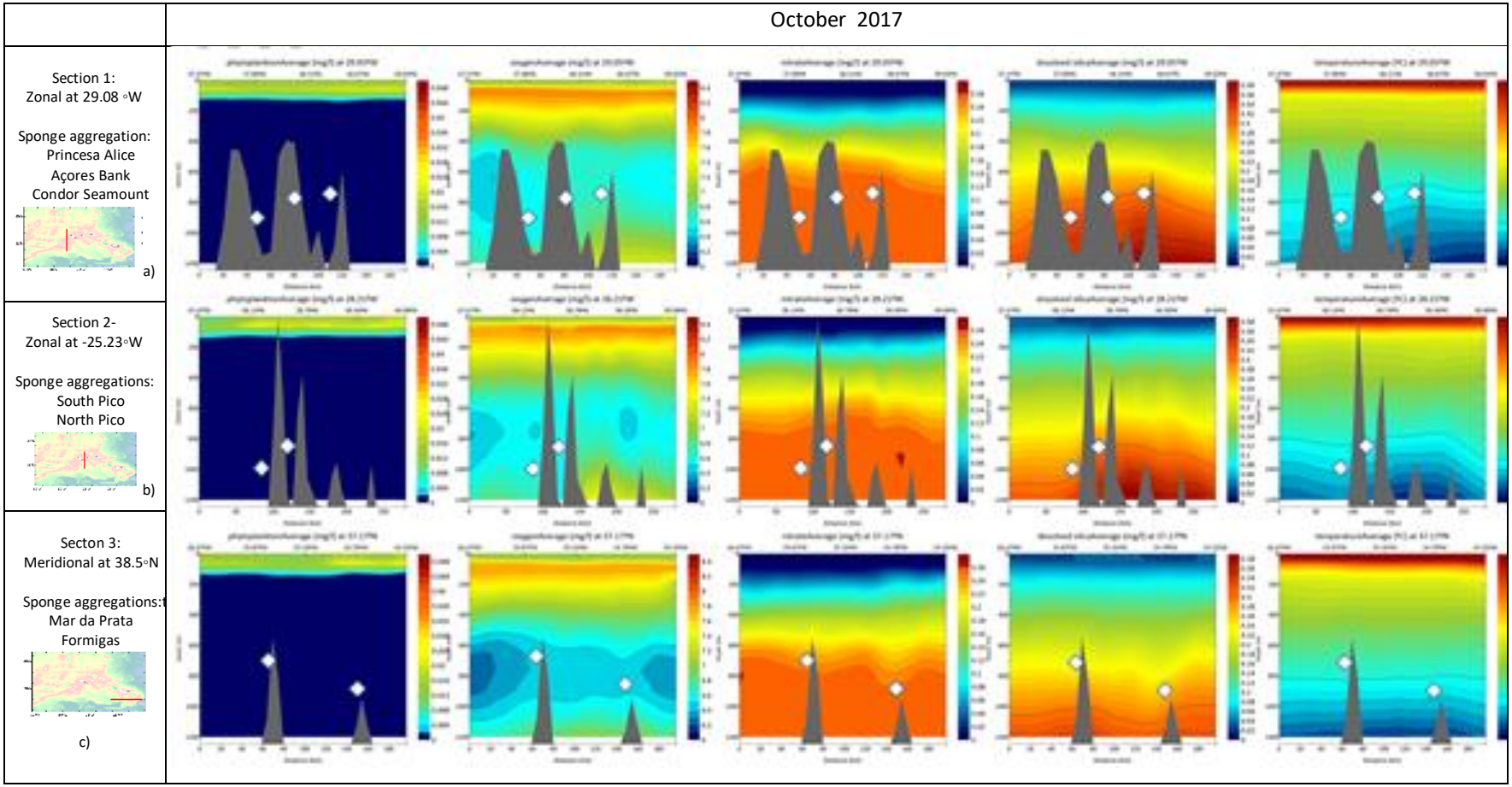

Figure 5.8- Monthly average of model results for October 2017, from the surface up to 1200 meters depth, for dissolved oxygen, nitrate, silcate and temperature, for sections 1, 2, and 3 (top to down respectively). White mark represents sponge location. Bottom topography is represented in grey.

Sponge aggregations are located in regions with lower velocities (Figure 5.9). The velocity is generally lower at the sea bottom, with lower values following the seamounts and deep-sea features. Results for vertical velocity (velocity w) have a high variability along the domain without a clear spatial pattern. This higher variability can be a sequence of its lower values. Only ate the South of Pico, and North of Pico, sponge locations a similar pattern can be recognized. At the sponge aggregations location, the velocity w is positive, indicating a vertical upwards direction. Model results suggest that sponge aggregations are located in regions with low velocity, but adjacent to locals with higher velocity (**Error! Reference source not found.**). This is visible for all t he sponge locations except for the South of Pico and North of Pico locations.

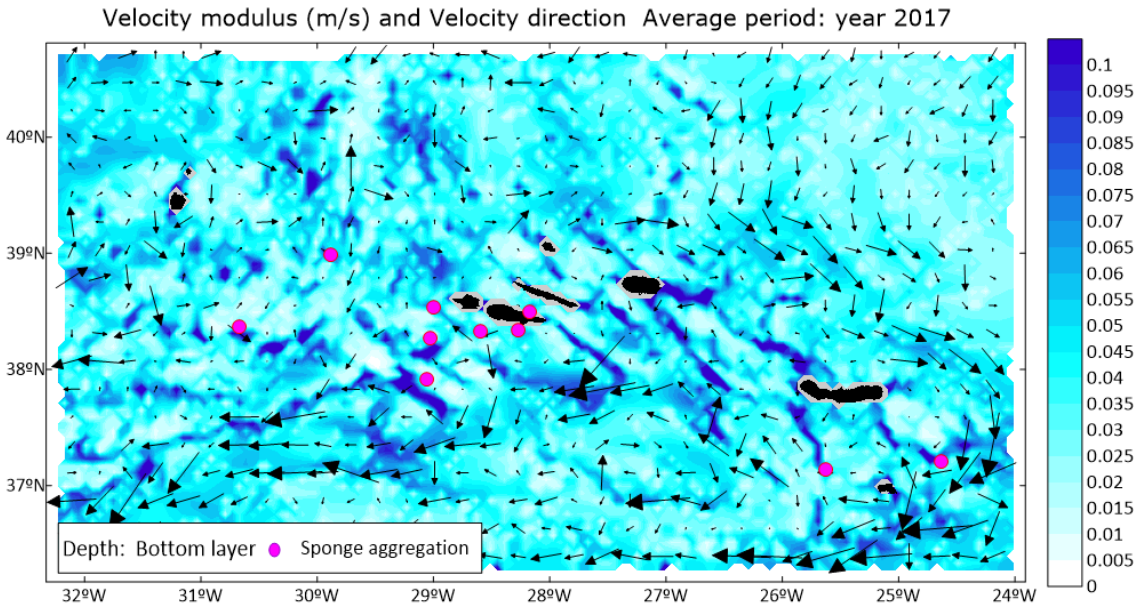

Figure 5.9- Average model results for velocity modulus at the bottom layer. Sponge locations are represented with a pink circle

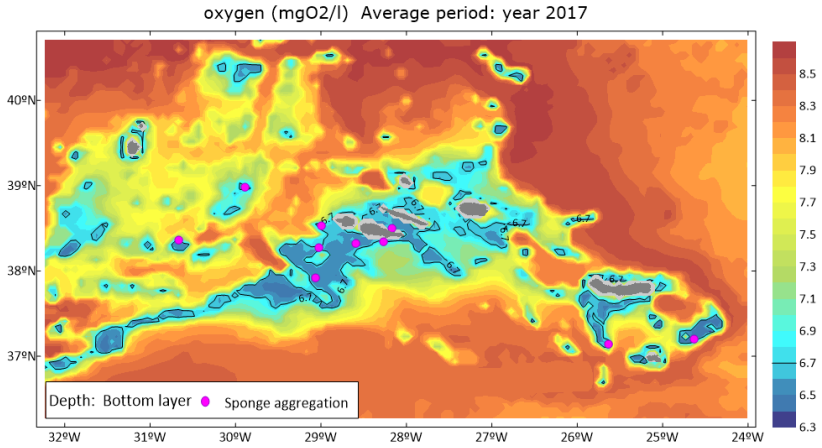

Figure 5.10- Average model results for dissolved oxygen at the bottom layer. Sponge locations are represented with a pink circle

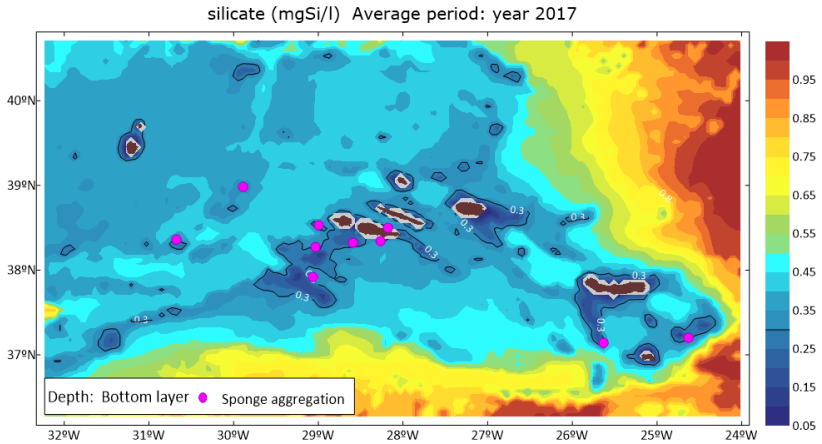

Figure 5.11- Average model results for dissolved silica at the bottom layer. Sponge locations are represented with a pink circle

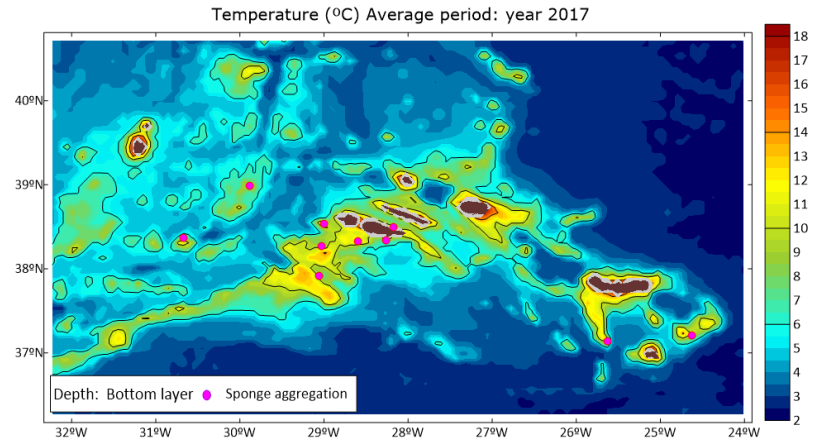

Figure 5.12-Average model results for temperature at the bottom layer. Sponge locations are represented with a pink circle

5.5. Discussion

Pheronema carpenteri aggregations in the Azores are found in a bathymetric range from 600m to 1200m. Of the 10 sponge aggregations in the study, even without a quantitative evaluation of the different aggregations' density, 3 locations are recognized as dense sponge grounds, at Condor, Princesa Alice and South of Pico, based on deep-sea observations (Creemers et al. 2019, Colaço et al. 2020).

Contrasting with the gradients in the water column, at the deep-sea floor the nutrient variation is very restricted, with lower spatial and temporal variations. Benthic fauna is believed to be very responsive to the episodic deposition of fresh phytodetritus in food variation (Ragueneau et al. 2000). So, small differences in nutrient concentrations may be relevant. Nutrient variation along the year is very tenue, however with higher concentrations during winter (Figure 5.7, Figure 5.8). Mainly related to winter convection (Yamanaka et al. 2004) and also by the absence of primary production and the settling of organic matter (Hirose and Kamiya, 2003). This nutrient distribution is also related to the water masses circulation in the region (Hirose & Kamiya 2003, Palma et al. 2012). These deep-sea sponge grounds are believed to have an important role in biogeochemical cycling, by filtering large quantities of water and serving as a sink of silicate (Maldonado et al. 2019). These inputs are not considered in this model dynamics, nor either in the other biogeochemical models (Samuelsen et al. 2022).

Sponge aggregations in the study are located in different temperature ranges, from 8.77 to 11.90 ◦C. Globally. In the North Atlantic, these sponges are found in a large temperature range, from 2.73 to 20.9 °C (Howell et al. 2016).

One of the sponge locations in the study, South of Pico, distinguish from the other by the lower water temperature variance (0.18°C), ranging from 10.05 to 10.87 °C. This is one of the known dense aggregations. This result might indicate that this range of temperature can be advantageous for this species, or that a lower variance of temperatures is beneficial. This lower temperature range also occurs for the North of Pico location. It can be related to their proximity to the island, being less exposed to the different water masses and seasonal currents.

Besides inhabiting regions above 700meters depth, these deep-sea sponges are under the influence of the primary production from the euphotic zone. Phytoplankton concentration at the surface, is higher for the locations near the islands of the Central Group (Condor, South of Faial and South and North of Pico). The phytoplankton concentration presents strong seasonal and spatial gradients. A deeper spatial and temporal analysis should be performed to study the relation of phytoplankton concentration and sponge locations. Also, phytoplankton influence is not immediate at the bottom layer and can take days months up to several months to reach these depths (Samuelsen et al. 2022).

Sponges aggregations are located in locations with lower velocities, Figure 5.9**Error! Reference s ource not found.**, but in the proximity of enhanced velocities. Only the South and North of Pico don't show any higher-velocity patterns in the vicinity. However, results along the different sections and at different periods show that at these sponge aggregations the vertical velocity vector is positive.

This supports the hypothesis of Bett and Rice (1992), White (2013), and Howell (2016) that these sponges might Inhabitat areas with lower bottom velocities, but under the influence of vertical velocities that induces the resuspension of particulate matter. However, a deeper analysis should be performed to better study these relations. This model resolution, 6*6 km might be insufficient to provide a categorical result. Also, the measurement of deep-sea currents can provide additional data to support this hypothesis.

5.6. Conclusions

Spatial and temporal biogeochemical properties at specific sponge grounds of the species *Pheronema carpenteri*, were studied, taking advantage of the 3-D hydrodynamic and biogeochemical models implemented in Chapter 2 and Chapter 3 of this thesis. Results show that sponges are located under steady environmental conditions.

Sponge aggregations are located in regions with lower nutrient gradients and low current velocity. Nutrients concentrations at these deep-sea sponges' locations varies from 0.21 to 0.262 (SD 0.012) mgN/l, 0.191 to 0.322 (SD 0.028) mgSi/l, and 0.027 to 0.037 (SD 0.0019) mgP/l. The seasonal variations of temperature range at the sponge locations is less than 2 degrees, over the

time period in the study (2 years). At the South of Pico location, a dense sponge aggregation in the Azores, this fluctuation has the minimum values, with 0.18ºC variation. This corroborates the finding of other studies, revealing that deep-sea sponges inhabit locations with low nutrients and water temperature and salinity variations. The temperature at sponge aggregations ranges from 8.77 to 11.90 ◦C.

To improve this analysis, other locations can be considered, the new sponge locations identified in recent oceanographic campaigns, and also a comparison analysis with locations without sponges. Also, the density of each sponge aggregation can be considered.

The use of a higher resolution model and the analysis of the tidal components can provide additional information for this study. Also, in-situ currents measurement at one of these sponge aggregations will provide useful information for this study.

This application shows that model results can be used to better describe deep-sea sponge habitats characteristics. This study also contributed to a comprehensive knowledge of the spatial and temporal near-bottom variability of the environmental parameters characterizing the Azores.

Chapter 6- Final remarks

The overall objective of this thesis was to implement biological and biophysical 3-D models to simulate the main physical and biological processes in the Azores, and assess larval dispersal and population connectivity in the Azores deep-sea. Major results highlight the advantages of using coupled model systems to simulate complex marine systems dynamics and different scenarios.

The marine systems are driven mainly by physical processes. The validation of the hydrodynamic model its utmost importance. Also, the biogeochemical and biophysical models used in this work, are coupled with this 3-D MOHID hydrodynamic model results. The hydrodynamic model was validated against Argo buoys data, tide gauge stations and remote sensing data, revealing the model's capability to simulate the general hydrodynamic features in the Azores. The model allows characterizing the dominant currents in the Azores and the major water masses that influence the oceanographic features in the Azores region: Mediterranean Water (MW), East North Atlantic Central Water (ENACW), and the North Atlantic Deep water (NADW).

This study included the implementation of a biogeochemical model for the Azores region. The versatility of the numerical modelling approach of this water quality module of MOHID allows the parameterization of different processes that govern the biogeochemical cycles. Validated against remote sensing data, seasonal phytoplankton patterns are well reproduced, with the typically strong spring bloom, and the lower autumn bloom. The model can simulate the typical deep chlorophyll maximum (DCM), with a higher phytoplankton concentration between 25 and 100 meters in depth, with its characteristics of spatial and temporal variations. Model assessment reveals that MOHID can simulate the general biogeochemical patterns in the entire water column. However, the degree of approximation to the real system and the complexity of biogeochemical models is a challenge to biogeochemical modelling (Vichi et al., 2007). Models

can always improve and reproduce more small-scale processes. This methodology also leaves open the possibility of future model improvements, to better represent the biological and physical processes, responding to new scientific objectives.

The results of the Chapters 2 and 3 are of most importance to characterize marine dynamics, from the surface up to deep-sea. Taking advantage of the hydrodynamic model validated in chapter 1, a particle tracking model was implemented to study larval dispersal in the deep-sea. Larval dispersal studies were performed for a deep-sea sessile organism, *Pheronema carpenteri* a deep-sea sponge, and for non sessile organism, *Chaceon affinis*, a deep-sea red crab (DSRC). Different scenarios and biologic traits were studied: spawning seasonality, larval pelagic duration (PLD), and larval behaviour (including surface-oriented swimming). The model assessment shows how the larval behaviour (either a passive or swimming behaviour) impacts their dispersal patterns, and consequently population connectivity.

The finding of this works shows how the regional patterns of the currents drive the larval dispersion, shaping the population connectivity. Spawning time and the PLD are determinant factors for larval dispersion and population connectivity. Model results indicate the existence of connectivity between Pheronema carpenteri sponge aggregations in the Azores. Central Group seems to have well-connected populations including the MAR. The East Group populations are isolated. The West Group has connectivity with the Central Group. East populations shall be preserved, as also the Central Group populations as source populations for several locations. These results reinforce the importance of maintaining the protection efforts in the MPA (Condor and Princesa Alice), once they are important source populations.

In what regards *Chaceon sp.* Despite the high connectivity of the most plausible scenario, the low percentage of successfully settled larvae demands caution towards any future exploitation.

Model results show how the larval behaviour (either a passive or swimming behaviour) impacts their dispersal patterns, and consequently population connectivity. The swimming behaviour simulated for DSRC larvae contributes to the higher larval travel distance and dispersion patterns. Larval dispersal shows potential connectivity between populations across the Azores archipelago. Model results indicate that the populations in MAR, namely Voador

seamount may be an important source and retaining area for *Chaceon sp*. larvae in the Azores region.

The ultimate goal of this thesis was to showcase the utilization of the constructed models to better understand the ecology of the target sponge species. Taking advantage of the 3-D biogeochemical model results, spatial and temporal biogeochemical properties at specific sponge grounds of the species *Pheronema carpenteri*, were studied. Sponge aggregations are located in regions with low nutrient gradients and low velocities. Nutrients concentrations at these deep-sea sponges locations varies from 0.21 to 0.262 mgN/l, 0.191 to 0.322 mgSi/l. Temperature varies from 8.77 to 11.90 ◦C. South of Pico, a dense sponge ground distinguish from the others by the lowest variance in temperature values (0.18°C).

The current thesis provides fundamental knowledge of the processes driving larval dispersion in the deep sea. As well as a characterization of the biogeochemical environment at the deep-sea sponge grounds in the Azores. It further demonstrated model capabilities to study different biological traits, serving as a baseline to assess deep-sea connectivity and to support management actions and marine spatial plan studies.

This biogeochemical model parameterized for the Azores can now provide data for different ecological and environmental studies. Coupled with the particle tracking model, it can be used to study future climate change scenarios, habitat suitability modelling and species distribution modelling. Furthermore, this modelling approach can provide valuable information for the implementation of protection plans and the establishment and prioritization of future management plans.

As future work, I want to continue running the model until the present date. And improve the parameterization to optimize the solution and surpass the problems identified during the development of this dissertation. MOHID water quality model reveals robustness and versatility leaving room for further improvements. Furthermore, new biogeochemical data from BioGeoArgo buoys or any new insitu data will provide a new opportunity to improve this model solution.

Moreover, it would be interesting to downscale this model for a seamount domain, or coastal areas to increase model resolution and its applicability to other studies.

Regarding the *Pheronema carpenteri* case study, it is my objective to expand the connectivity study including the sponge aggregations recently identified in the Azores region. In addition, a quantitative study, including the size and density of the populations will also be an added value.

As final remarks, the uttermost objective of this thesis was achieved by providing modelling tools and useful data to increase the knowledge of the ecology of the Azores, not only in the deep-sea but in the entire marine ecosystem, contributing to a better representation of the biogeochemical processes, as well the larvae dispersal through numerical model approaches.

References

Abecasis RC, Longnecker N, Schmidt L, Clifton J (2013) Marine conservation in remote small island settings: Factors influencing marine protected area establishment in the Azores. Mar Policy 40:1–9.

Allen JI, Somerfield PJ (2009) A multivariate approach to model skill assessment. J Mar Syst 76:83–94.

Alvarez B, J., N.J. van SRWM (2022) de V, N. B-E, J.L. C, P. C, M.-C. D, M. D, R. D, E. H, J.N.A. H, M. K, M. K, R. M, A.B. MCCP, P. R, K. R, C. S, Vacelet (2022) World Porifera Database. Pheronema carpenteri (Thomson, 1869)

Amorim P, Perán AD, Pham CK, Juliano M (2017) Overview of the Ocean Climatology and Its Variability in the Azores Region of the North Atlantic Including Environmental Characteristics at the Seabed. 4:1–16.

Andutta FP, Kingsford MJ, Wolanski E (2012) 'Sticky water' enables the retention of larvae in a reef mosaic. Estuar Coast Shelf Sci 101:54–63.

Antonio Baeza J, Holstein D, Umaña-Castro R, Mejía-Ortíz LM (2019) Population genetics and biophysical modeling inform metapopulation connectivity of the Caribbean king crab Maguimithrax spinosissimus. Mar Ecol Prog Ser 610:83–97.

Anugerahanti P, Kerimoglu O, Smith SL (2021) Enhancing Ocean Biogeochemical Models With Phytoplankton Variable Composition. Front Mar Sci 8:1–20.

Arhonditsis GB, Adams-Vanharn BA, Nielsen L, Stow CA, Reckhow KH (2006) Evaluation of the current state of mechanistic aquatic biogeochemical modeling: Citation analysis and future perspectives. Environ Sci Technol 40:6547–6554.

Arteaga L, Pahlow M, Oschlies A (2016) Modeled Chl:C ratio and derived estimates of phytoplankton carbon biomass and its contribution to total particulate organic carbon in the global surface ocean. Global Biogeochem Cycles 30:1791–1810.

Aumont O (2005) PISCES biogeochemical model. Report:1–36.

Aumont O, Ethé C, Tagliabue A, Bopp L, Gehlen M (2015) PISCES-v2: An ocean biogeochemical model for carbon and ecosystem studies. Geosci Model Dev 8:2465–2513.

Ayata SD, Lévy M, Aumont O, Sciandra A, Sainte-Marie J, Tagliabue A, Bernard O (2013) Phytoplankton growth formulation in marine ecosystem models: Should we take into account photo-acclimation and variable stoichiometry in oligotrophic areas? J Mar Syst 125:29–40.

Baird ME, Emsley SM, Mcglade JM (2001) Modelling the interacting effects of nutrient uptake, light capture and temperature on phytoplankton growth. J Plankton Res 23:829–840.

Barcelos Ramos EJ, Schulz KG, Voss M, Narciso Á, Müller MN, Reis F V., Cachão M, Azevedo EB (2017) Nutrient-specific responses of a phytoplankton community: A case study of the North Atlantic Gyre, Azores. J Plankton Res 39:744–761.

Barthel D, Tendal OS, Thiel H (1996) A Wandering Population of the Hexactinellid Sponge Pheronema carpenteri on the Continental Slope off Morocco, Northwest Africa. Mar Ecol 17:603–616.

Bashmachnikov I, Nascimento Â, Neves F, Menezes T, Koldunov N V (2015) Distribution of intermediate water masses in the. Ocean Model 11:803–827.

Beazley L, Kenchington E, Murillo FJ, Brickman D, Wang Z, Davies AJ, Roberts EM, Rapp HT (2021) Climate change winner in the deep sea? predicting the impacts of climate change on the distribution of the glass sponge vazella pourtalesii. Mar Ecol Prog Ser 657:1–23.

Bell MJ, Barciela R, Hines A, Martin M, Sellar A, Storkey D (2004) FOAM. Met Office, Exeter

Berline L, Brankart JM, Brasseur P, Ourmières Y, Verron J (2007) Improving the physics of a coupled physical-biogeochemical model of the North Atlantic through data assimilation: Impact on the ecosystem. J Mar Syst 64:153–172.

Bernardes BDL (2007) Hydrodynamical and Ecological Modelling of the North Sea

Bett BJ, Rice AL (1992) The influence of hexactinellid sponge (Pheronema carpenteri) spicules on the patchy distribution of macrobenthos in the porcupine seabight (Bathyal ne atlantic). Ophelia 36:217–226.

Biscoito M, Freitas M, Pajuelo JG, Triay-Portella R, Santana JI, Costa AL, Delgado J, González JA (2015) Sex-structure, depth distribution, intermoult period and reproductive pattern of the deep-sea red crab Chaceon affinis (Brachyura, Geryonidae) in two populations in the north-eastern Atlantic. Deep Res Part I Oceanogr Res Pap 95:99–114.

Black KS, Peppe OC, Gust G (2003) Erodibility of pelagic carbonate ooze in the northeast Atlantic. J Exp Mar Bio Ecol 285–286:143–163.

Bode M, Leis JM, Mason LB, Williamson DH, Harrison HB, Choukroun S, Jones GP (2019) Successful validation of a larval dispersal model using genetic parentage data. PLoS Biol 17:1–13.

Bonfardeci A, Caruso A, Bartolini A, Bassinot F, Blanc-Valleron MM (2018) Distribution and ecology of the Globigerinoides ruber — Globigerinoides elongatus morphotypes in the Azores region during the late Pleistocene-Holocene. Palaeogeogr Palaeoclimatol Palaeoecol 491:92–111.

Botsford LW, White JW, Coffroth MA, Paris CB, Planes S, Shearer TL, Thorrold SR, Jones GP (2009) Connectivity and resilience of coral reef metapopulations in marine protected areas: Matching empirical efforts to predictive needs. Coral Reefs 28:327–337.

Boury-Esnault N, Efremova S, BÉzac C, Vacelet J (1999) Reproduction of a hexactinellid sponge: First description of gastrulation by cellular delamination in the porifera. Invertebr Reprod Dev 35:187–201.

Bowie GL, Mills WB, Porcella DB, Campbell CL, Pagenkopf JR, Rupp GL, Johnson KM, Chan PWH, Gherini SA (1985) Rates , Constants , and Kinetics Formulations in S urface Water Quali , t y Modeling (Second Edition).

Bracco A, Liu G, Galaska MP, Quattrini AM, Herrera S (2019) Integrating physical circulation models and genetic approaches to investigate population connectivity in deep-sea corals. J Mar Syst 198:103189.

Bracher A, Bouman HA, Brewin RJW, Bricaud A, Brotas V, Ciotti AM, Clementson L, Devred E, Di Cicco A, Dutkiewicz S, Hardman-Mountford NJ, Hickman AE, Hieronymi M, Hirata T, Losa SN, Mouw CB, Organelli E, Raitsos DE, Uitz J, Vogt M, Wolanin A (2017) Obtaining phytoplankton diversity from ocean color: A scientific roadmap for future development. Front Mar Sci 4:1–15.

Braga-Henriques A, Porteiro FM, Ribeiro PA, De Matos V, Sampaio Í, Ocaña O, Santos RS (2013) Diversity, distribution and spatial structure of the cold-water coral fauna of the Azores (NE Atlantic). Biogeosciences 10:4009–4036.

Brzezinski MA (1985) THE Si:C:N RATIO OF MARINE DIATOMS: INTERSPECIFIC VARIABILITY AND THE EFFECT OF SOME ENVIRONMENTAL VARIABLES. J Phycol 21:347–357.

Buchanan PJ, Matear RJ, Chase Z, Phipps SJ, Bindoff NL (2018) Dynamic Biological Functioning Important for Simulating and Stabilizing Ocean Biogeochemistry. Global Biogeochem Cycles 32:565–593.

Buitenhuis ET, Rivkin RB, Séailley S, Le Quéré C (2010) Biogeochemical fluxes through microzooplankton. Global Biogeochem Cycles 24.

Burchard, H., Bolding, K., Villarreal M (1999) GOTM – a general ocean turbulence model. Theory, applications and test cases.

Busch K, Taboada S, Riesgo A, Koutsouveli V, Ríos P, Cristobo J, Franke A, Getzlaff K, Schmidt C, Biastoch A, Hentschel U (2021) Population connectivity of fan-shaped sponge holobionts in the deep Cantabrian Sea. Deep Res Part I Oceanogr Res Pap 167:103427.

Cáceres C, Taboada FG, Höfer J, Anadón R (2013) Phytoplankton Growth and Microzooplankton Grazing in the Subtropical Northeast Atlantic. PLoS One 8.

Calbet A, Atienza D, Henriksen CI, Saiz E, Adey TR (2009) Zooplankton grazing in the Atlantic Ocean: A

latitudinal study. Deep Res Part II Top Stud Oceanogr 56:954–963.
Caldeira RMA, Reis JC (2017) The Azores confluence zone. Front Mar Sci 4:1–14.
Campuzano FJ, Juliano M, Fernandes R, Pinto L, Neves R (2013) Downscalling From the Deep Ocean To the Estuarine Intertidal Areas: an Operational Framework for the Portuguese Exclusive Economic Zone. 6th SCACR – Int Short Course/Conference Appl Coast Res Fig:1–9.
Capotondi A, Jacox M, Bowler C, Kavanaugh M, Lehodey P, Barrie D, Brodie S, Chaffron S, Cheng W, Dias DF, Eveillard D, Guidi L, Iudicone D, Lovenduski NS, Nye JA, Ortiz I, Pirhalla D, Pozo Buil M, Saba V, Sheridan S, Siedlecki S, Subramanian A, de Vargas C, Di Lorenzo E, Doney SC, Hermann AJ, Joyce T, Merrifield M, Miller AJ, Not F, Pesant S (2019) Observational Needs Supporting Marine Ecosystems Modeling and Forecasting: From the Global Ocean to Regional and Coastal Systems. Front Mar Sci 6:1–30.
Carmo V, Santos M, Menezes GM, Loureiro CM, Lambardi P, Martins A (2013) Variability of zooplankton communities at Condor seamount and surrounding areas, Azores (NE Atlantic). Deep Res Part II Top Stud Oceanogr 98:63–74.
Cathalot C, Van Oevelen D, Cox TJS, Kutti T, Lavaleye M, Duineveld G, Meysman FJR (2015) Cold-water coral reefs and adjacent sponge grounds: Hotspots of benthic respiration and organic carbon cycling in the deep sea. Front Mar Sci 2:1–12.
Chai F, Dugdale RC, Barber RT, Peng TH, Wilkerson FP (2002) One-dimensional ecosystem model of the equatorial Pacific upwelling system. Part II: Sensitivity analysis and comparison with JGOFS EqPac data. Deep Res Part II Top Stud Oceanogr 49:2747–2768.
Chen B, Laws EA, Liu H, Huang B (2014) Estimating microzooplankton grazing half-saturation constants from dilution experiments with nonlinear feeding kinetics. Limnol Oceanogr 59:639–644.
Chenillat F, Rivière P, Ohman MD (2021) On the sensitivity of plankton ecosystem models to the formulation of zooplankton grazing. PLoS One 16.
Colaço A, Creemers M, Mienis F, Beazley L, Hanz U, Bouchard-Marmen M, Kenchington E, Pham C (2020) Deliverable D4.5 (SponGES) - Deep-sea Sponge Grounds Ecosystems of the North Atlantic: an integrated approach towards their preservation and sustainable exploitation.
Collins CD (1980) Formulation and Validation of a Mathematical Model of Phytoplankton Growth. Ecology 61.
Comas-Rodríguez I, Hernández-Guerra A, Fraile-Nuez E, Martínez-Marrero A, Benítez-Barrios VM, Pérez-Hernández MD, Vélez-Belchí P (2011) The Azores Current System from a meridional section at 24.5°W. J Geophys Res Ocean 116:1–9.
Combes M, Vaz S, Grehan A, Morato T, Arnaud-Haond S, Dominguez-Carrió C, Fox A, González-Irusta JM, Johnson D, Callery O, Davies A, Fauconnet L, Kenchington E, Orejas C, Roberts JM, Taranto G, Menot L (2021) Systematic Conservation Planning at an Ocean Basin Scale: Identifying a Viable Network of Deep-Sea Protected Areas in the North Atlantic and the Mediterranean. Front Mar Sci 8:1–27.
Connolly SR, Baird AH (2010) Estimating dispersal potential for marine larvae: Dynamic models applied to scleractinian corals. Ecology 91:3572–3583.
Cornec M, Claustre H, Mignot A, Guidi L, Lacour L, Poteau A, D'Ortenzio F, Gentili B, Schmechtig C (2021) Deep Chlorophyll Maxima in the Global Ocean: Occurrences, Drivers and Characteristics. Global Biogeochem Cycles 35:1–30.
Costa P, Gómez B, Venâncio A, Pérez E, Pérez-Muñuzuri V (2012) Using the Regional Ocean Modelling System (ROMS) to improve the sea surface temperature predictions of the MERCATOR Ocean System. Sci Mar 76:165–175.
Cowen RK, Sponaugle S (2009) Larval dispersal and marine population connectivity. Ann Rev Mar Sci 1:443–466.
Creemers MF, Pham C, Defise A, Goulard J, Smith V, Silva AP, Colaço A (2019) Sponges On The Rocks:

Exploring A New Deep-Sea Sponge Ground Of The Azores (Portugal). Deep Life Vol 12 Vol 12 7-8.

Criales MM, Chérubin L, Gandy R, Garavelli L, Ghannami MA, Crowley C (2019) Blue crab larval dispersal highlights population connectivity and implications for fishery management. Mar Ecol Prog Ser 625:53–70.

Cunha M, Génio L, Pradillon F, Clavel Henry M, Beaulieu S, Birch J, Campuzano F, Carretón M, De Leo F, Gula J, Laming S, Lindsay D, Matos F, Metaxas A, Meyer-Kaiser K, Mills S, Queiroga H, Rodrigues C, Sarrazin J, Watanabe H, Young R, Young C (2020) Foresight Workshop on Advances in Ocean Biological Observations: a sustained system for deep-ocean meroplankton. Res Ideas Outcomes 6.

Daewel U, Schrum C, MacDonald JI (2019) Towards end-to-end (E2E) modelling in a consistent NPZD-F modelling framework (ECOSMO E2E-v1.0): Application to the North Sea and Baltic Sea. Geosci Model Dev 12:1765–1789.

DeMaster DJ (2001) Marine Silica Cycle. In: *Encyclopedia of Ocean Sciences*. Steele JH (ed) Academic Press, Oxford, p 1659–1667

Doney SC, Doney SC, Lima I, Lima I, Lindsay K, Lindsay K, Moore JK, Moore JK, Dutkiewicz S, Dutkiewicz S (2001) Marine Biogeochemical Modeling: Society 14:93–107.

Dorandeu J, Le Traon PY (1999) Effects of global mean atmospheric pressure variations on mean sea level changes from TOPEX/Poseidon. J Atmos Ocean Technol 16:1279–1283.

Edwards KP, Barciela R, Butenschön M (2012) Validation of the NEMO-ERSEM operational ecosystem model for the North West European continental shelf. Ocean Sci 8:983–1000.

EMODnet Bathymetry Consortium (2018) No Title.

Eppley RW, Thomas WH (1969) Comparison of Half-Saturation Constants for Growth and Nitrate Uptake of Marine Phytoplankton. J Phycol 5:375–379.

Espinoza-Morriberon D, Echevin V, Tam J, Ledesma J, Oliveros-Ramos R, Ramos J, Romero CY (2016) Biogeochemical validation of an interannual simulation of the ROMS-PISCES coupled model in the Southeast Pacific. Rev Peru Biol 23:159–168.

FAO (2008) International guidelines: Management of deep-sea fisheries in the high seas. Rome.

Fasham MJR, Ducklow HW, McKelvie SM (1990) A nitrogen-based model of plankton dynamics in the oceanic mixed layer. J Mar Res 48:591–639.

Fasham MJR, Platt T, Irwin B, Jones K (1985) Factors affecting the spatial pattern of the deep chlorophyll maximum in the region of the Azores front. Prog Oceanogr 14:129–165.

Fennel K, Gehlen M, Brasseur P, Brown CW, Ciavatta S, Cossarini G, Crise A, Edwards CA, Ford D, Friedrichs MAM, Gregoire M, Jones E, Kim HC, Lamouroux J, Murtugudde R, Perruche C (2019) Advancing marine biogeochemical and ecosystem reanalyses and forecasts as tools for monitoring and managing ecosystem health. Front Mar Sci 6:1–9.

Fennel K, Wilkin J, Levin J, Moisan J, O'Reilly J, Haidvogel D (2006) Nitrogen cycling in the Middle Atlantic Bight: Results from a three-dimensional model and implications for the North Atlantic nitrogen budget. Global Biogeochem Cycles 20:1–14.

Fennel W (2009) Parameterizations of truncated food web models from the perspective of an end-to-end model approach. J Mar Syst 76:171–185.

Fogarty MJ, Botsford LW (2007) Population connectivity and spatial management of marine fisheries. Oceanography 20:112–123.

Foster NL, Paris CB, Kool JT, Baums IB, Stevens JR, Sanchez JA, Bastidas C, Agudelo C, Bush P, Day O, Ferrari R, Gonzalez P, Gore S, Guppy R, McCartney MA, McCoy C, Mendes J, Srinivasan A, Steiner S, Vermeij MJA, Weil E, Mumby PJ (2012) Connectivity of Caribbean coral populations: Complementary insights from empirical and modelled gene flow. Mol Ecol 21:1143–1157.

Franz G, Delpey TM, Brito D, Neves R, Leitão P, Pinto L (2017) Modelling of sediment transport and morphological evolution under the combined action of waves and currents. Ocean Sci 13:673–690.

Friedlander A, Afonso P, Morato T, Carreiro-Silva M, Fontes J, Abecasis D, Ballesteros E, Botelho A, Diaz D, Das D, Dominguez-Carrió C, Caselle J, Estep A, Goodell W, Milla D, Ocaña O, Pham C, Pipa T, Rose P, Salinas de León P, Schmiing M, Silva C, Taranto G, Tempera F, Thompson C, Verdura J, Sala E, Gonçalves E (2019) Blue Azores - The best kept secret in the Atlantic. Sci Rep to Reg Gov Azores:1–107.

Gaines SD, Gaylord B, Gerber LR, Hastings PA, Kinlan BP (2005) The ecological consequences of dispersal in the sea. Oceanography 20:90–99.

Garcia HE, Boyer TP, Baranova OK, Locarnini RA, Mishonov AV, Grodsky A, Paver CR, Weathers KW, Smolyar IV, Reagan JR, Seidov D, Zweng MM (2018) World Ocean Atlas 2018: Product Documentation. A. Mishonov, Technical Editor. 1:1–20.

Gary SF, Fox AD, Biastoch A, Roberts JM, Cunningham SA (2020) Larval behaviour, dispersal and population connectivity in the deep sea. Sci Rep 10:1–12.

Giacomello E, Menezes G (2012) CONDOR Observatory for long-term study and monitoring of Azorean seamount ecosystems. Final Project Report. 261 PP + 9 ANNEXES.

Gnanadesikan A, Dunne JP, John J (2011) What ocean biogeochemical models can tell us about bottom-up control of ecosystem variability. ICES J Mar Sci 68:1030–1044.

Gomes-Pereira JN, Carmo V, Catarino D, Jakobsen J, Alvarez H, Aguilar R, Hart J, Giacomello E, Menezes G, Stefanni S, Colaço A, Morato T, Santos RS, Tempera F, Porteiro F (2017) Cold-water corals and large hydrozoans provide essential fish habitat for Lappanella fasciata and Benthocometes robustus. Deep Res Part II Top Stud Oceanogr 145:33–48.

Gómez-Zambrano HJ, López-Ríos VI, Toro-Botero FM (2017) New methodology for calibration of hydrodynamic models in curved open-channel flow. Rev Fac Ing 2017:82–91.

Guerao G, Abelló P, Castejón MR (1996) Morphology of the larval stages of the deep-sea crab geryon longipes (Brachyura: Geryonidae). J Nat Hist 30:505–521.

Guillas KC, Kahn AS, Grant N, Archer SK, Dunham A, Leys SP (2019) Settlement of juvenile glass sponges and other invertebrate cryptofauna on the Hecate Strait glass sponge reefs. Invertebr Biol 138:1–11.

Guillou N, Neill SP, Robins PE (2018) Characterising the tidal stream power resource around France using a high-resolution harmonic database. Renew Energy 123:706–718.

Gutknecht E, Reffray G, Gehlen M, Triyulianti I, Berlianty D, Gaspar P (2016) Evaluation of an operational ocean model configuration at 1/12° spatial resolution for the Indonesian seas (NEMO2.3/INDO12) - Part 2: Biogeochemistry. Geosci Model Dev 9:1523–1543.

Haney JD, Jackson GA (1996) Modeling phytoplankton growth rates. J Plankton Res 18:63–85.

Hashioka T, Vogt M, Yamanaka Y, Le Quéré C, Buitenhuis ET, Aita MN, Alvain S, Bopp L, Hirata T, Lima I, Sailley S, Doney SC (2013) Phytoplankton competition during the spring bloom in four plankton functional type models. Biogeosciences 10:6833–6850.

Helgers J, Paris CB, Sebille E Van (2013) Connectivity Modeling System User ' s Guide Authors : 1–49.

Henriksen HJ, Troldborg L, Nyegaard P, Sonnenborg TO, Refsgaard JC, Madsen B (2003) Methodology for construction, calibration and validation of a national hydrological model for Denmark. J Hydrol 280:52–71.

Henry LA, Roberts JM (2014) Applying the OSPAR habitat definition of deep-sea sponge aggregations to verify suspected records of the habitat in UK waters. JNCC Report.

Hilário A, Cunha MR (2013) Notes on a mating event of the deep-sea crab Chaecon affinis in the Gorringe Bank (NE Atlantic). Deep Res Part II Top Stud Oceanogr 92:58–62.

Hilário A, Metaxas A, Gaudron SM, Howell KL, Mercier A, Mestre NC, Ross RE, Thurnherr AM, Young C (2015) Estimating dispersal distance in the deep sea: Challenges and applications to marine reserves. Front Mar Sci 2:1–14.

Hinrichsen HH, Dickey-Collas M, Huret M, Peck MA, Vikebø FB (2011) Evaluating the suitability of coupled

biophysical models for fishery management. ICES J Mar Sci 68:1478–1487.
Hirose K, Kamiya H (2003) Vertical nutrient distributions in the western North Pacific ocean: Simple model for estimating nutrient upwelling, export flux and consumption rates. J Oceanogr 59:149–161.
Hjelmervik K (2012) Demonstration of Comparison Methods for Ocean Model Validation. Open Ocean Eng J 5:1–14.
Holgate SJ, Matthews A, Woodworth PL, Rickards LJ, Tamisiea ME, Bradshaw E, Foden PR, Gordon KM, Jevrejeva S, Pugh J (2013) New Data Systems and Products at the Permanent Service for Mean Sea Level. 493–504.
Holstein DM, Paris CB, Mumby PJ (2014) Consistency and inconsistency in multispecies population network dynamics of coral reef ecosystems. Mar Ecol Prog Ser 499:1–18.
Howell KL, Piechaud N, Downie AL, Kenny A (2016) The distribution of deep-sea sponge aggregations in the North Atlantic and implications for their effective spatial management. Deep Res Part I Oceanogr Res Pap 115:309–320.
Ilyina T, Six KD, Segschneider J, Maier-Reimer E, Li H, Núñez-Riboni I (2013) Global ocean biogeochemistry model HAMOCC: Model architecture and performance as component of the MPI-Earth system model in different CMIP5 experimental realizations. J Adv Model Earth Syst 5:287–315.
IMAR (2018) BLUE AZORES PROGRAM : EXPEDITION 2018 ON BOARD THE NRP GAGO COUTINHO BLUE AZORES PROGRAM : EXPEDITION 2018 (NRP Almirante Gago Coutinho).
Instituto Superior Técnico (2003) Mohid Description: Description of the 3D water modeling system Mohid (2003).
IST (2003) Water System model Hydrodynamic Module, MOHID.
Itoh S, Yasuda I, Saito H, Tsuda A, Komatsu K (2015) Mixed layer depth and chlorophyll a: Profiling float observations in the Kuroshio-Oyashio Extension region. J Mar Syst 151:1–14.
J. C. Leitão PLFBRFRNPM (2003) Emergency activities support by an operational forecast system ’e The Prestige accident \n. 4th Semin Mar Environ .
Janjic ZI (2003) A nonhydrostatic model based on a new approach. Meteorol Atmos Phys 82:271–285.
Jones BT, Solow A, Ji R (2016) Resource allocation for lagrangian tracking. J Atmos Ocean Technol 33:1225–1235.
Juliano MF, Alves M (2006) The South Atlantic Subtropical Front / Current of St . Helena. Proc 8 ICSHMO, Foz do Iguaçu, Brazil, April 24-28, 2006, INPE:1283–1288.
Juliano MF, Alves MLGR (2007) The atlantic subtropical front/current systems of Azores and St. Helena. J Phys Oceanogr 37:2573–2598.
Juliano MMF, Neves R, Rodrigues PPGW, Junior JL, Fernandes R (2012) Aplicação da Plataforma MOHID para simulação computacional de deriva oceânica de petróleo na bacia de Campos - RJ. 161–172.
Julien P (2019) Global_Analysis_Forecast_Bio_001_028. EU Copernicus Mar Serv Inf:18.
Jung HC, Moon BK, Lee H, Choi JH, Kim HK, Park JY, Byun YH, Lim YJ, Lee J (2020) Development and Assessment of NEMO(v3.6)-TOPAZ(v2), a Coupled Global Ocean Biogeochemistry Model. Asia-Pacific J Atmos Sci 56:411–428.
Kane A, Moulin C, Thiria S, Bopp L, Berrada M, Tagliabue A, Crépon M, Aumont O, Badran F (2011) Improving the parameters of a global ocean biogeochemical model via variational assimilation of in situ data at five time series stations. J Geophys Res Ocean 116:1–14.
Karpowicz M, Ejsmont-Karabin J, Kozłowska J, Feniova I, Dzialowski AR (2020) Zooplankton community responses to oxygen stress. Water (Switzerland) 12:1–20.
Katavouta A, Thompson KR (2016) Downscaling ocean conditions with application to the Gulf of Maine, Scotian Shelf and adjacent deep ocean. Ocean Model 104:54–72.
Kelly P, Sulkin SD, Van Heukelem WF (1982) A dispersal model for larvae of the deep sea red crab Geryon quinquedens based upon behavioral regulation of vertical migration in the hatching stage. Mar Biol

72:35–43.
Kenchington E, Wang Z, Lirette C, Murillo FJ, Guijarro J, Yashayaev I, Maldonado M (2019) Connectivity modelling of areas closed to protect vulnerable marine ecosystems in the northwest Atlantic. Deep Res Part I Oceanogr Res Pap 143:85–103.
Kishi MJ, Kashiwai M, Ware DM, Megrey BA, Eslinger DL, Werner FE, Noguchi-Aita M, Azumaya T, Fujii M, Hashimoto S, Huang D, Iizumi H, Ishida Y, Kang S, Kantakov GA, Kim H cheol, Komatsu K, Navrotsky V V., Smith SL, Tadokoro K, Tsuda A, Yamamura O, Yamanaka Y, Yokouchi K, Yoshie N, Zhang J, Zuenko YI, Zvalinsky VI (2007) NEMURO-a lower trophic level model for the North Pacific marine ecosystem. Ecol Modell 202:12–25.
Kool JT, Moilanen A, Treml EA (2013) Population connectivity: Recent advances and new perspectives. Landsc Ecol 28:165–185.
Kough AS (2014) Population connectivity and larval dispersal of caribbean spiny lobster. Diss Abstr Int Vol 76, no 01, suppl B, 191 p 2014:1–191.
Kough AS, Paris CB, Butler IV MJ (2013) Larval Connectivity and the International Management of Fisheries. PLoS One 8.
Kwiatkowski L, Yool A, Allen JI, Anderson TR, Barciela R, Buitenhuis ET, Butenschön M, Enright C, Halloran PR, Le Quéré C, De Mora L, Racault MF, Sinha B, Totterdell IJ, Cox PM (2014) IMarNet: An ocean biogeochemistry model intercomparison project within a common physical ocean modelling framework. Biogeosciences 11:7291–7304.
Lafon V, Martins A, Figueiredo M, Rodrigues M, Bashmachnikov I, Mendonça A, Macedo L, Goulart N (2004) Sea surface temperature distribution in the Azores region. Part I: AVHRR imagery and in situ data processing.
Lan Smith S, Pahlow M, Merico A, Wirtz KW (2011) Optimality-based modeling of planktonic organisms. Limnol Oceanogr 56:2080–2094.
Lancelot C, Spitz Y, Gypens N, Ruddick K, Becquevort S, Rousseau V, Lacroix G, Billen G (2005) Modelling diatom and Phaeocystis blooms and nutrient cycles in the Southern Bight of the North Sea: The MIRO model. Mar Ecol Prog Ser 289:63–78.
Landeria JM, Tamura H (2018) Morphology of the first zoea of Chaceon affinis (A. Milne-Edwards & Bouvier, 1894) and occurrence of Chaceon spp. larvae (Decapoda: Brachyura: Gerynonidae) in the Canary Islands waters, Northeastern Atlantic. Zootaxa 4413:579–585.
Lázaro C, Juliano MF, Fernandes MJ (2013) Semi-automatic determination of the Azores Current axis using satellite altimetry: Application to the study of the current variability during 1995-2006. Adv Sp Res 51:2155–2170.
Legaloudec O, Desportes C, Levier B (2015) For Global Sea Physical Analysis and Forecasting Product GLOBAL _ ANALYSIS _ FORECAST _ PHYS _ 001 _ 002. 1–100.
Leis JM (2020) Perspectives on Larval Behaviour in Biophysical Modelling of Larval Dispersal in Marine, Demersal Fishes. Oceans 2:1–25.
Leitão PC, Mateus M, Braunschweig F, Fernandes L, Neves R (2008) Modelling coastal systems: the MOHID water numerical lab. Perspect Integr Coast Zo Manag South Am:77–88.
Lellouche JM, Greiner E, Le Galloudec O, Garric G, Regnier C, Drevillon M, Benkiran M, Testut CE, Bourdalle-Badie R, Gasparin F, Hernandez O, Levier B, Drillet Y, Remy E, Le Traon PY (2018) Recent updates to the Copernicus Marine Service global ocean monitoring and forecasting real-time 1g 12° high-resolution system. Ocean Sci 14:1093–1126.
Lenz J, Harris R, Wiebe P, Skjoldal H-R, Huntley ME (Ed. . (2000) ICES Zooplankton Methodology Manual.
Leonardo HDP (2022) Environmental quality assessment in a coastal area by the integration of monitoring data and modelling.
Leys SP, Lauzon NRJ (1998) Hexactinellid sponge ecology: Growth rates and seasonality in deep water

sponges. J Exp Mar Bio Ecol 230:111–129.
Lima MJ, Sala I, Caldeira RMA (2020) Physical Connectivity Between the NE Atlantic Seamounts. Front Mar Sci 7:1–17.
Lin P, Li CW (2002) A σ-coordinate three-dimensional numerical model for surface wave propagation. Int J Numer Methods Fluids 38:1045–1068.
Lindemann C, St. John MA (2014) A seasonal diary of phytoplankton in the North Atlantic. Front Mar Sci 1:1–6.
Litchman E, Klausmeier CA, Schofield OM, Falkowski PG (2007) The role of functional traits and trade-offs in structuring phytoplankton communities: Scaling from cellular to ecosystem level. Ecol Lett 10:1170–1181.
Litchman E, de Tezanos Pinto P, Edwards KF, Klausmeier CA, Kremer CT, Thomas MK (2015) Global biogeochemical impacts of phytoplankton: A trait-based perspective. J Ecol 103:1384–1396.
Longmore C, Trueman CN, Neat F, Jorde PE, Knutsen H, Stefanni S, Catarino D, Milton JA, Mariani S (2014) Ocean-scale connectivity and life cycle reconstruction in a deep-sea fish. Can J Fish Aquat Sci 71:1312–1323.
Lopes D (2005) Zootaxa, Hexactinosida (Porifera, Hexactinellida). 56:43–56.
López Abellán LJ, Balguerías E, Fernández-Vergaz V (2002) Life history characteristics of the deep-sea crab Chaceon affinis population off Tenerife (Canary Islands). Fish Res 58:231–239.
Losa S, Dutkiewicz S, Losch M, Oelker J, Soppa M, Trimborn S, Xi H, Bracher A (2019) On modeling the Southern Ocean Phytoplankton Functional Types. Biogeosciences Discuss:1–37.
Losa SN, Soppa MA, Dinter T, Wolanin A, Brewin RJW, Bricaud A, Oelker J, Peeken I, Gentili B, Rozanov V, Bracher A (2017) Synergistic exploitation of hyper- and multi-spectral precursor sentinel measurements to determine phytoplankton functional types (SynSenPFT). Front Mar Sci 4:1–22.
Lyard FH, Allain DJ, Cancet M, Carrère L, Picot N (2021) FES2014 global ocean tides atlas: design and performances Florent. Ocean Sci 17:615–649.
Macedo MF, Duarte P, Ferreira JG, Alves M, Costa V (2000) Analysis of the deep chlorophyll maximum across the Azores Front. Hydrobiologia 441:155–172.
Maldonado M (2006) The ecology of the sponge larva. Can J Zool 84:175–194.
Maldonado M, Aguilar R, Bannister RJ, James J, Conway KW, Dayton PK, Cristina D, Gutt J, Kelly M, Kenchington ELR, Leys SP, Shirley A, Tendal OS, Rapp HT, Klaus R, Young CM (2016) Marine Animal Forests.
Maldonado M, Aguilar R, Bannister RJ, James J, Conway KW, Dayton PK, Cristina D, Gutt J, Kelly M, Kenchington ELR, Leys SP, Shirley A, Tendal OS, Rapp HT, Klaus R, Young CM (2015) Sponge Grounds as Key Marine Habitats: A Synthetic Review of Types, Structure, Functional Roles, and Conservation Concerns. In: *Marine Animal Forests*. Rossi S, Bramanti L, Gori A, Orejas Saco del Valle C (eds) Springer International Publishing
Maldonado M, Carmona MC, Velásquez Z, Puig A, Cruzado A, López A, Young CM (2005) Siliceous sponges as a silicon sink: An overlooked aspect of benthopelagic coupling in the marine silicon cycle. Limnol Oceanogr 50:799–809.
Maldonado M, López-Acosta M, Sitjà C, García-Puig M, Galobart C, Ercilla G, Leynaert A (2019) Sponge skeletons as an important sink of silicon in the global oceans. Nat Geosci 12:815–822.
Maldonado M, Young CM (1999) Effects of the duration of larval life on postlarval stages of the demosponge Sigmadocia caerulea. J Exp Mar Bio Ecol 232:9–21.
Marañón E (2005) Phytoplankton growth rates in the Atlantic subtropical gyres. Limnol Oceanogr 50:299–310.
Marañón E, Behrenfeld MJ, González N, Mouriño B, Zubkov M V. (2003) High variability of primary production in oligotrophic waters of the Atlantic Ocean: Uncoupling from phytoplankton biomass

and size structure. Mar Ecol Prog Ser 257:1–11.
Marañón E, Pérez V, Fernández E, Anadón R, Bode A, González N, Huskin I, Isla A, Morán XAG, Mouriño B, Quevedo M, Robinson C, Serret P, Teira E, Varela MM, Woodward EMS, Zubkov M V. (2007) Planktonic carbon budget in the eastern subtropical North Atlantic. Aquat Microb Ecol 48:261–275.
Mariani S, Uriz MJ, Turon X, Alcoverro T (2006) Dispersal strategies in sponge larvae: Integrating the life history of larvae and the hydrologic component. Oecologia 149:174–184.
Marrero-Díaz Á, Rodríguez-Santana Á, Machín F, Pelegrí JL (2006) Analytic salinity-temperature relations for the upper-thermocline waters of the eastern North Atlantic subtropical gyre. Sci Mar 70:167–175.
Martínez-Rivera S, Stevens BG (2020) Embryonic development and fecundity of the red deep-sea crab Chaceon quinquedens (Smith, 1879) (Decapoda: Brachyura: Geryonidae) in the Mid-Atlantic Bight determined by image analysis. J Crustac Biol 40:230–236.
Martinez E, Antoine D, D'Ortenzio F, De Boyer Montégut C (2011) Phytoplankton spring and fall blooms in the North Atlantic in the 1980s and 2000s. J Geophys Res Ocean 116:1–11.
Martins F. RN e PCL (1998) A three-dimensional hydrodynamic model with generic vertical coordinate. Proc Hydroinformatics:1403–1410.
Matear RJ, Hirst AC (2003) Long-term changes in dissolved oxygen concentrations in the ocean caused by protracted global warming. Global Biogeochem Cycles 17:1125.
Mateus M (2006) A process-oriented biogeochemical model for marine ecosystems: development, numerical study, and application. 246.
Mattern JP, Song H, Edwards CA, Moore AM, Fiechter J (2017) Data assimilation of physical and chlorophyll a observations in the California Current System using two biogeochemical models. Ocean Model 109:55–71.
McKinley GA, Ritzer AL, Lovenduski NS (2018) Mechanisms of northern North Atlantic biomass variability. Biogeosciences 15:6049–6066.
Ménesguen A, Cugier P, Loyer S, Vanhoutte-Brunier A, Hoch T, Guillaud JF, Gohin F (2007) Two- or three-layered box-models versus fine 3D models for coastal ecological modelling? A comparative study in the English Channel (Western Europe). J Mar Syst 64:47–65.
Metaxas A, Saunders M (2009) Quantifying the "Bio-" Components in Biophysical Models of Larval Transport in Marine Benthic Invertebrates: Advances and Pitfalls. Biol Bull 216:257–272.
Mitra A, Castellani C, Gentleman WC, Jónasdóttir SH, Flynn KJ, Bode A, Halsband C, Kuhn P, Licandro P, Agersted MD, Calbet A, Lindeque PK, Koppelmann R, Møller EF, Gislason A, Nielsen TG, St. John M (2014) Bridging the gap between marine biogeochemical and fisheries sciences; configuring the zooplankton link. Prog Oceanogr 129:176–199.
Moll A, Radach G (2003) Review of three-dimensional ecological modelling related to the North Sea shelf system. Prog Oceanogr 57:175–217.
Moore JK, Doney SC, Kleypas JA, Glover DM, Fung IY (2001) An intermediate complexity marine ecosystem model for the global domain. Deep Res Part II Top Stud Oceanogr 49:403–462.
Morato T, Afonso P, Menezes GM, Santos RS, Silva MA (2020a) Editorial: The Azores Marine Ecosystem: An Open Window Into North Atlantic Open Ocean and Deep-Sea Environments. Front Mar Sci 7:1–3.
Morato T, Colaço MA, Juliano M (2016a) Azores case study. MIDAS Newsl Summer 201.
Morato T, Dominguez-Carrió C, Mohn C, Ocaña Vicente O, Ramos M, Rodrigues L, Sampaio Í, Taranto GH, Fauconnet L, Tojeira I, Gonçalves, J. E, Carreiro-Silva M (2021) Dense cold-water coral garden of Paragorgia johnsoni suggests the importance of the Mid-Atlantic Ridge for deep-sea biodiversity. Ecol Evol 11:16426–16433.
Morato T, González-Irusta JM, Dominguez-Carrió C, Wei CL, Davies A, Sweetman AK, Taranto GH, Beazley

L, García-Alegre A, Grehan A, Laffargue P, Murillo FJ, Sacau M, Vaz S, Kenchington E, Arnaud-Haond S, Callery O, Chimienti G, Cordes E, Egilsdottir H, Freiwald A, Gasbarro R, Gutiérrez-Zárate C, Gianni M, Gilkinson K, Wareham Hayes VE, Hebbeln D, Hedges K, Henry LA, Johnson D, Koen-Alonso M, Lirette C, Mastrototaro F, Menot L, Molodtsova T, Durán Muñoz P, Orejas C, Pennino MG, Puerta P, Ragnarsson S, Ramiro-Sánchez B, Rice J, Rivera J, Roberts JM, Ross SW, Rueda JL, Sampaio Í, Snelgrove P, Stirling D, Treble MA, Urra J, Vad J, van Oevelen D, Watling L, Walkusz W, Wienberg C, Woillez M, Levin LA, Carreiro-Silva M (2020b) Climate-induced changes in the suitable habitat of cold-water corals and commercially important deep-sea fishes in the North Atlantic. Glob Chang Biol 26:2181–2202.

Morato T, Lemey E, Menezes G, Pham CK, Brito J, Soszynski A, Pitcher TJ, Heymans JJ (2016b) Food-web and ecosystem structure of the open-ocean and deep-sea environments of the azores, NE Atlantic. Front Mar Sci 3:1–13.

Morato T, Machete M, Kitchingman A, Tempera F, Lai S, Menezes G, Pitcher TJ, Santos RS (2008) Abundance and distribution of seamounts in the Azores. Mar Ecol Prog Ser 357:17–21.

Mouw CB, Barnett A, McKinley GA, Gloege L, Pilcher D (2016) Global ocean particulate organic carbon flux merged with satellite parameters. Earth Syst Sci Data 8:531–541.

Mulder C, Hendriks AJ (2014) Half-saturation constants in functional responses. Glob Ecol Conserv 2:161–169.

Narciso Á, Gallo F, Valente A, Cachão M, Cros L, Azevedo EB, e Ramos JB (2016) Seasonal and interannual variations in coccolithophore abundance off Terceira Island, Azores (Central North Atlantic). Cont Shelf Res 117:43–56.

National Centers for Environmental Prediction, National Weather Service, NOAA USD of C (2015) NCEP GFS 0.25 Degree Global Forecast Grids Historical Archive.

Neves RJJ, Coelho H, Taborda R (2003) Ocean Margin Systems.

North EW, Gallego A, Petitgas P, Ådlandsvik B, Bartsch J, Brickman D, Browman HI, Edwards K, Fiksen Ø, Hermann AJ, others (2009) Manual of recommended practices for modelling physical-biological interactions during fish early life.

Ospar (2010) Background Document for Deep-sea sponge aggregations Biodiversity Series. 88.

de Pablo H, Sobrinho J, Garcia M, Campuzano F, Juliano M, Neves R (2019) Validation of the 3D-MOHID hydrodynamic model for the Tagus coastal area. Water (Switzerland) 11.

Palma C, Lillebø AI, Borges C, Souto M, Pereira E, Duarte AC, Abreu MP de (2012) Water column characterisation on the Azores platform and at the sea mounts south of the archipelago. Mar Pollut Bull 64:1884–1894.

Paris CB, Helgers J, van Sebille E, Srinivasan A (2013) Connectivity Modeling System: A probabilistic modeling tool for the multi-scale tracking of biotic and abiotic variability in the ocean. Environ Model Softw 42:47–54.

Pata PR, Yñiguez AT, Deauna JDL, De Guzman AB, Jimenez CR, Rosario RTB Del, Villanoy CL (2021) Insights into the environmental conditions contributing to variability in the larval recruitment of the tropical sardine Sardinella lemuru. Ecol Modell 451.

Peña MA, Masson D, Callendar W (2016) Annual plankton dynamics in a coupled physical–biological model of the Strait of Georgia, British Columbia. Prog Oceanogr 146:58–74.

Peran AD, Pham CK, Amorim P, Cardigos F, Tempera F, Morato T (2016) Seafloor characteristics in the azores region (North Atlantic). Front Mar Sci 3:2014–2017.

Perruche C, Hameau A, Paul J, Régnier C, Drévillon M (2016) QUALITY INFORMATION DOCUMENT For Global Biogeochemical Analysis and Forecast Product GLOBAL_ANALYSIS_FORECAST_BIO_001_014 CHANGE RECORD Issue Date Description of Change Author Validated By. 1–38.

Pham CK, Vandeperre F, Menezes G, Porteiro F, Isidro E, Morato T (2015) The importance of deep-sea

vulnerable marine ecosystems for demersal fish in the Azores. Deep Res Part I Oceanogr Res Pap 96:80–88.

Phelps JJC (2015) Modelling Hydrodynamic Transport and Larval Dispersal in North-East Atlantic Shelf Seas.

Pinho M., Santos R., Melo O., Isidro E., Medeiros-Leal W., Gonçalves J. (2020) Estimates of biomass and potential yield for the deep-water red crab, Chaceon affinis and the toothed rock crab, Cancer bellianus (Decapoda: Brachyura) off the Azores (Mid-North Atlantic). Arquipel Life Mar Sci 37:21–36.

Pinho MR, Gonçalves JM, Martins HR, Menezes GM (2001) Some aspects of the biology of the deep-water crab, Chaceon affinis (Milne-Edwards and Bouvier, 1894) off the Azores. Fish Res 51:283–295.

Pinto L, Campuzano F, Juliano M, Fernandes R, Neves R (2014) Implementation and validation of an operational model for the Portuguese exclusive economic zone. 3.as JORNADAS Eng HIDROGRÁFICA.

Piroddi C, Teixeira H, Lynam CP, Smith C, Alvarez MC, Mazik K, Andonegi E, Churilova T, Tedesco L, Chifflet M, Chust G, Galparsoro I, Garcia AC, Kämäri M, Kryvenko O, Lassalle G, Neville S, Niquil N, Papadopoulou N, Rossberg AG, Suslin V, Uyarra MC (2015) Using ecological models to assess ecosystem status in support of the European Marine Strategy Framework Directive. Ecol Indic 58:175–191.

PSMSL (2018) Tide Gauge data. http://www.psmsl.org/data/obtaining/ (accessed 1 March 2018)

Puerta P, Johnson C, Carreiro-silva M, Henry L, Kenchington E, Morato T, Kazanidis G, Rueda JL, Urra J, Ross S, Wei C, González-irusta JM, Muller-karger FE (2020) Influence of Water Masses on the Biodiversity and Biogeography of Deep-Sea Benthic Ecosystems in the North Atlantic. 7:1–25.

Ragueneau O, Tréguer P, Leynaert A, Anderson RF, Brzezinski MA, DeMaster DJ, Dugdale RC, Dymond J, Fischer G, François R, Heinze C, Maier-Reimer E, Martin-Jézéquel V, Nelson DM, Quéguiner B (2000) A review of the Si cycle in the modern ocean: Recent progress and missing gaps in the application of biogenic opal as a paleoproductivity proxy. Glob Planet Change 26:317–365.

Rice AL, Thurston MH, New AL (1990) Dense aggregations of a hexactinellid sponge, Pheronema carpenteri, in the Porcupine Seabight (northeast Atlantic Ocean), and possible causes. Prog Oceanogr:179–196.

Riflet G, Juliano M, Fernandes L, Leitão, Paulo Chambel Neves R (2008) Operational Ocean forecasting of the Portuguese waters. Mercat Ocean Q Newsl 30.

Rivera SM (2018) Reproductive Biology of the Female Deep-Sea Red Crab, CHACEON QUINQUEDENS (SMITH, 1879), IN THE MID-ATLANTIC BIGHT

Roberts E, Bowers D, Meyer H, Samuelsen A, Rapp H, Cárdenas P (2021) Water masses constrain the distribution of deep-sea sponges in the North Atlantic Ocean and Nordic Seas. Mar Ecol Prog Ser 659:75–96.

Robson BJ (2014) State of the art in modelling of phosphorus in aquatic systems: Review, criticisms and commentary. Environ Model Softw 61:339–359.

Rocha C, Edwards CA, Roughan M, Cetina-Heredia P, Kerry C (2019) A high-resolution biogeochemical model (ROMS 3.4+bio-Fennel) of the East Australian current system. Geosci Model Dev 12:441–456.

Roemmich D, Alford MH, Claustre H, Johnson KS, King B, Moum J, Oke PR, Owens WB, Pouliquen S, Purkey S, Scanderbeg M, Suga T, Wijffels SE, Zilberman N, Bakker D, Baringer MO, Belbeoch M, Bittig HC, Boss E, Calil P, Carse F, Carval T, Chai F, Conchubhair DO, D'Ortenzio F, Dall'Olmo G, Desbruyères D, Fennel K, Fer I, Ferrari R, Forget G, Freeland H, Fujiki T, Gehlen M, Greenan B, Hallberg R, Hibiya T, Hosoda S, Jayne S, Jochum M, Johnson GC, Kang KR, Kolodziejczyk N, Koertzinger A, Le Traon PY, Lenn YD, Maze G, Mork KA, Morris T, Nagai T, Nash J, Garabato AN, Olsen A, Pattabhi RR, Prakash S, Riser S, Schmechtig C, Shroyer E, Sterl A, Sutton P, Talley L, Tanhua T, Thierry V, Thomalla S, Toole J, Troisi A, Trull T, Turton JD, Velez-Belchi PJ, Walczowski W, Wang H, Wanninkhof R, Waterhouse A,

Watson A, Wilson C, Wong AP, Xu J, Yasuda I (2019) On the future of Argo: A global, full-depth, multi-disciplinary array. Front Mar Sci 6.

Roman MR, Boicourt WC (1999) Dispersion and recruitment of crab larvae in the Chesapeake Bay plume: Physical and biological controls. Estuaries 22:563–574.

Ross RE, Howell KL (2013) Use of predictive habitat modelling to assess the distribution and extent of the current protection of 'listed' deep-sea habitats. Divers Distrib 19:433–445.

Ross RE, Nimmo-Smith WAM, Howell KL (2016) Increasing the depth of current understanding: Sensitivity testing of deep-sea larval dispersal models for ecologists. PLoS One 11:1–25.

Ross RE, Nimmo-Smith WAM, Howell KL (2017) Towards 'ecological coherence': Assessing larval dispersal within a network of existing Marine Protected Areas. Deep Res Part I Oceanogr Res Pap 126:128–138.

Ross RE, Nimmo-Smith WAM, Torres R, Howell KL (2020) Comparing Deep-Sea Larval Dispersal Models: A Cautionary Tale for Ecology and Conservation. Front Mar Sci 7:1–15.

Ross RE, Wort EJG, Howell KL (2019) Combining Distribution and Dispersal Models to Identify a Particularly Vulnerable Marine Ecosystem. Front Mar Sci 6:1–12.

Sala I, Caldeira RMA, Estrada-allis SN, Froufe E, Couvelard X (2013) Lagrangian transport pathways in the northeast Atlantic and their environmental impact. 3:40–60.

Sala I, Harrison CS, Caldeira RMA (2016) The role of the Azores Archipelago in capturing and retaining incoming particles. J Mar Syst 154:146–156.

Salon S, Cossarini G, Bolzon G, Feudale L, Lazzari P, Teruzzi A, Solidoro C, Crise A (2019) Novel metrics based on biogeochemical argo data to improve the model uncertainty evaluation of the cmems mediterranean marine ecosystem forecasts. Ocean Sci 15:997–1022.

Samuelsen A, Schrum C, Yumruktepe VÇ, Daewel U, Roberts EM (2022) Environmental Change at Deep-Sea Sponge Habitats Over the Last Half Century: A Model Hindcast Study for the Age of Anthropogenic Climate Change. Front Mar Sci 9:1–17.

Santos M, Moita MT, Bashmachnikov I, Menezes GM, Carmo V, Loureiro CM, Mendonça A, Silva AF, Martins A (2013) Phytoplankton variability and oceanographic conditions at Condor seamount, Azores (NE Atlantic). Deep Res Part II Top Stud Oceanogr 98:52–62.

Santos R, Medeiros-Leal W, Novoa-Pabon A, Silva H, Pinho M (2021) Demersal fish assemblages on seamounts exploited by fishing in the Azores (NE Atlantic). J Appl Ichthyol 37:198–215.

Santos R, Medeiros-Leal W, Pinho M (2020) Stock assessment prioritization in the Azores: procedures, current challenges and recommendations. Arquipelago Life Mar Sci 37:20–45.

Santos R, Pinho M, Melo O, Gonçalves J, Leocádio A, Menezes G, Isidro E (2019) Biological and ecological aspects of the deep-water red crab populations inhabiting isolated seamounts to the west of the Azores (Mid-Atlantic Ridge). Fish Oceanogr 28:723–734.

Sathyendranath S, Brewin RJW, Brockmann C, Brotas V, Calton B, Chuprin A, Cipollini P, Couto AB, Dingle J, Doerffer R, Donlon C, Dowell M, Farman A, Grant M, Groom S, Horseman A, Jackson T, Krasemann H, Lavender S, Martinez-Vicente V, Mazeran C, Mélin F, Moore TS, Müller D, Regner P, Roy S, Steele CJ, Steinmetz F, Swinton J, Taberner M, Thompson A, Valente A, Zühlke M, Brando VE, Feng H, Feldman G, Franz BA, Frouin R, Gould RW, Hooker SB, Kahru M, Kratzer S, Mitchell BG, Muller-Karger FE, Sosik HM, Voss KJ, Werdell J, Platt T (2019) An ocean-colour time series for use in climate studies: The experience of the ocean-colour climate change initiative (OC-CCI). Sensors (Switzerland) 19.

Sathyendranath S, Jackson T, Brockmann C, Brotas V, Calton B, Chuprin A, Clements O, Cipollini P, Danne O, Dingle J, Donlon C, Grant M, Groom S, Krasemann H, Lavender S, Mazeran C, Mélin F, Müller D, Steinmetz F, Valente A, Zühlke M, Feldman G, Franz B, Frouin R, Werdell J, Platt T (2021) ESA Ocean Colour Climate Change Initiative (Ocean_Colour_cci): Version 5.0 Data. https://catalogue.ceda.ac.uk/uuid/66534da90ed44abebfc1b08adca4f9c3%0A

van Sebille E, Griffies SM, Abernathey R, Adams TP, Berloff P, Biastoch A, Blanke B, Chassignet EP, Cheng Y, Cotter CJ, Deleersnijder E, Döös K, Drake HF, Drijfhout S, Gary SF, Heemink AW, Kjellsson J, Koszalka IM, Lange M, Lique C, MacGilchrist GA, Marsh R, Mayorga Adame CG, McAdam R, Nencioli F, Paris CB, Piggott MD, Polton JA, Rühs S, Shah SHAM, Thomas MD, Wang J, Wolfram PJ, Zanna L, Zika JD (2018) Lagrangian ocean analysis: Fundamentals and practices. Ocean Model 121:49–75.

Selkoe KA, Toonen RJ (2011) Marine connectivity: A new look at pelagic larval duration and genetic metrics of dispersal. Mar Ecol Prog Ser 436:291–305.

Sharada MK, Yajnik KS, Swathi PS (2005) Evaluation of six relations of the kinetics of uptake by phytoplankton in multi-nutrient environment using JGOFS experimental results. Deep Res Part II Top Stud Oceanogr 52:1892–1909.

Shen M, Duan H, Cao Z, Xue K, Loiselle S, Yesou H (2017) Determination of the downwelling diffuse attenuation coefficient of lakewater with the sentinel-3A OLCI. Remote Sens 9.

Siddorn JR, Allen JI, Blackford JC, Gilbert FJ, Holt JT, Holt MW, Osborne JP, Proctor R, Mills DK (2007) Modelling the hydrodynamics and ecosystem of the North-West European continental shelf for operational oceanography. 65:417–429.

Silva A, Brotas V, Valente A, Sá C, Diniz T, Patarra RF, álvaro N V., Neto AI (2013) Coccolithophore species as indicators of surface oceanographic conditions in the vicinity of Azores islands. Estuar Coast Shelf Sci 118:50–59.

Da Silva Cortinhas MC, Ortega I, de Souza Alves Teodoro S, Proietti M, Masello A, Kersanach R, Barutot R, Ramos Vieira RR, Firpo C, Mauna C, Cestari Dumont LF (2022) Defining deep-sea fishery stocks through multiple methods: The case of the red crab Chaceon notialis Manning & Holthuis, 1989 (Crustacea, Decapoda, Geryonidae) in the Southwestern Atlantic. Deep Res Part I Oceanogr Res Pap 179:103659.

Simons RD, Siegel DA, Brown KS (2013) Model sensitivity and robustness in the estimation of larval transport: A study of particle tracking parameters. J Mar Syst 119–120:19–29.

Sommer U, Charalampous E, Genitsaris S, Moustaka-Gouni M (2017) Benefits, costs and taxonomic distribution of marine phytoplankton body size. J Plankton Res 39:494–508.

Somoza L, Medialdea T, González FJ, Calado A, Afonso A, Albuquerque M, Asensio-Ramos M, Bettencourt R, Blasco I, Candón JA, Carreiro-Silva M, Cid C, De Ignacio C, López-Pamo E, Machancoses S, Ramos B, Ribeiro LP, Rincón-Tomás B, Santofimia E, Souto M, Tojeira I, Viegas C, Madureira P (2020) Multidisciplinary Scientific Cruise to the Northern Mid-Atlantic Ridge and Azores Archipelago. Front Mar Sci 7:1–9.

Stark, J.D., C. J. Donlon MJM and MEM (2007) STIA : An operational, high resolution, real time, global sea surface temperature analysis systemOceans 07 IEEE Aberdeen, conference proceedings. Marine challenges: coastline to deep sea. Aberdeen, Scotland.IEEE.

Stevens BG, Guida V (2016) Depth and temperature distribution, morphometrics, and sex ratios of red deepsea crab (Chaceon quinquedens) at 4 sampling sites in the mid-atlantic bight. Fish Bull 114:343–359.

Stow CA, Jolliff J, McGillicuddy DJ, Doney SC, Allen JI, Friedrichs MAM, Rose KA, Wallhead P, Lynch DR, McGillicuddy DJ, Werner FE (2009) Skill assessment for coupled biological/physical models of marine systems. J Mar Syst 76:4–15.

Sulkin S, van Heukelem W (1980) Ecological and Evolutionary Significance of Nutritional Flexibility in Planktotrophic Larvae of the Deep Sea Red Crab Geryon quinquedens and the Stone Crab (Menippe mercenaria). Mar Ecol Prog Ser 2:91–95.

Sverdrup HU (1953) On conditions for the vernal blooming of phytoplankton. ICES J Mar Sci 18:287–295.

Swearer SE, Treml EA, Shima JS (2019) A review of biophysical models of marine larval dispersal. Oceanogr Mar Biol 57:325–356.

Taylorl AH, Geider RJ, Gilbertl FJH (1997) Seasonal and latitudinal dependencies of phytoplankton carbon-to-chlorophyll a ratios: results of a modelling study. Mar Ecol Prog Ser 152:51–66.

Teira E, Mouriño B, Marañón E, Pérez V, Pazó MJ, Serret P, De Armas D, Escánez J, Woodward EMS, Fernández E (2005) Variability of chlorophyll and primary production in the Eastern North Atlantic Subtropical Gyre: Potential factors affecting phytoplankton activity. Deep Res Part I Oceanogr Res Pap 52:569–588.

Tempera F, Atchoi E, Amorim P, Gomes-pereira J (2013) Adding new Macaronesian habitat types from the Azores.

Thomson RE, Fine I V. (2003) Estimating mixed layer depth from oceanic profile data. J Atmos Ocean Technol 20:319–329.

Toublanc F, Ayoub NK, Lyard F, Marsaleix P, Allain DJ (2018) Tidal downscaling from the open ocean to the coast: a new approach applied to the Bay of Biscay. Ocean Model 124:16–32.

Trancoso AR, Braunschweig F, Chambel Leitão P, Obermann M, Neves R (2009) An advanced modelling tool for simulating complex river systems. Sci Total Environ 407:3004–3016.

Treml EA, Roberts JJ, Chao Y, Halpin PN, Possingham HP, Riginos C (2012) Reproductive output and duration of the pelagic larval stage determine seascape-wide connectivity of marine populations. Integr Comp Biol 52:525–537.

Tuset VM, Espinosa DI, García-Mederos A, Santana JI, González JA (2011) Egg development and fecundity estimation in deep-sea red crab, Chaceon affinis (Geryonidae), off the Canary Islands (NE Atlantic). Fish Res 109:373–378.

UK Met Office (2005) GHRSST Level 4 OSTIA Global Foundation Sea Surface Temperature Analysis. http://podaac.jpl.nasa.gov/dataset/UKMO-L4HRfnd-GLOB-OSTIA (accessed 1 March 2020)

Valente A dos SFG (2013) Climatic patterns and physical controls of chlorophyll-a in the northeast Atlantic. University of the Azores

Vallino JJ (2000) Improving marine ecosystem models: Use of data assimilation and mesocosm experiments. J Mar Res 58:117–164.

Vic C, Gula J, Roullet G, Pradillon F (2018) Dispersion of deep-sea hydrothermal vent effluents and larvae by submesoscale and tidal currents. Deep Res Part I Oceanogr Res Pap 133:1–18.

Vichi M, Masina S, Navarra A (2007a) A generalized model of pelagic biogeochemistry for the global ocean ecosystem. Part II: Numerical simulations. J Mar Syst 64:110–134.

Vichi M, Pinardi N, Masina S (2007b) A generalized model of pelagic biogeochemistry for the global ocean ecosystem. Part I: Theory. J Mar Syst.

Viegas CN, Nunes S, Fernandes R, Neves R (2009) Streams contribution on bathing water quality after rainfall events in Costa do Estoril - A tool to implement an alert system for bathing water quality. J Coast Res 2009:1691–1695.

Vieira RP, Bett BJ, Jones DOB, Durden JM, Morris KJ, Cunha MR, Trueman CN, Ruhl HA (2020) Deep-sea sponge aggregations (Pheronema carpenteri) in the Porcupine Seabight (NE Atlantic) potentially degraded by demersal fishing. Prog Oceanogr 183:102189.

Wang S, Kenchington E, Wang Z, Davies AJ (2021) Life in the Fast Lane: Modeling the Fate of Glass Sponge Larvae in the Gulf Stream. Front Mar Sci 8:1–24.

Wang S, Kenchington EL, Wang Z, Yashayaev I, Davies AJ (2020) 3-D ocean particle tracking modeling reveals extensive vertical movement and downstream interdependence of closed areas in the northwest Atlantic. Sci Rep 10:1–18.

Ward BA, Friedrichs MAM, Anderson TR, Oschlies A (2010) Parameter optimisation techniques and the problem of underdetermination in marine biogeochemical models. J Mar Syst.

Ward BA, Schartau M, Oschlies A, Martin AP, Follows MJ, Anderson TR (2013) When is a biogeochemical model too complex? Objective model reduction and selection for North Atlantic time-series sites.

Prog Oceanogr 116:49–65.
Water I, Water LS (2019) Azores ecoregion – Ecosystem overview. 1–18.
Weber TS, Deutsch C (2010) Ocean nutrient ratios governed by plankton biogeography. Nature 467:550–554.
Weinberg JR, Dahlgren TG, Trowbridge N, Halanych KM (2003) Genetic differences within and between species of deep-sea crabs (Chaceon) from the North Atlantic Ocean. Biol Bull 204:318–326.
Werdell PJ, Bailey SW (2005) An improved in-situ bio-optical data set for ocean color algorithm development and satellite data product validation. Remote Sens Environ 98:122–140.
Werner FE, Cowen RK, Paris CB (2007) Coupled Biological and Physical Models. Oceanography 20:54–69.
White M (2003) Comparison of near seabed currents at two locations in the Porcupine Sea Bight - Implications for benthic fauna. J Mar Biol Assoc United Kingdom 83:683–686.
Wong APS, Wijffels SE, Riser SC, Pouliquen S, Hosoda S, Roemmich D, Gilson J, Johnson GC, Martini K, Murphy DJ, Scanderbeg M, Bhaskar TVSU, Buck JJH, Merceur F, Carval T, Maze G, Cabanes C, André X, Belbéoch M, Ignaszewski M, Baringer MON, Schmid C, Lyman JM, Mctaggart KE, Purkey SG, Zilberman N, Alkire MB, Swift D, Owens WB, Jayne SR, Hersh C, Robbins P, West-mack D, Bahr F, Yoshida S, Sutton PJH, Cancouët R, Coatanoan C, Dobbler D, Juan AG, Gourrion J, Kolodziejczyk N, Bernard V, Bourlès B, Loch SG, Mowat M, Turton J, Rao EPR (2020) Argo Data 1999 – 2019 : Two Million Temperature-Salinity Profiles and Subsurface Velocity Observations From a Global Array of Profiling Floats Edited by : 7:1–23.
Wood S, Paris CB, Ridgwell A, Hendy EJ (2014) Modelling dispersal and connectivity of broadcast spawning corals at the global scale. Glob Ecol Biogeogr 23:1–11.
Xavier JR, Rees DJ, Pereira R, Colaço A, Pham CK, Carvalho FC (2021) Diversity, Distribution and Phylogenetic Relationships of Deep-Sea Lithistids (Porifera, Heteroscleromorpha) of the Azores Archipelago. Front Mar Sci 8.
Xavier JR, Tojeira I, Van Soest RWM (2015) On a hexactinellid sponge aggregation at the Great Meteor seamount (North-east Atlantic). J Mar Biol Assoc United Kingdom 95:1389–1394.
Xi H, Losa SN, Mangin A, Soppa MA, Garnesson P, Demaria J, Liu Y, d'Andon OHF, Bracher A (2020) Global retrieval of phytoplankton functional types based on empirical orthogonal functions using CMEMS GlobColour merged products and further extension to OLCI data. Remote Sens Environ 240:111704.
Xu Q, Lin H, Liu Y, Lv X, Cheng Y (2008) Data assimilation in a coupled physical-biological model for the Bohai Sea and the Northern Yellow Sea. Mar Freshw Res 59:529–539.
Yamanaka Y, Yoshie N, Fujii M, Aita MN, Kishi MJ (2004) An ecosystem model coupled with nitrogen-silicon-carbon cycles applied to station A7 in the northwestern Pacific. J Oceanogr 60:227–241.
Yearsley JM, Sigwart JD (2011) Larval transport modeling of deep-sea invertebrates can aid the search for undiscovered populations. PLoS One 6.
Yool A, Popova EE, Anderson TR (2013) MEDUSA-2.0: An intermediate complexity biogeochemical model of the marine carbon cycle for climate change and ocean acidification studies. Geosci Model Dev 6:1767–1811.
Yool A, Tyrrell T (2003) Role of diatoms in regulating the ocean's silicon cycle. Global Biogeochem Cycles 17.
Young CM, He R, Emlet RB, Li Y, Qian H, Arellano SM, Van Gaest A, Bennett KC, Wolf M, Smart TI, Rice ME (2012) Dispersal of deep-sea larvae from the intra-American seas: Simulations of trajectories using ocean models. Integr Comp Biol 52:483–496.
Zhang RH, Tian F, Wang X (2018) A New Hybrid Coupled Model of Atmosphere, Ocean Physics, and Ocean Biogeochemistry to Represent Biogeophysical Feedback Effects in the Tropical Pacific. J Adv Model Earth Syst 10:1901–1923.

List of Figures

List of Tables

List of Acronyms

ADW- Atlantic Deep Water

AEEZ- Azores Economic Exclusive Zone

BGC- BioGeoChemical

CG- Central group

Chl_a- Chlorophyll_a

CMEMS- Copernicus Marine Environment Monitoring Service

CMS- Connectivity Modelling System

DSRC- Deep-Sea Red Crab

EEZ- Economic Exclusive Zone

EG- Eastern group

ENACW-Eastern North Atlantic Central Water

FES -Finite Element Solution

FUV- Fraction of Unexplained Variation

GFS- Global Forecast System

HAMMOC-Hamburg ocean carbon cycle model

Kd- Diffuse attenuation coefficient (of downwelling radiative flux in sea water)

MAR- Mid-Atlantic Ridge

MOHID- MOdelling HYDrodynamics (in portuguese MOdelação Hidrodinâmica)

MPA- Marine Protected Areas

MW- Mediterranean Water

N- Nitrogen

NASA'sOBPG- North American Spatial Agency -Ocean Biology Processing Group

NEMURO - North Pacific Ecosystem Model for Understanding Regional Oceanography

O- Oxygen

P Phosphorous

PDD- Particle Density Distribution

PISCES - Pelagic Interactions Scheme for Carbon and Ecosystem Studies)

PLD- Pelagic Larval Duration

RMSE- Root Mean Squared Error

Si Silicate

SSS- Sea Surface Salinity

SST- Sea Surface Temperature

VME- Vulnerable Marine Ecosystems

WG- Western group

WOA- World Ocean Atlas

Annex I

Inorganic phosphorous- Surface

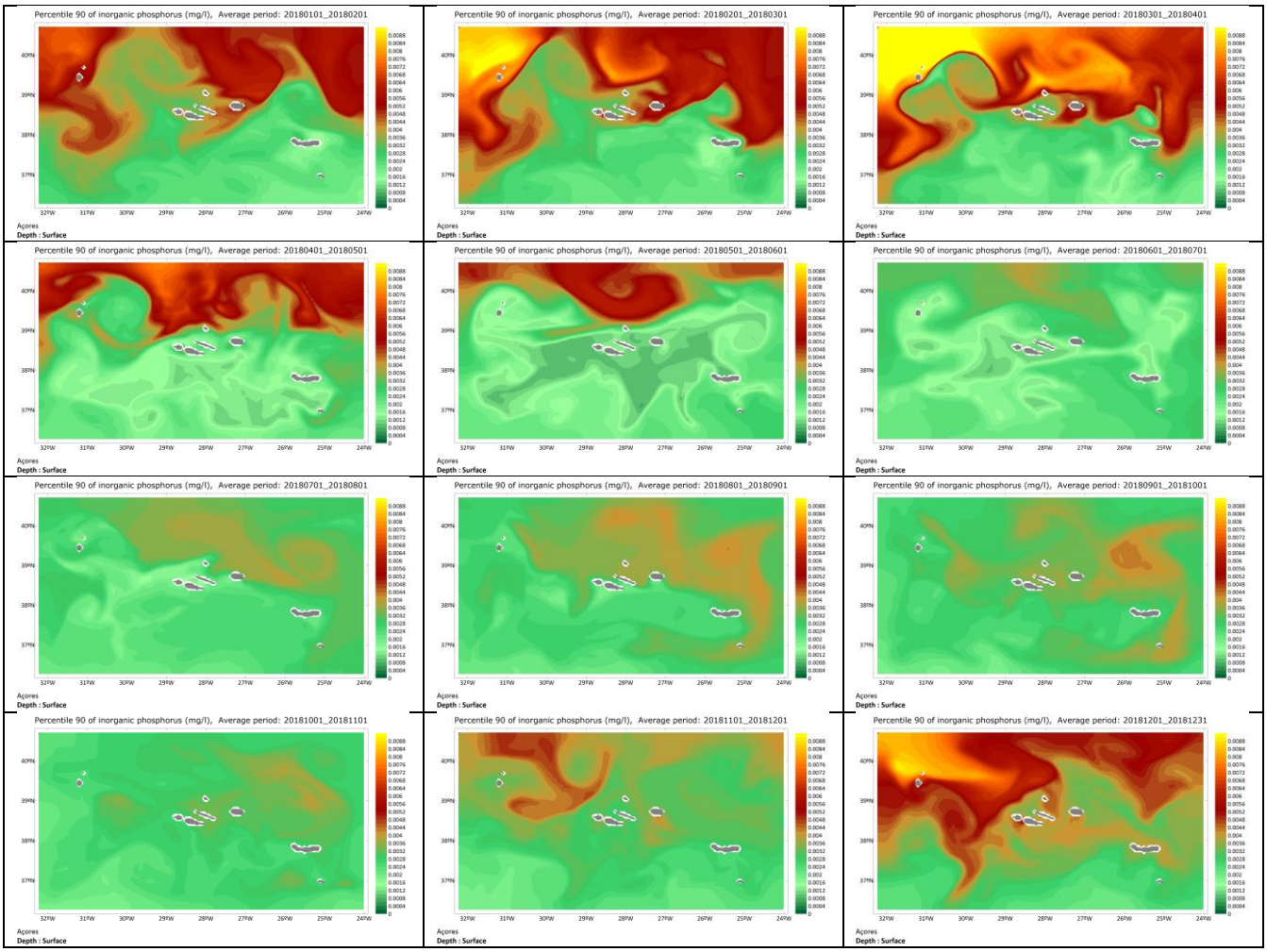

Figure A1- Monthly average of inorganic phosphorous at the surface for 2018

Dissolved silica- surface

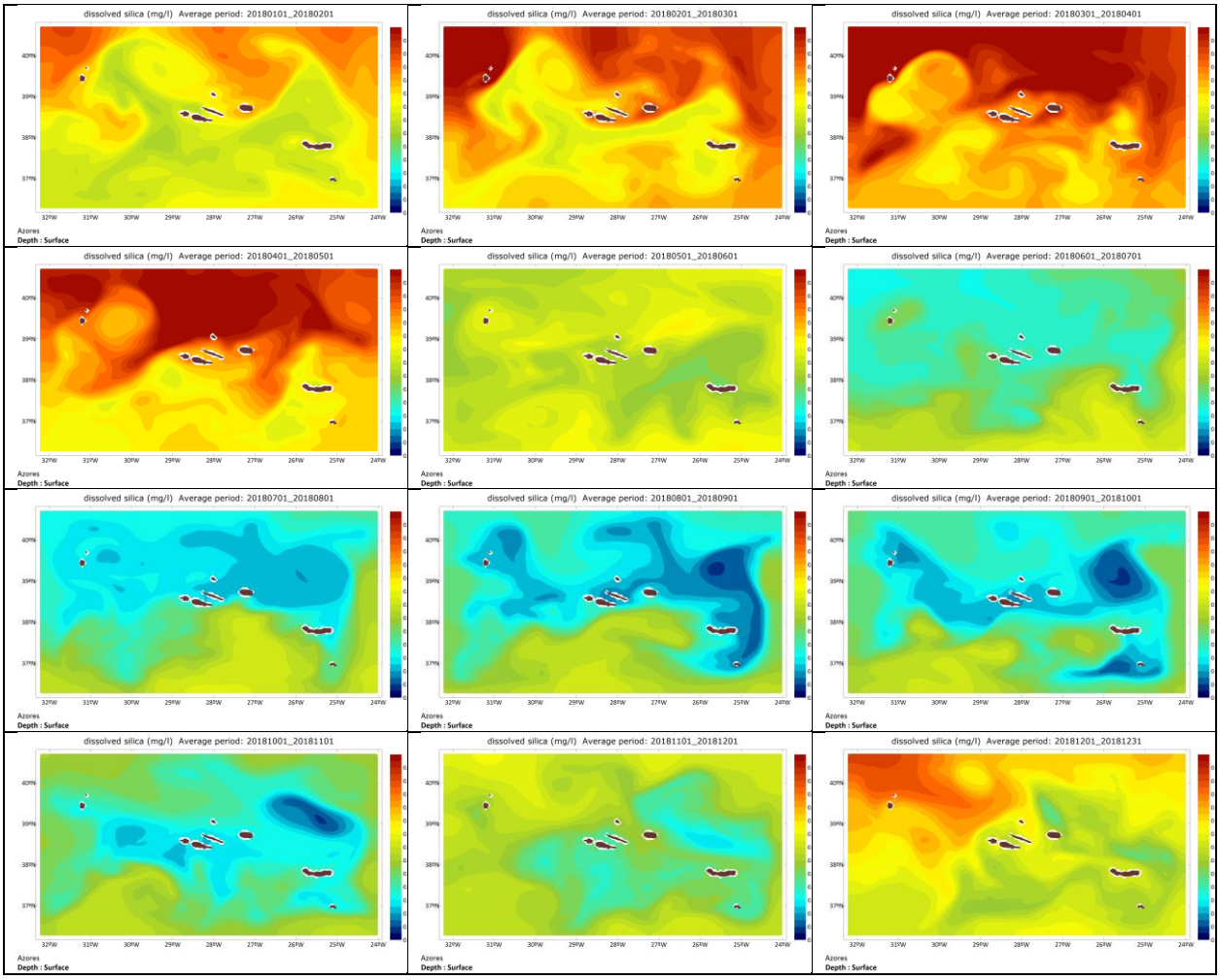

Figure A2 Monthly average of dissolved silica at the surface for 2018

Annex II

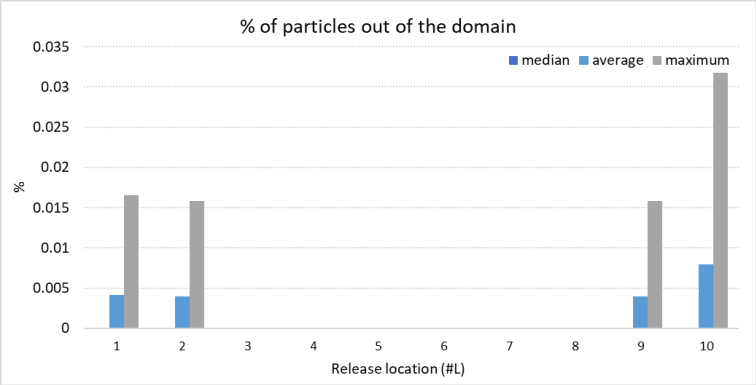

Figure A- Median, average and maximum percentage of particles advected out of the domain, from all the locations, considering all the scenarios

Table 1A- Connectivity tables detailing the percentage of particles released in each location (rows) that settled in each recruitment area (columns). For the different scenarios: a) Annual PLD15; b) Annual PLD30; c)March PLD 15; d) March PLD30; e) and PL330Annual/March and October for 2017

a)Annual PLD 15

location	1	2	3	4	5	6	7	8	9	10
1	0.5713%									
2	0.0397%	0.0000%		0.0001%	0.0000%					
3			5.6448%							
4				5.6540%	0.4207%					
5				0.0093%	1.7308%					
6			0.0145%	0.0545%	0.1381%	1.0909%	0.6496%			
7						0.0005%	2.4358%			
8								4.7421%		
9									1.6738%	
10									0.0003%	0.7600%

b) Annual PLD30

location	1	2	3	4	5	6	7	8	9	10
1	0.1367%	0.0768%		0.0086%	0.0037%					
2	0.2493%	0.0000%	0.0002%	0.0311%	0.0069%					
3			3.9452%			0.0004%	0.0001%			
4		0.0001%	0.0004%	3.4696%	1.1518%	0.0093%	0.0000%			
5	0.0002%	0.0201%	0.0001%	0.1699%	0.9759%	0.0002%	0.0002%	0.1040%		
6		0.0037%	0.2970%	0.1073%	0.1316%	0.8052%	0.7177%			
7			0.0001%	0.0008%	0.0001%	0.0118%	1.6633%	0.0001%		
8					0.0010%	0.0000%	0.0009%	2.3386%		
9									1.1073%	0.0062%
10									0.0636%	0.5057%

c) March_PLD_15_2017

location	1	2	3	4	5	6	7	8	9	10
1	0.0012%									
2		0.0000%								
3			4.8707%							
4				4.1795%	0.0591%					
5					1.5391%					
6						0.3511%	4.9544%			
7							1.4782%			
8								1.9522%		
9									2.7241%	
10										1.5824%

d) March_PLD_30_2017

location	1	2	3	4	5	6	7	8	9	10
1	0.0053%									
2	0.0638%	0.0000%								
3			2.8944%							
4			0.0006%	0.9000%	0.1879%	0.0328%				
5				0.0023%	0.1001%		0.0006%	0.9065%		
6						0.8093%	2.2109%			
7						0.0152%	1.0674%			
8								0.1381%		
9									3.2022%	
10										2.1869%

e) Outubro_PLD_15_2017

location	1	2	3	4	5	6	7	8	9	10
1	0.0901%									
2		0.0000%								
3			7.8418%							
4				0.2903%	2.7546%					
5					3.0864%					
6			0.0936%	0.0006%	0.0012%	0.0778%				
7							3.0126%			
8								3.3895%		
9										
10									0.0006%	2.2975%

f) Outubro_PLD_15_2017

location	1	2	3	4	5	6	7	8	9	10
1	0.1563%									
2		0.0000%								
3			17.1366%							
4				0.6033%	7.2004%					
5				0.0012%	6.9037%					
6			0.2885%	0.0023%	0.0047%	0.2025%				
7							6.4267%			
8								6.8931%		
9										
10										5.5665%